TESIS DE LA UNIVERSIDAD DE ZARAGOZA

2013

102

José Rufino Solera Ureña

Evaluation of blood-tissue tracer exchange taking account of diffusion and consumption: application to MRI

Departamento
Instituto de Investigación en Ingeniería [I3A]

Director/es
Kiselev, Valerij G.
Olmos Gassó, Salvador

ISSN 2254-7606

Prensas de la Universidad Universidad Zaragoza

Universidad Zaragoza
1542

Tesis Doctoral

EVALUATION OF BLOOD-TISSUE TRACER EXCHANGE TAKING ACCOUNT OF DIFFUSION AND CONSUMPTION: APPLICATION TO MRI

Autor

José Rufino Solera Ureña

Director/es

Kiselev, Valerij G.
Olmos Gasso, Salvador

UNIVERSIDAD DE ZARAGOZA

Instituto de Investigación en Ingeniería [I3A]

2013

Instituto Universitario de Investigación
en Ingeniería de Aragón
Universidad Zaragoza

Doctoral Thesis — Tesis Doctoral

Evaluation of Blood–Tissue Tracer Exchange Taking Account of Diffusion and Consumption: Application to MRI

Evaluación del intercambio capilar–tisular considerando difusión y consumo de trazadores: aplicación en MRI

Author/Autor:
José Rufino Solera Ureña

Supervisors/Directores:
Dr Salvador Olmos Gassó
Dr Valerij G. Kiselev

Zaragoza 2013

Abstract

This Thesis presents the results of a theoretical investigation into the exchange of substances between a capillary network and its surrounding tissue, a process referred to as *blood–tissue exchange*. As is well known, related physiological phenomena include, among others, the microcirculation, the diffusion of blood-borne substances in the extravascular extracellular space, as well as various mechanisms for transmembrane exchange and intracellular transport. In particular, diffusion has long been known to play a crucial role in the supply of oxygen and nutrients to the cells, and in the removal of metabolic waste products.

A number of experimental techniques have been introduced over the years for the assessment of transport and exchange processes in the tissues, and simultaneously a number of transport and exchange models have been developed in order to estimate relevant transport and exchange parameters for numerous applications. In practice, physiological transport and exchange phenomena are often assessed with the aid of appropriate tracer substances. Both endogenous (e.g., magnetically tagged blood water and partially deoxygenated blood) and exogenous (e.g., paramagnetic gadolinium chelates) tracers are widely employed in both research and clinical studies in magnetic resonance imaging (MRI).

Importantly, the effect on blood–tissue tracer exchange under non-steady-state conditions of (i) extravascular diffusion of tracer, and (ii) different compartmental rates of tracer consumption has, to the best of this author's knowledge, not been thoroughly addressed in the tracer-exchange literature. Both these processes, however, are highly relevant to tracer-exchange modelling in MRI applications.

A survey of the literature reveals that most blood–tissue models currently used for the analysis of arterial spin labelling (ASL) MRI data belong in the class of lumped tracer-exchange models. The basic postulate of any lumped-tracer exchange model is that well-mixed compartments can be defined in which the concentration of tracer becomes rapidly uniform by the action of, for example, efficient diffusion of tracer molecules. One such model, namely the lumped model of Parkes and Tofts [34], will be considered in this Thesis as explained below.

Nonetheless, spatiotemporal models also have been proposed in the literature for use in ASL studies; for example, the water-exchange model of St. Lawrence, Frank and McLaughlin [31], to be discussed in this Thesis. Although it takes into account intracapillary convection, this model does not consider the effect of diffusion. On the other hand, certain literature models (e.g., Lee and Fronek [44]; Kuo *et al.* [45]) of tracer-dilution studies do take into account extravascular diffusion, but not the effect of non-zero consumption rates, and hence they are not adequate for use in ASL studies. Models of tissue oxygen delivery also are not, in principle, adequate because oxygen consumption depends non-linearly with tissue oxygen tension.

The aim of this Thesis is, therefore, to investigate theoretically diffusion and consumption phenomena as they jointly affect the exchange of tracer substances between blood and tissue. To this end, a spatiotemporal model of blood–tissue tracer exchange is presented which takes into account blood flow, diffusive transcapillary permeation, first-order consumption in blood and extravascular tissue, and extravascular diffusion of tracers. Both transient and steady-state conditions are investigated.

Making use of linearity and time invariance, a framework for whole tissue (i.e., tissue including its contained blood) is developed. In this framework, the impulse response function, which characterises the passage of tracer from capillary blood into the extravascular tissue, is expressed in very compact, general form with the use of the Green's function of extravascular space. Because the analytical evaluation of this latter function is unfeasible, a reasonably realistic, analytically tractable model is produced that describes tracer exchange on the scale of individual capillary segments and their surrounding (i.e., pericapillary) tissue. The model describes non-uniform concentrations of tracer for diffusion times smaller than those required to cover typical half-intercapillary distances.

This 'single-capillary approximation' is shown in this Thesis to be appropriate for tissues such as brain and myocardium. Several tracer-exchange quantities for this simplified model are evaluated, namely the arterial-to-intracapillary impulse response function, the intracapillary-to-extravascular (i.e., blood-to-tissue) impulse response function and step response function, and the effective extravascular depolarised vol-

ume. The latter is a time-dependent function which characterises the removal of extravascular tracer under conditions of fast intracapillary consumption, and has been validated numerically using Monte Carlo simulations.

The conditions under which diffusion- and permeability-limited exchange are each expected to occur in practice are identified from the tracer-exchange quantities developed, and the effects of extravascular diffusion and consumption in blood and extravascular space are investigated for both these regimes. The regions of validity of lumped and spatiotemporal tracer-exchange models are identified according as which mechanism – capillary permeability or extravascular diffusion – limits the transcapillary flux of tracer.

As an important application of the spatiotemporal tracer-exchange model developed in this Thesis, an expression for the ASL signal is obtained for both continuous and pulsed labelling approaches, under the assumption that the inflowing arterial magnetisation is well modelled by a sharp bolus with exponentially decaying amplitude. These theoretical results are then compared to analogous results provided by two well-known literature models, neither of which takes into account water diffusion. The presented model has also been compared to several literature models of gas exchange in tissue, a situation in which extravascular diffusion plays a prominent role. In addition, the steady state has been evaluated as a limiting case against which to test the accuracy of lumped tracer-exchange models. The above comparisons allow tracer-exchange regimes to be identified for which the model presented in this Thesis might predict the spatially varying concentration of tracer more accurately than the literature models considered. Any potential improvements in model performance can, however, only be validated through model fitting to measured data.

In conclusion, it is anticipated that the spatiotemporal model set forth in this Thesis will prove useful in the analysis of tracer transport and exchange when compartmental diffusion becomes the rate-limiting mechanism of transmembrane tracer exchange between physiological compartments with different tracer consumption rates, thereby overcoming a theoretical limitation of lumped tracer-exchange modelling approaches.

Resumen

En esta tesis se presentan los resultados de una investigación teórica concerniente al intercambio de sustratos entre vasos capilares y los tejidos circundantes, un conjunto de procesos fisiológicos a los que nos referimos colectivamente como *intercambio capilar–tisular* ("blood–tissue exchange" en el texto). Como es sabido, los fenómenos de transporte e intercambio de sustratos en tejidos biológicos comprenden, entre otros, el transporte sanguíneo en la red de vasos capilares, la difusión en el espacio extravascular extracelular y diversos mecanismos de intercambio a través de membranas, así como de transporte intracelular. En particular, es bien conocida la importantísima función que desempeña la difusión en el aporte de oxígeno y nutrientes a las células y en la excreción de los productos de desecho del metabolismo.

Existe una amplia gama de técnicas experimentales, basadas en diversos principios físicos, para el estudio de los fenómenos de transporte e intercambio tisulares. Asimismo, se ha propuesto un gran número de modelos cuantitativos para estimar los parámetros fisiológicos relevantes en dichos fenómenos. En la práctica, los fenómenos de transporte e intercambio se estudian con ayuda de trazadores (también llamados medios o agentes de contraste) cuyas propiedades de transporte e intercambio sean análogas a las de un sustrato de interés. Por ejemplo, en ciertas modalidades de imagen por resonancia magnética ("magnetic resonance imaging", MRI) se emplean trazadores endógenos (v. g., moléculas de agua marcadas magnéticamente en el plasma arterial; sangre parcialmente desoxigenada durante su paso por los capilares) y en otras se usan trazadores exógenos (v. g., quelatos paramagnéticos de ciertos lantanoides, como el gadolinio).

Atañe directamente al objeto de esta tesis la observación de que el efecto ejercido concomitantemente por la difusión extravascular y por las diversas tasas de consumo (v. g., relajación magnética intravascular y extravascular) de trazadores, en particular en el estado transitorio, no ha sido suficientemente analizado en la literatura sobre intercambio capilar–tisular. Los modelos de transporte e intercambio empleados actualmente en las técnicas ASL ("arterial spin labelling") de imagen por resonancia magnética son, por lo general, modelos de parámetros concentrados (abreviadamente:

modelos concentrados, "lumped tracer-exchange models" en el texto). El postulado básico de dichos modelos es que los procesos de intercambio tienen lugar entre así llamados compartimentos cinéticos, en los que las concentraciones de trazador se consideran espacialmente homogéneas y, por tanto, variables únicamente en el tiempo.

Otra clase de modelos empleados en ASL, entre otras técnicas, es la de los modelos espaciotemporales ("spatiotemporal models"). En un modelo espaciotemporal las concentraciones se consideran funciones del tiempo y la posición en compartimentos cuya geometría —parte esencial del modelo— ha de aproximarse razonablemente a los compartimentos fisiológicos de interés. Entre los modelos espaciotemporales empleados en ASL, el de St. Lawrence, Frank y McLaughlin [31] tiene en cuenta la convección del trazador en el lumen capilar, pero omite el efecto de la difusión. Por otra parte, diversos autores (Lee y Fronek [44]; Kuo *et al.* [45]) han propuesto modelos espaciotemporales de "dilución" de trazadores como la inulina y la sacarosa, considerando la difusión de estos en el espacio extravascular de diversos órganos; no obstante, dichos trazadores no se consumen en los tejidos y emergen finalmente en el sistema venoso. Asimismo, los modelos espaciotemporales de suministro de oxígeno a los tejidos tienen en cuenta la difusión de esta molécula. Sin embargo, dichos modelos tampoco son aplicables en ASL, pues el consumo tisular de oxígeno depende de forma no lineal de su presión parcial local, mientras que la relajación magnética es proporcional (consumo de primer orden) a la densidad de momento magnético (magnetización).

Por las razones antedichas, el propósito de esta tesis es investigar teóricamente el efecto de los fenómenos de difusión y consumo de trazadores en el intercambio capilar–tisular. A tal fin presentamos un modelo espaciotemporal de transporte e intercambio que describe la convección en el lumen capilar, la permeación de tipo difusivo a través de la pared capilar, el consumo de primer orden —tanto en los capilares como en el espacio extravascular— y la difusión extravascular de trazadores. No hemos considerado otros mecanismos de intercambio a través de la pared capilar como, por ejemplo, la difusión facilitada por proteínas específicas. Por sencillez del tratamiento matemático, representamos el espacio extravascular como un medio homogéneo a

efectos del consumo y la difusión de trazadores.

El método de solución del modelo expuesto en esta tesis está basado en la función de Green de la ecuación de difusión–consumo/relajación en el espacio extravascular. Por medio de la función de Green hemos expresado con toda generalidad la función matemática que describe la respuesta extravascular a un aporte de trazador en la red capilar en forma de impulso en el tiempo ("blood-to-tissue impulse response function"). Empero, el cálculo analítico de la función de Green para una muestra macroscópica de tejido es, como puede suponerse, inabordable. Por ello, a partir del citado marco teórico general hemos desarrollado un modelo analíticamente manejable, pero razonablemente realista, que permite cuantificar tanto el transporte capilar como el intercambio capilar–tisular en la escala de segmentos capilares y de tiempos de difusión inferiores a los correspondientes a semidistancias intercapilares típicas. Esta aproximación cuantitativa de segmentos capilares individuales (denominada "single-capillary approximation" en el texto) está justificada en tejidos con reducido volumen capilar (v. g., el tejido cerebral y el miocardio) y para intervalos de tiempos de difusión en el espacio extravascular típicos en MRI.

Mediante este modelo físico simplificado hemos evaluado las funciones de respuesta arterial–capilar y capilar–tisular, tanto a un impulso como a un escalón, suponiendo condiciones ideales de linealidad y estacionariedad. Estas funciones caracterizan el intercambio capilar–tisular. También hemos obtenido, y validado numéricamente mediante simulaciones de tipo Monte Carlo, el volumen extravascular despolarizado equivalente, una función del tiempo que cuantifica la remoción de trazador debido al flujo del mismo desde el espacio extravascular al capilar, en condiciones de rápida eliminación del trazador en los capilares. Dichas funciones permiten identificar dos regímenes diferenciados, según que el intercambio capilar–tisular esté limitado por la permeabilidad de la pared capilar ("permeability-limited regime") o bien por la difusión del trazador en el espacio extravascular ("diffusion-limited regime").

La literatura proporciona diversos estudios, varios de ellos citados en el texto, que comparan las prestaciones de diversos modelos concentrados. Sin embargo, se echan en falta análisis teóricos comparativos entre dichos modelos y los modelos

espaciotemporales, que poseen mayor generalidad física. El estudio de los diferentes regímenes de intercambio capilar–tisular nos ha permitido determinar las regiones de validez tanto de los modelos concentrados como del modelo espaciotemporal descrito en esta tesis, según cuál de los citados fenómenos (permeabilidad o difusión) restrinja más acusadamente la tasa de intercambio de trazador a través de la pared capilar.

También hemos calculado la distribución espacial del trazador en el régimen estacionario suponiendo, en la aproximación de segmentos capilares individuales, la existencia de barreras fijas entre regiones pericapilares contiguas (caso ciertamente irreal en la arquitectura tisular) con flujo neto de trazador nulo a través de las mismas.

Como aplicación importante del modelo espaciotemporal de transporte e intercambio capilar–tisular presentado en esta tesis, hemos obtenido la expresión de la señal ASL para las variantes de marcado magnético continuo (CASL) y pulsado (PASL). Seguidamente hemos comparado estos resultados con la señal ASL predicha por dos conocidos modelos de la literatura —el ya mencionado de St. Lawrence *et al.* y el de Parkes y Tofts [34]— ninguno de los cuales considera la difusión en el espacio extravascular. De esta comparación deducimos intervalos temporales, así como órdenes de magnitud de los parámetros de transporte e intercambio, en los que el modelo descrito en esta tesis logra resultados (presumiblemente más exactos, pero esto solo puede confirmarse experimentalmente) que difieren de aquellos de los citados modelos de la literatura.

También hemos aplicado el modelo al análisis teórico (con hipótesis notablemente simplificadas) del intercambio gaseoso tisular, fenómeno en el que la difusión extravascular desempeña un papel muy destacado. El modelo presentado en esta tesis proporciona los mismos resultados que dos estudios anteriores.

En lo concerniente a los métodos empleados en esta tesis, el enfoque teórico queda resumido en los párrafos precedentes. Hemos realizado simulaciones de tipo Monte Carlo (mediante trayectos aleatorios) para validar ciertos resultados teóricos del modelo presentado. Las comparaciones entre modelos se han realizado a partir de los respectivos resultados analíticos de aquellos. No hemos contado con datos experimentales para la estimación de parámetros de transporte e intercambio capilar–tisular.

Contribuciones y conclusiones

A continuación se describen las principales contribuciones y conclusiones de esta tesis.

Modelos de transporte e intercambio capilar–tisular

Los fenómenos físicos considerados en el modelo espaciotemporal de transporte e intercambio capilar–tisular presentado en esta tesis han sido descritos en el *Resumen* precedente. Aquí ponemos de relieve una característica del presente modelo que lo distingue de otros de la literatura, a saber: la descripción del efecto de la difusión extravascular y de las diferentes tasas de consumo (o relajación) de un trazador en los espacios intracapilar y extravascular; en particular, en el estado transitorio y para valores arbitrarios de permeabilidad capilar. Dicha característica permite, en principio, aplicar este modelo de transporte e intercambio a las técnicas de marcado magnético de los protones de agua del plasma arterial (ASL).

Hemos demostrado que el modelo espaciotemporal propuesto por Lee y Fronek [44] (para estudios de dilución de trazadores que atraviesan sin consumirse la red vascular de un órgano) no es aplicable a la estimación del momento magnético total en experimentos ASL. En efecto, para tiempos de difusión en el espacio extravascular cerebral de varios cientos de milisegundos, típicos en ASL y asimismo compatibles con el método de solución aquí descrito, la desviación del modelo de Lee y Fronek con respecto al modelo presentado en esta tesis puede llegar a ser, teóricamente, del orden de varias decenas porcentuales. Dicha desviación es mayor cuanto más impermeable sea la pared capilar, pues esto dificulta que el flujo de momento magnético arterial compense la pérdida de momento magnético extravascular por relajación.

No obstante, se observa teóricamente que, si la permeabilidad capilar al trazador considerado es suficientemente baja, la mencionada desviación aumenta con el tiempo más lentamente que en el caso de permeabilidades más altas. Esto es debido a que el flujo arterial incrementa la fracción de momento magnético en el espacio intravascular que compensa, en cierta medida, la pérdida por flujo venoso del momento magnético

remanente, ya parcialmente relajado. En consecuencia, disminuye la desviación del modelo de Lee y Fronek con respecto al modelo descrito en esta tesis.

Aplicabilidad de los modelos concentrados de transporte e intercambio

El estudio de las funciones matemáticas que caracterizan el intercambio capilar–tisular (véase el *Resumen*) demuestra que el principal mecanismo limitante de dicho intercambio puede variar en el transcurso del proceso. Consideremos dos ejemplos no exhaustivos de todas las posibilidades: a) para tiempos de difusión en el espacio extravascular tales que la distancia eficaz de difusión sea mucho menor que el radio capilar y también que el grosor eficaz de la pared capilar (parámetro adimensional que depende de la permeabilidad y del coeficiente de difusión extravascular), el intercambio está limitado por la permeabilidad de la pared capilar al trazador en cuestión; b) cuando la distancia eficaz de difusión sea superior al radio capilar y del orden de la semidistancia intercapilar; y cuando, además, el parámetro que representa la eficacia relativa de los mecanismos de permeabilidad capilar y difusión extravascular (dado por la razón del coeficiente de difusión al producto de la permeabilidad y el radio capilar) valga del orden de la unidad; en este caso, se deduce teóricamente que la difusión extravascular del trazador regula apreciablemente el flujo de trazador a través de la pared capilar.

Hemos demostrado teóricamente que los modelos concentrados no evalúan adecuadamente las condiciones de contorno entre compartimentos adyacentes, lo cual conduce a sobrestimaciones del flujo de trazador a través de la membrana intercompartimental. Hemos comprobado que en el régimen de intercambio capilar–tisular limitado por la difusión en el espacio extravascular, el perfil de la concentración extravascular de trazador difiere acusadamente de aquel predicho por los modelos concentrados. Este resultado es razonable, puesto que el postulado básico de dichos modelos (véase el *Resumen*) asume la rápida redistribución del trazador en los espacios intracompartimentales por efecto de la difusión.

También hemos mostrado que, incluso cuando el intercambio está limitado por la permeabilidad de la pared capilar, y aun en el régimen estacionario, el postulado

fundamental de los modelos concentrados puede desviarse marcadamente de las predicciones del modelo espaciotemporal propuesto en esta tesis. (Hemos evaluado el régimen estacionario como caso límite para verificar la validez teórica de los modelos concentrados, pues cabría esperar que, en dicho régimen, el postulado de concentraciones homogéneas se verificase con mayor aproximación que durante los transitorios difusivos). Concretamente, en relación con un segmento capilar y su región pericapilar, definidos geométricamente como sendos cilindros concéntricos según el conocido modelo de Krogh [47], la comparación entre el modelo espaciotemporal descrito en esta tesis y el correspondiente modelo concentrado demuestra que, en el caso de intercambio limitado por permeabilidad, el modelo concentrado predice con buena aproximación la cantidad de trazador en el espacio extravascular, pero subestima la concentración en un entorno de la pared capilar y la sobrestima en zonas alejadas de la misma. Por el contrario, en el caso de intercambio limitado por difusión, el modelo concentrado predice con gran exactitud la concentración extravascular en la pared capilar, pero sobrestima considerablemente la cantidad de trazador en el espacio extravascular.

Mejoras con respecto a modelos de ASL tomados de la literatura

Hemos comparado el modelo espaciotemporal descrito en esta tesis con otros dos modelos de intercambio capilar–tisular, a saber: el modelo concentrado bicompartimental de Parkes y Tofts [34] y el modelo espaciotemporal bicompartimental de St. Lawrence, Frank y McLaughlin [31], ambos formulados en el contexto de estudios ASL en el tejido cerebral. Este último modelo describe la distribución de trazador en el interior del capilar debida a la convección y al flujo a través de la pared capilar, pero presupone que la concentración extravascular es homogénea. En concreto, hemos obtenido la señal ASL predicha por cada uno de los tres modelos para un conjunto común de parámetros típicos para estudios CASL y PASL en miocardio y tejido cerebral.

Nuestros resultados teóricos indican que el modelo de St. Lawrence *et al.* produce resultados similares a los del modelo espaciotemporal presentado en esta tesis solo

en el régimen de intercambio capilar–tisular limitado por permeabilidad. En cambio, para valores de los parámetros correspondientes al intercambio limitado por difusión extravascular, los resultados del modelo de estos autores se desvían apreciablemente de los del modelo espaciotemporal aquí descrito. Hemos evaluado dichas desviaciones en función del tiempo de difusión en el espacio extravascular y para un amplio rango de valores de la razón del coeficiente de difusión al producto de permeabilidad y radio capilar.

Asimismo hemos observado que, en comparación con el modelo presentado en esta tesis, el modelo concentrado bicompartimental de Parkes y Tofts subestima la cantidad de trazador tanto en el espacio capilar como en el extravascular cuando la permeabilidad capilar es relativamente baja (v. g., la permeabilidad al agua en capilares cerebrales o cardiacos). Lo atribuimos al hecho de que los modelos concentrados evalúan el flujo convectivo capilar con un modelo de "caja negra" que dificulta la estimación del flujo convectivo de trazador en el extremo venoso de los capilares. En cambio, para permeabilidades elevadas puede ocurrir un efecto compensatorio tal que los resultados del modelo de Parkes y Tofts se aproximen al modelo espaciotemporal presentado en esta tesis más que los del modelo de St. Lawrence *et al.*

Consideraciones finales

Como se ha indicado en el *Resumen*, el trabajo de investigación realizado en esta tesis es eminentemente teórico. Los resultados analíticos obtenidos a partir del modelo de intercambio capilar–tisular han sido ilustrados gráficamente, contrastados con simulaciones Monte Carlo en algunos casos y comparados con diversos modelos publicados en la literatura sobre MRI. El modelo de intercambio capilar–tisular no ha sido evaluado en sujetos en esta etapa. Ulteriores avances requerirán refinamientos del modelo y la realización de experimentos de MRI encaminados a dilucidar cuestiones teóricas y a demostrar la estimación robusta de parámetros de transporte e intercambio capilar–tisular en sujetos.

A modo de conclusión, consideramos que el modelo espaciotemporal de intercambio capilar–tisular propuesto en esta tesis será útil en aquellas situaciones en

que la difusión del trazador en el espacio extravascular sea el principal fenómeno físico limitador de la tasa de intercambio y, especialmente, en aquellos casos en que, además, difieran las tasas de consumo de trazador en los diversos compartimentos fisiológicos. Esto supone, en principio, un avance frente a una limitación teórica de los modelos concentrados. Como ejemplo de aplicación práctica del modelo presentado, mencionamos la cuantificación del intercambio de magnetización en diversos tejidos mediante técnicas ASL en imagen por resonancia magnética.

Agradecimientos

Querría haber demostrado, cotidianamente, mi gratitud a quienes me han acompañado —de diversas maneras y en diferente tiempo— hasta aquí: las faltas a este deber justifican estos sucintos agradecimientos.

En primer lugar, quiero agradecer el apadrinamiento científico, las enseñanzas y la generosa dedicación de Salvador Olmos y Valerij Kiselev, mis directores de tesis: sin ellos este empeño no habría culminado. Valerij me acogió durante dos estancias de investigación en la Sección de Física Médica del Departamento de Radiodiagnóstico de la Albert-Ludwigs Universität (Freiburg im Breisgau, Alemania); él y Laurence, Steffi, Sabine, Anna, Julian, Peter, Nico y Marco Vicari hicieron muy grata esta experiencia. Asimismo, agradezco a los Dres. D. Grebenkov y S. Jespersen su labor como revisores de esta Tesis.

Gracias a quienes dejaron su primera impronta escolar: Rosi, Isabel, Reyes, Gerardo y Alfonso Arcas, maestros, y Carmen Griñán, mi primera profesora de inglés. El veterano Instituto de Bachillerato *Matemático Puig Adam* de Getafe es mi *alma mater*. Recuerdo con cariño la memoria del Dr. D. José García Alonso, que me rescató de la impotencia y me enseñó matemáticas: su persona destilaba bonhomía. Sin su estímulo ni el de Pedro Valera —que me prestaba su tomo de *Mecánica*—, tal vez no habría iniciado, veinte años después, este trabajo. Gracias a Josefrancisco Pinilla, mi profesor de latín, por su amistad todos estos años, y a Carmen, M.ª Dolores y Gregorio por su labor y por recibirme siempre con afecto.

Gracias a Jim Saxton: haber sido su alumno, en aquella época dorada, me ha ayudado a disfrutar del proceso de escritura de esta tesis; a Roger Ford, Jeff M^{c}Cauley, David Hartley, Wes Williams y Cindi Sempert, también de Sandy Union High School (Sandy, Oregón, EE.UU.), por su aliento. La familia Emrich me hizo uno más entre los suyos y Lorene ha estado siempre pendiente de mi devenir.

Ignacio Alcalde, Pepe López, Pedro Pindado, Rafa Belinchón, Mariano Casado y Fernando Sendra compartieron conmigo su calidad personal y su caudal de experiencia profesional. Sé que eso ayudó a que Iain Richardson e Iain Maclean me dieran trabajo en Aberdeen (Escocia), donde entré en contacto con el mundo de la

investigación. Gracias a Rosalind, Christine, Irene, Alison y Brian, Angela y Dave C., Lorna y Dave S., Anna y Alan, y Dietrich por su amistad. Tengo una gran deuda de amistad con Martin y Freda, quienes, además, me han ayudado a mejorar la redacción del texto en inglés y han seguido de cerca las postrimerías del proceso.

Gracias a mis compañeros del Depto. de Ingeniería Electrónica y Comunicaciones de la Universidad de Zaragoza. En particular, a Pablo Laguna, por su estímulo y consejo, y a Pedro, Ángela, Paloma, Mariola, Juan Pablo, Alfonso, Juanma, Santi, Toni y Fernando. A Eva Cerezo por su afecto, a Lola Berrade y Jesús Asín por su apoyo. A Julia, David, Juan, Iñaki, Clara, Nieves, Chema, Luis, Guillermo, Rosa y Rebeca por alegrar las jornadas de trabajo. A Maricruz, Marian, Pilar, Ana y Yolanda por su simpatía y eficaz labor de gestión. Y al personal de la biblioteca universitaria por atender con prontitud mis frecuentes demandas de bibliografía.

Mis amigos de siempre, Ángel, Francis, Rober, Julio y Yolanda han soportado lejanía y desatenciones durante largas temporadas: sirva este reconocimiento de los hechos como gratitud y sincera disculpa. Gracias a Ana y Pablo, Félix y Belén, Luisa, Cristina, Isa y Rose, desde la distancia. Gracias a Ana, veterana compañera de estudios de doctorado y amiga, por su empatía y afecto. A Ernesto y Celia, por tantos momentos compartidos —verdaderos regalos de amistad— y también a Toño: por esos montes de Aragón hemos caminado fraternalmente.

Los años van destilando el cariño a la familia de una forma sutil que, con paciencia, he llegado a saborear aunque no siempre a donar con reciprocidad. Vosotros —Rufino, Sagrario, Andreína, Tomás y Victoria, Tomás y Jesús— habéis estado tan pendientes. Andrea lo intuye y Tomás, Anastasia y Basiliso, Juliana y Felipe, lo contemplan todo desde un punto de vista más elevado. Mi hermana Myriam y mi cuñado Christian transmiten su empatía y cariño desde la distancia. ¡Ánimo, hermana, también tú has dado ya los primeros pasos! Aixa y Jimena son la bendición del tión. Mi hermano menor, Rubén, me ha precedido en el logro del grado de doctor: gracias por tu ejemplo fraterno. Finalmente, a mis padres, María del Prado y José María, sencillamente no sé corresponderles por cuanto han dado de sí mismos para ayudarme a ser quien soy. Os quiero a todos.

Asistencia económica

Esta Tesis contó con ayuda económica del Ministerio de Ciencia e Innovación español (TEC2009 – 14587 – C03 – 01) y del Centro para el Desarrollo Tecnológico Industrial (proyecto AMIT del Programa CENIT CEN – 20101014), así como del Fondo Social Europeo – Diputación General de Aragón. Las estancias de investigación en la Sección de Física Médica del Departamento de Radiodiagnóstico de la Albert-Ludwigs Universität (Freiburg im Breisgau, Alemania) contaron con el generoso patrocinio económico (becas IT 18/08 y CM 3/09) del *Programa Europa XXI* de la Diputación General de Aragón y la Caja de Ahorros de la Inmaculada.

Zaragoza, jueves 6 de junio de 2013

A mis padres,
a mi hermana y a mi hermano,
a mi familia:
con todo mi cariño.

Contents

List of Figures

List of Tables

List of Abbreviations

1BDP	one-barrier distributed parameter (model)
1d	one-dimensional
2d	two-dimensional
ASL	arterial spin labelling
BOLD	blood-oxygenation-level dependent
CASL	continuous arterial spin labelling
CT	computed tomography
dc	direct current
DCE	dynamic contrast-enhanced (imaging)
DSC	dynamic susceptibility contrast
DWI	diffusion-weighted imaging
Gd-DTPA	gadolinium diethylenetriamine pentaacetic acid
iv, IV	intracapillary
ev, EV	extravascular
μm	micrometre
mm	millimetre

mM	millimole per litre
ms	millisecond
MHz	megahertz
MRI	magnetic resonance imaging
NMR	nuclear magnetic resonance
PASL	pulsed arterial spin labelling
PET	positron emission tomography
ppm	parts per million
RF	radiofrequency
SI	système international d'unités, international system of units
SPA	single-pass approximation
SPECT	single photon emission computed tomography
T	Tesla
TI	inversion time

List of Symbols

$*$	time convolution
$*_z$	spatial convolution with respect to axial coordinate z
∇	gradient operator
$\nabla\cdot$	divergence operator
∇^2	Laplace operator
γ	Euler's constant ≈ 0.5772
δ_n	scattering phase shift
Δ	increment
ϵ	relative error
η_{visc}	viscosity
κ	diffusive membrane permeability $[\mu\text{m}\,\text{ms}^{-1}]$
λ	tortuosity coefficient; tissue–blood partition coefficient
λ_n	nth eigenvalue
$\mu(t)$	total amount of tracer; total magnetic moment
$\mu_\nu(t)$	amount of tracer; magnetic moment ($\nu =$ iv, ev)
ℓ	effective membrane thickness

ϱ	fluid density
τ_{c}	mean capillary-segment transit time
τ_D	characteristic radial extravascular diffusion time
τ_{ev}	mean extravascular residence time of well-mixed tracer molecules
τ_{iv}	mean intracapillary residence time of well-mixed tracer molecules
χ	magnetic susceptibility, in SI units
$\psi_{\mathrm{ev}}(\mathbf{r},t)$	extravascular concentration
$\psi_{\mathrm{ev}}^{\mathrm{abs}}(\mathbf{r},t)$	extravascular concentration under absorbing intracapillary conditions
$\psi_{\mathrm{iv}}(\mathbf{r},t)$	intracapillary concentration
$\psi_\nu(t)$	spatially averaged concentration ($\nu = \mathrm{iv}, \mathrm{ev}$)
$\psi_\nu(r,t)$	$\psi_\nu(\mathbf{r},t)$, averaged over both axial and angular coordinates ($\nu = \mathrm{iv}, \mathrm{ev}$)
$\psi_\nu(z,t)$	$\psi_\nu(\mathbf{r},t)$, averaged over both radial and angular coordinates ($\nu = \mathrm{iv}, \mathrm{ev}$)
$\langle\psi_\nu(\mathbf{r},t)\rangle$	ν-phase average concentration
$\langle\psi_\nu(\mathbf{r},t)\rangle^\nu$	ν-phase intrinsic average concentration
ω	time-conjugate Fourier transform variable
a	capillary radius
A	half-intercapillary distance
$^{13}\mathrm{C}$	carbon-13
D_{ev}	extravascular diffusion coefficient [$\mu\mathrm{m}^2\,\mathrm{ms}^{-1}$]
E	extraction fraction
$\mathcal{F}^{-1}\{\cdot\}$	inverse Fourier transform

$\mathcal{F}\{\cdot\}$	Fourier transform
f_{iv}	capillary tracer flow per volume of whole tissue [ms^{-1}, min^{-1}]
f_n	nth eigenfunction
$^{19}\mathrm{F}$	fluorine-19
$G(\mathbf{r}, \mathbf{r}', t)$	Green's function of diffusion–consumption equation for whole EV space
$G_{\mathrm{c}}(\mathbf{r}, \mathbf{r}', t)$	*Id.*, for a pericapillary region
$G_{\mathrm{free}}(\mathbf{r}, \mathbf{r}', t)$	*Id.*, for free space (free propagator)
Gd	gadolinium
$^{1}\mathrm{H}$	hydrogen-1
$h_{\mathrm{a}}^{\mathrm{iv}}(\mathbf{r}, t)$	arterial-to-intracapillary impulse response function
$h_{\mathrm{a}}^{\mathrm{ev}}(\mathbf{r}, t)$	arterial-to-extravascular impulse response function
Hct	haematocrit
Hg	mercury
$\mathbf{j}_{\kappa}(\mathbf{a}, t)$	diffusive permeation (transmembrane) flux [$\mathrm{mM}\,\mu\mathrm{m}^{-2}\,\mathrm{ms}^{-1}$]
K^{trans}	volume transfer constant [min^{-1}]
L	capillary segment length
$\mathbf{n}$	unit normal vector
$^{15}\mathrm{O}$	oxygen-15
O_2	oxygen molecule
$\mathcal{O}[\cdot]$	Big-O notation (for order-of-magnitude estimates)
$^{31}\mathrm{P}$	phosphorus-31

P	oxygen partial pressure, or tension
PS	capillary permeability surface area product [min^{-1}]
q_n	nth eigenfrequency
$\mathbf{r}$	position vector
t	time
R_{ev}	extravascular consumption (or relaxation) rate [ms^{-1}]
R_{iv}	intracapillary consumption (or relaxation) rate [ms^{-1}]
R_{tiss}	consumption (or relaxation) rate in whole tissue [ms^{-1}]
T_1	longitudinal relaxation time
T_2	transverse relaxation time
T_{E}	echo time
u_z	average axial velocity in capillaries
v_ν	ν-phase volume fraction
v_{ev}	tracer-accessible extravascular volume per volume of whole tissue
v_{iv}	tracer-accessible intracapillary volume per volume of whole tissue
$w(\mathbf{r}, t)$	blood-to-tissue impulse response function
$W(\mathbf{r}, t)$	blood-to-tissue step response function
z	distance along capillary axis, measured from inflow end of capillary

Chapter 1

Introduction

This Chapter describes the background, aims and organisation of this Thesis.

1.1 Background: quantification of physiological transport and exchange processes

Physiological transport and exchange processes are essential to maintain tissue function [1, p. 140]. They involve a variety of transport mechanisms, including the supply of solutes to the immediate vicinity of the tissues by the microcirculation; passive, facilitated and active transmembrane exchange; see, e.g., Refs [1, pp. 140 ff.], [2, p. 507 ff.] and [3, pp. 18 ff.]; diffusion in the interstitial space; and various types of intracellular transport mechanism [2]. In particular, diffusion plays a key role in the delivery of oxygen and nutrients to the cells, and in the removal of waste products of the cell metabolism [4].

Accurate quantification of physiological exchange processes is a key step in the assessment of a number of diseases and conditions, including tumours, stroke, multiple sclerosis [5], myocardial perfusion [6] and renal function [7], and also for evaluation of metabolic function and antiangiogenic agents [8]. A number of experimental techniques are currently available which provide varying levels of spatiotemporal res-

olution and sensitivity to various tissues and disease conditions. Imaging techniques at the whole-organ level include, but are not limited to, magnetic resonance imaging (MRI), positron emission tomography (PET), single-photon emission computed tomography (SPECT), computed tomography (CT), and combined techniques like PET–CT and PET–MRI [8]. In all of these techniques, tissue structure and physiology are probed with the aid of suitable tracers, also referred to as indicators, contrast agents and contrast media. Tracers can be either endogenous, i.e., intrinsic, or produced from bodily substances like magnetically tagged arterial blood water; or exogenous, i.e., extrinsic substances which are introduced in the body, like paramagnetic gadolinium chelates and superparamagnetic iron oxide nanoparticles.[1]

The main aim of this Thesis is to evaluate the interactive effects of diffusive transport and first-order consumption[2] of tracer substances involved in transcapillary exchange between blood and tissue (referred to as *blood–tissue exchange*). Because in this Thesis an emphasis will be placed on MRI applications, we begin with a brief discussion of MRI basics, followed by a review of relevant tracer-exchange models that have found widespread application in MRI, PET, indicator-dilution and oxygen-delivery studies. Subsequently, we formulate the research aims of this Thesis and close this Chapter with a description of the structure of this Thesis.

1.1.1 Magnetic resonance imaging

A fundamental quantum-mechanical property of atomic nuclei with odd atomic or mass numbers is that they possess non-zero *nuclear spin* [11, p. 60]. Nuclear magnetism is coupled to the nuclear spin and is represented by the *nuclear magnetic*

[1]The term *indicator* is also often used in the literature. Sourbron and Buckley, quoting Perl, Lassen and Effros, made a distinction between indicators and tracers as follows: 'A tracer is a particular type of indicator which is chemically identical to a systemic substance of interest, but separately detectable.' (see Ref. [9], p. R3). Because most of the applications considered in this Thesis (Chapter 4) involve use of endogenous tracers, we use the term 'tracer' throughout except when referring specifically to indicator-dilution techniques.

[2]In first-order consumption processes, the rate at which a substance is consumed is proportional to the amount of remaining substance; see, e.g., Ref. [10], pp. 305 – 310.

dipole moment. For any given nucleus, the magnitude of its nuclear spin can only assume certain discrete values (it is said to be quantised). On the other hand, in the absence of an external magnetic field, the individual nuclear spins point in completely random directions, due to thermal motion. However, if an external constant magnetic field (the so-called *main field*) is applied, then each nuclear spin will take on one of a discrete set of orientations with respect to the direction of the main field. For spin-1/2 nuclei like ^{1}H, this causes the population of spins to split between a lower-energy state (with magnetic moments parallel to the main field) and a higher-energy state (with magnetic moments anti-parallel to the main field) [11, pp. 64 ff.]. The number of spins in the lower-energy state exceeds the number of spins in the higher-energy state by just a few parts per million, thereby giving rise to a detectable net macroscopic (bulk) magnetisation. Moreover, the nuclear spins, hence also the net magnetisation, precess about the external field at the Larmor frequency, which is proportional to the magnetic flux density [11, p. 68], measured in Tesla (T) and sometimes loosely referred to as the main field strength. This constitutes the basic nuclear magnetic resonance (NMR) phenomenon. In loose parlance, one says that the main field converts the random nuclear magnetic moments to a bulk magnetisation which is aligned in the direction of the field.

The question then arises, how can the NMR phenomenon be exploited so as to generate an image, i.e., how does one actually go from NMR to MRI? The basic physical principles involved in any MRI pulse sequence are (i) the generation of a net transverse (i.e., perpendicular to the main field) magnetisation; (ii) spatial encoding of spin position into the Larmor frequency by means of magnetic field gradients, and (iii) Faraday's law of electromagnetic induction for NMR signal detection [11]. A simplified description of the main MRI processes is given below; it draws mainly from the book by Liang and Lauterbur [11], in particular Chapters 1, 3 – 6:[3]

- The bulk magnetisation is first driven out of equilibrium using radiofrequency (RF) excitation pulses. In this step, the magnetisation is usually manipulated

[3] Additional information on physical principles and pulse-sequence topics can be found in, for example, the book by Haacke *et al.* [12].

by means of a preparation module that imparts the desired NMR contrast 'weighting' to the magnetisation (see below) as it relaxes back to equilibrium. Magnetic relaxation is characterised by the longitudinal (T_1) and transverse (T_2) relaxation times, which respectively refer to the components of the bulk magnetisation aligned with, and perpendicular to, the main field. The spontaneous return to equilibrium of the magnetisation gives rise to a free induction decay (FID); alternatively, spin-echo and gradient-echo signals can be elicited through application of suitable RF pulses and magnetic gradients, respectively. In this time interval, additional gradients can be applied to, for example, sensitise the experiment to diffusion of tissue water [5]. Importantly, it is the transverse magnetisation that, in subsequent stages, will be detected, sampled and transformed into an image.

- Spatial encoding, or signal localisation, of the nuclear magnetisation is the key MRI step [11, p. 8]. During the relaxation period, linear gradients are applied in order to impart specific position-dependent Larmor frequencies and phase offsets to the net magnetisation.

- According to Faraday's law, the transverse, time-varying component of the spatially encoded magnetisation induces a voltage in a receiver coil. This voltage is sampled, digitised and stored during the read-out interval for subsequent digital processing.

- Lastly, a conventional image reconstruction approach involves taking the spatial Fourier transform of the detected voltage to yield an image or a set of images.

MRI is a versatile technique that can provide structural and/or functional information about the imaged object with a broad range of image contrast possibilities, as determined by the choice of MRI pulse sequence. This means that the local NMR signal can be made sensitive to any of a number of physical parameters, including tissue proton density, longitudinal and/or transverse relaxation rates, spin diffusion and both micro- and macrovascular blood flow. A wealth of information on MRI pulse sequences can be found in, e.g., the book by Bernstein, King and Zhou [13].

MRI tracers, or contrast agents, are designed to provide two primary mechanisms of enhanced image contrast, namely relaxivity and susceptibility effects [14]. Relaxation effects are caused by short-range dipolar interactions between the nuclear spins of mobile MRI-active nuclei, and the unpaired electrons in the tracer molecules. Such interactions enhance both the longitudinal and transverse spin relaxation rates in large, and equal, proportion. However, because in tissue the longitudinal relaxation rate is smaller than the transverse relaxation rate, the tracer-induced percentage change is much greater for the longitudinal relaxation rate [14]. Susceptibility effects, on the other hand, rely on compartmentalisation of the tracer to create magnetic susceptibility gradients which increase the spread of tissue Larmor frequencies [15], thereby enhancing the spin transverse relaxation rate [14]. Importantly, it is the relaxation of the proton (H^+) magnetic moments of tissue molecules (including water and fat molecules), not the nuclear and/or electronic magnetic dipole moments[4] of the paramagnetic tracer, that is imaged in an MRI experiment.

Because the hydrogen nucleus has spin one-half and because it is largely abundant in living systems as a constituent of water and fat, most clinical MRI studies are based on the ^{1}H nucleus; other NMR-visible nuclei of biochemical importance include ^{13}C, ^{19}F and ^{31}P [11]. Current field strengths for clinical human scanning are 1.5 to 3 T, resulting in Larmor frequencies of the order of 10^2 MHz, i.e., well in the familiar radiofrequency range. While MRI avoids the downsides of ionising radiation and injected radiotracers, potential side effects of exogenous MRI tracers should be considered (refer to, e.g., Ref. [17] for a review of Gd-based tracers). Strict MR compatibility and patient safety rules are to be observed on an individual basis before undergoing an MRI scan.

For the above reasons, MRI has established itself as a potent clinical tool for the assessment of both tissue structure and function. Anatomical MRI is widely employed clinically for brain [5], whole-body and musculo-skeletal imaging. In addition, MRI techniques can be used to assess a variety of biophysical processes, including blood

[4]The electron has spin 1/2 and its associated magnetic dipole moment precesses at a much higher Larmor frequency than that of the proton when placed in an external magnetic field [16].

flow in the large vessels (e.g., MR angiography and venography) [13]; perfusion of brain [18, 19], kidney [7] and myocardium [6]; water diffusion in biological compartments [20, 21] and blood-oxygenation-level-dependent (BOLD) changes associated with neuronal activation patterns [22].

Arterial spin labelling

In this Section we briefly discuss a class of MRI techniques known as arterial spin labelling (ASL)[5]. This background material shall prove useful in Chapter 4.

The underlying physical principle of ASL is that the difference in the longitudinal magnetisation of arterial blood water between a 'tag' and a 'control' state can be used as an endogenous MRI tracer to evaluate tissue blood flow and transcapillary exchange. Tagging typically involves inversion (i.e., creating a net spin-down population) of the longitudinal magnetisation by RF pulses. The difference in longitudinal magnetisation between the tag and control states is referred to as the tagged magnetisation, the tagged bolus or simply the tag [23]. In an ASL experiment, a tagged bolus is first created in an artery feeding the tissue of interest. This bolus travels along the arterial tree, reaches the capillary network, exchanges with the tissue to some extent and is eventually cleared by longitudinal relaxation and venous outflow [23, 24]. It is the change in tissue magnetisation caused by blood–tissue exchange of tagged spins that is actually imaged in an ASL experiment.

A generic ASL pulse sequence therefore consists of a magnetisation preparation module, which differs somewhat for the tag and control states, and an imaging module, which can be single-slice, multi-slice or fully three-dimensional. The sequence is played twice, with and without tagging, and the spatial change in tissue magnetisation is estimated by subtracting the tag and control images. Ideally, the difference between the tagged and control NMR signals is only due to the delivery of tagged spins to the tissue by the microcirculation, whereas the signal from the static tissue and from larger, non-exchanging vessels will both be perfectly suppressed upon image subtraction [24]. Because the signal-to-noise ratio of subtraction images is inherently

[5] Also referred to as arterial spin tagging (AST) [13].

low owing to the small volume fraction of capillaries, multiple images are usually averaged to improve image quality. The time course of the tagged bolus in the tissue can be obtained by imaging over a range of tagging–imaging delays.

There exist various schemes for the preparation of the tagged spins [13, 23] and only the two most basic of these will be considered here. In the continuous ASL (CASL) scheme, an RF excitation inverts the arterial magnetisation at a proximal position, relative to the imaged tissue, for a relatively long tagging interval (e.g., 2 – 4 seconds [25]; RF power deposition limits must not be exceeded). This causes the amplitude of the arterial magnetisation to reach a steady state. On the other hand, in the pulsed ASL (PASL) class of pulse sequences, the magnetisation in a thick (10 – 15 cm [23, 25]) slab below the imaging region is inverted for a relatively short interval of time, thus creating a transient bolus [13].[6]

Further information on ASL pulse sequences can be found in Ref. [13]. For an overview of the physical principles, practical issues and clinical applications (e.g., estimation of tissue perfusion in brain, kidney and myocardium) of ASL, see, for example, the reviews by Petersen *et al.* [25] and Golay *et al.* [26].

1.1.2 Review of tracer-exchange models

Tracer-exchange models have long been utilised for the analysis of tracer exchange data in indicator-dilution studies, nuclear medicine and MRI. For the class of *spatiotemporal* models the concentration of tracer is defined as a function of both position and time, whereas for *lumped* models the concentration is considered only a function of time [27].[7]

[6] An alternative PASL scheme inverts the magnetisation in the slice of interest (tag) and in the entire sensitive region of the transmit RF coil (control) [13].

[7] *Note on terminology*: tracer-exchange models are also commonly referred to as tracer kinetic [9] or pharmacokinetic [28] models. Spatiotemporal and lumped models are alternatively referred to as distributed-parameter (or heterogenous) and concentrated-parameter (or homogenous) models, respectively [29, 30]. Kinetic compartments are also referred to as 'pools' or 'sites'. Sometimes the terms one- and two-barrier models are used synonymously with two- and three-compartment models, respectively [29, 31].

Lumped models

Specifically, a defining assumption of any lumped tracer-exchange model is that well-mixed compartments can be defined in which the concentration of tracer is spatially uniform (see Refs [9, p. R5], [29, p. 443], [32, p. 93]). For this *well-mixed assumption* to hold approximately, the distribution of tracer by diffusive transport must prevent the build-up (or depletion) of tracer near the boundaries of the exchanging compartments [29].

Kety's single-compartment model of gas exchange at the lungs and tissues [33] has been the basis for many later modelling developments in, e.g., PET, ASL and dynamic contrast-enhanced (DCE) MRI. In this model, tracer conservation was expressed in terms of time rates of average arterial, venous and tissue concentrations of tracer. An inherent assumption of single-compartment lumped models is that the tracer is able to permeate freely across physiological membranes [31, 34], so that the extravascular space is assumed to be in diffusive equilibrium with venous blood. If incorrect, this assumption can cause quantification errors like the so-called *falling flow* phenomenon [29, p. 444]: it has been observed that cerebral blood flow estimates obtained from PET data using the Kety model progressively decrease at sufficiently high cerebral blood flow values (Ref. [29] and references therein) and/or sufficiently long measurement times [31].

Larson, Markham and Raichle [29] investigated the falling flow effect in PET measurements of $H_2^{15}O$ uptake in monkey brains using a set of two lumped and two spatiotemporal models. Both the one-compartment (Kety) model and a two-compartment lumped model failed to track the amount of radio-tracer in whole tissue at most measurement times ($\gtrsim 2-5$ s). A two-compartment spatiotemporal model taking into account intracapillary convection and capillary wall permeability to radiotracer also did not improve over the lumped models. The closest fit to the measured data was obtained using a three-compartment spatiotemporal model incorporating, besides intracapillary convection and capillary wall permeability, a radial 'tissue conductance' governing tracer flux between the two extravascular compartments [29, Fig. 4]. Larson and co-workers interpreted their "'tissue-conductance"

parameter (...) to be a lumped representation of a hypothetical radially distributed diffusive conductance.' [29, p. 459]. They argued that its estimated value was too low to be ascribable to the permeability–surface-area product of neurons and glial cells. These authors' work suggests that it is important to account for extravascular $H_2^{15}O$ diffusion in PET studies. In another study of the cerebral microcirculation, Kassissia and co-workers [35] arrived at the same conclusion concerning the inaccuracy of a single-compartment model for description of tritiated water outflow curves in the dog brain.

Modelling water exchange in ASL experiments must incorporate the effect of longitudinal magnetic relaxation. In the single-compartment model of Detre *et al.* [36], the Bloch equation is augmented with the net flow of tissue magnetisation. Alternatively, the single-compartment model of Buxton *et al.* [23, 24] draws explicitly on the theory of linear, time-invariant systems to express the tissue magnetisation as the convolution of the arteriolar magnetisation and the product of the tissue relaxation and tissue residue functions. Parkes and Tofts [34] developed a model of water exchange between the intracapillary and extravascular spaces of brain tissue and demonstrated parameter estimation errors associated with the use of single-compartment models in ASL.

Contrary to water PET observations, the falling flow effect has not been demonstrated in ASL studies [31]. Instead, the so-called T_1 and *outflow* effects [34] can also lead to biased capillary flow estimates. The error magnitude depends on such factors as flow rate, capillary water permeability, host tissue, field strength and measurement technique employed [34]. More recently, Kelly, Blau and Kerskens [37], have produced a model of the ASL signal that describes pseudo-diffusion of the tagged spins within the microvasculature using a completely different approach based on the theory of stochastic differential equations.

The lumped models of Tofts and Kermode, Brix *et al.* and Larsson *et al.* have been used in DCE MRI studies to estimate the influence of capillary flow and permeability on the distribution of paramagnetic tracers in the extravascular space of the tissues; see Refs [28, 32, 38] for details. More recently, Li, Rooney and Springer [30] have

developed a three-compartment model (i.e., whole blood, extravascular extracellular[8] space and intracellular space) for the use of paramagnetic tracers in T_1-weighted MRI studies.

Spatiotemporal models

Spatiotemporal models have found application in, for example, whole-organ indicator dilution studies, two-compartment modelling of the diffusion NMR signal, and in gas exchange in tissue.

Sangren and Sheppard [39] in 1953 considered capillary flow and transcapillary exchange of a tracer substance. In the extravascular space, there was assumed to be fast diffusive mixing of the tracer only in the direction perpendicular, but not parallel to, the capillary axis. The models of Johnson and Wilson [40], Goresky *et al.* [27] and St. Lawrence and Lee [41] all account for intracapillary convection but treat the extravascular space as a well-mixed compartment. The model of Perl and Chinard [42] postulates instantaneous tracer equilibration in the radial direction, but takes into account axial diffusion in both the intracapillary and extravascular spaces as well as intracapillary convection; this model was tested in indicator studies of dog kidney. Bassingthwaighte *et al.* [43] developed a four-compartment (i.e., intravascular, endothelial, interstitial and parenchymal spaces), multiple parallel-pathway model of blood–tissue exchange that takes into account flow heterogeneity, axial diffusion and first-order consumption but not extravascular radial diffusion.

Lee and Fronek [44] investigated the influence of extravascular diffusion of an indicator on extraction ratio and venous outflow curves, as assessed with the double indicator-dilution method. They modelled intracapillary convection, transcapillary permeation and extravascular diffusion of indicator substances (e.g., inulin and sucrose) within a radially unbounded, homogenous extravascular region. Kuo, Gustafson and Friedman [45] later modified this model to represent the interstitial space as a cylindrical annulus, its lateral inner and outer surfaces representing

[8] In this Thesis, the terms 'extravascular extracellular space' and 'interstitial space' shall be used interchangeably.

permeable capillary and cell walls, respectively. More recently, Beard and Bassingthwaighte [46] have simulated tracer convection and extravascular diffusion numerically in a three-dimensional network of regularly spaced, fully permeable capillaries with cross-connecting segments among them (as found in striated mammalian muscle [47]). Tracer consumption was not considered.

Kärger [48] considered molecular transport and exchange in systems consisting of two distinct 'subregions' (also called 'pools' [49, p. 712]) with differing diffusion coefficients. In this model, the pools may be physical entities (e.g., cells) or they may also represent distinct mechanisms of molecular migration for, typically, different chemical species [48, p. 143]. The main modelling assumptions are as follows: (i) the spatial scale on which the Kärger equations apply exceeds the typical dimension of an individual pool but is much smaller than the dimension of, say, a voxel, thus providing a coarse-grained description of transport phenomena [49, p. 714]; and (ii) the exchange between pools is uncorrelated with diffusion in the pools. As Kärger himself noted [48, p. 143], the latter assumption is not justified when diffusive transport in each pool is relatively inefficient compared to exchange between the pools. The Kärger model has been investigated numerically by Fieremans *et al.* [49] in connection with the diffusion-weighted signal due to an ensemble of long, parallel cylinders with a random in-plane arrangement. In this study, the authors showed that the Kärger model is correct in the long-time limit for the case of poorly permeable cylinder walls. However, the effect of differing relaxation rates inside and outside the cylinders was not considered.

Danish physiologist and 1920 Nobel Laureate, August Krogh,[9] introduced his famous capillary–tissue cylinder model in the course of his investigations on oxygen delivery to striated muscle of mammals [47]. Hoofd [50, 51] extended the steady-state Erlang–Krogh [52] solution[10] to consider a network of randomly distributed parallel

[9]See "The Nobel Prize in Physiology or Medicine 1920". Nobelprize.org. 31 Jul 2012, `http://www.nobelprize.org/nobel_prizes/medicine/laureates/1920/.`

[10]The Danish mathematician A. K. Erlang was acknowledged by Krogh for having provided the oxygen-tension formula appearing in his paper [47]. Erlang is best-known for his pioneering contributions to the field of telephone traffic engineering [53].

capillaries. Wang and Bassingthwaighte [54] studied the shape of capillary supply regions in the steady state, assuming a constant consumption rate per volume of tissue. Secomb and co-workers [55] presented a model of steady-state oxygen delivery to tissue in which the microvessels and the tissue are modelled as a set of discrete oxygen sources and sinks, respectively.

Time-dependent models of gas exchange in Krogh geometries have been set forth by a number of investigators. Roughton [56] considered the exchange of a substance in a long, cylindrical, homogenous annulus, assuming a fixed concentration at the inner annular surface. Diffusion and both zero- and first-order reactions[11] were taken into account. A simplified version of Roughton's results were later considered by Hudson and Cater [52]. In both these models, the assumption of such a fixed concentration implies a very high capillary wall permeability.

The influence of capillary transport has been considered more recently by Reneau *et al.* [57], Lagerlund and Low [58] and Sharma and Jain [59]. While these models take into account oxygen delivery, as well as diffusion and consumption in both the capillaries and extravascular tissue, they are not directly applicable to magnetically tagged water or paramagnetic tracers as employed in MRI. This is mainly due to the fact that tissue oxygen consumption obeys non-linear kinetics.

1.2 Aims of this Thesis

Diffusion and consumption of solutes delivered to the tissues by the microcirculation are both key to tissue physiology [54]. For example, diffusion plays an important role in the distribution of ions, metabolites and neuroactive substances, and hence in how neurons interact with their environment [60]. Furthermore, as argued by Kety [33, p. 8], diffusion of solutes during blood–tissue exchange cannot be expected to occur only across the capillary wall. Equilibration of the extravascular concentration of tracer by radial diffusion (i.e., in any direction perpendicular to a given straight

[11] In zero-order reactions, the reaction rate is constant and independent of the concentration of reactants; see, e.g., Ref. [10], p. 310.

capillary segment) may be considered fast in the well-perfused visceral organs [27, 42] due to relatively small intercapillary distances, so that the time to reach a diffusive steady state in the radial direction may be assumed smaller than typical capillary transit times [27]. On the other hand, spatial diffusive gradients in solute concentration are expected to develop in tissues with greater intercapillary distances and/or a greater proportion of non-perfused capillaries (e.g., resting skeletal muscle) [27] and owing to the presence of physiological barriers which tend to slow down the diffusion [42, p. 276].

Diffusion and first-order consumption processes are both directly relevant to arterial spin labelling MRI. Nonetheless, the manner in which they jointly affect the time course of blood–tissue water exchange has been so far incompletely addressed in the MRI literature. Models of the contribution of extravascular diffusion to transcapillary exchange have appeared in the works of Lee and Fronek [44] and Kuo, Gustafson and Friedman [45]. However, since these spatiotemporal models were both developed for use in indicator-dilution studies involving non-metabolised (or otherwise non-consumed) tracers, they cannot be directly applied to analyse ASL data. Also, spatiotemporal models of oxygen delivery to tissue do not appear to be adequate for the evaluation of blood–tissue tracer exchange mediated by extravascular diffusion and first-order consumption: the reason is that oxygen consumption in the tissues varies non-linearly with tissue oxygen concentration, as discussed in Section 1.1.2.

The main research aims undertaken in this Thesis are therefore as follows:

1. *To develop a spatiotemporal model of blood–tissue exchange of tracer substances* which takes into account capillary flow, diffusive transcapillary permeation, first-order consumption (both in blood and in extravascular tissue) and diffusion in extravascular space. Based on anatomo-physiological facts, a capillary–tissue model will be developed that is reasonably realistic on the mesoscopic scale of individual capillary segments and their surrounding tissue, yet is also analytically tractable. Blood–tissue tracer-exchange will be evaluated under both diffusion- and permeability-limited conditions.

2. *To develop validity conditions for the class of lumped tracer-exchange models*, dependent upon capillary tracer permeability, tracer diffusion coefficient and diffusion time, as well as and geometrical parameters of the capillary network. A number of performance comparisons among various lumped tracer-exchange models have been reported in the literature (e.g., Refs [28, 31, 32, 34, 61, 62]). However, to the best of this author's knowledge, validity conditions for lumped tracer-exchange models, as compared to the class of spatiotemporal models, have to date not been explicitly discussed in the literature, and will be given herein.

   The spatiotemporal tracer-exchange model set forth in this Thesis shall therefore be compared in some generality to the class of lumped tracer-exchange models, for which spatially uniform tracer concentrations are postulated. The predictions of both kinds of modelling approach will be compared in both the non-steady and steady states. The latter case represents an extreme case for assessment of the validity of the well-mixed assumption in lumped modelling approaches, since interplay of diffusion and first-order consumption results in non-uniform concentration profiles also when the concentration becomes stable over time.

3. *To develop a model of the ASL signal which takes into account diffusion of magnetically tagged water in extravascular space.* Mathematical expressions for the intracapillary and extravascular magnetisation for a generic ASL experiment, including both continuous and pulsed ASL approaches, will be obtained based on the spatiotemporal model presented in this Thesis. They will then be compared to the expressions predicted by the lumped model of Parkes and Tofts [34] and the spatiotemporal model of St. Lawrence, Frank and McLaughlin [31], neither of which considers water diffusion. The model presented here will also be compared to the spatiotemporal model of Lee and Fronek [44], which does include diffusion but not magnetic relaxation.

   As a result, both the time scale and appropriate range of values of characteristic

tracer-exchange parameters will be identified for which the model presented here is expected to predict the ASL signal more accurately than the literature models considered for comparison purposes.

The accuracy of selected analytical and numerical results is validated using Monte Carlo simulations. Literature data, as available, is analysed using the presented spatiotemporal tracer-exchange model. Although the main applications with which we shall be concerned in this Thesis pertain to MRI, and in particular to ASL, we expect our results to remain applicable – with appropriate modifications and extensions – to other tracer-based techniques in which compartmental diffusion may be expected to play a significant role.

1.3 Organisation of this Thesis

The contents of this Thesis are organised as follows:

- Chapter 2 describes the adopted capillary–tissue model, introduces the governing equations of transport, exchange and consumption of tracers in whole tissue and defines the main quantities which characterise blood–tissue tracer exchange.

- Chapter 3 evaluates the spatiotemporal model for one- and two-dimensional extravascular diffusion.

- Chapter 4 is devoted to the practical applications of the theory developed in the previous Chapter. Specifically, this Chapter first discusses the various blood–tissue tracer-exchange regimes identified from the spatiotemporal model solution and provides general criteria for the validity of the class of lumped tracer-exchange models. Relevant situations involving diffusion- and permeability-limited exchange are discussed in detail as exemplified, respectively, by gas exchange in the tissues and by water exchange between blood and extravascular tissue. In the latter case, the presented spatiotemporal tracer-exchange model affords an expression of the ASL signal for standard continuous and pulsed

tagging schemes; this result is then compared against the results of several literature models, both lumped and spatiotemporal.

- Chapter 5 reviews the main contributions of this Thesis, suggests further related work and gives concluding remarks.

Chapters 2 – 4 each include a Discussion section and a number of accompanying Appendices.

Chapter 2

Blood–Tissue Tracer Exchange: Model

This Chapter describes the capillary–tissue model, governing equations, and time- and position-dependent quantities that are required for evaluation of blood–tissue tracer exchange.

2.1 Capillary–tissue model

Biological tissues are highly specialised structures with a high degree of microscopic heterogeneity. Microvascular networks are specific to each tissue [63] and form quite complex structures, as demonstrated by anatomical and/or stereological studies in, e.g., the brain cortex [64, 65], myocardium [66], skeletal muscle [67], kidney [68] and liver [69] of several mammalian species. The interstitial space is a highly tortuous medium [70] and is filled with the interstitial fluid that bathes[1] the parenchymal cells

[1]The interstitial fluid is similar in composition to blood plasma (except that the latter has a much higher protein content [1, p. 831]) and serves a number of important functions, including allowing the delivery of nutrients to, and removal of waste products from, parenchymal cells; providing a low-resistance return path for cell transmembrane currents; and providing a channel for extrasynaptic cell communication (Refs [1, p. 790] and [70]).

and an extracellular matrix of glycoproteins [1, p. 134].

Owing to their microscopic heterogeneity, it is unfeasible to incorporate a comprehensive microscopic description of parenchymal tissues and microvascular networks into a theoretical model of transport and exchange in whole tissue; cf. the discussion in Ref. [71, p. 682]. However, blood–tissue exchange in whole tissue can be described on a *mesoscopic scale*. On this 'intermediate' scale, any microscopic fluctuations in physical quantities of interest (e.g., the concentration of a given tracer) are effectively smoothed out, yet significant variations in these quantities over tissue lengths ranging between this scale and the actual measurement scale are preserved. If the measurement scale is defined by the smallest linear dimension of, e.g., a typical imaging voxel, this latter condition ensures that sub-voxel variations can be taken into account. As an example, a characteristic mesoscopic length for ionic diffusion in the interstitial space of the rat cerebellum was estimated by Nicholson and Phillips [60] as ~ 6 μm, given by the geometric mean of the interstitial width (≤ 0.04 μm) and the dimension of a cerebellar folium (≥ 1000 μm). Note that this length is comparable to cell size and is smaller than intercapillary distance, as required. A similar result is obtained if the dimension of a typical MRI voxel are considered.

In this Thesis, a simplified mesoscopic tissue model is considered that includes (i) the intracapillary space contained in the exchanging capillaries[2] and (ii) the surrounding extravascular space, in particular pericapillary regions associated with individual capillary segments (Fig. 2.1a, b). On a mesoscopic scale, relevant anatomo-functional units include, besides capillary segments, erythrocytes, and parenchymal cells and cell clusters, with characteristic lengths of the order of $1-100$ μm; see, for example, Refs [1, Fig. 7.1], [72, pp. 1067 ff.] and [74, 75]. For transport and exchange processes of the kind to be discussed in this Thesis, the corresponding characteristic times are of the order of $1-1000$ ms. Further technical details concerning the mesoscopic scale

[2]Blood–tissue exchange, however, is not restricted to the capillaries. According to Zweifach [72, p. 1066], 'the phenomenon referred to as "capillary permeability" encompasses exchange across the wall of vessels ranging from the terminal arteriolar class down through all of the various capillary subdivisions and including the large collecting venules'. Also, the arterioles are involved in O_2 exchange between blood and extravascular tissue [73].

are found in Appendix 2.5.1 (p. 59).

2.1.1 Intracapillary space

The microvascular network enables the bulk of blood–tissue exchange via the exchanging arterioles, capillaries and venules. In this Thesis we only consider flow and exchange phenomena which occur at the level of the capillaries, i.e., in the intracapillary space. Our main modelling assumptions pertaining to intracapillary space are described below.

We treat the time-dependent intracapillary concentration of tracer as uniform at every capillary cross-section, but allow for variations with distance along the capillary axis. This assumption is plausible due to the mixing of blood-borne substances, including both endogenous and exogenous tracers, effected by the motion of erythrocytes [43]. Specifically, this assumption seems to be justified for tracer blood water, since exchange of water between plasma and the erythrocytes is about two orders of magnitude faster than between plasma and the interstitial fluid, with respective time rates of the order of 100 s^{-1} and 1 s^{-1} [76, 77].

The capillary wall anatomically consists of an endothelium (i.e., a one-layer array of flattened cells) and an outer basement membrane [1, p. 830] and has a thickness of about 1 μm [63, 78, 79]. This thickness is smaller than typical capillary radii as well as typical diffusion lengths involved in MRI experiments; hence, for present purposes we model the capillary wall not as a distinct compartment, but rather as a negligibly thin membrane characterised by its diffusive permeability coefficient, κ [80, p. 509].

The diffusive permeability of a membrane to a given solute is defined as the amount of that solute which traverses unit surface area of the membrane in unit time, when unit concentration difference is maintained across each face of the membrane [81, p. 294]. Mathematically, the diffusive permeability is equal to the ratio of the solute diffusion coefficient inside the membrane to the thickness of the membrane, in the limit when both these quantities become vanishingly small [80]. Neither osmotic permeation nor forced permeation due to hydraulic pressure gradients will be included in the presented model of blood–tissue exchange; osmotic permeation, however, is

briefly discussed in Section 2.4.3.

Section 2.4.1 of Discussion to this Chapter gives a brief description of the capillary anatomy and flow properties in relation to the tissue modelling assumptions made above. Detailed descriptions of various aspects of the microcirculation can be found in, for example, Refs [65, 72, 82].

2.1.2 Extravascular space

In this Section we consider the extravascular space from the viewpoint of its diffusion properties. In this Thesis, the term 'diffusion' shall refer to the random motions of tracer molecules in the extravascular space, whereas the term 'diffusive permeation' shall refer to non-osmotic, passive transmembrane transport – thus excluding any active transport processes.

Diffusion in heterogenous media, hence in biological tissues, is a scale-dependent process (for a discussion see, e.g., Refs [83, 84]). Due to microscopic heterogeneities (e.g., cell membranes and axonal fibre crossings; Fig. 2.1b), the probability density function of molecular displacements in tissue is, in general, non-Gaussian and the diffusion coefficient is time- and position-dependent [71, 80]. This is in contrast to diffusion in a homogenous medium [80], which is Gaussian and hence is characterised by a constant and uniform diffusion coefficient.

However, diffusion in tissue becomes Gaussian over diffusion times for which a length scale known as the correlation length of the tissue [71, p. 689] is exceeded; the corresponding time scale is referred to as the *tortuosity asymptote* or *tortuosity limit* [84]. On this spatiotemporal scale the molecules of tracer have had ample time to probe the connectivity and geometrical tortuosity of the medium, so the molecular displacements become statistically independent (cf. Refs [48, p. 138] and [85, p. 160]). Because the parenchymal cells are densely packed, the tissue correlation length is dependent upon cell size (i.e., individual cells, cell organelles and cell clusters) and additional tissue-specific parameters like (in white matter) the distribution of axonal radii. Typical tissue correlation lengths are in the range $1-10$ μm [71, 86]. Importantly, in the tortuosity limit the tracer diffusion coefficient attains its long-time

asymptotic value, which is lower than the tracer diffusion coefficient in bulk aqueous or gel media [84, 87]. Experimental results in brain white matter suggest that typical correlation times are of the order of $1-50$ ms. For this and further details concerning the time dependence of the diffusion coefficient the reader is referred to Section 2.4.4 of the Discussion to this Chapter.

The kinetics of tracer exchange between the intracapillary, interstitial and intracellular spaces affects how the tortuosity limit is approached; see, e.g., Ref. [49] for the case of a random in-plane packing of parallel permeable cylinders. We consider three different cases. First, since the intracellular volume fraction is usually large, when interstitial–intracellular exchange is much faster than intracapillary–interstitial exchange, the extravascular space can be regarded as a single compartment described by average parameters. At the other extreme, for extravascular extracellular tracers (e.g., gadopentetate dimeglumine, Gd-DTPA) the intricate geometry of the interstitial space results in non-Gaussian diffusion prior to attainment of the tortuosity limit. Lastly, when the rates of intracapillary–interstitial and interstitial–intracellular tracer exchange are comparable, the tissue correlation time is expected to depend markedly on tracer exchange. In particular, water is able to exchange between the intracapillary, interstitial and intracellular spaces. Figure 2.1b represents, schematically, a hypothetical situation in which the passage of tracer molecules into, and subsequent diffusion in, the intracellular space is significantly impeded by a low cell membrane permeability. Experiments in brain and myocardial tissue indicate that interstitial–intracellular water-exchange rates are moderate to fast; refer to Section 2.4.3 in the Discussion to this Chapter for more details.

In conclusion, in this Thesis the extravascular space is modelled as an effective homogenous medium with spatially uniform properties governing diffusion and first-order consumption of tracers on a mesoscopic spatiotemporal scale. Specifically, diffusion of tracer molecules in the presence of multiple extravascular barriers is assumed to occur in the tortuosity limit, hence to be Gaussian and therefore characterised by a uniform and constant tracer diffusion coefficient.

2.1.3 The single-capillary approximation

We regard the pericapillary region supplied by any given capillary segment as being notionally bounded by a diffusion watershed that is responsive to changing microvascular conditions [54, p. 104]. In this Thesis we only consider the case in which tracer exchange between any given capillary segment and its attendant pericapillary region – to be jointly regarded as a basic blood–tissue exchange unit – is largely unaffected by tracer exchange in the neighbouring microvessels; we shall refer to this approach as the *single-capillary approximation* (Fig. 2.1a, b). This approximation is expected to be reasonably accurate for tracer diffusion times such that the diffusion length of tracer molecules does not exceed typical half-intercapillary distances, A, in the tissue of interest.

A basic blood–tissue tracer exchange unit shall be modelled taking into account relevant anatomical features of capillary networks. For example, in dog myocardium Bassingthwaighte *et al.* [66, p. 229] described 'large groups of capillaries running parallel to muscle fibers and extending for up to a few centimeters', capillary diameter (at maximum dilation) and average unbranched capillary length being 5.6 μm and 100 μm, respectively. On the other hand, cortical brain capillary segments are noticeably curved, cf. Fig. 6 of Ref. [65]. Pawlik *et al.* [65, p. 35] estimated the mean capillary diameter, median radius of curvature and median segment length in cat brain cortex as 5.1 μm, 57 μm and 108 μm, respectively. However, for the purpose of evaluating tracer diffusion in the pericapillary region, cortical brain capillary segments can be treated as straight provided that the tracer diffusion length is much smaller than both the length and radius of curvature of a typical capillary segment.

We thus model a capillary segment as a straight cylinder of radius a and length L, whose lateral surface has diffusive tracer permeability κ. The pericapillary region extends radially outwards from the capillary segment for distances comparable to, but not greater than, a typical half-intercapillary distance, A; its shape, however, is immaterial to a spatiotemporal analysis of blood–tissue exchange when only relatively short diffusion lengths are considered. The average net flux of tracer between adjacent pericapillary regions represents the time-averaged effect of the surrounding

microvasculature on any given capillary segment, and is assumed zero. A blood–tissue exchange unit is illustrated in Fig. 2.1c.

All three parameters a, L, and A can be determined by stereological methods [64, 65, 67]. Brain and, to a lesser extent, myocardial capillary networks may be referred to as sparse capillary networks in that intercapillary distances are relatively large (i.e., $a/A \ll 1$) and capillary volume fractions correspondingly low (Table 2.1).

In the idealised situation described, the distribution of tracer in whole tissue is given by the sum of contributions from all capillary segments and pericapillary regions. The simplest assumption that can be made in order to quantify blood–tissue exchange is that in any given volume of whole tissue there is a collection of straight capillary segments consistent with typical values of capillary radius, intercapillary distance and capillary volume fraction, all capillary segments connecting one and the same notional pair of arterial inflow and venous outflow ends in the given volume. This simple parallel arrangement overlooks capillary branching. In fact, at and near to any capillary branching the exchange must be strongly dependent on the functional state of all the capillary segments joined at that branching point. However, because capillary segment lengths are, on average, much larger than both capillary radii and intercapillary distances (see examples in Table 2.1), the surface area associated with capillary branchings is only a small fraction of the total surface area available for tracer exchange. Thus, capillary branching effects shall not be considered further here.

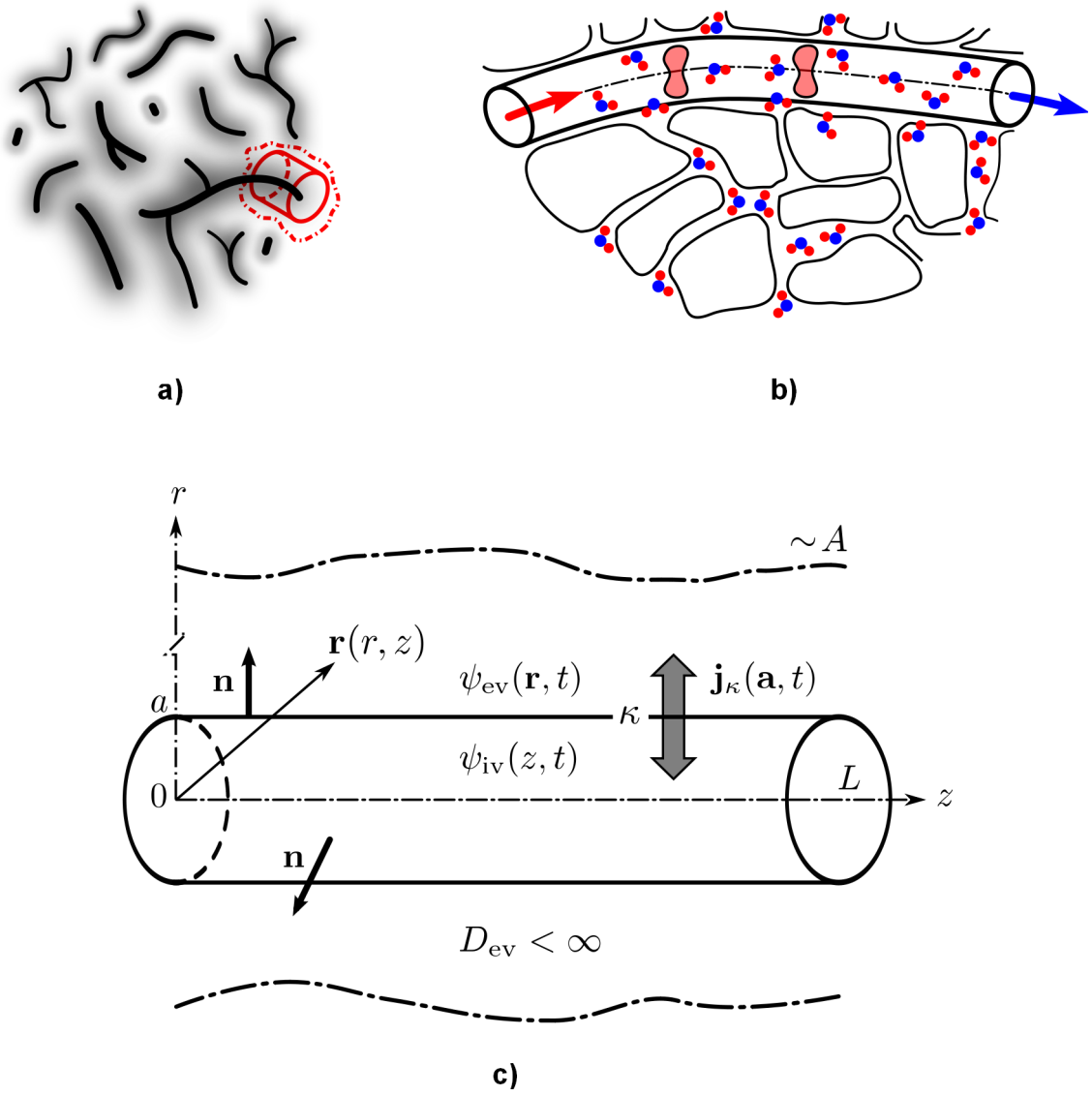

Figure 2.1: **a) Cross-sectional view of a hypothetical capillary network**. Shaded regions represent the distribution of tracer in extravascular space; the diffusion watershed is suggested by brighter areas in the space surrounding the capillaries. **b) Diagram of capillary segment** illustrating convection, transcapillary permeation and extravascular diffusion and cell transmembrane permeation of tracer molecules. **c) Single-capillary approximation**. A capillary segment of length L is shown indicating a permeable capillary wall (broken line) and the diffusion watershed between adjacent pericapillary regions (thicker dash-dot line). Dimensions are not to scale. Notations are defined in Sections 2.1.3 and 2.2.1.

2.2 Mathematical model

In this Section the governing equations for mesoscopic blood–tissue exchange are set forth and the method of solution is described.

2.2.1 Governing equations

The spatiotemporal governing equations of blood–tissue exchange, Eqs (2.1a) – (2.1d) below, are set on a mesoscopic scale (introduced in Section 2.1.2). The reason is that on a microscopic (i.e., subcellular) scale the tracer concentration will vary irregularly and the concentration gradients may fluctuate significantly [60, p. 227] and be ill-defined [87, p. 826], whereas on a mesoscopic scale both these quantities are well behaved; cf. Refs [49], [60, pp. 227 – 228] and [87, p. 826]. A method for expressing the microscopic transport and exchange equations on a mesoscopic scale is detailed in Appendix 2.5.1 (p. 58); a summary is found on pp. 95 ff. of this Appendix.

Let $\psi_{\mathrm{iv}}(z,t)$ and $\psi_{\mathrm{ev}}(\mathbf{r},t)$ denote the time- and position-dependent concentration of tracer in intracapillary and extravascular space, respectively, expressed in units of quantity of tracer per unit of tracer-accessible volume in the respective spaces. As an example, in ASL experiments the tracer concentration represents the difference in longitudinal magnetisation, with respect to equilibrium values, between the 'tag' and 'control' states and is usually expressed in units of magnetic moment per volume of water in blood and in extravascular space; in PET and DCE MRI it is the concentration of, respectively, a radiotracer and an exogenous paramagnetic tracer that is monitored, and both plasma and whole-blood concentrations may be employed.

The argument $\mathbf{r} \equiv (r,z)$ is a position vector, r denoting radial distance from the capillary axis and z denoting axial distance from the inflow end of the capillary segment (Fig. 2.1c); t denotes the time, with $t = 0$ at the time of first arrival of tracer molecules in the considered capillary segment. As mentioned in Section 2.1.1, the intracapillary concentration is assumed uniform across any capillary cross-section, hence independent of angular coordinate. In the pericapillary region, the concentration varies both in the radial and axial directions, but not with angular coordinate due

to the assumed negligible influence of the neighbouring capillaries (Section 2.1.3).[3]

For a generic capillary segment and its adjacent pericapillary region, we consider the case in which the blood–tissue exchange is driven by the concentration of tracer at the inflow end of the capillary segment, $\psi_{\mathrm{iv}}(z = 0, t)$. The time course of the intracapillary and extravascular concentrations of tracer is described by the pair of partial differential equations

$$\frac{\partial \psi_{\mathrm{iv}}(z,t)}{\partial t} = -\,u_z \frac{\partial \psi_{\mathrm{iv}}(z,t)}{\partial z} - \frac{\psi_{\mathrm{iv}}(\mathbf{a}_-,t) - \psi_{\mathrm{ev}}(\mathbf{a}_+,t)}{\tau_{\mathrm{iv}}} - R_{\mathrm{iv}}\psi_{\mathrm{iv}}(z,t) \tag{2.1a}$$

and

$$\frac{\partial \psi_{\mathrm{ev}}(\mathbf{r},t)}{\partial t} = D_{\mathrm{ev}}\nabla^2\psi_{\mathrm{ev}}(\mathbf{r},t) - R_{\mathrm{ev}}\psi_{\mathrm{ev}}(\mathbf{r},t)\,, \tag{2.1b}$$

which are coupled through the diffusive transcapillary permeation flux $\mathbf{j}_\kappa$, i.e., the amount of tracer crossing unit capillary surface area per unit time, given by

$$\begin{aligned} \mathbf{n}\mathbf{j}_\kappa(\mathbf{a},t) &= -D_{\mathrm{ev}}\mathbf{n}\nabla\psi_{\mathrm{ev}}(\mathbf{a}_+,t) \\ &= \kappa\left[\psi_{\mathrm{iv}}(\mathbf{a}_-,t) - \psi_{\mathrm{ev}}(\mathbf{a}_+,t)\right]. \end{aligned} \tag{2.1c}$$

Similarly, in the single-capillary approximation the zero-flux at the diffusion watershed is expressed as

$$D_{\mathrm{ev}}\mathbf{n}\nabla\psi_{\mathrm{ev}}(\mathbf{r},t)|_{\text{diffusion watershed}} = 0\,. \tag{2.1d}$$

However, for actual calculations (see Chapters 3 and 4) we shall replace this condition by the simpler one given by

$$D_{\mathrm{ev}}\mathbf{n}\nabla\psi_{\mathrm{ev}}(r = A,t) = 0\,. \tag{2.1e}$$

In the above equations, $\mathbf{a}_\mp = (a_\mp, z)$ denotes a point on, respectively, the luminal (i.e., intracapillary) and abluminal (i.e., extravascular) face of the capillary wall; $\mathbf{n}$

[3] *Remark on notation*: where confusion does not arise, the average of any dependent variable with respect to any one of its arguments shall simply be denoted by dropping that argument. For example, $\psi_{\mathrm{iv}}(z,t)$ denotes the average intracapillary concentration with respect to radial distance and angular coordinate, and $\psi_{\mathrm{ev}}(t)$ denotes a spatially averaged extravascular concentration of tracer.

is a unit normal directed outwards from the abluminal capillary surface (Fig. 2.1c). Since the intracapillary concentration has been considered uniform at every capillary cross-section (Section 2.1.1), the concentration at the luminal face of the capillary wall a distance z from the inflow end of the capillary segment, $\psi_{\mathrm{iv}}(\mathbf{a}_-, t) \equiv \psi_{\mathrm{iv}}(a_-, z, t)$, is taken to be approximately equal to the average intracapillary concentration over the entire capillary cross-section, $\psi_{\mathrm{iv}}(z, t)$.

The rest of the variables have the following meaning: u_z is the mean speed of tracer flow in a direction parallel to the capillary axis, and it is comparable to the erythrocyte speed (see Table on p. 362 of Ref. [82]); D_{ev} is the diffusion coefficient for tracer in extravascular space; and R_{iv} and R_{ev} are the rates of tracer production or consumption/relaxation. Here, all four parameters, κ, D_{ev}, R_{iv} and R_{ev}, shall be assumed spatially uniform (by the modelling assumption of extravascular homogeneity; p. 21) and time independent. The mean intracapillary residence time, or first-order lifetime, τ_{iv}, for well-mixed tracer molecules [88, 89] in the absence of convection and consumption, is equal to the volume of tracer-accessible intracapillary space divided by the product of capillary permeability and surface area parameters; see the development leading to Eqs (2.70a) and (2.70b) of Appendix 2.5.1. For a cylindrical capillary segment of radius a we have

$$\tau_{\mathrm{iv}} = \frac{a}{2\kappa} \times \text{fraction of tracer-accessible intracapillary space}\,. \tag{2.2a}$$

Often, estimates for the anatomo-physiological parameters that enter in (2.2a) are available only on a coarser spatial scale (e.g., an MRI voxel) and the mean intracapillary residence time is thus rewritten as

$$\tau_{\mathrm{iv}} = \frac{v_{\mathrm{iv}}}{PS}\,, \tag{2.2b}$$

where v_{iv} is the fraction of tracer-accessible intracapillary volume and PS is standard notation for the product of capillary tracer permeability and capillary surface area; both v_{iv} and PS are expressed per unit volume of whole tissue (i.e., including its contained blood).[4] Likewise, the mean extravascular residence time for well-mixed

[4]It is noted that the parameters v_{iv}, v_{ev}, τ_{iv} and τ_{ev} can be specified on various spatiotemporal

tracer molecules [88, 89] in the absence of convection and consumption is given by

$$\begin{aligned}\tau_{\mathrm{ev}} &\sim \frac{A^2}{2a\kappa} \times \text{fraction of tracer-accessible extravascular space} \\ &= \frac{v_{\mathrm{ev}}}{PS}\,, \end{aligned} \tag{2.2c}$$

where v_{ev} is the tracer-accessible extravascular volume per unit volume of whole tissue. In the case in which all space is accessible to tracer, $v_{\mathrm{iv}} + v_{\mathrm{ev}} = 1$; this has been assumed for the estimation of mean water residence times in grey matter and myocardium (Table 2.1). Comparing (2.2b) and (2.2c) gives the well-known relation $\tau_{\mathrm{iv}}/\tau_{\mathrm{ev}} = v_{\mathrm{iv}}/v_{\mathrm{ev}}$.

Equation (2.1a) expresses tracer mass balance in a capillary segment, as determined by capillary flow (convection), intracapillary relaxation and blood–tissue permeation; see pp. 66 ff. of Appendix 2.5.1. The mean transit time of tracer through a capillary segment is

$$\tau_{\mathrm{c}} = \frac{L}{u_z} \tag{2.3a}$$

and the capillary tracer flow per volume of whole tissue is given by

$$f_{\mathrm{iv}} = \frac{v_{\mathrm{iv}}}{\tau_{\mathrm{c}}}\,. \tag{2.3b}$$

Here, f_{iv} is defined in terms of tracer-accessible volume of capillary blood; for tracers which do not exchange with the erythrocytes, capillary tracer flow is equal to capillary blood flow times haematocrit, i.e., the cell volume fraction of whole blood [3, p. 25]; the effect of other plasma-borne cells is neglected as their count number per cubic millimetre of blood is much less than for erythrocytes [3, pp. 27 ff.].

Equation (2.1b) is a diffusion–consumption (or diffusion–relaxation) equation. The Laplace operator is indicative of Gaussian diffusion [49, p. 714], since for non-Gaussian diffusion higher-order time and space derivatives would arise in Eq. (2.1b) [71, p. 685].

scales, e.g., those associated with generic mesoscopic volume elements (Appendix 2.5.1), capillary segments and their associated pericapillary regions, and imaging voxels. However, since the appropriate scale shall be clear from the context, we use a scale-independent notation for these parameters throughout.

Importantly, for tracers which can permeate the parenchymal cell membrane (e.g., tracer water), transcellular exchange as well as diffusive transport and first-order consumption in the interstitial and intracellular spaces can be jointly described by an equation of the form (2.1b) when the intracellular concentration is negligibly low or when nearly-equilibrium conditions exist (these are sufficient conditions). In this latter case, the tracer concentrations per unit tracer-accessible volume in the interstitial and extravascular spaces are nearly equal, and hence they are also approximately equal to the tracer concentration per volume of whole extravascular space. More details can be found in Appendix 2.5.1 (pp. 76 ff.).

Lastly, Eq. (2.1c) expresses that the tracer concentration has a jump discontinuity at the capillary wall, whereas the flux of tracer is continuous everywhere. Using this equation, the effective thickness of the capillary wall is defined by

$$\ell \equiv \frac{D_{\mathrm{ev}}}{\kappa}\,, \tag{2.4}$$

which is the thickness of a notional, one-dimensional slab of extravascular tissue such that the difference between the steady-state tracer concentrations at each side of the slab equals the actual concentration difference at the capillary wall (Fig. 2.2).[5]

It is the coupling between Eqs (2.1a) and (2.1b) through the boundary condition (2.1c) that prevents, insofar as this author is aware, obtaining the solution to the above system of differential equations for arbitrary values of R_{iv} and R_{ev}, from the solution for the case in which $R_{\mathrm{iv}} = R_{\mathrm{ev}}$. In particular, the expression for the ASL signal cannot be constructed from the solution given by Lee and Fronek [44] for the case appropriate to indicator-dilution studies, i.e., $R_{\mathrm{iv}} = R_{\mathrm{ev}} = 0$.

In the single-capillary approximation, the postulated time-averaged net zero flux between adjacent pericapillary regions is represented approximately by the more stringent condition (2.1d), which is interpreted as imposing elastic molecular reflections at the notional pericapillary wall [90].

As shown in Eqs (2.1a) and in (2.1b), here axial diffusion of tracer is assumed negligibly low on account of smooth concentration profiles at both the capillary and

[5] In Ref. [80, p. 509] the effective membrane thickness is defined as one-half the quantity on the right-hand side of our Eq. (2.4).

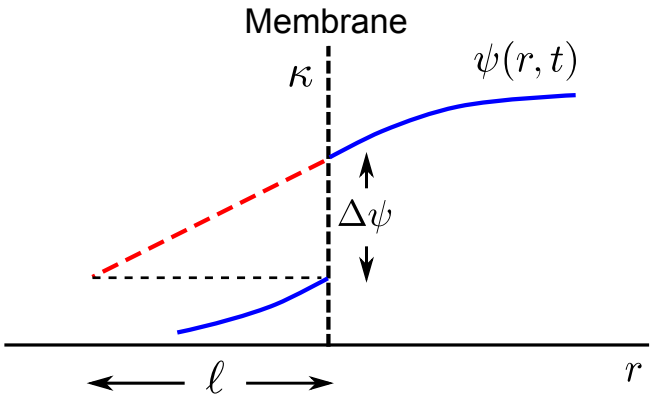

Figure 2.2: **Effective membrane thickness,** ℓ.

tissue levels. In this situation, the extravascular concentration of tracer at any given position $\mathbf{r}' = (r', z')$ at time t' is only dependent upon the concentration at positions on the same transverse section ($z = z'$) for times t earlier than t' (Fig. 2.3a). However, $\psi_{\text{ev}}(\mathbf{r}', t')$ will, in general, depend upon the concentration of tracer at arbitrary positions at times $t < t'$ (Fig. 2.3b). In the following paragraphs the effect of axial diffusion in both intracapillary and extravascular space is discussed.

For magnetically tagged water [24, 34] and low-molecular-weight paramagnetic tracers [14, 91, 92], arterial dispersion causes the intracapillary concentration to peak at approximately 1 s and 10 s, respectively, after arrival of the tracer bolus at a brain voxel; see, e.g., Fig. 1 of Ref. [14] and Fig. 6 of Ref. [24]. Assuming an erythrocyte speed of $0.39-1.5\ \mu\text{m}\,\text{ms}^{-1}$ [65, 93],[6] we estimate the build-up of tracer concentration to occur over vessel lengths not smaller than about 400 μm, thus it is reasonable to assume negligible axial diffusion gradients in the capillaries. Because axial diffusion times are much greater than mean transit times through a capillary segment, convection dominates tracer transport for times ($t \gtrsim D_z/u_z^2$) greater than a few milliseconds. For typical values of the parameters, e.g., $L = 100\ \mu$m, $u_z = 0.4-1.5\ \mu\text{m}\,\text{ms}^{-1}$ and $D_z = 0.8\ \mu\text{m}^2\,\text{ms}^{-1}$ [94], these times are $L^2/(2D_z) = 5$ s and $L/u_z \leq 250$ ms, respectively; the resultant Péclet number, a measure of the strength of convective versus axial diffusive phenomena, is estimated as $(L^2/(2D_z))/(L/u_z) = u_z L/(2D_z) \geq 20$.

[6] Pawlik *et al.* [65] provide a median value, whereas Seylaz *et al.* [93] quote an average value.

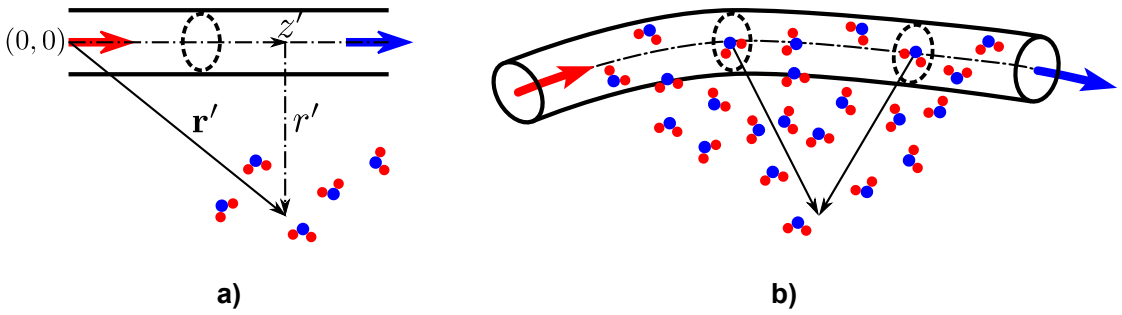

Figure 2.3: Axial diffusion dependence of extravascular concentration at position $\mathbf{r}'$. **a)** Negligibly low axial diffusion. **b)** Non-negligible axial diffusion. More details on p. 30.

In the extravascular space we only consider the situation where axial diffusive fluxes are much lower than any radial diffusive fluxes. This is expected if the transport of tracer by convection and transcapillary permeation is more efficient than by axial extravascular diffusion,[7] e.g., for capillary-segment parameters $\tau_c \lesssim 280$ ms, $\tau_{iv} \sim 300-900$ ms (Table 2.1) and $L^2/2D_z \sim 2$ s (using $D_z = 2.26\ \mu m^2\,ms^{-1}$ for water in human brain white matter [86]). In this situation, for times of the order of one mean capillary-segment transit time, the concentration of tracer at the abluminal side of the capillary wall is expected to be virtually uniform, provided that the capillary permeability varies not too abruptly with axial distance. This argument is somewhat less accurate for times much smaller than the capillary-segment transit time, and for high capillary wall permeabilities to tracer, since in both these situations the exchanged tracer tends to accumulate near the inflow end of the capillary. In Appendix 2.5.3 we estimate the magnitude of some axial and radial diffusive fluxes.

2.2.2 Method of solution

Tracer capillary flow, transcapillary permeation and extravascular diffusion are modelled as linear, time-invariant (stationary) phenomena through Eqs (2.1a)–(2.1c). Thus, the *arterial-to-intracapillary impulse response function*, $h_a^{iv}(z,t)$, and *arterial-to-extravascular impulse response function*, $h_a^{ev}(\mathbf{r},t)$, are respectively defined through

[7] It is misleading to speak of a diffusion rate or diffusion speed because, at sufficiently short times, the value of $\sqrt{D_{ev}/t}$ exceeds the instantaneous velocity of the diffusing molecules [95, p. 11].

the relations:

$$\psi_{\mathrm{iv}}(z,t) = h_{\mathrm{a}}^{\mathrm{iv}}(z,t) * \psi_{\mathrm{iv}}(z=0,t) \equiv \int_0^t h_{\mathrm{a}}^{\mathrm{iv}}(z,t-t')\psi_{\mathrm{iv}}(z=0,t')\,\mathrm{d}t' \,, \tag{2.5a}$$

$$\psi_{\mathrm{ev}}(\mathbf{r},t) = h_{\mathrm{a}}^{\mathrm{ev}}(\mathbf{r},t) * \psi_{\mathrm{iv}}(z=0,t) \,, \tag{2.5b}$$

where $*$ denotes time convolution; the limits of integration in Eq. (2.5a) correspond to causal concentrations, i.e., $\psi_{\mathrm{iv}}(z,t<0)=0$, $\psi_{\mathrm{ev}}(\mathbf{r},t<0)=0$.

Furthermore, we make the modelling assumption that the concentration of tracer at the inflow end of a capillary segment drives the intracapillary concentration, which, in turn, drives the tracer concentration in the pericapillary region associated with that capillary. Thus, the *blood-to-tissue* (i.e., intracapillary-to-extravascular) *impulse response function*, $w(\mathbf{r},t)$, may similarly be defined by the relation

$$\psi_{\mathrm{ev}}(\mathbf{r},t) = w(\mathbf{r},t) * \psi_{\mathrm{iv}}(z,t) \,, \tag{2.5c}$$

where z is the z-component of position vector $\mathbf{r}$ (Fig. 2.1c, Fig. 2.3b). The arterial-to-extravascular impulse response function is therefore given by

$$h_{\mathrm{a}}^{\mathrm{ev}}(\mathbf{r},t) = w(\mathbf{r},t) * h_{\mathrm{a}}^{\mathrm{iv}}(z,t) \,. \tag{2.5d}$$

In this Thesis, we evaluate the blood-to-tissue impulse response function for the case where the intracapillary concentration is not significantly altered by any tracer back-flux from extravascular space into the blood. In the tracer kinetic literature this is usually assumed to be the case when the ratio $v_{\mathrm{iv}}/v_{\mathrm{ev}}$ of tracer-accessible spaces is small [34]. However, it must be borne in mind that it is not the spatially averaged concentration, but the abluminal tracer concentration, that determines the transcapillary flux. Conditions for the rapid clearance of tracer from the blood by capillary flow and/or relaxation may be obtained by evaluating the intracapillary concentration due to a constant, axially uniform concentration at the abluminal face of the capillary wall, i.e., $\psi_{\mathrm{iv}}(z,t<0)=0$ and $\psi_{\mathrm{ev}}(a_+,0\le z\le L,t\ge 0)=1$. (In Ref. [96] we considered the simpler case in which only the effect of relaxation

was relevant). The difference between intracapillary and extravascular relaxation rates is accounted for by putting $R_{\mathrm{iv}} \mapsto R_{\mathrm{iv}} - R_{\mathrm{ev}}$. Then, for each position z, the intracapillary concentration increases during the interval $t < z/u_z$ due to increasing amounts of tracer flowing in from upstream positions, and then remains stationary. The steady-state concentration is greatest at the outflow end of the capillary segment; the ratio of 'venous' to extravascular concentration at time τ_{c} is given by[8]

$$\psi_{\mathrm{iv}}(z = L, t = \tau_{\mathrm{c}}) = \frac{1 - \exp\{-[1 + (R_{\mathrm{iv}} - R_{\mathrm{ev}})\tau_{\mathrm{iv}}]\tau_{\mathrm{c}}/\tau_{\mathrm{iv}}\}}{1 + (R_{\mathrm{iv}} - R_{\mathrm{ev}})\tau_{\mathrm{iv}}} \,. \tag{2.6}$$

Thus, the tracer will be rapidly cleared from intracapillary space if

$$\frac{\tau_{\mathrm{c}}}{\tau_{\mathrm{iv}}} \sim \frac{PS}{f_{\mathrm{iv}}} \ll 1 \tag{2.7a}$$

or if

$$(R_{\mathrm{iv}} - R_{\mathrm{ev}})\tau_{\mathrm{iv}} \gg 1 \,. \tag{2.7b}$$

Constraint (2.7a) implies that the wash-out of tracer molecules is much faster than their accumulation in the capillary due to back-flux from the extravascular space; hence in Eq. (2.6) the ratio of intracapillary to extravascular concentration is as small as $\tau_{\mathrm{c}}/\tau_{\mathrm{iv}}$. Constraint (2.7b) implies that intracapillary relaxation is nearly complete on the scale of typical intracapillary residence times, in contrast to much slower extravascular relaxation/consumption.

In the absence of paramagnetic tracers, we estimated $|R_{\mathrm{iv}} - R_{\mathrm{ev}}|\tau_{\mathrm{iv}} \sim 10^{-2} - 10^{-1}$ for longitudinal relaxation in brain and myocardium (see Table 2.1 and Appendix 2.5.2), hence rapid clearance from the blood requires that (2.7a) hold. This condition is well satisfied in brain cortex but is perhaps less well satisfied in myocardium, owing to higher capillary water permeability and greater capillary segment lengths (see Table 2.1). On the other hand, when intravascular paramagnetic tracers are used, enhancement of the proton relaxation rate results in $R_{\mathrm{iv}} \gg R_{\mathrm{ev}}$, hence either (2.7a) or (2.7b) must hold (numerical estimates are given in Appendix 2.5.4).

[8] For $R_{\mathrm{iv}} = R_{\mathrm{ev}}$, the right-hand side of (2.6) is identical with the steady-state tracer extraction ratio, which for low extravascular concentrations is given by $E = 1 - \exp(-PS/f_{\mathrm{iv}})$; see Ref. [81].

It may be useful to highlight the analogy between the basic unit of blood–tissue tracer exchange, under conditions of rapid tracer clearance, and a simple electric circuit in the stationary regime after all transients have died out. In this situation, the intracapillary space can be likened to an ideal voltage generator with zero internal impedance (analogous to the case of fast capillary flow and/or intracapillary relaxation rate), whose output voltage [i.e., $\psi_{\mathrm{iv}}(z,t)$] is therefore independent of the current [i.e., the transcapillary tracer flux $\mathbf{j}_{\kappa}(t)$] delivered to, or absorbed from, the circuit (i.e., the extravascular space) at any time. In this analogy, each nodal current and each branch voltage [i.e., $\psi_{\mathrm{ev}}(\mathbf{r},t)$] can be calculated using a specific impulse response function analogous to (2.5c).

In conclusion, if either relation (2.7a) or relation (2.7b) holds, then the blood-to-tissue impulse response function, $w(\mathbf{r},t)$, can be meaningfully defined as a spatiotemporal filter which characterises the blood-to-tissue tracer flux and the diffusion of tracer in the extravascular space. The method of solution of the blood–tissue exchange equations developed herein involves three main sequential steps:

1. The blood-to-tissue impulse response function, $w(\mathbf{r},t)$, is evaluated as described in Section 2.3.1.

2. The blood-to-tissue impulse response function is substituted into Eq. (2.1a) for the intracapillary tracer concentration, and the resultant equation is solved to obtain the arterial-to-intracapillary impulse response function, $h_{\mathrm{a}}^{\mathrm{iv}}(z,t)$.

3. The arterial-to-extravascular impulse response function, $h_{\mathrm{a}}^{\mathrm{ev}}(\mathbf{r},t)$, is evaluated with the use of (2.5d).

2.3 Blood–tissue exchange quantities

2.3.1 Blood-to-tissue impulse and step response functions

The function $w(\mathbf{r}, t)$ represents the response to an idealised, impulse-like intracapillary concentration, i.e., $\psi_{\mathrm{iv}}(z, t) = \delta(t)$, where $\delta(\cdot)$ is the Dirac delta function and $\mathbf{r} = (z, r)$ denotes a position in extravascular space (Fig. 2.3). As is well known, an equivalent description of blood–tissue exchange is given by the *blood-to-tissue step response function*, $W(\mathbf{r}, t)$, which represents the extravascular concentration driven by a unit step increase in intracapillary concentration, i.e., $\psi_{\mathrm{iv}}(z, t < 0) = \theta(t)$, where

$$\theta(t) = \begin{cases} 0, & \text{if } t < 0\,; \\ 1, & \text{otherwise}\,, \end{cases} \tag{2.8}$$

is the Heaviside unit step function (Ref. [97], p. 492). Thus

$$W(\mathbf{r}, t) = \int_0^t w(\mathbf{r}, t')\,\mathrm{d}t'\,. \tag{2.9}$$

By definition, both the blood-to-tissue impulse response and step response functions satisfy the diffusion–consumption equation (2.1b) and the transcapillary tracer flux condition (2.1c). The diffusion–consumption equation is, in general, hard to solve because of the inhomogenous boundary condition (2.1c) arising from the non-zero, time-varying intracapillary concentration $\psi_{\mathrm{iv}}(\mathbf{a}_-, t)$.

Nonetheless, the analysis of blood–tissue exchange with zero initial conditions (in intracapillary space) and with an inhomogenous boundary condition (at the capillary wall) may be reduced to the case in which (i) the extravascular concentration satisfies the diffusion–consumption equation with a non-zero initial condition, and (ii) the intracapillary concentration satisfies the homogenous *absorbing intracapillary boundary condition*, $\psi_{\mathrm{iv}}(\mathbf{a}_-, t) = 0$. The extravascular tracer concentration for absorbing intracapillary boundary conditions will be denoted by $\psi_{\mathrm{ev}}^{\mathrm{abs}}(\mathbf{r}, t)$, to avoid

confusion with the concentration for general intracapillary conditions, and satisfies

$$\frac{\partial \psi_{\mathrm{ev}}^{\mathrm{abs}}(\mathbf{r},t)}{\partial t} = \nabla \cdot D_{\mathrm{ev}} \nabla \psi_{\mathrm{ev}}^{\mathrm{abs}}(\mathbf{r},t)\,, \tag{2.10a}$$

$$D_{\mathrm{ev}} \mathbf{n} \nabla \psi_{\mathrm{ev}}^{\mathrm{abs}}(\mathbf{a}_+,t) = \kappa \psi_{\mathrm{ev}}^{\mathrm{abs}}(\mathbf{a}_+,t)\,, \tag{2.10b}$$

$$D_{\mathrm{ev}} \mathbf{n} \nabla \psi_{\mathrm{ev}}^{\mathrm{abs}}(\mathbf{r},t)|_{\text{diffusion watershed}} = 0\,, \tag{2.10c}$$

and the initial condition

$$\psi_{\mathrm{ev}}^{\mathrm{abs}}(\mathbf{r},0) = 1 \tag{2.10d}$$

without loss of generality, by linearity and time-invariance.

In practice, absorbing intracapillary boundary conditions hold when the intracapillary tracer concentration is much lower than the extravascular concentration, in particular if $\psi_{\mathrm{iv}}(\mathbf{a}_-,t) \ll \psi_{\mathrm{ev}}^{\mathrm{abs}}(\mathbf{r},t)$, hence (2.10b). Further note that the exponential term, $\exp(-R_{\mathrm{ev}}t)$, has been factored out via the change of function $\psi_{\mathrm{ev}} \mapsto \psi_{\mathrm{ev}} \exp(-R_{\mathrm{ev}}t)$.

The calculation of $W(\mathbf{r},t)$ is accomplished by means of the transformation

$$W(\mathbf{r},t;R_{\mathrm{ev}}=0) \equiv 1 - \psi_{\mathrm{ev}}^{\mathrm{abs}}(\mathbf{r},t)\,, \tag{2.11}$$

with $\mathbf{r}$ in extravascular space (Fig. 2.4). Equation (2.11) is only valid in the absence of extravascular relaxation; the effect of extravascular relaxation will be taken into account below. $W(\mathbf{r},t;R_{\mathrm{ev}}=0)$ satisfies (2.10a) as well as the initial and boundary conditions

$$W(\mathbf{r},0) = 0\,, \tag{2.12a}$$

$$-D_{\mathrm{ev}} \mathbf{n} \nabla W(\mathbf{a}_+,t) = \kappa\,[1 - W(\mathbf{a}_+,t)]\,. \tag{2.12b}$$

Differentiating (2.9) with respect to time with the use of (2.11), and taking account of the extravascular relaxation, yields the blood-to-tissue impulse response function as

$$\begin{aligned} w(\mathbf{r},t) &= \frac{\partial W(\mathbf{r},t;R_{\mathrm{ev}}=0)}{\partial t} \exp(-R_{\mathrm{ev}}t) \\ &= -\frac{\partial \psi_{\mathrm{ev}}^{\mathrm{abs}}(\mathbf{r},t)}{\partial t} \exp(-R_{\mathrm{ev}}t)\,. \end{aligned} \tag{2.13}$$

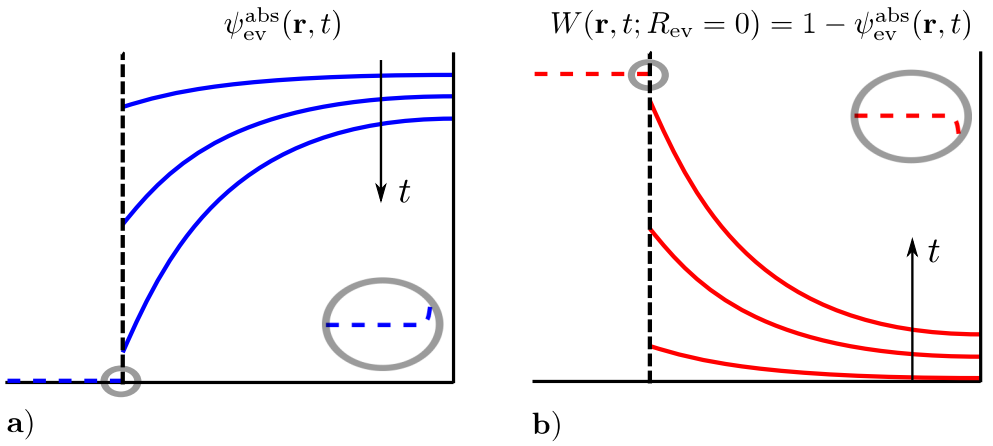

Figure 2.4: **Construction of blood-to-tissue (intracapillary-to-extravascular) step response function**. **a)** Extravascular concentration under absorbing intracapillary boundary conditions. **b)** Blood-to-tissue step response function in the absence of extravascular consumption. Insets show the gradient of the concentration at the capillary wall that produce the correct transcapillary flux (2.1c).

The blood-to-tissue impulse response function is independent of intracapillary consumption/relaxation, since the assumed input $\psi_{\mathrm{iv}}(a_-,z,t)=\delta(r-a_-,z,t)$ is zero for $t\neq 0$. Equation (2.9) and Eq. (2.13) can now be used to obtain $W(\mathbf{r},t)$ taking full account of the extravascular relaxation. Integrating (2.13) by parts gives

$$\begin{aligned} W(r,t) &= \int_0^t w(r,t';R_{\mathrm{ev}}=0)\exp(-R_{\mathrm{ev}}t')\,\mathrm{d}t' \\ &= W(r,t;R_{\mathrm{ev}}=0)\exp(-R_{\mathrm{ev}}t)+R_{\mathrm{ev}}\int_0^t W(r,t';R_{\mathrm{ev}}=0)\exp(-R_{\mathrm{ev}}t')\,\mathrm{d}t'\,. \end{aligned} \tag{2.14}$$

The above expression agrees with a general relationship developed by Danckwerts [98] which expresses the solution of the diffusion–consumption equation for the case of non-zero relaxation in terms of that for the case of zero relaxation with zero initial conditions; appropriate boundary conditions include the absorbing intracapillary condition considered here and must be the same for both cases.

Unless otherwise specified, the relaxation term in (2.13) will be omitted in the remainder of this Chapter for simplicity.

Importantly, the homogeneity of the absorbing intracapillary boundary condition (2.10b) allows introduction of the *Green's function* $G(\mathbf{r}, \mathbf{r}', t)$ [99] of the diffusion–consumption equation (2.10a) for whole extravascular space.[9] This is the key technical feature of the method developed in this Thesis. As is well-known, the Green's function represents the response of the system at position $\mathbf{r}$ and time t, due to an impulse-like excitation at position $\mathbf{r}'$ at time $t' = 0$. (It is noted that for time-invariant systems the choice of the time origin is arbitrary).

Thus, in the physical situation considered here, $G(\mathbf{r}, \mathbf{r}', t)$ is interpreted as the concentration of tracer at $\mathbf{r}$ at time t due to an impulse-like injection delivered at $\mathbf{r}'$ at time zero, both these positions being in extravascular space. Integrating over all positions $\mathbf{r}$ therefore gives the fraction of tracer, delivered as an impulse, that remains in the extravascular space at time $t > 0$. If the tracer is conserved, $G(\mathbf{r}, \mathbf{r}', t)$ is also interpreted as the probability density function for a 'packet' of tracer molecules delivered at position $\mathbf{r}'$ initially to be found at position $\mathbf{r}$ at the time $t > 0$ [71, p. 684]. Mathematical details are found in Appendix 2.5.5.

The blood-to-tissue impulse response function (2.13) is expressed exactly in terms of the Green's function for whole extravascular tissue as

$$w(\mathbf{r}, t) = \int_S \kappa \, G(\mathbf{r}, \mathbf{a}_+, t) \, \mathrm{d}S \,, \tag{2.15}$$

where $\mathbf{a}_+$ denotes a point on the abluminal capillary surface S, and the factor $\exp(-R_{\mathrm{ev}} t)$ has been absorbed into $G(\mathbf{r}, \mathbf{a}_+, t)$. The above equation is derived in Appendix 2.5.5 with the use of the Gauss theorem (Ref. [101], p. 315) and the absorbing intracapillary boundary condition.

Importantly, Eq. (2.15) is valid in all extravascular space and is not restricted to the spatiotemporal limits of validity of the single-capillary approximation. However, this equation relies on the assumption that the intracapillary concentration of tracer is not affected by any back-flux of tracer from extravascular space into the blood. Provided this latter condition holds, the extravascular concentration in whole tissue may

[9] For an appraisal of the work of the English mathematician George Green (1793 – 1841) concerning both the theorem and the class of functions named after him, see for example Ref. [100].

then be expressed as the spatiotemporal convolution of the blood-to-tissue impulse response function (2.15) and the concentration of tracer in the capillary network.

To see the physical content of Eq. (2.15), it may first be noted that the product $\kappa\,\mathrm{d}S$ gives the time rate of the amount of tracer that permeates from intracapillary into extravascular space across a small capillary surface element, $\mathrm{d}S$, due to unit concentration difference between the luminal and abluminal faces of the capillary wall; cf. Eq. (2.10b). In particular, the time rate of permeation of tracer due to a unit-step intracapillary concentration, with zero initial extravascular concentration, is equal to $\kappa\,\mathrm{d}S$. Thus, multiplying by $G(\mathbf{r},\mathbf{a}_+,t)$ and integrating over the capillary surface, one obtains the time rate of the concentration of tracer at $\mathbf{r}$ due to a unit step increase in intracapillary concentration, in agreement with the first line of Eq. (2.13).

Lastly, a related blood-to-tissue impulse response function, $w_\mu(t)$, can be defined that gives the amount of tracer in extravascular space in terms of the average intracapillary concentration, $\psi_{\mathrm{iv}}(t)$. Integrating $\psi_{\mathrm{ev}}(\mathbf{r},t)$ in Eq. (2.5c) over extravascular space, and noting that $w(\mathbf{r},t)$ does vary with distance z along the capillary, gives

$$\mu_{\mathrm{ev}}(t) = w_\mu(t) * \psi_{\mathrm{iv}}(t)\,, \tag{2.16a}$$

where

$$\begin{aligned} w_\mu(t) &= \int_{\mathrm{ev}} w(\mathbf{r},t)\,\mathrm{d}^d\mathbf{r} \\ &= \int_S \kappa\,\psi_{\mathrm{ev}}^{\mathrm{abs}}(\mathbf{a}_+,t)\exp(-R_{\mathrm{ev}}t)\,\mathrm{d}S \end{aligned} \tag{2.16b}$$

is obtained using the representation of $\psi_{\mathrm{ev}}^{\mathrm{abs}}(\mathbf{r},t)$ in terms of the Green's function [Eq. (2.75) of Appendix 2.5.5]; here $d = 1, 2, 3$ is the space dimensionality.

It is clear from Eq. (2.16a) and from the physical meaning of $w(\mathbf{r},t)$ that Eq. (2.16b) gives the time rate of the amount of tracer in the extravascular space due to a unit step change in spatially averaged intracapillary concentration, for zero initial conditions. This may also be understood by noting that (i) the product $\kappa\,\psi_{\mathrm{ev}}^{\mathrm{abs}}(\mathbf{a}_+,t)$ in (2.16b) gives the tissue-to-blood flux due to an extravascular concentration $\psi_{\mathrm{ev}}^{\mathrm{abs}}(\mathbf{r},t)$, under absorbing intracapillary boundary conditions; and that (ii), in the absence of extravascular consumption, this flux is also numerically equal

to the blood-to-tissue flux due to a step intracapillary concentration, with zero initial extravascular concentration [see Eq. (2.11) and Fig. 2.4]; the effect of consumption is accounted for by the factor $\exp(-R_{\mathrm{ev}}t)$. Therefore, integration of the quantity $\kappa\,\psi_{\mathrm{ev}}^{\mathrm{abs}}(\mathbf{a}_+,t)\,\exp(-R_{\mathrm{ev}}t)$ over the capillary surface yields the time rate of the amount of tracer permeating into extravascular space in response to a step intracapillary concentration.

We conclude this Subsection with a short list of properties of the impulse response and step response functions:

- $w(\mathbf{r},t) \geq 0$, since the integrand of (2.15) is non-negative by definition of the Green's function.
- $w(\mathbf{r},t) \to \kappa\delta(|\mathbf{nr}| - |\mathbf{a}_+|)$ as $t \to 0$. This follows from a standard property of the Green's function given by Eq. (2.80) of Appendix 2.5.5.
- In the vicinity of the abluminal capillary surface, $w(\mathbf{r},t)$ is a non-decreasing function of radial distance, since $\mathbf{n}\nabla w(\mathbf{a}_+,t) = (\kappa/D_{\mathrm{ev}})w(\mathbf{a}_+,t) \geq 0$ for $t > 0$.
- On the other hand, $W(\mathbf{r},t)$ is a non-increasing function of radial distance, since $\mathbf{n}\nabla W(\mathbf{a}_+,t) = -\mathbf{n}\nabla\psi_{\mathrm{ev}}^{\mathrm{abs}}(\mathbf{a}_+,t) = -(\kappa/D_{\mathrm{ev}})\psi_{\mathrm{ev}}^{\mathrm{abs}}(\mathbf{a}_+,t) \leq 0$.

2.3.2 Arterial-to-intracapillary impulse response function

The arterial-to-intracapillary impulse response function gives the intracapillary tracer concentration due to an impulse-like amount of tracer appearing at the inflow end of the capillary segment at time $t = 0$, i.e., $\psi_{\mathrm{iv}}(z = 0, t) = \delta(t)$. The intracapillary space is assumed void of tracer initially.

Substituting (2.5c) into the governing equation (2.1a) and putting $\psi_{\mathrm{iv}}(\mathbf{a}_-,t) \approx \psi_{\mathrm{iv}}(z,t)$ gives

$$\frac{\partial\psi_{\mathrm{iv}}(z,t)}{\partial t} = -u_z\frac{\partial\psi_{\mathrm{iv}}(z,t)}{\partial z} - R_{\mathrm{iv}}\psi_{\mathrm{iv}}(z,t) - \frac{\psi_{\mathrm{iv}}(z,t) - \psi_{\mathrm{iv}}(z,t) * w(\mathbf{a}_+,t)}{\tau_{\mathrm{iv}}}\,. \quad (2.17)$$

The general solution of this equation is given in Appendix 2.5.6. The arterial-to-intracapillary impulse response function is the solution to (2.17) with initial condition

$\psi_{\rm iv}(0 < z \le L, t = 0) = 0$ and boundary condition at the inflow end of the capillary $\psi_{\rm iv}(z = 0, t) = \delta(t)$. In Appendix 2.5.6 we show that for times t after the arrival of the tracer bolus at the capillary such that

$$\sqrt{(\tau_{\rm c}/\tau_{\rm iv})(t/\tau_{\rm ev})} \ll 1\,, \tag{2.18}$$

the arterial-to-intracapillary impulse response function takes the form

$$h_{\rm a}^{\rm iv}(z,t) \approx \left[\delta(t - t_z) + \frac{t_z}{\tau_{\rm iv}}\, w(\mathbf{a}_+, t - t_z)\right] \exp(-R_{\rm iv}^+ t_z) \tag{2.19a}$$

for $0 < t_z \le t$, and is zero at $0 < z \le L$ for times $t < t_z$, where

$$t_z \equiv \frac{z}{u_z} = \frac{z}{L}\,\tau_{\rm c}\,, \qquad\qquad R_{\rm iv}^+ \equiv R_{\rm iv} + \frac{1}{\tau_{\rm iv}}\,. \tag{2.19b}$$

The above simplified expression is the sum of two terms: the first one represents the fraction of tracer that travels without dispersion along the capillary lumen and exchanges with extravascular space, and the other represents the back-flux of the extracted fraction of tracer from the extravascular space into the capillaries.

Quantitatively, in the absence of tracer consumption and back-flux, the fraction of tracer extracted in one capillary transit time is seen to be given by the well-known extraction, $E = 1 - \exp(-\tau_{\rm c}/\tau_{\rm iv}) = 1 - \exp(-PS/f_{\rm iv})$. The second term inside the brackets in (2.19a) gives the time rate of the amount of tracer (per unit of tracer-accessible intracapillary volume) due to back-flux from extravascular space into the blood after the passage of an impulse-like quantity of tracer. This is seen by noting that the product $\kappa S \times t_z w(\mathbf{a}_+, t - t_z)$ gives, to a first approximation, the amount of tracer passing from extravascular space into the capillary per unit time. Dividing this term by the capillary volume and recalling the definition of mean intracapillary residence time, one obtains the term $(t_z/\tau_{\rm iv})\, w(\mathbf{a}_+, t - t_z)$ in Eq. (2.18).

The arterial-to-extravascular concentration results from (2.5c) and (2.19a):

$$h_{\rm a}^{\rm ev}(z,t) \approx \left[w(\mathbf{r}, t - t_z) + \frac{t_z}{\tau_{\rm iv}}\, w(\mathbf{a}_+, t - t_z) * w(\mathbf{r}, t)\right] \exp(-R_{\rm iv}^+ t_z)\,. \tag{2.20}$$

Using the above-defined impulse response functions, the amount of tracer in a given blood–tissue exchange unit is expressed as

$$\mu(t) = \left[\int_{\rm iv} h_{\rm a}^{\rm iv}(z,t)\,{\rm d}^d\mathbf{r} + \int_{\rm ev} w(\mathbf{r},t) * h_{\rm a}^{\rm iv}(z,t)\,{\rm d}^d\mathbf{r}\right] * \psi_{\rm iv}(z = 0, t)\,. \tag{2.21}$$

2.3.3 Effective extravascular depolarised volume

The *effective extravascular depolarised volume*, $\Lambda(t)$, quantifies the amount of tracer cleared from the extravascular space by the tissue-to-blood flux under absorbing intracapillary conditions. The concept applies to any exchanging species whose concentration in intracapillary space is much lower than in extravascular space, and is not restricted, as the term 'depolarised' might suggest, to extravascular (longitudinal) magnetisation. We introduced part of the material presented in this Section in Ref. [96].

The amount of tracer in extravascular space is given by

$$\mu_{\mathrm{ev}}^{\mathrm{abs}}(t) = \int_{\mathrm{ev}} \psi_{\mathrm{ev}}^{\mathrm{abs}}(\mathbf{r}, t)\, \mathrm{d}^d\mathbf{r} = \int_{\mathrm{ev}} \int_{\mathrm{ev}} G(\mathbf{r}, \mathbf{r}', t)\, \mathrm{d}^d\mathbf{r}\, \mathrm{d}^d\mathbf{r}' \,, \tag{2.22}$$

where the representation of $\psi_{\mathrm{ev}}^{\mathrm{abs}}(\mathbf{r}, t)$ in terms of the Green's function has been used; see Eq. (2.75) of Appendix 2.5.5. The concept of the effective extravascular depolarised volume in one spatial dimension is illustrated in Fig. 2.5, where the 'effective' concentration, $\psi_{\mathrm{eff}}(\mathbf{r}, t)$, is equal to $\psi_{\mathrm{ev}}^{\mathrm{abs}}(\mathbf{r}, 0) = 1$ for $|\mathbf{r}| > \Lambda(t)$, and is zero elsewhere. Thus, at time t the amount of tracer cleared from extravascular space is given by

$$\mu_{\mathrm{ev}}^{\mathrm{abs}}(0) - \mu_{\mathrm{ev}}^{\mathrm{abs}}(t) \equiv \psi_{\mathrm{ev}}^{\mathrm{abs}}(\mathbf{r}, 0)\, \Lambda(t) \,, \tag{2.23a}$$

which, since $\psi_{\mathrm{ev}}^{\mathrm{abs}}(\mathbf{r}, 0)$ is spatially uniform by definition, is rewritten as

$$\frac{\Lambda(t)}{V_{\mathrm{ev}}} = \frac{\mu_{\mathrm{ev}}^{\mathrm{abs}}(0) - \mu_{\mathrm{ev}}^{\mathrm{abs}}(t)}{\mu_{\mathrm{ev}}^{\mathrm{abs}}(0)} \tag{2.23b}$$

with $\mu_{\mathrm{ev}}^{\mathrm{abs}}(0) = V_{\mathrm{ev}} \psi_{\mathrm{ev}}^{\mathrm{abs}}(\mathbf{r}, 0)$.

Substituting the right-most term of (2.22) into Eq. (2.23a) and making use of the initial condition for the Green's function, Eq. (2.80) of Appendix 2.5.5, gives

$$\Lambda(t) = \int_{\mathrm{ev}} \left[1 - \int_{\mathrm{ev}} G(\mathbf{r}, \mathbf{r}', t)\, \mathrm{d}^d\mathbf{r} \right] \mathrm{d}^d\mathbf{r}' \,. \tag{2.24}$$

The right-hand side of this equation is analogous to a quantity introduced by Yablonskiy and Haacke [102] which represents the volume of the region where NMR signal dephasing due to magnetic susceptibility effects, is strongest [74]. In the context of (longitudinal) magnetic relaxation, the inner integral in (2.24) gives the normalised magnetic moment, $\psi_{\mathrm{ev}}^{\mathrm{abs}}(t; \mathbf{r}')$, due to a point source (or *spin packet*) placed

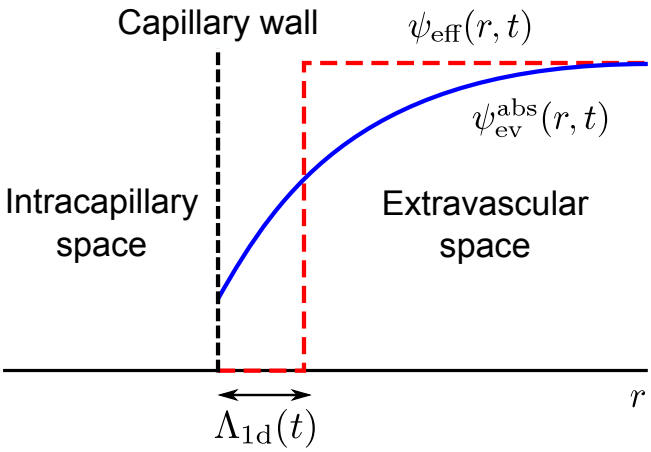

Figure 2.5: **Effective extravascular depolarised volume in one spatial dimension**. The extravascular concentration $\psi_{\mathrm{ev}}^{\mathrm{abs}}(r,t)$ (solid line) and the 'effective' concentration $\psi_{\mathrm{eff}}(r,t)$ (broken line) are evaluated under absorbing intracapillary boundary conditions; the areas under both curves are equal.

at position $\mathbf{r}'$ at time $t = 0$, such that $\psi_{\mathrm{ev}}^{\mathrm{abs}}(0;\mathbf{r}') = \int_{\mathrm{ev}} G(\mathbf{r},\mathbf{r}',0)\,\mathrm{d}^d\mathbf{r} = 1$. The term in brackets in (2.24) therefore represents the fractional reduction in extravascular magnetic moment. Integration over the extravascular space then gives, numerically, the volume of a region adjacent to the capillary in which the extravascular magnetisation is deemed to have become effectively depolarised by time t. In this example, $\Lambda(t)$ represents the normalised extravascular NMR signal.

If the capillary wall is impermeable ($\kappa = 0$) to tracer the extravascular magnetic moment $\mu_{\mathrm{ev}}^{\mathrm{abs}}(t)$ is conserved, hence the integral of $G(\mathbf{r},\mathbf{r}',t)$ is equal to unity at all times; this results in $\Lambda(t \geq 0) = 0$, as expected. On the other hand, if the capillary wall is permeable to tracer ($\kappa > 0$) the extravascular magnetic moment decreases steadily over time. Hence, at long times the integral of $G(\mathbf{r},\mathbf{r}',t)$ over the extravascular space vanishes and $\Lambda(t)$ approaches its limiting value, V_{ev}.

Differentiating (2.23a) and (2.24) gives an expression for the effective extravascular depolarised volume in terms of the (normalised) blood-to-tissue tracer flux under absorbing intracapillary conditions:

$$\frac{\mathrm{d}\Lambda(t)}{\mathrm{d}t} = -\frac{\mathrm{d}\mu_{\mathrm{ev}}^{\mathrm{abs}}(t)}{\mathrm{d}t} = \int_S \kappa\psi_{\mathrm{ev}}^{\mathrm{abs}}(\mathbf{a}_+,t)\,\mathrm{d}S\,. \tag{2.25}$$

Finally, we note that if there is a net flux of tracer outward from the capillaries, then the *effective extravascular diffusion volume* can be defined by

$$\Lambda_D(t) = \frac{\mu_{\mathrm{ev}}(t)}{\psi_{\mathrm{ev}}(\mathbf{a}_+, t)}\,. \tag{2.26}$$

This definition is meaningful because diffusion causes the concentration of extravascular tracer to fall off away from the capillary wall. $\Lambda_D(t)$ does not depend on the extravascular relaxation rate.

The simplest case is that of one-dimensional free Gaussian diffusion, whose diffusion profile is $\psi_{\mathrm{ev}}(r,t) = (2\pi\sigma^2(t))^{-1/2}\exp(-r^2/2\sigma(t)^2)$, with $\sigma(t) = \sqrt{2D_{\mathrm{ev}}t}$. The effective extravascular diffusion volume is proportional to tracer diffusion length: $\Lambda_D(t) = \sqrt{2\pi}\sigma(t) = \sqrt{4\pi D_{\mathrm{ev}}t}$.

2.3.4 Spatially averaged concentration

The spatially averaged concentrations, denoted by $\psi_{\mathrm{iv}}(t)$ and $\psi_{\mathrm{ev}}(t)$, are the quantities of interest for lumped tracer-exchange models. They are defined as average concentrations over the tracer-accessible volume in, respectively, intracapillary and extravascular space. Differential equations for $\psi_{\mathrm{iv}}(t)$ and $\psi_{\mathrm{ev}}(t)$ are obtained by integrating the governing spatiotemporal equations (2.1a) and (2.1b), and they are basic to the discussion on the validity of lumped tracer-exchange models given in Section 4.2.

However, the spatially averaged extravascular concentration for absorbing intracapillary boundary conditions is written very simply in terms of the effective extravascular depolarised volume as

$$\begin{aligned}\psi_{\mathrm{ev}}^{\mathrm{abs}}(t) &= \frac{1}{V_{\mathrm{ev}}}\int_{\mathrm{ev}} \psi_{\mathrm{ev}}^{\mathrm{abs}}(\mathbf{r},t)\,\mathrm{d}^d\mathbf{r} = \frac{\mu_{\mathrm{ev}}^{\mathrm{abs}}(t)}{V_{\mathrm{ev}}} \\ &= 1 - \frac{\Lambda(t)}{V_{\mathrm{ev}}}\,,\end{aligned} \tag{2.27}$$

where Eq. (2.23b), with $\psi_{\mathrm{ev}}^{\mathrm{abs}}(\mathbf{r},0) = 1$, has been used.

2.3.5 Green's function for the single-capillary approximation

The role of the Green's function for whole extravascular space, $G(\mathbf{r}, \mathbf{r}', t)$, has become apparent in the previous Subsections. However, evaluation of this quantity for realistic tissue samples is, in general, unfeasible. This difficulty can be overcome in part if there is an interval of diffusion times during which the value of the Green's function is largely independent of the geometry of the surrounding capillary network, for positions $\mathbf{r}$ sufficiently close to the abluminal surface of the nearest capillary segment.

For diffusion times and extravascular positions for which this condition holds, the exchange of tracer between any given capillary segment and its surrounding tissue may be supposed independent of that occurring in the neighbouring capillaries. Thus, in this case we expect the single-capillary approximation to hold true. Since the root mean square displacement of tracer molecules is $\langle|\mathbf{r}-\mathbf{r}'|^2\rangle^{1/2} \sim \sqrt{D_{\mathrm{ev}}t}$, and since the distance from the capillary segment to the diffusion watershed is comparable to the typical half-intercapillary distance, A, the single-capillary approximation is expected to hold for diffusion times such that

$$\frac{\sqrt{D_{\mathrm{ev}}t}}{A} \ll 1\,. \tag{2.28}$$

A key simplifying assumption can now be made on the basis of the single-capillary approximation: for short diffusion lengths, as given by (2.28), the Green's function, $G_{\mathrm{c}}(\mathbf{r}, \mathbf{r}', t)$, for a geometrically simpler pericapillary region approximates the Green's function for whole extravascular space, $G(\mathbf{r}, \mathbf{r}', t)$. This is of practical importance, since it simplifies considerably the evaluation of the blood-to-tissue impulse response function (2.15), which requires the knowledge of $G(\mathbf{r}, \mathbf{a}_+, t)$.

The foregoing assumption can be made plausible by a qualitative argument.[10] In Fig. 2.6 a cross-sectional view of a hypothetical tissue containing a network of parallel capillaries is considered, for simplicity; the capillaries are regarded as sinks for tracer molecules and the net flux of tracer between adjacent pericapillary regions is assumed, on average, zero. A test molecule of tracer is found initially at position

[10] Here we have adapted an argument by Kac [103] concerning a plane region which was divided up into a square grid with absorbing edges, but containing no discrete sinks.

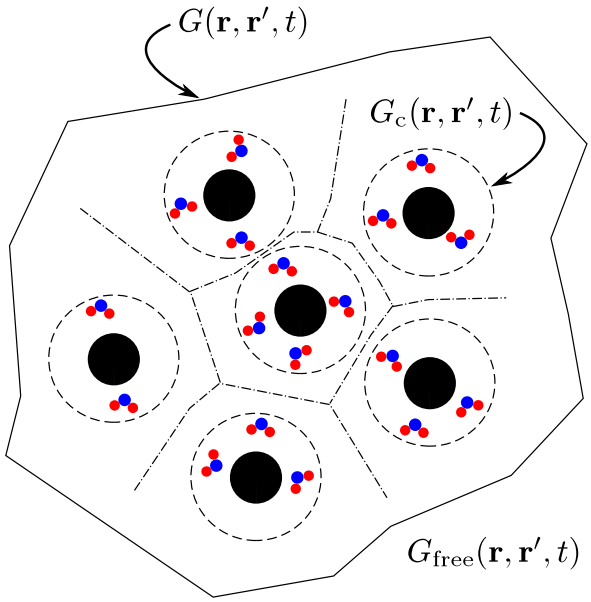

Figure 2.6: **Concerning the Green's function for the single-capillary approximation**. Capillary lumina are depicted as black circles surrounded by diffusing tracer molecules. Also shown are the diffusion watershed (dash-dot lines) and the tissue boundary (solid line). Broken lines indicate maximal diffusion lengths for which the single-capillary approximation remains valid; see also Fig. 2.1c. Lines with arrowheads point at the tissue regions associated with the various Green's functions considered in the analysis.

$\mathbf{r}'$ within the pericapillary region of a capillary whose lumen centre is at position $\mathbf{r}$. A consideration of the survival probability of this molecule when diffusing within the considered pericapillary region (with reflective, or zero-flux, boundary conditions), within the whole extravascular space (i.e., tracer exchange with zero net flux between neighbouring pericapillary regions) and in free (i.e., void of absorbing capillaries) space, leads to the chain of inequalities

$$0 \leq G_{\mathrm{c}}(\mathbf{r},\mathbf{r}',t) \leq G(\mathbf{r},\mathbf{r}',t) \leq G_{\mathrm{free}}(\mathbf{r},\mathbf{r}',t)\,, \tag{2.29}$$

where $G_{\mathrm{free}}(\mathbf{r},\mathbf{r}',t)$ denotes the well-known Green's function for free space, or 'free propagator' [103, 104]. Because at sufficiently short times the molecules of tracer do not sense the presence of the more distant capillaries, it is assumed that $G(\mathbf{r},\mathbf{r}',t) \approx G_{\mathrm{c}}(\mathbf{r},\mathbf{r}',t)$. Moreover, in the limit of short diffusion distances, the molecules of tracer

are unable to probe their milieu and hence the Green's function of extravascular space can be approximated by the free propagator [103, 104].

The calculations presented in Chapter 3 have been obtained with the aid of the Green's function, $G_{\mathrm{c}}(\mathbf{r}, \mathbf{r}', t)$, for a long, straight annulus with capillary radius a and pericapillary radius A. In the single-capillary approximation, the parameter A is treated as large relative to both capillary radius and tracer diffusion length. Thus, none of the blood–tissue exchange quantities will be expressed in final form as functions of pericapillary radius A. This parameter shall only be used to obtain order-of-magnitude estimates and in the analysis of the steady state found in Section 4.5.

For simplicity, in the sequel we write $G(\mathbf{r}, \mathbf{r}', t)$ to denote both the Green's function for whole extravascular space and that for a given pericapillary region; the meaning will be clear from the context.

2.4 Discussion

In 1966 Johnson and Wilson wrote [40, p. 1299]: 'The complexity of the capillary circulation in many tissues has made it difficult to achieve a general, quantitative treatment of transcapillary exchange. This means that each tissue must be examined carefully to see if certain simplifying assumptions are plausible in order to set up models which lead to tractable equations'.

The deterministic spatiotemporal model of blood–tissue exchange introduced in this Chapter may be regarded as a zero-order approximation to a statistical theory of transport and exchange in complex heterogenous media, referred to as an *effective medium theory* [71], in that inside their respective physiological compartments, and at compartment boundaries, the tissue- and tracer-related parameters (e.g., diffusion coefficient, consumption/relaxation rates and capillary-wall permeability) considered have all been assumed spatially uniform; see Ref. [71, p. 683]. The aim of any effective medium theory is to represent a microscopically heterogenous medium by means of an 'effective', or 'apparent', homogenous medium whose observable properties depend on

such relevant microscopic features as 'survive' the spatiotemporal averaging inherent to any measurement process [71, pp. 682, 691]. The appropriate effective medium would therefore behave under specified measurement conditions in the same manner as would the actual heterogenous medium considered [71, p. 691].

The presented model includes capillary flow, diffusive transcapillary permeation, first-order consumption in both blood and extravascular tissue, and extravascular diffusion of a tracer substance. By allowing for spatial as well as temporal variations of the concentrations of tracer, and by taking into account the effect of extravascular diffusion, the model aims to overcome an inherent theoretical limitation of the class of lumped tracer-exchange models when the exchange is rate-limited not by transcapillary permeation but by diffusive transport in extravascular space. Such variations in concentration are described on a mesoscopic scale (p. 18) in order that the partial differential operators in Eqs (2.1a) – (2.1e) be well posed.

The assumption of linearity and time invariance is pervasive [9, 105, 106] in the literature on mass transport and exchange in biological systems and is also a basic feature of the model presented in this Thesis. We consider blood–tissue exchange to be driven by the concentration of tracer in the capillaries, which is therefore barely influenced by the back-flux of tracer from extravascular space into the blood. (This modelling assumption will be assessed practically in Chapter 4). In this physical situation, the exchange of tracer is jointly characterised by the arterial-to-intracapillary impulse response function and the blood-to-tissue impulse response function.

In the method proposed in this Thesis, the blood-to-tissue impulse response function is evaluated by first examining a simpler tracer exchange situation defined by a non-zero, spatially uniform concentration of tracer in extravascular space at initial time, with an absorbing intracapillary boundary condition at the luminal face of the capillary wall. Importantly, this homogenous boundary condition allows introduction of the Green's function of the diffusion–consumption equation for whole extravascular space. This formulation has a transparent physical interpretation and is the basis for expressing the blood–tissue tracer-exchange-related quantities (transcapillary flux, intracapillary and extravascular concentration, effective extravascular

depolarised volume).

The presented model can be extended to account for different types of microvessels and non-uniform concentrations of tracer in the capillaries. In the range of validity of the single-capillary approximation, one can account for a non-uniform distribution of intracapillary concentrations by averaging these contributions over the appropriate distribution of capillary parameters, as determined from stereological measurements. For example, Honig *et al.* [67] found that capillary segment length, total capillary length and number of capillary anastomoses in rat gracilis muscle were described by Weibull, gamma and negative binomial distributions, respectively. Capillary segment lengths in cat brain cortex were also found to be Weibull-distributed [65].

In the following sections we discuss several aspects, both anatomical and physiological, of microvascular networks, all of which have a bearing on the modelling assumptions adopted in this Thesis.

2.4.1 Capillary networks

Blood–tissue exchange relies on the structural and functional properties of capillary networks [72].

Anatomically, the capillary network demonstrates arterio-venous anastomoses, bifurcations and junctions, bends, loops and dead-ends. Capillary length and calibre is observed to vary widely both within and among tissues [65, 72, 82]. The modelling assumption of straight capillary segments is justified for myocardial tissue, as was demonstrated by Bassingthwaighte, Yipintsoi and Harvey [66] in dog myocardium: the capillary network of a main branch of a coronary artery comprises dense arrays of capillaries running parallel to muscle fibres for lengths of up to a few centimetres; functional capillary lengths range between $500-1000$ μm; unbranched capillary lengths average 100 μm, with a strongly right-tailed distribution; and capillary diameters average 5.6 μm. These authors noted that this anatomic arrangement facilitates concurrent flow in neighbouring capillaries, as well as diffusive exchange between inflow and outflow regions [66]. The model set forth in this Thesis does not deal with such possible diffusive interactions.

In marked contrast to myocardial capillaries, the brain cortex reveals a highly tortuous capillary network with significant interregional variability, as was demonstrated by Pawlik *et al.* [65] in the *in vivo* cat brain cortex. In regions with a reduced capillary volume fraction, the curvature of capillaries was observed to increase so as to keep intercapillary distances comparatively short. Nevertheless, for typical values of capillary diameter, radius of curvature and segment length of brain capillaries (p. 22) these can reasonably be modelled as long straight cylinders.

The flow of blood in the capillaries is a highly complex phenomenon. Because erythrocytes often have diameters greater than those of the capillaries through which they pass [72, 82], capillary blood flow is often described in the tracer kinetic literature as being approximately of plug-flow type. In reality, the erythrocytes are surrounded by a thin (< 1 μm) annulus of plasma which lubricates the gap between the erythrocytes and the capillary wall ([107, pp. 302 – 303], [108, Fig. 5]); in the space between adjacent erythrocytes, the plasma velocity is characterised by eddy-like streamlines [107] with both axial and radial velocity components [82]. This is referred to as two-phase flow (Ref. [109] and references therein). Indeed, because in the narrower capillaries the erythrocytes undergo deformations, and because the number of erythrocytes in any one capillary varies stochastically, intermittent capillary flow is observed [82]. At a higher hierarchical level, intermittent flow is largely due to opening and closure of the precapillary sphincters, thus channelling the blood flow through different capillaries. The local regulatory action on blood flow, referred to as *vasomotion* [72], matches physical conditions in the microvascular network to tissue requirements; for example, the action of these precapillary sphincters largely determines the available permeability surface area for tissue–blood exchange. As a result of this and other physiological variables, blood flow through most capillaries is a non-steady-state phenomenon [72].

2.4.2 Krogh-type models

Krogh in 1919 proposed the first quantitative model of steady-state diffusion of oxygen in striated muscle of mammals. He assumed ‘(...) each capillary to supply

oxygen independently of all the others to a cylinder of tissue surrounding it. In a transverse section such a cylinder is represented by an area which can be taken as circular and the average area belonging to each capillary can be calculated from a counting of the number of capillaries in a transverse section by division of its total area with the number found.' [47, p. 410]. Krogh's modelling assumptions have been reviewed in detail by Hudson and Cater [52] and by Goldman [73].

The Krogh model is a much simplified depiction of real capillary networks, yet it is analytically tractable and yields quantitative physical insight. The single-capillary model has been utilised in both theoretical and experimental studies of indicator-dilution [44], exchange-dependent tracer-induced relaxation [90, 110], and the BOLD effect [111]. Multiple-capillary models have been proposed and investigated numerically in more realistic modelling approaches of oxygen delivery to tissue (reviewed in Ref. [73]).

In considering the enhancement of the longitudinal relaxation in tissue due to transcapillary water exchange and extravascular diffusion of paramagnetic tracers, several authors [45, 90, 110] have extended the Krogh model to consider three concentric cylinders representing intracapillary, interstitial and intracellular space, with radii determined by the volume fraction of the respective physiological compartments. In this author's opinion, however, it is unclear that this modelling can yield comparable results to those obtained by including the geometrical tortuosity of interstitial space, since in normal tissue the distances between the parenchymal cells and their supplying capillaries can be much smaller than the radius of the interstitial–intracellular boundary predicted by the three-cylinder model. For example, for realistic values of intracapillary, interstitial and intracellular volume fractions in brain cortex of 1%, 15% and 84% [112, 113, 114], the corresponding cylinder radii are in the ratios $1:4:10$. Thus, for a capillary radius of 3 μm, the corresponding width of the interstitial cylinder in the three-cylinder model is 9 μm. Kuo *et al.* [45] evaluated blood–tissue exchange, interstitial diffusion and interstitial–intracellular exchange using a three-cylinder model. As another example, in their study on the effect of water exchange on the estimation of rabbit myocardial perfusion using paramagnetic trac-

ers, Judd *et al.* [110] chose cylinder radii of 2.5, 5.0 and 10 μm, and a common water diffusion coefficient of 1.5 $\mu m^2\,ms^{-1}$. These two examples point to a further difficulty with the three-cylinder model, namely the selection of reasonable values of the diffusion coefficient in the interstitial and intracellular cylinders. It is not immediately obvious that, even if all cylinder compartments conform to correct compartmental volume fractions in whole tissue, their apparent compartmental diffusion coefficients should be equal among them, and also equal to the diffusion coefficient of tracer in whole tissue in the tortuosity limit.

It is emphasised that, in this Thesis, the representation of intracapillary and extravascular space is not made by means of the above-described Krogh capillary–tissue model. Instead, we investigate the effect of diffusion and consumption of a tracer substance under conditions where the exchange between any given capillary and its surrounding extravascular space is supposed largely independent of that occurring in neighbouring capillaries (refer to Section 2.1.3). In this physical situation, both the contour surface of the pericapillary region and the form of the pericapillary boundary conditions become immaterial (Sections 2.1.3 and 2.3.5).

2.4.3 Water transmembrane exchange

Osmotic permeation

Biological membranes are semipermeable: they allow the passage of water and other small molecules through them, but are impermeable to all solutes above a certain size. It is well known that when two solutions at different concentrations are separated by a semipermeable membrane, solvent will flow across the membrane from the more dilute towards the more concentrated solution (osmosis). This osmotic flow of solvent convects solute molecules towards the membrane in the dilute solution, and away from the membrane in the concentrated solution [115, p. 281]. As a result, the solute concentrations at each face of the membrane will differ from those at greater distances from the membrane. This creates so-called ‘unstirred’, ‘stagnant’ or ‘concentration boundary’ layers. The apparent permeability of an extravascular

unstirred layer of thickness δ is expressed as $\kappa_{\mathrm{usl}} = D_{\mathrm{ev}}/\delta$ [116]. Patlak and Paulson [117] found theoretically that the presence of unstirred layers around cerebral capillaries and in endothelial cells of the blood-brain barrier does not affect significantly the determination of diffusive capillary permeabilities by the indicator-dilution method.

Osmotic flow still occurs, to some extent, for solutes which encounter somewhat greater resistance in crossing the membrane than does water [118, p. 843]. We hypothesise that this concomitant flow might be of significance if water itself is employed as a tracer, but this issue is outwith the scope of this Thesis.

Water exchange in brain tissue

Water molecules are able to exchange between the intracapillary, interstitial and intracellular spaces. The mechanisms which enable the passage of water across the blood–brain barrier and into the interstitial space and the brain parenchyma are, to date, the subject of ongoing research [119]. In particular, a number of MRI studies performed in brain, myocardium and skeletal tissue, suggest that water exchange between the interstitial fluid and parenchymal cells is an order of magnitude faster than between the blood and interstitial fluid. Donahue *et al.* [120] estimated the net interstitial–intracellular water exchange rate in isolated perfused rat hearts to range between $8-27\ \mathrm{s}^{-1}$; these investigators also estimated an upper bound of $7\ \mathrm{s}^{-1}$ on the intracapillary–interstitial rate. Judd *et al.* [110] estimated a net intracapillary–interstitial rate of $2.7\ \mathrm{s}^{-1}$ in isolated perfused rabbit hearts. Quirk *et al.* [114] estimated the interstitial-to-intracellular and intracellular-to-interstitial water exchange rates in *in vivo* rat brains as $8.5\ \mathrm{s}^{-1}$ and $1.8\ \mathrm{s}^{-1}$, respectively; the estimated net interstitial–intracellular rate ($\sim 10\ \mathrm{s}^{-1}$) is approximately an order of magnitude faster than typical intracapillary-to-interstitial water exchange rates in cortical brain capillaries ($\sim 1\ \mathrm{s}^{-1}$). Landis *et al.* [76] estimated an average residence time of water in the sarcoplasm of rat thigh muscle of 1.1 s, hence an intracellular-to-interstitial rate of $1.1^{-1} = 0.91\ \mathrm{s}^{-1}$); since intracapillary and interstitial volume fractions in normal rat thigh muscle are about 3% and 18% [121], respectively, one estimates the net interstitial–intracellular water exchange rate as $(1 + 79/18) \times 1.1^{-1} = 5\ \mathrm{s}^{-1}$.

All the above-mentioned studies involved T_1-weighted and, in Ref. [120], also T_2-weighted MRI measurements using intravascular and/or extravascular, extracellular paramagnetic tracers; in all cases, two-compartment lumped tracer-exchange models were fitted to the MRI data. More recently, evidence of fast water exchange between the highly permeable glial cells and the extracellular matrix has been invoked by Fieremans *et al.* [86] to model brain extra-axonal white matter as a homogenous medium in diffusional kurtosis imaging.

On the other hand, He *et al.* [119], using a hybrid BOLD–ASL approach, estimated an intraneuronal water residence time of the order of tens of seconds. This implies that the interstitial–parenchymal water exchange rate in the human brain may be an order of magnitude smaller than the value estimated by Quirk *et al.* [114] using DCE MRI. An explanation for slow exchange suggested by He *et al.* [119, pp. 6 – 7] relies on a consensus that most neurons do not express water-specific membrane-channel proteins, aquaporins.

The experiments of Larson *et al.* [29] with $H_2^{15}O$ PET also appear to support the hypothesis of slow water exchange. Since the two-barrier spatiotemporal model utilised by these authors (see Section 1.1.2) showed good agreement with the measured data up to times (some tens of seconds) far exceeding diffusion times of the radiolabelled water in extravascular tissue, it may be argued that water exchange between the interstitial and intracellular spaces may be a slower process than has been estimated in some studies.

2.4.4 Time-dependent diffusion coefficient

In heterogenous media, the tracer diffusion coefficient, or diffusivity, is position-dependent and decreases with time [80, 84]. At short diffusion times, tracer molecules approximately one diffusion length from the medium boundary experience restricted, non-Gaussian diffusion owing to random collisions with the boundary [83, 85], whereas molecules at greater distances from the boundaries are assumed to undergo free Gaussian diffusion. In this limit, the diffusion coefficient is reduced by an amount approximately proportional to the fraction of molecules undergoing restricted diffu-

sion, hence to the product of diffusion length and surface-to-volume ratio of the medium 'pores' [83, 122].

On the other hand, over diffusion times exceeding the correlation time of the call packing, diffusion becomes essentially Gaussian (Section 2.1.2) while reflecting the connectivity and geometrical tortuosity of the medium. The tortuosity coefficient, λ, is defined as the ratio of the diffusion coefficient in bulk to the long-time diffusion coefficient in the tissue [84, 123]. This parameter quantifies the reduction in diffusion length, for fixed time t, owing to hindrance to diffusion in the medium.[11] Numerous studies have estimated $\lambda^{1/2}$ for various mammalian brain tissues and the values obtained are in the range 1.39 – 2.50 (see, e.g., Refs [70, 87]). For example, Nicholson and Phillips [60] found $\lambda^{1/2} = 1.48 - 1.55$ in the extravascular space of rat cerebellum for a number of ionic species having diffusion coefficients in agar gel between 0.76 and 1.4 $\mu\text{m}^2\,\text{ms}^{-1}$.

According to Fieremans *et al.* [86, p. 179], in brain white matter the tortuosity limit is already well established at diffusion times of about 50 ms, since the corresponding diffusion length (~ 14 μm) is approximately an order of magnitude higher than the correlation length (~ 1 μm, Ref. [86]) of the axonal packing. We note that a diffusion time of 50 ms is well within the range of measurement times typically employed in diffusion-weighted imaging (DWI), ASL and DCE MRI. To gain additional insight, we have estimated the time to reach the tortuosity limit in the corpus callosum by rescaling earlier simulation data of Fieremans *et al.* [125] with the use of white matter parameters quoted by Nicholson and Syková [70]. Specifically, the results of Fieremans *et al.* in fibre phantoms with fibre packing densities similar to normal axonal densities in the corpus callosum (i.e., 0.7 – 0.8; our estimate from Table I of Ref. [70]) suggest that the diffusion coefficient reached a long-time value of, approximately, 40% that of self-diffusion of water ($D_{\text{free}} \approx 3$ $\mu\text{m}^2\,\text{ms}^{-1}$ at 35°C [126]) over diffusion lengths $l_D \approx 50$ μm (cf. Fig. 3c of Ref. [125]). Taking into account the fibre diameter ($d_{\text{fibre}} = 20$ μm) and the distribution of axonal diameters

[11] Some authors define the tortuosity coefficient as the square root of the aforementioned diffusion coefficient ratio. See, e.g., Refs [60, 113, 124].

($d_{\mathrm{axon}} = 0.5-3$ μm, our estimate from Fig. 1 of Ref. [127]), the time to the tortuosity limit is estimated as $t_\lambda = (l_D d_{\mathrm{axon}}/d_{\mathrm{fibre}})^2/(0.40 D_{\mathrm{free}}) \approx 1-50$ ms.

As will become apparent in Section 4.1, under permeability-limited conditions for times below typical correlation times for molecular displacements a time-dependent tracer diffusion coefficient is expected to have a negligible effect on the exchange.

2.4.5 Time-dependent relaxation rate

The relaxation terms in Eqs (2.1a) and (2.1b) represent the longitudinal relaxation rates experienced by the diffusing tracer molecules as they sample the medium. They should not be confused with the apparent relaxation rates which are measured in an NMR experiment. It is well known that water exchange across physiological compartments can give rise to apparent compartmental relaxation rates which differ significantly from those found in the absence of exchange [88]. This effect is demonstrated even when no paramagnetic tracers are present. The influence of relaxation rates on the exchange has been assessed using both lumped and spatiotemporal approaches, both of which are briefly discussed next.

In the theory of chemical exchange, the Bloch equations are augmented by adding first-order exchange terms proportional to compartmental concentrations [128]; diffusive mixing is assumed to be much faster than both relaxation and exchange. Formulae for apparent relaxation rates are given in, e.g., Refs [88, 129, 130], with discussion of important special cases. For any given exchanging species, a compartmental system is said to be in slow chemical exchange if the difference between the relaxation rates in the exchanging compartments greatly exceeds the first-order exchange rates involved [129] [compare to Eq. (2.7b)] and is said to be in fast exchange in the opposite case. In addition to exchange, Bauer *et al.* [131] considered the effect of capillary flow on the apparent longitudinal relaxation in whole tissue. They used a two-compartment lumped model and assumed steady-state relaxation in the capillaries.

Bauer and Schulten [90] evaluated the effect of water diffusion and exchange on the enhancement of the mean intracapillary, interstitial and intracellular relaxation rates, due to the presence of an intravascular paramagnetic tracer.

Parameter	Definition	Grey matter[a]	Myocardium[b]	Renal tubule[c]	Units
$2a$	capillary diameter	6.38	5.6	44	μm
$2A$	intercapillary distance	24.2 – 58.18	17.5 – 19	—	μm
L	capillary segment length	108	100	—	μm
v_{iv}	capillary volume fraction[d]	2.32	12.9	22 – 80	%
D_{ev}	tracer diffusion coefficient	0.8	1.8	2.0	$\mu\mathrm{m}^2\,\mathrm{ms}^{-1}$
κ	capillary water permeability[e]	1.7×10^{-3}	5.2×10^{-3}	7×10^{-1}	$\mu\mathrm{m}\,\mathrm{ms}^{-1}$
R_{iv}	IV longitudinal relaxation rate	1664^{-1}	1340^{-1}	4300^{-1}	ms^{-1}
R_{ev}	EV longitudinal relaxation rate	1763^{-1}	920^{-1}	—	ms^{-1}
$D_{\mathrm{ev}}/\kappa a$	$\sim \tau_{\mathrm{ev}}/(2\tau_D)$ (see below)	1.5×10^2	1.2×10^2	1×10^{-1}	—
τ_{c}	capillary-segment transit time (2.3a)[f]	70 – 280	70 – 260	—	ms
τ_{iv}	IV residence time, Eq. (2.2a)	9.3×10^2	3×10^2	—	ms
τ_{ev}	EV residence time, Eq. (2.2c)	4.0×10^4	1.8×10^3	56 – 3.6	ms
τ_D	EV radial diffusion time, Eq. (4.1)	40 – 300	10	—	ms

Table 2.1: **Summary of water-exchange parameter values.** [a]$2a$, v_{iv} in human brain cortex [64]; $2A$ in cat [65] and human [64] cerebral cortex, respectively; L in cat cerebral cortex [65]; D_{ev} of water in brain tissue [94]; longitudinal relaxation rate of blood (haematocrit = 0.42) [132] and in human prefrontal cortex [133], both at 3 T. [b]Capillary dimensions in dog ventricular myocardium [66]; v_{iv} of human myocardium [134]; D_{ev} of water in excised rat myocardium [135]; longitudinal relaxation rate in rat heart ventricle and myocardium at 2.0 T [136]. [c]Renal proximal tubule parameters are defined as follows: basolateral diameter; tubular volume fraction of exchangeable water for a sparse suspension of *ex vivo* tubules [137] and for *in vivo* tubules [138]; diffusion coefficient of water in human renal cortex [139]; basolateral permeability to water [140]; longitudinal relaxation rate of water in peritubular space, assumed equal to that of cerebro-spinal fluid, given in Ref. [141]). [d]All space is assumed accessible to water, hence $v_{\mathrm{iv}} + v_{\mathrm{ev}} = 1$; cf. Eq. (2.2b). [e]Cf. Appendix 2.5.2. [f]For $u_z = 0.39 – 1.5\ \mu\mathrm{m}\,\mathrm{ms}^{-1}$ [65, 93].

2.5 Appendices

2.5.1 A derivation of the governing equations of blood–tissue exchange

In this Appendix we develop equations (2.1a) – (2.1c) of the blood–tissue exchange model.

Conserved quantities. Equation of continuity

The state of a homogenous fluid is described mathematically by specifying the fluid velocity and any two thermodynamic quantities like the fluid pressure and density [142, p. 1]. Thus, five equations are required to specify completely the state of motion of a fluid, namely the equation of continuity (i.e., the conservation of fluid mass); the vector equation of motion (i.e., the conservation of momentum); and the thermodynamic equation of state of the fluid (i.e., the conservation of energy); see Ref. [142, pp. 1 – 12, 523].

In the present simplified treatment of capillary flow and blood–tissue exchange, the effects of blood viscosity and heat transfer between different parts in the intra-capillary and extravascular spaces are assumed to be negligibly low. As a result, the blood–tissue exchange model reduces to the statement of the conservation of tracer mass. This simplified 'kinematic' approach seems adequate for present purposes and is discussed at some length in the remainder of this Appendix.

First we obtain an equation of continuity for the tracer on a microscopic scale; a homogenous fluid is considered for simplicity. The fluxes $\mathbf{j}_{\text{conv}}$, $\mathbf{j}_D$ and $\mathbf{j}_\kappa$ give the mass of fluid passing in unit time through unit surface area due to, respectively, convection, extravascular diffusion and diffusive transcapillary permeation; see Refs [142, p. 2] and [143, p. 136]. As is well known, the divergence $\nabla\cdot\mathbf{j}$ of a vector quantity $\mathbf{j}$ at a point in space P is the net outflow of $\mathbf{j}$ across the surface of a volume element enclosing P, divided by the size of the volume element [144, vol. 2, pp. 3–5].[12] Thus, the divergence of the mass of fluid which in unit time flows through unit surface

[12]The outflow has the dimensions of the magnitude of the vector quantity times a surface area.

area enclosing a given volume element is equal to minus the rate of increase of the contained mass of fluid. Because this rate is also given by minus the time derivative of the fluid density, ϱ, the continuity equation is expressed as

$$\frac{\partial \varrho}{\partial t} = -\nabla \cdot (\mathbf{j}_{\text{conv}} + \mathbf{j}_D + \mathbf{j}_\kappa) - s\,, \tag{2.30}$$

where s is the rate of tracer consumption per unit volume.

A similar argument indicates that Eq. (2.30) also holds for a quantity of tracer in solution by introducing the appropriate concentration of tracer and the various fluxes of tracer molecules [142, p. 219 – 220]. In the sequel we examine the appropriate form of the continuity equation for analysis of blood–tissue exchange in, e.g., MRI experiments at (sub)millimetre resolution.

Mesoscopic volume averaging

As stated by Nicholson and Phillips, 'The definition of a complex medium demands the notion of scale' [60, p. 227]. Solving the equations of transport and exchange in complex heterogenous media on a microscopic scale is, in general, unfeasible. For example, on the scale of tissue interstitial spaces the boundary conditions become extremely complex and the microscopic concentration of a substance of interest will vary irregularly [60, pp. 226 – 227].

The method of volume averaging is one of several well-known approaches, including statistical [71] and geometric modelling, that have been proposed to overcome this difficulty [145]. To quote Wood and Whitaker [146, p. 398]: 'When the length scales in a hierarchical system are disparate, the method of volume averaging can be used to transport information from a smaller scale to a larger one and eventually to the length scale at which the system analysis takes place'. Thus, one seeks to define an appropriate representative elementary volume [87, p. 826], or volume element, ΔV (Fig. 2.7), with the following properties: (i) the volume element is sufficiently large as to encompass microscopic heterogeneities, hence allowing for meaningful averages

Note that, in the literature, the term 'flux' is also used to refer to the net flow across any given surface area. In each case the meaning should be clear from the context.

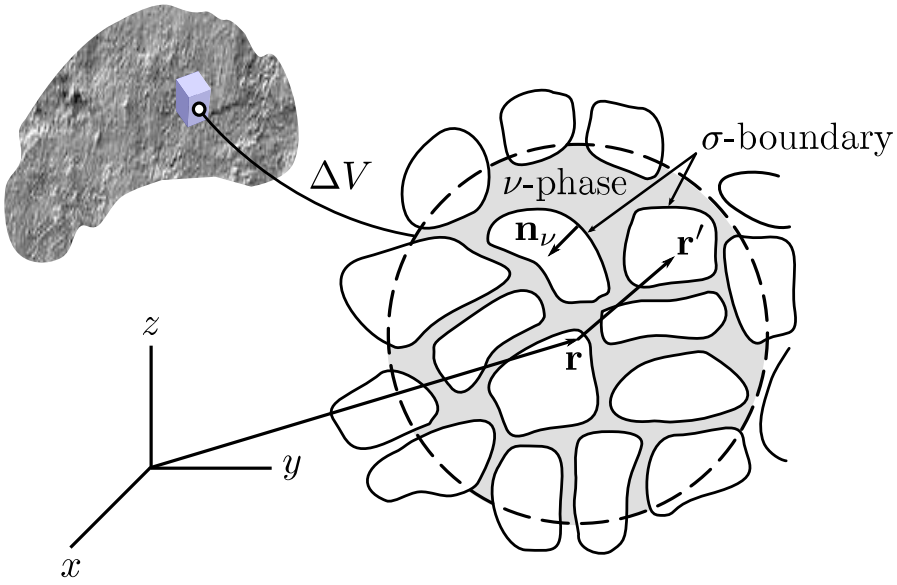

Figure 2.7: **Macroscopic tissue sample, macroscopic voxel and representative mesoscopic volume element** ΔV, adapted from Figs 2 and 3 of Ref. [146] and Fig. 3 of Ref. [147]. Here, the ν-phase may be regarded as a tissue interstitial phase (or the pore space in a soil sample) and bathes an (unlabelled) intracellular phase (or grain space). The σ-boundary is the dividing surface between both phases. Dimensions are not to scale.

of the physical quantities of interest, yet (ii) it is sufficiently small, compared to the size of the body under consideration, as to retain some local meaning with respect to those quantities, which (iii) should vary smoothly from one volume element to another in order that differential operators may be used in the model equations; see Refs [60, pp. 227 – 228], [87, p. 826], [145, pp. 16 – 17] and [147, p. 336].

In other words, after averaging over a volume element, the quantities of interest are expected to vary appreciably only over lengths greater than the characteristic length of the volume element; cf. Refs [145, p. 16] and [148, p. 822]. The following

examples are pertinent to the discussion given in this Appendix:

1. In homogenous fluids, the characteristic length of a volume element must be much greater than intermolecular distances, yet much smaller than the size of the fluid container. A volume element will then contain a very large number of molecules, and hence the fluid may be regarded as a continuous medium.[13] The expression 'point in a fluid' refers not to individual molecules, but to such a volume element; see Ref. [142, p. 1].

2. For blood–tissue exchange applications, a volume element must include enough cellular elements (e.g., erythrocytes and parenchymal cells) to yield physically meaningful volume-element averages [87, p. 826], yet it must be much smaller than the considered tissue sample. In MRI such a mesoscopic volume element must be much smaller than a typical imaging voxel if spatial variations on a sub-voxel scale are to be incorporated in the analysis.

   This criterion specifies the mesoscopic scale introduced in Section 2.1. The single-capillary approximation (Section 2.1.3) places an upper limit on the characteristic length of a volume element of whole tissue at typical capillary-segment lengths and intercapillary distances. In brain tissue, the characteristic length of a volume element is of the order of a few micrometres (Section 2.1, p. 18). Figure 2.7 shows diagrammatically a large tissue sample, an MRI voxel and a mesoscopic volume element with respective characteristic lengths of the order of 1 – 10 cm, 1 mm and 10 μm, say.

We make a comment on terminology. In this Thesis, the term 'microscopic' shall refer to physical phenomena and related quantities on a molecular length scale; the

[13] Consider liquid water: its molecular weight is 18 g mole^{-1} and its density 1.0 g cm^{-3} [16, pp. 420, 426 – 427]. With the use of Avogadro's number, 6.02×10^{23} mole^{-1} [16, p. 96], the number of water molecules in a 1-μm^3 volume is found to be 3×10^{10}. Further, since the concentration of water molecules in liquid water is approximately 55 M [143, p. 613], the same volume of a 10 mM solution (of a Gd-based contrast agent, say) will contain of the order of 5×10^6 molecules, with an expected statistical deviation of less than 0.1%.

term ‘mesoscopic’ shall denote an intermediate length scale in which the microscopic fluctuations of a physical quantity of interest are smoothed out, yet cannot be regarded as ‘bulk’ averages. Alternatively, the term ‘macroscopic’ appears frequently in both the biological [60, 149] and porous media literature [148] in this latter context. Here, the term ‘macroscopic’ shall refer to the characteristic scale (e.g., an imaging voxel) of the measurement process. In MRI, the macroscopic scale also refers to the bulk tissue under examination [150]. The term ‘local’ shall occasionally be used where the appropriate length scale is understood from the context and no confusion arises.

In both the biological and porous media literature (e.g., Refs [60] and [147, 148], respectively) a volume element is often regarded as comprising a number of distinct regions, or phases. To quote Pauling, ‘A phase is a homogeneous part of a system, separated from other parts by physical boundaries. (. . .) A phase in a system comprises all of the parts that have the same properties and composition.’ [16, p. 9]. In this Appendix this concept shall be used rather loosely in such phrases as ‘the intrinsic concentration of tracer molecules in the interstitial phase’, say, since the concentration may vary from point to point. We thereby intend to avoid confusion with the notion of kinetic compartment which appears elsewhere in this Thesis and which involves macroscopic, rather than mesoscopic, spatial averaging.

The above-discussed volume-element properties (i) – (iii) (p. 59) allow one to set up appropriate partial differential equations for transport and exchange on a mesoscopic scale. Specifically, the spatiotemporal differential equations describing blood–tissue exchange provide deterministic predictions of observable phenomena arising from the collective behaviour of a very large number of independent random molecular events [143, Section 4.4.3]. Equations (2.31a) – (2.31j) below summarise several well-known definitions and results that are needed for spatial averaging of the continuity equation (2.30).

It is assumed that intraphase transport and consumption/relaxation, as well as interfacial exchange, can all be described, on a microscopic scale, by an equation of the form (2.30). The microscopic concentration in the ν-phase is denoted by $\psi_\nu(\mathbf{r}, t)$

and is zero outwith that phase. The phase-averaged concentration is defined by (e.g., Eq. [10] of Ref. [147])

$$\langle \psi_\nu \rangle(\mathbf{r}, t) = \frac{1}{\Delta V} \int_{\Delta V_\nu(\mathbf{r},t)} \psi_\nu(\mathbf{r} + \mathbf{r}', t)\, \mathrm{d}^d\mathbf{r}' \,, \tag{2.31a}$$

where $\mathbf{r}$ may be chosen as the centroid position of the volume element and need not be a point in the ν-phase (Refs [145, p. 17] and [147, p. 336]); $\mathbf{r}'$ is a position vector defined with respect to the local reference frame of the volume element; and $\Delta V_\nu(\mathbf{r}, t)$ is the volume within ΔV occupied by the ν-phase and it may change with time, whereas the shape, size and orientation of the volume element itself may not [147, p. 336]. The intrinsic phase-averaged concentration is defined by (e.g., Eq. [11] of Ref. [147])

$$\langle \psi_\nu \rangle^\nu(\mathbf{r}, t) = \frac{1}{\Delta V_\nu(\mathbf{r}, t)} \int_{\Delta V_\nu(\mathbf{r},t)} \psi_\nu(\mathbf{r} + \mathbf{r}', t)\, \mathrm{d}^d\mathbf{r}' \tag{2.31b}$$

and is usually the preferred quantity since it gives the correct value when $\psi_\nu(\mathbf{r}, t)$ is spatially uniform in the volume element [151, p. 9]. Definitions analogous to (2.31a) and (2.31b) hold for a phase-averaged flux $\langle \mathbf{j} \rangle$.

The volume fraction of the ν-phase is defined by

$$v_\nu(\mathbf{r}, t) = \frac{\Delta V_\nu(\mathbf{r}, t)}{\Delta V} \,, \tag{2.31c}$$

hence

$$\langle \psi_\nu \rangle = v_\nu \langle \psi_\nu \rangle^\nu \,. \tag{2.31d}$$

It is useful to consider the volume-weighted sum of the interstitial and intracellular concentrations, or average extravascular concentration over a volume element, defined by

$$\langle \psi_{\mathrm{ev}} \rangle = \langle \psi_{\mathrm{is}} \rangle + \langle \psi_{\mathrm{ic}} \rangle = v_{\mathrm{is}} \langle \psi_{\mathrm{is}} \rangle^{\mathrm{is}} + v_{\mathrm{ic}} \langle \psi_{\mathrm{ic}} \rangle^{\mathrm{ic}} \tag{2.31e}$$

from (2.31a) – (2.31d). Furthermore, it is often convenient to decompose the microscopic concentration into the intrinsic phase-averaged concentration and the spatial

deviation concentration, $\widetilde{\psi}_\nu$ as[14]

$$\psi_\nu(\mathbf{r}+\mathbf{r}',t) = \langle\psi_\nu\rangle^\nu(\mathbf{r},t) + \widetilde{\psi}_\nu(\mathbf{r}+\mathbf{r}',t)\,; \tag{2.31f}$$

see Refs [146, Eq. (20)], [148, Eq. (8)] and [152, Eq. (11a)]. The intrinsic phase-averaged concentration changes on the scale of a volume element while the spatial deviation concentration fluctuates over the characteristic length of the ν-phase. Hence $\widetilde{\psi}_\nu \ll \langle\psi_\nu\rangle^\nu$ [146, Eq. (26b)].

Next we summarise the required results involving averages of time and spatial derivatives. Let σ, $\mathbf{u}_\sigma$ and $\mathbf{n}_\nu$ respectively denote the dividing surface between the ν-phase and the remainder of the volume element, the velocity of the σ-boundary as observed in a fixed reference frame, and a unit normal on σ directed outwards from the ν-phase (Fig. 2.7). The spatial average of the time derivative of $\psi_\nu(\mathbf{r}+\mathbf{r}',t)$ is related to the time derivative of $\langle\psi_\nu\rangle(\mathbf{r},t)$ by

$$\begin{aligned}\left\langle\frac{\partial\psi_\nu}{\partial t}\right\rangle &= \frac{\partial\langle\psi_\nu\rangle}{\partial t} - \frac{1}{\Delta V}\int_\sigma \psi_\nu \mathbf{u}_\sigma\cdot\mathbf{n}_\nu\,\mathrm{d}\sigma \\ &= v_\nu\frac{\partial\langle\psi_\nu\rangle^\nu}{\partial t} + \langle\psi_\nu\rangle^\nu\frac{\partial v_\nu}{\partial t} - \frac{1}{\Delta V}\int_\sigma \psi_\nu\mathbf{u}_\sigma\cdot\mathbf{n}_\nu\,\mathrm{d}\sigma\,,\end{aligned} \tag{2.31g}$$

cf., for instance, Eq. [33] of Ref. [147]. The integral on the right-hand side takes into account the rate of expansion of the ν-phase, given by $\mathbf{u}_\sigma\cdot\mathbf{n}_\nu\,\mathrm{d}\sigma$.

The formula for the spatial average of a gradient is (Eq. [15] of Ref. [147])

$$\langle\nabla\psi_\nu\rangle = \nabla_{\mathbf{r}}\langle\psi_\nu\rangle + \frac{1}{\Delta V}\int_\sigma \psi_\nu\mathbf{n}_\nu\,\mathrm{d}\sigma\,, \tag{2.31h}$$

where the integral takes account of any jump discontinuities at the phase boundary, since ψ_ν is, by definition, zero outwith the ν-phase (Refs [147, pp. 338–339] and [152, p. 231]). Equation (2.31h) indicates that the spatial average of a divergence is given by

$$\langle\nabla\cdot\mathbf{j}\rangle = \nabla\cdot\langle\mathbf{j}\rangle + \frac{1}{\Delta V}\int_\sigma \mathbf{j}\cdot\mathbf{n}_\nu\,\mathrm{d}\sigma\,, \tag{2.31i}$$

[14]Both tilde and circumflex accent superscripts have been used in the literature to indicate the spatial deviation concentration.

where the last term is due to the outward flux through the σ-boundary; cf. Eq. (9) of Ref. [152] and Eq. [10] of Ref. [148].

Lastly, the integral of the intrinsic phase-averaged concentration over the phase boundary is given by [152, Eq. (26)]

$$\frac{1}{\Delta V}\int_{\sigma}\langle\psi_{\nu}\rangle^{\nu}\mathbf{n}_{\nu}\,\mathrm{d}\sigma = -\langle\psi_{\nu}\rangle^{\nu}\nabla v_{\nu}\,. \tag{2.31j}$$

To conclude this summary of 'local volume averaging' [147] results we note the following points:

1. The above phase averages are taken not over an entire physiological compartment (as they would for use in a generic lumped tracer exchange model), but over only a small volume element. Moreover, phase averages may be regarded as functions of centroid position of some volume element (e.g., Refs [147, p. 336] and [148, p. 822]). However, the ν-phase average is defined for all points in any given volume element, not just those points belonging in the ν-phase; see Refs [145, p. 17] and [152, p. 229]. This property is of importance when mesoscopic equations are to be integrated over some volume consisting of different phases (as shall be the case in Chapter 4).

2. If a given phase occupies the volume element in its entirety, the boundary σ vanishes and so do the integrals in Eqs (2.31g) – (2.31j). As a result, spatial averaging commutes with the ∇ operator.

3. If the flow of the ν-phase (e.g., the flow of whole blood containing a tracer solute) is spatially uniform throughout any given volume element, then the integral on the right-hand side of (2.31g) vanishes even though the velocity $\mathbf{u}_{\sigma}$ of the σ-boundary may not be zero in the fixed reference frame of Fig. 2.7. In this case, spatial averaging commutes with time differentiation.

In the remainder of this Appendix we evaluate the mesoscopic form

$$\left\langle\frac{\partial\psi_{\nu}}{\partial t}\right\rangle = -\langle\nabla\cdot(\mathbf{j}_{\mathrm{conv}}+\mathbf{j}_{D}+\mathbf{j}_{\kappa})_{\nu}\rangle - \langle s_{\nu}\rangle \tag{2.32}$$

of the microscopic continuity equation (2.30). Gray [152] worked the above equation further with the use of the results summarised in the foregoing paragraphs as well as further mathematical results involving repeated phase averages. In the sequel we also quote the work of other investigators for additional physical discussion. This we do by considering each flux term of (2.32) in turn.

Convective flux

Convection involves the flow transport of volume elements of fluid whose composition, hence also the concentration of the tracer under consideration, remains unchanged; cf. Ref. [142, p. 219]. The concentration of tracer in any given volume element may of course change due to diffusive transport (discussed in later subsections) between different volume elements.

Let $\mathbf{u}(\mathbf{r}, t)$ denote the fluid velocity at a fixed point in space $\mathbf{r}$ at the time t; this velocity is, in general, not the same as that of a given volume element of fluid as it moves with the flow; cf. Ref. [142, p. 1]. Point $\mathbf{r}$ is regarded as the centroid of a volume element of fluid which contains a large enough number of molecules of tracer (and solute) that both the microscopic tracer concentration, $\psi_{\text{iv}}(\mathbf{r}, t)$, and the microscopic convective flux, $\mathbf{j}_{\text{conv}}(\mathbf{r}, t)$, are well defined; refer to Item 1 on p. 61.

Next, an expression for $\mathbf{j}_{\text{conv}}(\mathbf{r}, t)$ is obtained. In Fig. 2.8, the mass of tracer which crosses in the interval $\mathrm{d}t$ the small, fixed cross-sectional area $\mathrm{d}A$ perpendicular to the capillary axis, is equal to the mass of tracer molecules contained in a volume of fluid of size $\mathrm{d}A \times u_z \mathrm{d}t$; cf. Ref. [144, vol. 1, Section 43–5]. The mass of this quantity of tracer is given by $\psi_{\text{iv}} u_z \times \mathrm{d}A\,\mathrm{d}t$, provided that the microscopic concentration of tracer does not change appreciably during $\mathrm{d}t$ in the small volume of fluid. Thus, the magnitude of the convective flux of tracer is equal to the product of the concentration and the component of the fluid velocity perpendicular to the capillary cross section, and its direction is that of $\mathbf{u}$ [142, pp. 2, 220]. In vector form,

$$\mathbf{j}_{\text{conv}} = \psi_{\text{iv}} \mathbf{u}\,. \tag{2.33a}$$

We now make several simplifying assumptions in order to evaluate the divergence $\nabla \cdot \mathbf{j}_{\text{conv}}$. First we note from (2.33a) that for a solution (e.g., one of some tracer in the

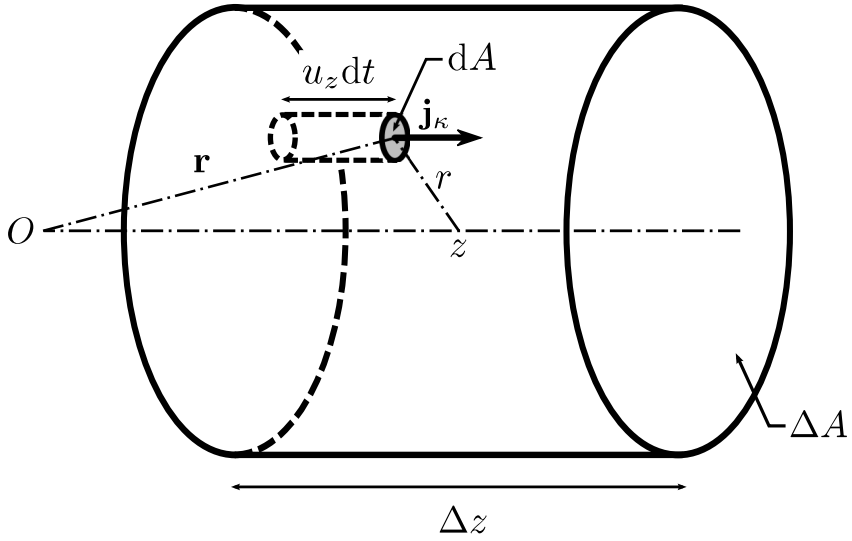

Figure 2.8: **Evaluation of convective flux inside a capillary segment**. The smaller-sized, fixed volume element (shaded circle, magnified for clarity) represents a 'point in the fluid' and is used for evaluation of the microscopic convective flux, $\mathbf{j}_{\mathrm{conv}}$. The larger-sized volume element (of size $\Delta A \Delta z$) is appropriate for evaluation of flux on a mesoscopic scale.

blood), $\mathbf{u}$ represents the total momentum of unit mass of the solution; cf. Ref. [142, p. 219]. A basic assumption of numerous models of tracer transport and exchange is that the flow of the tracer molecules is representative of that of the total fluid [105, p. 732]. Therefore, instead of having to follow the course of individual volume elements of the fluid, one needs only consider fluid velocities as observed at fixed points in space and time; the above definition of $\mathbf{u}$ is consistent with this modelling assumption.

Second, if incompressible blood flow is assumed, Eq. (2.30) shows that the divergence of the blood velocity is zero. Since the presence of an exogenous tracer in low concentration causes only a negligible change in the density of the blood, also

$$\nabla \cdot \mathbf{u} = 0 \tag{2.33b}$$

for the blood–tracer solution, from the above assumption.

We further assume that, as a result of the rapid mixing of tracer molecules, the concentration of tracer is uniform at any capillary cross-section and varies only along

the capillary axis. The magnitude of $\mathbf{u}$ is assumed constant in time (i.e., steady flow [142, p. 9]) and its direction everywhere parallel to the capillary axis:

$$\mathbf{u} = u_z(r)\,\mathbf{z} \tag{2.33c}$$

and the average speed may be reasonably estimated as a typical erythrocyte speed (p. 30). With the use of the Navier–Stokes equation of momentum conservation for incompressible flow (e.g., Eq. (15.7) of Ref. [142]),

$$\frac{\partial(\varrho\mathbf{u})}{\partial t} + (\mathbf{u}\cdot\nabla)(\varrho\mathbf{u}) = -\nabla p + \eta_{\text{visc}}\nabla^2\mathbf{u}\,, \tag{2.34}$$

(p is the pressure and η_{visc} is the viscosity) it is seen that $\mathbf{u}$ in Eq. (2.33c) has perhaps the simplest form compatible with the existence of pressure gradients (due to blood viscosity) in the capillary network.[15] On the other hand, the more drastic simplifying assumption of a constant and uniform flow velocity would imply the absence of pressure gradients inside the capillaries. Viscosity, vorticity and pulsatility effects are not considered further in this analysis.

Under the above assumptions, the divergence of the microscopic convective flux is given by

$$\begin{aligned}\nabla\cdot\mathbf{j}_{\text{conv}} &= \mathbf{u}\cdot\nabla\psi_{\text{iv}} + \psi_{\text{iv}}\nabla\cdot\mathbf{u}\\ &= \mathbf{u}\cdot\nabla\psi_{\text{iv}}\\ &= u_z(r)\,\frac{\partial\psi_{\text{iv}}(z,t)}{\partial z}\end{aligned} \tag{2.35a}$$

with the use of a well-known vector identity [101, Eq. (3.22)]. Spatial averaging over the larger-sized volume element in Fig. 2.8 yields

$$\begin{aligned}\langle\nabla\cdot\mathbf{j}_{\text{conv}}\rangle &= \int_{\Delta A} u_z(r)\,\frac{\mathrm{d}A}{\Delta A}\int_{\Delta z}\frac{\partial\psi_{\text{iv}}(z,t)}{\partial z}\,\frac{\mathrm{d}z}{\Delta z}\\ &= \langle u_{z,\text{iv}}\rangle\,\frac{\psi_{\text{iv}}(z+\Delta z/2,t)-\psi_{\text{iv}}(z-\Delta z/2,t)}{\Delta z}\,.\end{aligned} \tag{2.35b}$$

At this point we make the key assumption that a sufficiently smooth change in microscopic concentration over the volume-element length Δz can be approximated

[15] The actual pressure drop in the capillary network is ca. 20 mm Hg, or about one-fifth the average pressure at the aorta [1, Figs 38.8 and 38.11].

with the corresponding change in intrinsic phase-averaged concentration. In other words, the spatial deviation concentration $\widetilde{\psi}_{\mathrm{iv}} = \psi_{\mathrm{iv}} - \langle\psi_{\mathrm{iv}}\rangle^{\mathrm{iv}}$, given by (2.31f), is assumed to be relatively uniform along the capillary lumen. Thus,

$$\begin{aligned}\langle\nabla\cdot\mathbf{j}_{\mathrm{conv}}\rangle &\approx \langle u_{z,\mathrm{iv}}\rangle\,\frac{\langle\psi_{\mathrm{iv}}\rangle^{\mathrm{iv}}(z+\Delta z/2,t)-\langle\psi_{\mathrm{iv}}\rangle^{\mathrm{iv}}(z-\Delta z/2,t)}{\Delta z}\\ &\approx \langle u_{z,\mathrm{iv}}\rangle\,\frac{\partial\langle\psi_{\mathrm{iv}}\rangle^{\mathrm{iv}}(z,t)}{\partial z}\,.\end{aligned}\tag{2.35c}$$

For tracers which exchange slowly (or not at all) with the erythrocytes, the intrinsic plasma-averaged concentration, $\langle\psi_{\mathrm{iv}}\rangle^{\mathrm{iv}}$, is the more relevant quantity and is higher than the whole-blood-averaged concentration, $\langle\psi_{\mathrm{iv}}\rangle$, by a factor of Hct^{-1}, where Hct is the haematocrit. In this case, the characteristic length Δz of a mesoscopic volume element should be large compared to erythrocyte thickness (2.4 μm [82, p. 357]) and inter-erythrocyte distance in order that the intrinsic plasma-averaged concentration may change smoothly along the capillary. On the other hand, for tracers in fast exchange with erythrocytes, the intrinsic plasma-averaged and whole-blood-averaged concentrations are approximately equal, hence Δz may be chosen independently of erythrocyte thickness and inter-erythrocyte distance.

We assume that the fraction $(v_\nu \mapsto v_{\mathrm{iv}})$[16] of tracer-accessible intracapillary space in the volume element does not change with time and further note that the surface integral involving the phase velocity $\mathbf{u}_\sigma$ vanishes on account of (2.33c). Thus, equating the right-hand sides of (2.31g) and (2.35c), and dividing by this volume fraction gives

$$\frac{\partial\langle\psi_{\mathrm{iv}}\rangle^{\mathrm{iv}}}{\partial t} = -\langle u_{z,\mathrm{iv}}\rangle^{\mathrm{iv}}\,\frac{\partial\langle\psi_{\mathrm{iv}}\rangle^{\mathrm{iv}}(z,t)}{\partial z}\,,\tag{2.36}$$

where $\langle u_{z,\mathrm{iv}}\rangle^{\mathrm{iv}}$ denotes the intrinsic average of the volume-element velocity in that part of the lumen which is accessible to tracer. This result is a particular case of a more general expression for the convection term given by Gray [152, Eq. (36)].

Equation (2.36) is formally identical with the convective part of Eq. (2.1a), where the intrinsic concentration of tracer with respect to the tracer-accessible phase in intracapillary space has been denoted more concisely as $\psi_{\mathrm{iv}}(z,t)$.

[16] See footnote 4 on p. 28.

Diffusive flux in homogenous media

In contrast to convective transport, diffusion involves the change in the composition of the medium[17] due to molecular transfer among different volume elements [142, p. 219]. Before turning to the more complicated case where the molecules of tracer are allowed to diffuse in a tortuous medium like the extravascular space, we consider the 'free' diffusion of a small amount of tracer molecules in a container of water in thermal equilibrium (Ref. [144, vol. 1, Section 43–5] discusses this case for a gas mixture).

Qualitatively, the molecules of tracer move about independently of each other (because of their low concentration) and experience incessant random collisions, most frequently with the much more abundant water molecules. The diffusive motion of tracer molecules is to be described on a time scale much larger than that governing their collisions with the water molecules [144, p. 41–8]. Because molecular collisions are random, and because the concentration of tracer varies within the container, there is a net flow of tracer molecules from regions of higher concentration towards regions of lower concentration until the concentration becomes everywhere uniform; see Refs [142, p. 219] and [144, vol. 1, p. 43–7].

The mass of tracer molecules which diffuses in unit time through unit surface area inside the container is proportional to the concentration difference across the surface and to the velocity of the tracer molecules.[18] Here, the number of molecules which diffuse across the considered surface from the right must be subtracted from the number of them which diffuse from the left. Both these concentrations should be evaluated a distance from the surface of the order of the mean free path between collisions [144, pp. 43–7, 8]. If the concentration of tracer molecules is further assumed to be described by a smooth function, denoted by $\psi_\nu(\mathbf{r}, t)$, the concentration difference can be replaced by the differential. Thus, the microscopic diffusive flux is proportional

[17] Diffusion can occur not only in fluids (liquids and gases) but in solids as well.

[18] In this semi-quantitative argument we ignore the fact that molecular velocities are actually statistically distributed.

to the concentration gradient, as stated by Fick's law (Ref. [153], p. 66)[19]

$$\mathbf{j}_D = -D_\nu \nabla \psi_\nu(\mathbf{r}, t)\,, \tag{2.37a}$$

where the molecular, or microscopic, diffusion coefficient D_ν is proportional to the molecular velocity and to the mean free path between collisions for tracer molecules [144, Eq. (43.27)]. This parameter varies with temperature [143, p. 126], but not with time or position in the free diffusion case. Thus

$$-\nabla \cdot \mathbf{j}_D = D_\nu \nabla^2 \psi_\nu(\mathbf{r}, t)\,. \tag{2.37b}$$

Equation (2.37a) applies to spatial scales such that the concentration of diffusing tracer molecules varies smoothly, in order that the gradient be physically meaningful; see Refs [49, p. 714] and [60, p. 228]. Since it is the action of multiple random collisions that tends to smooth out any concentration non-uniformity, it is intuitively clear that the characteristic length of a volume element must be much greater than the mean free path between collisions in order for Eq. (2.37a) to hold.[20]

The constraint that the concentration of tracer molecules be low in comparison to that of the molecules of the medium in which they diffuse is fulfilled in typical MRI experiments. For instance, the peak concentration in brain blood of certain gadolinium-based tracers is $\sim$ 18 mM for a single dose of the tracer [91, Fig. 2]; this value is much lower than that for the concentration of water molecules in liquid water, approximately 55 mole litre^{-1} [143, p. 613]. As a second example, the fraction of magnetically tagged blood water spins which originate the net magnetisation is just a few parts per million [11, p. 67].

Lastly, we note that the diffusive flux depends, in general, not only on the concentration gradient but also on temperature and pressure gradients [142, pp. 222 – 224].

[19] In general, the flux of solute and solvents is driven by the difference in electrochemical potential between different parts of a solution [154, p. 1]; the electrochemical potential is a function of pressure, temperature and composition [154, pp. 5 ff.]. Refer to, e.g., Chapter 2 of Friedman's book [154] for a discussion of free diffusion and a derivation of Fick's law based on thermodynamic considerations.

[20] At the other extreme, Eq. (2.37a) also requires for its validity that the mean free path between collisions be much smaller than any container dimensions [144, vol. 2, p. 43–10].

According to Landau and Lifshitz [142, pp. 225 – 226], the effect of temperature gradients can be neglected whenever the concentration of tracer is low, whereas the effect of pressure is important only under considerable pressure gradients. As mentioned earlier, in this Thesis we neglect the effect of pressure and further assume all biological processes to occur at constant temperature. The diffusive flux $\mathbf{j}_D$ then reduces to Eq. (2.37a).

Diffusive flux in heterogenous media

Unlike the case just discussed, the diffusion of tracer molecules in the extravascular space of biological tissues (and, generally, in highly heterogenous environments) is hindered by the tortuous geometry of the milieu. However, it is intuitively recognised that the molecules of tracer are undergoing some sort of random motion [143, p. 144] despite the inherent complexity of biological tissues. This process may be characterised, on a mesoscopic scale, by an appropriate diffusion coefficient which differs, in general, from that of Eq. (2.37a) for the microscopic scale.

We begin by substituting (2.31g) and (2.31i) into the spatially averaged continuity equation (2.32) for the diffusive flux. This gives

$$v_\nu \frac{\partial \langle \psi_\nu \rangle^\nu}{\partial t} + \langle \psi_\nu \rangle^\nu \frac{\partial v_\nu}{\partial t} - \frac{1}{\Delta V} \int_\sigma \psi_\nu \mathbf{u}_\sigma \cdot \mathbf{n}_\nu = -\nabla \cdot \langle \mathbf{j}_D \rangle - \frac{1}{\Delta V} \int_\sigma \mathbf{j}_D \cdot \mathbf{n}_\nu \, \mathrm{d}\sigma \,. \tag{2.38a}$$

The last term on the right-hand side is due to the flux of tracer between the ν-phase and the adjacent phases within a volume element. Thus, the boundary condition for $\psi_\nu(\mathbf{r}, t)$ is joined to the mesoscopic equation of continuity in the ν-phase as a result of spatial averaging (Section 1.2.1 of Ref. [151]).

The divergence of the volume-element-averaged diffusive flux in (2.38a) is further developed by substituting the microscopic flux (2.37a) and making use of previous

results to get

$$\begin{aligned}
-\nabla\cdot\langle\mathbf{j}_D\rangle &= \nabla\cdot\langle D_\nu\nabla\psi_\nu\rangle \\
&= \nabla\cdot\left\{D_\nu\left[\nabla_{\mathbf{r}}\langle\psi_\nu\rangle + \frac{1}{\Delta V}\int_\sigma \psi_\nu\mathbf{n}_\nu\,\mathrm{d}\sigma\right]\right\} \\
&= \nabla\cdot\left\{D_\nu\left[v_\nu\nabla_{\mathbf{r}}\langle\psi_\nu\rangle^\nu + \langle\psi_\nu\rangle^\nu\nabla_{\mathbf{r}}v_\nu + \frac{1}{\Delta V}\int_\sigma \psi_\nu\mathbf{n}_\nu\,\mathrm{d}\sigma\right]\right\} \\
&= \nabla\cdot\left\{v_\nu D_\nu\left[\nabla_{\mathbf{r}}\langle\psi_\nu\rangle^\nu + \frac{1}{\Delta V_\nu}\int_\sigma \widetilde{\psi}_\nu\mathbf{n}_\nu\,\mathrm{d}\sigma\right]\right\},
\end{aligned} \tag{2.38b}$$

where D_ν is assumed spatially uniform in the ν-phase. Equation (2.31h) has been used in the second line of the above expression. The third line of the above equation requires the use of (2.31c) together with a well-known vector identity, and Eq. (2.31j) has been used in the last line. Substituting this latter expression into Eq. (2.38a) and rearranging gives

$$\begin{aligned}
v_\nu\frac{\partial\langle\psi_\nu\rangle^\nu}{\partial t} + \langle\psi_\nu\rangle^\nu\frac{\partial v_\nu}{\partial t} &= \nabla\cdot\left\{v_\nu D_\nu\left[\nabla_{\mathbf{r}}\langle\psi_\nu\rangle^\nu + \frac{1}{\Delta V_\nu}\int_\sigma \widetilde{\psi}_\nu\mathbf{n}_\nu\,\mathrm{d}\sigma\right]\right\} \\
&\quad - \frac{1}{\Delta V}\int_\sigma[\mathbf{j}_D - \psi_\nu\mathbf{u}_\sigma]\cdot\mathbf{n}_\nu\,\mathrm{d}\sigma\,.
\end{aligned} \tag{2.38c}$$

If the ν-phase is static (i.e., $\mathbf{u}_\sigma = 0$ everywhere on the σ-boundary) and its size remains unchanged (i.e., $v_\nu = \text{const.}$) the above equation simplifies to

$$v_\nu\frac{\partial\langle\psi_\nu\rangle^\nu}{\partial t} = \nabla\cdot\left\{v_\nu D_\nu\left[\nabla_{\mathbf{r}}\langle\psi_\nu\rangle^\nu + \frac{1}{\Delta V_\nu}\int_\sigma \widetilde{\psi}_\nu\mathbf{n}_\nu\,\mathrm{d}\sigma\right]\right\} - \frac{1}{\Delta V}\int_\sigma \mathbf{j}_D\cdot\mathbf{n}_\nu\,\mathrm{d}\sigma\,. \tag{2.38d}$$

It is recalled that in this equation the term in curly brackets is equal to $-\langle\mathbf{j}_D\rangle$; compare to Eq. (2.38a). Lehner used a reciprocity argument involving the quantities $\langle\nabla\psi_\nu\rangle$ and $\nabla\langle\psi_\nu\rangle^\nu$ to derive the mesoscopic[21] form of Fick's law as [148, Eq. (24)]

$$\langle\mathbf{j}_D\rangle = -v_\nu D_\nu\mathbf{K}_\nu\nabla\langle\psi_\nu\rangle^\nu \tag{2.39a}$$

and the effective diffusion tensor is defined by [148, Eq. (35)]

$$\mathbf{D}_\nu^{\text{eff}} = D_\nu\mathbf{K}_\nu\,, \tag{2.39b}$$

[21] Lehner alluded to his result as "the macroscopic form of Fick's law". See the comment on terminology on p. 61 of this text.

and $\mathbf{K}_\nu$, a dimensionless tensor, was termed the 'intrinsic conductivity': it quantifies hindrance to free diffusion in the ν-phase due to the structure of the heterogenous medium; for the special case of an isotropic porous medium, the intrinsic conductivity is a non-negative scalar at most unity [148, p. 824]. This parameter can be related to the reciprocal of the tortuosity coefficient [87, p. 827]. Previously Gray had defined a 'dispersion tensor' [22] which afforded an expression of the form given by (2.39a); cf. Eqs (32) and (35) of Ref. [152], and references therein.

To arrive at the mesoscopic form (2.39a) of Fick's law, Lehner required the following physical assumptions [148, pp. 822 – 824]:

1. A statistically homogenous, rigid porous medium is considered whose pores (the ν-phase) are filled with a dilute solution of some tracer.

2. The diffusion coefficient, D_ν, of tracer molecules in the ν-phase is spatially uniform. Moreover, diffusion should be nearly steady-state on a microscopic scale. This latter condition is expected to be satisfied if any diffusive transients of microscopic concentration of tracer in the ν-phase are allowed to decay over times of the order of

$$\frac{[\nu\text{-phase microscopic characteristic length}]^2}{D_\nu} \tag{2.40a}$$

and if any changes in phase-averaged quantities occur over much longer times of the order of the characteristic diffusion time inside a volume element, given by

$$\frac{[\text{volume-element characteristic length}]^2}{D_\nu}\,. \tag{2.40b}$$

From the mesoscopic-scale condition (2.40b) it may reasonably be assumed that the microscopic-scale condition (2.40a) will be satisfied when changes in phase-averaged concentrations occur over time scales much longer than that given by (2.40a) [148]. For example, given a characteristic length of 0.1 μm,

[22] The tensor defined by Gray also included a convective term due to the spatial deviation velocity and spatial deviation concentration [refer to Eq. (2.31f) in the text] in the ν-phase.

which is less than the typical cell diameter, and using a typical value of $D_\nu \sim 1\ \mu\text{m}^2\,\text{ms}^{-1}$, mesoscopic processes should have characteristic times greater than about 10 μs. In this regard, we shall assume that the condition of nearly steady-state microscopic diffusion in extravascular space is satisfied in the tortuosity limit (Section 2.4.4).

3. The microscopic flux of tracer across the ν-phase boundary is either uniform (possibly zero) or proportional to the difference between the amplitude of the microscopic concentration ψ_ν at the ν-boundary and a 'mean equilibrium concentration' [148] along the surface of the boundary; this latter concentration does not vary throughout a given volume element.

Substituting (2.39a) and (2.39b) in (2.38d), and introducing the appropriate consumption/relaxation term, the mesoscopic equation of continuity involving diffusive transport and consumption/relaxation in the ν-phase reduces to

$$v_\nu \frac{\partial \langle \psi_\nu \rangle^\nu}{\partial t} = \nabla \cdot v_\nu \mathbf{D}_\nu^{\text{eff}} \nabla \langle \psi_\nu \rangle^\nu - v_\nu R_\nu \langle \psi_\nu \rangle^\nu - \frac{1}{\Delta V} \int_\sigma \mathbf{j}_D \cdot \mathbf{n}_\nu \, \mathrm{d}\sigma \,; \tag{2.41}$$

see Eqs (10) and (38) of Ref. [148] and Eq. (37) of Ref. [152]. At the interface between the capillary wall and the interstitial space, $\mathbf{j}_D$ represents the diffusive permeation flux between the plasma and interstitial phases; this flux is evaluated in the next Subsection of this Appendix.

We base the subsequent discussion of diffusion and consumption/relaxation in extravascular space on the foregoing results. The extravascular space shall be modelled as a two-phase system consisting of interstitial ($\nu \to$ is) and intracellular ($\nu \to$ ic) phases; transport and exchange associated with cell membranes are regarded as negligible in this Thesis. Transport and exchange in whole extravascular tissue are then determined by processes (i.e., diffusion and consumption/relaxation in our simplified model) which occur at the interstitial and intracellular scale; cf. Ref. [146, p. 399].

Case 1 *Impermeable parenchymal cell membranes*

The simplest case is that of extravascular tracers which do not cross poorly permeable parenchymal cell membranes to any appreciable extent. The flux $\mathbf{j}_D$ is thus either very small or zero and Eq. (2.41) simplifies to

$$\frac{\partial \langle \psi_{\mathrm{is}} \rangle^{\mathrm{is}}}{\partial t} = \nabla \cdot \mathbf{D}_{\mathrm{is}}^{\mathrm{eff}} \nabla \langle \psi_{\mathrm{is}} \rangle^{\mathrm{is}} - R_{\mathrm{is}} \langle \psi_{\mathrm{is}} \rangle^{\mathrm{is}} \tag{2.42a}$$

or, since in this case $\langle \psi_{\mathrm{ev}} \rangle = v_{\mathrm{is}} \langle \psi_{\mathrm{is}} \rangle^{\mathrm{is}}$,

$$\frac{\partial \langle \psi_{\mathrm{ev}} \rangle}{\partial t} = \nabla \cdot \mathbf{D}_{\mathrm{is}}^{\mathrm{eff}} \nabla \langle \psi_{\mathrm{ev}} \rangle - R_{\mathrm{is}} \langle \psi_{\mathrm{ev}} \rangle \,. \tag{2.42b}$$

Thus, for extravascular extracellular tracers the mesoscopic diffusion–consumption equation can be written in terms of either the intrinsic phase-averaged concentration or the average extravascular concentration, in each case involving the effective interstitial diffusion coefficient. The above equations are formally identical with governing equation (2.1b).

Case 2 *Weakly permeable parenchymal cell membranes*

On the other hand, for tracers which do permeate the parenchymal cell membrane the transmembrane flux will not, in general, be determined by a mean equilibrium concentration at any given time scale. In this case, Lehner's development (Ref. [148]; condition 3 on p. 75 above) will be applicable neither to plasma–interstitial exchange nor to interstitial–intracellular exchange. However, for weakly permeable membranes, we may assume that $\psi_{\mathrm{ic}} \ll \psi_{\mathrm{is}}$ at cell membranes. For example, in nervous system tissues the interstitial-to-intracellular volume ratio is ~ 0.2.[23] Hence the intracellular-to-interstitial flux can be assumed, on average, very small, and the interstitial-to-intracellular flux will be very nearly equal to $\kappa_\sigma \psi_{\mathrm{is}}$; in this case condition 3 above is approximately satisfied. Writing Eq. (2.41) for the both interstitial and intracellular

[23] See, e.g., Table I of Ref. [70] for values of interstitial volume fractions for various nervous system tissues.

phase, and adding this pair of equations, gives

$$\frac{\partial\langle\psi_{\mathrm{ev}}\rangle}{\partial t} = \nabla\cdot\left[v_{\mathrm{is}}\mathbf{D}_{\mathrm{is}}^{\mathrm{eff}}\,\nabla\langle\psi_{\mathrm{is}}\rangle^{\mathrm{is}} + v_{\mathrm{ic}}\mathbf{D}_{\mathrm{ic}}^{\mathrm{eff}}\,\nabla\langle\psi_{\mathrm{ic}}\rangle^{\mathrm{ic}}\right] - v_{\mathrm{is}}R_{\mathrm{is}}\langle\psi_{\mathrm{is}}\rangle^{\mathrm{is}} - v_{\mathrm{ic}}R_{\mathrm{ic}}\langle\psi_{\mathrm{ic}}\rangle^{\mathrm{ic}}\,. \tag{2.43}$$

For the case of nearly-equilibrium conditions on a mesoscopic scale, the average extravascular concentration is approximately equal to each of the intrinsic phase-averaged concentrations, i.e.,

$$\langle\psi_{\mathrm{ev}}\rangle \approx \langle\psi_{\mathrm{is}}\rangle^{\mathrm{is}} \approx \langle\psi_{\mathrm{ic}}\rangle^{\mathrm{ic}}\,, \tag{2.44}$$

thus Eq. (2.43) becomes

$$\frac{\partial\langle\psi_{\mathrm{ev}}\rangle}{\partial t} = \nabla\cdot\mathbf{D}^{\mathrm{eff}}\,\nabla\langle\psi_{\mathrm{ev}}\rangle - R^{\mathrm{eff}}\langle\psi_{\mathrm{ev}}\rangle \tag{2.45a}$$

with

$$\mathbf{D}^{\mathrm{eff}} \equiv v_{\mathrm{is}}\mathbf{D}_{\mathrm{is}}^{\mathrm{eff}} + v_{\mathrm{ic}}\mathbf{D}_{\mathrm{ic}}^{\mathrm{eff}}\,, \tag{2.45b}$$

$$R^{\mathrm{eff}} \equiv v_{\mathrm{is}}R_{\mathrm{is}} + v_{\mathrm{ic}}R_{\mathrm{ic}}\,. \tag{2.45c}$$

In what follows we examine under which conditions the intrinsic interstitial and intracellular concentrations may be considered sufficiently near to their equilibrium value, dependent upon diffusive transport and first-order consumption relaxation; such conditions are given by Eqs (2.48a), (2.48b) and, in terms of characteristic time and length scales, by Eqs (2.61a), (2.61b) below. In so doing we adapt for present purposes the approach taken by Wood and Whitaker [146] in their discussion of diffusion and reaction in biofilms.[24]

The concentration difference,

$$\psi_{\delta} = \langle\psi_{\mathrm{is}}\rangle^{\mathrm{is}} - \langle\psi_{\mathrm{ic}}\rangle^{\mathrm{ic}}\,, \tag{2.46a}$$

[24]The physical situation considered by Wood and Whitaker in Ref. [146] involves diffusive transport within the interstitial and intracellular phases, intracellular Michaelis–Menten reaction and transmembrane transport mediated by transporter enzymes.

is conveniently introduced as a measure of deviation from equilibrium. The intrinsic phase-averaged concentrations are then expressed as

$$\langle \psi_{\mathrm{is}} \rangle^{\mathrm{is}} = \langle \psi_{\mathrm{ev}} \rangle + v_{\mathrm{ic}} \psi_\delta \,, \tag{2.46b}$$

$$\langle \psi_{\mathrm{ic}} \rangle^{\mathrm{ic}} = \langle \psi_{\mathrm{ev}} \rangle - v_{\mathrm{is}} \psi_\delta \,. \tag{2.46c}$$

Equation (2.43) is recast in terms of $\langle \psi_{\mathrm{ev}} \rangle$ and ψ_δ as

$$\begin{aligned} \frac{\partial \langle \psi_{\mathrm{ev}} \rangle}{\partial t} &= \nabla \cdot \mathbf{D}^{\mathrm{eff}} \nabla \langle \psi_{\mathrm{ev}} \rangle - R^{\mathrm{eff}} \langle \psi_{\mathrm{ev}} \rangle \\ &\quad + \nabla \cdot \left[v_{\mathrm{is}} v_{\mathrm{ic}} (\mathbf{D}^{\mathrm{eff}}_{\mathrm{is}} - \mathbf{D}^{\mathrm{eff}}_{\mathrm{ic}}) \nabla \psi_\delta \right] - v_{\mathrm{is}} v_{\mathrm{ic}} (R_{\mathrm{is}} - R_{\mathrm{ic}}) \psi_\delta \,. \end{aligned} \tag{2.47}$$

This equation suggests that the following conditions should be valid for diffusive transport with first-order consumption/relaxation processes to be near to mesoscopic equilibrium:

$$v_{\mathrm{is}} v_{\mathrm{ic}} \frac{\left\| \mathbf{D}^{\mathrm{eff}}_{\mathrm{is}} - \mathbf{D}^{\mathrm{eff}}_{\mathrm{ic}} \right\|}{\| \mathbf{D}^{\mathrm{eff}} \|} \frac{\| \nabla \psi_\delta \|}{\| \nabla \langle \psi_{\mathrm{ev}} \rangle \|} \ll 1 \,, \tag{2.48a}$$

$$v_{\mathrm{is}} v_{\mathrm{ic}} \frac{|R_{\mathrm{is}} - R_{\mathrm{ic}}|}{R^{\mathrm{eff}}} \frac{|\psi_\delta|}{\langle \psi_{\mathrm{ev}} \rangle} \ll 1 \,. \tag{2.48b}$$

Estimates for $\| \nabla \psi_\delta \| \,/\, \| \nabla \langle \psi_{\mathrm{ev}} \rangle \|$ and $|\psi_\delta| \,/ \langle \psi_{\mathrm{ev}} \rangle$ involving transport and exchange parameters and appropriate length scales are developed in the sequel. When they are substituted in (2.48a) and (2.48b), the constraints (2.61a) and (2.61b) below are obtained.

Condition (2.48a) involves the product of a matrix norm ratio and a vector norm ratio rather than a ratio of scalars of the form $|\nabla \cdot (\text{a vector field})|$, see Eq. (2.47). This is reasonable since the use of the surface integral form of the gradient [155, pp. 119, 122 – 123] gives

$$\begin{aligned} \left| \nabla \cdot \mathbf{D}^{\mathrm{eff}} \nabla \langle \psi_{\mathrm{ev}} \rangle \right| &\equiv \left| \lim_{\Delta V' \to 0} \frac{1}{\Delta V'} \int_{\Delta S'} \mathbf{D}^{\mathrm{eff}} \nabla \langle \psi_{\mathrm{ev}} \rangle \cdot \mathbf{n} \, \mathrm{d}S' \right| \\ &\leq \lim_{\Delta V' \to 0} \frac{1}{\Delta V'} \int_{\Delta S'} \left| \mathbf{D}^{\mathrm{eff}} \nabla \langle \psi_{\mathrm{ev}} \rangle \cdot \mathbf{n} \right| \mathrm{d}S' \\ &= \mathcal{O} \left[\lim_{\Delta V' \to 0} \frac{1}{\Delta V'} \int_{\Delta S'} \| \mathbf{D}^{\mathrm{eff}} \nabla \langle \psi_{\mathrm{ev}} \rangle \| \, \mathrm{d}S' \right] \\ &= \mathcal{O} \left[\frac{\Delta S}{\Delta V} \| \mathbf{D}^{\mathrm{eff}} \nabla \langle \psi_{\mathrm{ev}} \rangle \| \right] , \end{aligned} \tag{2.49a}$$

and similarly for $\left|\nabla\cdot(\mathbf{D}_{\mathrm{is}}^{\mathrm{eff}}-\mathbf{D}_{\mathrm{ic}}^{\mathrm{eff}})\nabla\psi_\delta\right|$. $\Delta V'$ denotes a volume enclosed by the surface $\Delta S'$ and containing the point at which the left-hand side of (2.49a) is evaluated; the primed notation is used to avoid confusion with that employed for a physical volume element of size ΔV with surface area ΔS. In the last line of (2.49a) the mathematical limit has been approximated with its physical counterpart on a mesoscopic scale. This approximation is reasonable for sufficiently small volume elements. Further, since $\|\mathbf{D}^{\mathrm{eff}}\nabla\langle\psi_{\mathrm{ev}}\rangle\|\leq\|\mathbf{D}^{\mathrm{eff}}\|\|\nabla\langle\psi_{\mathrm{ev}}\rangle\|$, where the matrix norm is that induced by the considered vector norm [156, p. 8], we may use the constraint (2.48a) instead of the alternative condition, from Eq. (2.47),

$$v_{\mathrm{is}}v_{\mathrm{ic}}\,\frac{\left\|(\mathbf{D}_{\mathrm{is}}^{\mathrm{eff}}-\mathbf{D}_{\mathrm{ic}}^{\mathrm{eff}})\nabla\psi_\delta\right\|}{\|\mathbf{D}^{\mathrm{eff}}\,\nabla\langle\psi_{\mathrm{ev}}\rangle\|}\ll 1\,. \tag{2.49b}$$

When either one of the two consumption/relaxation rates markedly dominates, the two-phase system will not be near to equilibrium and the constraint (2.48b) will likely not be met; this situation might still be adequately described as one with totally absorbing boundary conditions (Section 2.3.1, p. 35). For example, when $R_{\mathrm{ic}}\gg R_{\mathrm{is}}$ we expect $\langle\psi_{\mathrm{ic}}\rangle^{\mathrm{ic}}\ll\langle\psi_{\mathrm{iv}}\rangle^{\mathrm{is}}$ for times $t\gtrsim R_{\mathrm{is}}^{-1}$, hence $\langle\psi_{\mathrm{ev}}\rangle\approx v_{\mathrm{is}}\langle\psi_{\mathrm{is}}\rangle^{\mathrm{is}}\approx v_{\mathrm{is}}\psi_\delta$ and the left-hand side of (2.48b) is close to unity.

On the other hand, if neither consumption/relaxation rate is clearly dominant, then by the use of (2.45c), and noting that $v_{\mathrm{is}},v_{\mathrm{ic}}<1$, the condition in (2.48b) can be replaced by the more conservative, but simpler, constraint

$$|\psi_\delta|\ll\langle\psi_{\mathrm{ev}}\rangle\,, \tag{2.49c}$$

which simply expresses that near to equilibrium the deviation of the intrinsic phase-averaged concentrations about their weighted sum should be small.

In order to obtain estimates for the ratios on the left-hand side of constraints (2.48a) and (2.48b), a differential equation for ψ_δ is derived below. Writing Eq. (2.41) for both the interstitial and intracellular phases, dividing each equation through by the respective volume fraction (ignoring variations in these parameters), and sub-

tracting the resultant expressions, yields

$$\frac{\partial \psi_\delta}{\partial t} = \nabla \cdot \left[\mathbf{D}_{\mathrm{is}}^{\mathrm{eff}} \nabla \langle \psi_{\mathrm{is}} \rangle^{\mathrm{is}} - \mathbf{D}_{\mathrm{ic}}^{\mathrm{eff}} \nabla \langle \psi_{\mathrm{ic}} \rangle^{\mathrm{ic}} \right] - \left[R_{\mathrm{is}} \langle \psi_{\mathrm{is}} \rangle^{\mathrm{is}} - R_{\mathrm{ic}} \langle \psi_{\mathrm{ic}} \rangle^{\mathrm{ic}} \right] - \frac{1}{v_{\mathrm{is}} v_{\mathrm{ic}} \Delta V} \int_\sigma \mathbf{j}_D \cdot \mathbf{n}_{\mathrm{is}} \, \mathrm{d}\sigma \,, \tag{2.50a}$$

where $\mathbf{n}_{\mathrm{is}}$ is an outwardly directed unit normal on the interstitial phase (Fig. 2.7). The total flux through the ν-boundary can be expressed in terms of the microscopic concentrations of tracer at each face of the boundary, as

$$\int_\sigma \mathbf{j}_D \cdot \mathbf{n}_{\mathrm{is}} \, \mathrm{d}\sigma = \int_\sigma \kappa_\sigma \left[\psi_{\mathrm{is}} - \psi_{\mathrm{ic}} \right] \mathrm{d}\sigma = \kappa_\sigma S_\sigma \left[\langle \psi_{\mathrm{is}} \rangle|_\sigma - \langle \psi_{\mathrm{ic}} \rangle|_\sigma \right] , \tag{2.50b}$$

where κ_σ is a mass transfer coefficient, S_σ denotes the surface area of the interstitial–intracellular boundary in a volume element, and an obvious notation has been used for the surface-averaged concentrations over the σ-boundary. Whitaker has shown that if the fluctuations in the microscopic concentration are small, and if the characteristic length of a volume element is much smaller than the respective characteristic lengths over which the intrinsic phased-averaged concentrations and their spatial derivatives change, then the surface-averaged concentrations can be substituted with good approximation by the intrinsic phase-averaged concentrations; see Ref. [151, Section 1.3.3] and Whitaker's earlier work [145, pp. 17 ff.]. If these conditions hold, Eq. (2.50a) becomes

$$\frac{\partial \psi_\delta}{\partial t} = \nabla \cdot \left[\mathbf{D}_{\mathrm{is}}^{\mathrm{eff}} \nabla \langle \psi_{\mathrm{is}} \rangle^{\mathrm{is}} - \mathbf{D}_{\mathrm{ic}}^{\mathrm{eff}} \nabla \langle \psi_{\mathrm{ic}} \rangle^{\mathrm{ic}} \right] - \left[R_{\mathrm{is}} \langle \psi_{\mathrm{is}} \rangle^{\mathrm{is}} - R_{\mathrm{ic}} \langle \psi_{\mathrm{ic}} \rangle^{\mathrm{ic}} \right] - \frac{\kappa_\sigma S_\sigma}{v_{\mathrm{is}} v_{\mathrm{ic}} \Delta V} \left[\langle \psi_{\mathrm{is}} \rangle^{\mathrm{is}} - \langle \psi_{\mathrm{ic}} \rangle^{\mathrm{ic}} \right] . \tag{2.50c}$$

Next, substituting the concentration decompositions (2.46b) and (2.46c) in (2.50c) and rearranging, gives

$$\frac{\partial \psi_\delta}{\partial t} = \nabla \cdot \mathbf{D}_{\mathrm{isic}} \nabla \psi_\delta - R_{\mathrm{isic}} \psi_\delta - \frac{\kappa_\sigma S_\sigma}{v_{\mathrm{is}} v_{\mathrm{ic}} \Delta V} \psi_\delta + \nabla \cdot (\mathbf{D}_{\mathrm{is}}^{\mathrm{eff}} - \mathbf{D}_{\mathrm{ic}}^{\mathrm{eff}}) \nabla \langle \psi_{\mathrm{ev}} \rangle - (R_{\mathrm{is}} - R_{\mathrm{ic}}) \langle \psi_{\mathrm{ev}} \rangle \tag{2.51a}$$

with

$$\mathbf{D}_{\mathrm{isic}} \equiv v_{\mathrm{ic}} \mathbf{D}_{\mathrm{is}}^{\mathrm{eff}} + v_{\mathrm{is}} \mathbf{D}_{\mathrm{ic}}^{\mathrm{eff}} \,, \tag{2.51b}$$

$$R_{\mathrm{isic}} \equiv v_{\mathrm{ic}} R_{\mathrm{is}} + v_{\mathrm{is}} R_{\mathrm{ic}} \,. \tag{2.51c}$$

Thus, $\mathbf{D}_{\text{isic}}$ and R_{isic} respectively describe the diffusion and consumption/relaxation for the concentration difference ψ_δ.

Equation (2.51a) affords the following order-of-magnitude estimates:

$$\frac{\partial \psi_\delta}{\partial t} = \mathcal{O}\left[\frac{\Delta\psi_\delta}{\tau_\delta}\right], \tag{2.52a}$$

$$\begin{aligned}\frac{\partial \psi_\delta}{\partial t} = {} & \mathcal{O}\left[\frac{\|\mathbf{D}_{\text{isic}}\|}{\ell_\delta \ell_{\delta 1}}\Delta\psi_\delta\right] - \mathcal{O}[R_{\text{isic}}\psi_\delta] - \mathcal{O}\left[\frac{\kappa_\sigma S_\sigma}{v_{\text{is}} v_{\text{ic}} \Delta V}\psi_\delta\right] \\ & + \mathcal{O}\left[\frac{\|\mathbf{D}_{\text{is}}^{\text{eff}} - \mathbf{D}_{\text{ic}}^{\text{eff}}\|}{\ell_{\text{av}}\ell_{\text{av}1}}\Delta\langle\psi_{\text{ev}}\rangle\right] - \mathcal{O}[(R_{\text{is}} - R_{\text{ic}})\langle\psi_{\text{ev}}\rangle],\end{aligned} \tag{2.52b}$$

where ℓ_δ and $\ell_{\delta 1}$ denote the characteristic lengths associated with changes in ψ_δ and $\nabla\psi_\delta$, respectively, over a characteristic time interval τ_δ; and the characteristic lengths ℓ_{av}, $\ell_{\text{av}1}$ refer to the concomitant changes in $\langle\psi_{\text{ev}}\rangle$ and $\nabla\langle\psi_{\text{ev}}\rangle$.

The right-hand side of (2.52b) shows that uncertainty in the magnitude of the time derivative $\partial\psi_\delta/\partial t$ may arise due to terms of the same order of magnitude having opposite algebraic signs. Equating the right-hand sides of (2.52a) and (2.52b), and rearranging, yields the estimate[25]

$$\frac{\Delta\psi_\delta}{\Delta\langle\psi_{\text{ev}}\rangle} \sim \frac{\mathcal{O}\left[\frac{\|\mathbf{D}_{\text{is}}^{\text{eff}} - \mathbf{D}_{\text{ic}}^{\text{eff}}\|\tau_\delta}{\ell_{\text{av}}\ell_{\text{av}1}}\right] - \mathcal{O}\left[\frac{\langle\psi_{\text{ev}}\rangle}{\Delta\langle\psi_{\text{ev}}\rangle}(R_{\text{is}} - R_{\text{ic}})\tau_\delta\right]}{\mathcal{O}[1] - \mathcal{O}\left[\frac{\|\mathbf{D}_{\text{isic}}\|\tau_\delta}{\ell_\delta\ell_{\delta 1}}\right] + \left\{\mathcal{O}[R_{\text{isic}}\tau_\delta] + \mathcal{O}\left[\frac{\kappa_\sigma S_\sigma \tau_\delta}{v_{\text{is}} v_{\text{ic}}\Delta V}\right]\right\}\frac{\psi_\delta}{\Delta\psi_\delta}}. \tag{2.53a}$$

In general the analysis of order-of-magnitude estimates should also take into account the effect of the initial and boundary conditions [146, p. 408]. Here, initial rest conditions are assumed. Hence, it may be expected that first $\langle\psi_{\text{ev}}\rangle$ and ψ_δ will both increase due to intracapillary inflow and finite cell membrane permeabilities; that then they will plateau at somewhat different time instants due to the interplay of diffusive and consumption/relaxation effects; and that, finally, they both will decrease due to the combined effects of outflow and consumption/relaxation.

[25] *Remark on notation.* Throughout this Appendix, any expression of the form $\alpha \sim \beta$ is to be understood in the sense that α and β are of the same order of magnitude, i.e., over the appropriate value ranges of α and β, the ratio $|\alpha/\beta|$ is bounded by some fixed positive number, M (cf. Ref. [157, pp. 273, 277 – 278]); the estimates given in this Appendix do not, in general, enable us to assert that $|\alpha/\beta| \approx 1$. Landau's notation, $\alpha = \mathcal{O}[\beta]$, also has been somewhat loosely employed in the text and conveys the same meaning.

Since ψ_δ is a deviation from the average concentration $\langle\psi_{\text{ev}}\rangle$, see Eq. (2.46a), its magnitude can be assumed of the same order as $\Delta\psi_\delta$, i.e., changes in ψ_δ can be approximated with ψ_δ itself [146, p. 408] and $|\Delta\psi_\delta/\psi_\delta| = \mathcal{O}[1]$.

If the difference between the interstitial and intracellular diffusion coefficients, and consumption relaxation rates, is small, the ratio $\langle\psi_{\text{ev}}\rangle/\Delta\langle\psi_{\text{ev}}\rangle$ is expected to be highest when τ_δ is of the order of the time to probe the geometrical tortuosity of the interstitial and intracellular spaces (i.e., the time to reach the tortuosity limit; Sections 2.1.2 and 2.4.4). Thus, neglecting in (2.47) both the concentration difference ψ_δ and its spatial variation, we get the estimate

$$\frac{\langle\psi_{\text{ev}}\rangle}{\Delta\langle\psi_{\text{ev}}\rangle} \sim \frac{-\mathcal{O}[1] + \mathcal{O}\big[\|\mathbf{D}^{\text{eff}}\|\tau_\delta/(\ell_{\text{av}}\ell_{\text{av1}})\big]}{\mathcal{O}[R^{\text{eff}}\tau_\delta]}\,. \tag{2.53b}$$

In order to simplify (2.53a) it is convenient to define a characteristic time, τ_{isic}, and a characteristic length, ℓ_{isic}, by

$$\tau_{\text{isic}} \equiv \left[R_{\text{isic}} + \frac{\kappa_\sigma S_\sigma}{v_{\text{is}}v_{\text{ic}}\Delta V}\right]^{-1} = \left[R_{\text{isic}} + \frac{1}{\tau_{\text{is}}} + \frac{1}{\tau_{\text{ic}}}\right]^{-1}, \tag{2.54a}$$

$$\ell_{\text{isic}}^2 \equiv \|\mathbf{D}_{\text{isic}}\|\tau_{\text{isic}}\,, \tag{2.54b}$$

where $\tau_\nu = v_\nu\Delta V/(\kappa_\sigma S_\sigma)$ is the mean residence time in the ν-phase under well-mixed conditions with negligible consumption/relaxation.[26] These parameters are discussed in detail below. Inserting (2.53b) in (2.53a), dividing through by $\|\mathbf{D}_{\text{isic}}\|\tau_\delta$ and using (2.54a) and (2.54b), the estimate in (2.53a) can be rearranged as

$$\begin{aligned}\frac{\Delta\psi_\delta}{\Delta\langle\psi_{\text{ev}}\rangle} \sim\ & \frac{\ell_{\text{isic}}^2}{\ell_{\text{av}}\ell_{\text{av1}}} \\ & \times \frac{\mathcal{O}\left[\dfrac{\|\mathbf{D}_{\text{is}}^{\text{eff}} - \mathbf{D}_{\text{ic}}^{\text{eff}}\|}{\|\mathbf{D}_{\text{isic}}\|}\right] - \mathcal{O}\left[\dfrac{R_{\text{is}} - R_{\text{ic}}}{R^{\text{eff}}}\dfrac{\|\mathbf{D}^{\text{eff}}\|}{\|\mathbf{D}_{\text{isic}}\|}\right] + \mathcal{O}\left[\dfrac{R_{\text{is}} - R_{\text{ic}}}{R^{\text{eff}}}\dfrac{\ell_{\text{av}}\ell_{\text{av1}}}{\|\mathbf{D}_{\text{isic}}\|\tau_\delta}\right]}{\mathcal{O}[1] - \mathcal{O}\left[\dfrac{\ell_{\text{isic}}^2}{\ell_\delta\ell_{\delta 1}}\right] + \mathcal{O}\left[\dfrac{\tau_{\text{isic}}}{\tau_\delta}\right]}\,.\end{aligned} \tag{2.55}$$

[26] Since, under well-mixed conditions, the net flux of tracer molecules between the ν-phases in adjacent volume elements will be zero, the characteristic time τ_ν can be defined on the scale of a single volume element up to the scale of an entire mesoscopically homogenous region.

The various order-of-magnitude terms which appear in this expression and in (2.53b) and are evaluated in the sequel. The final estimates are given by Eqs (2.58) – (2.60).

The parameters $\ell_{\rm av}$ and ℓ_δ may be estimated on physical grounds as follows. According to the diffusion–consumption equation (2.47) for the volume-element averaged concentration, $\langle\psi_{\rm ev}\rangle$, we may write the estimate

$$\ell_{\rm av}^2 \gtrsim \|\mathbf{D}^{\rm eff}\|\tau_\delta\,. \tag{2.56a}$$

Here the $\gtrsim$ sign is appropriate because $\ell_{\rm av}$ includes the effect not only of diffusion, but also of transmembrane transfer and consumption/relaxation. Since all these three processes tend to smooth out any concentration non-uniformities, the typical length $\ell_{\rm av}$ associated with a given change $\Delta\langle\psi_{\rm ev}\rangle$ during a fixed interval τ_δ is greater than that due only to diffusion, $\|\mathbf{D}^{\rm eff}\|\tau_\delta$. By a similar argument, from Eq. (2.51a), which describes the diffusive transport and consumption/relaxation of the concentration difference ψ_δ, we get

$$\ell_\delta^2 \gtrsim \|\mathbf{D}_{\rm isic}\|\tau_\delta\,. \tag{2.56b}$$

It is difficult to compare the parameters $\ell_{\rm av}$ and ℓ_δ *a priori*, since it can happen that the average concentration $\langle\psi_{\rm ev}\rangle$ changes while the concentration difference ψ_δ does not, and vice-versa. For example, these situations might occur in the case of tissues with, respectively, highly and poorly permeable cell membranes. However, based on (2.56a) and (2.56b) we may put

$$\ell_{\rm av} \sim \ell_\delta\,. \tag{2.56c}$$

We assume that the average concentration varies more smoothly than the concentration difference, and hence that the characteristic length associated with a change in $\nabla\langle\psi_{\rm ev}\rangle$ during an interval τ_δ is greater than the characteristic length associated with a change in $\nabla\psi_\delta$. Thus,

$$\ell_{\rm av1} \gtrsim \ell_{\delta 1}\,. \tag{2.56d}$$

We further assume that changes in $\nabla\langle\psi_{\text{ev}}\rangle$ and $\nabla\psi_\delta$ occur over distances greater than do the respective changes in $\langle\psi_{\text{ev}}\rangle$ and ψ_δ; for example, if $\nabla\langle\psi_{\text{ev}}\rangle$ is a constant, ℓ_{av} is finite but $\ell_{\text{av1}} \to \infty$; cf. Ref. [146, p. 408]. Thus,

$$\ell_{\text{av1}} \gtrsim \ell_{\text{av}} \,, \qquad\qquad \ell_{\delta 1} \gtrsim \ell_\delta \,. \tag{2.56e}$$

Combining the constraints given by (2.56c) – (2.56e) gives

$$\ell_{\text{av1}} \gtrsim \ell_{\text{av}} \sim \ell_\delta \,, \qquad\qquad \ell_{\text{av1}} \gtrsim \ell_{\delta 1} \gtrsim \ell_\delta \,. \tag{2.56f}$$

The parameter τ_{isic} is interpreted as a characteristic time for changes in the difference, $\psi_\delta = \langle\psi_{\text{is}}\rangle^{\text{is}} - \langle\psi_{\text{ic}}\rangle^{\text{ic}}$, between the intrinsic phase-averaged concentrations under well-mixed conditions. This may be understood qualitatively by noting that (i) τ_{isic} does not depend upon the phase diffusion coefficients but varies inversely with mass transfer coefficient, κ_σ; and that (ii) it is the mass transfer and consumption/relaxation parameters of the smaller-sized phase that dominate in (2.54b); intuitively, the influence of the smaller-sized phase on the concentration difference is greater than the influence on the volume-element averaged concentration. Consider, for instance, the case in which $v_{\text{is}} \ll v_{\text{ic}}$ and the two phases are initially void of tracer. If a given quantity of tracer is delivered to the smaller-sized interstitial compartment, we may assume that $\langle\psi_{\text{is}}\rangle^{\text{is}} \gg \langle\psi_{\text{ic}}\rangle^{\text{ic}}$ at not too long times after delivery, and for this case Eq. (2.54b) gives $\tau_{\text{isic}} \approx [R_{\text{is}} + 1/\tau_{\text{is}}]^{-1}$. This result is physically reasonable, for when $v_{\text{is}} \ll v_{\text{ic}}$ the intracellular concentration rises slowly, and hence the rate at which the large initial concentration difference diminishes is determined by the rate of interstitial-to-intracellular transfer and by consumption/relaxation in the interstitial phase.

When the transport of tracer molecules is not adequately described by ideal well-mixed conditions, diffusive transport must be taken into account and changes in the concentration difference ψ_δ take longer. Hence, it is reasonable to assume that the characteristic time, τ_δ, for changes in ψ_δ satisfies

$$\tau_\delta \gg \tau_\delta|_{\text{well-mixed}} = \tau_{\text{isic}} \,, \tag{2.56g}$$

whence $\tau_{\text{isic}}/\tau_\delta \ll 1$ in the denominator of (2.55).

Combining the relationships $\ell_{\text{isic}}^2 = \|D_{\text{isic}}\|\tau_{\text{isic}}$ and $\tau_{\text{isic}} \ll \tau_\delta$, and further making use of the estimates given by (2.56b) and (2.56f), yields the following inequality chain

$$\ell_{\text{isic}}^2 \ll \ell_\delta^2 \lesssim \ell_\delta \ell_{\delta 1} \lesssim \ell_{\text{av}} \ell_{\text{av}1} \,. \tag{2.56h}$$

Thus, the first term on the right-hand side of (2.55) and the second term in the denominator of that expression are estimated, respectively, as $\ell_{\text{isic}}^2/(\ell_{\text{av}}\ell_{\text{av}1}) \ll 1$ and $\ell_{\text{isic}}^2/(\ell_\delta \ell_{\delta 1}) \ll 1$.

We may note that, for a fixed time τ_δ, the characteristic lengths associated with the same change $\Delta\psi_\delta$ under both well-mixed and not-well-mixed conditions can be assumed to satisfy

$$\ell_{\text{isic}} > \ell_\delta \,. \tag{2.56i}$$

However, in order to satisfy the inequality $\ell_{\text{isic}}^2 \ll \ell_\delta \ell_{\delta 1}$ in (2.56h), it must be that

$$\ell_\delta < \ell_{\text{isic}} \ll \ell_{\delta 1} \,, \tag{2.56j}$$

which refines the second order-of-magnitude relationship in (2.56e).

Next, we estimate the terms in the numerator of (2.55). Assuming scalar diffusivity parameters for simplicity, it is easy to establish the bounds

$$\frac{|D_{\text{is}}^{\text{eff}} - D_{\text{ic}}^{\text{eff}}|}{D_{\text{isic}}}, \; \frac{|R_{\text{is}} - R_{\text{ic}}|}{R^{\text{eff}}} \leq \max\left\{\frac{1}{v_{\text{is}}}, \frac{1}{v_{\text{ic}}}\right\} \tag{2.57a}$$

and

$$\min\left\{\frac{v_{\text{ic}}}{v_{\text{is}}}, \frac{v_{\text{is}}}{v_{\text{ic}}}\right\} \leq \frac{D^{\text{eff}}}{D_{\text{isic}}} \leq \max\left\{\frac{v_{\text{ic}}}{v_{\text{is}}}, \frac{v_{\text{is}}}{v_{\text{ic}}}\right\} \tag{2.57b}$$

by expressing the considered ratios as functions of the variable $D_{\text{ic}}/D_{\text{is}}$, say, with v_{is} treated as a parameter. For typical values of the volume fractions v_{is} and v_{ic}, the ratio in (2.57b) spans approximately two orders of magnitude. Thus, a reasonable estimate of the magnitude of the first two terms in brackets in the numerator of (2.55) is given by the geometric mean of the minimum and maximum values and is $(v_{\text{is}}v_{\text{ic}})^{-1/2}$ in both cases.

The third term in the numerator of (2.55) includes a factor $\ell_{\rm av}\ell_{\rm av1}/(\|\mathbf{D}_{\rm isic}\|\tau_\delta) \gtrsim \ell_{\rm av}\ell_{\rm av1}/\ell_\delta^2$, from (2.56b). If this term is not too large, the estimate in (2.55) finally simplifies to[27]

$$\left|\frac{\Delta\psi_\delta}{\Delta\langle\psi_{\rm ev}\rangle}\right| \sim \frac{1}{\sqrt{v_{\rm is}v_{\rm ic}}}\,\frac{\ell_{\rm isic}^2}{\ell_{\rm av}\ell_{\rm av1}}\,, \tag{2.58}$$

and this is the desired estimate for the term $\|\nabla\psi_\delta\|/\|\nabla\langle\psi_{\rm ev}\rangle\|$ in (2.48a).

Next, we estimate the term in the numerator of (2.53b). By the use of (2.56a) and (2.56f) we get $\|\mathbf{D}^{\rm eff}\|\tau_\delta/(\ell_{\rm av}\ell_{\rm av1}) \lesssim \ell_{\rm av}/\ell_{\rm av1} \lesssim 1$. Thus, the order-of-magnitude estimate in (2.53b) simplifies to

$$\left|\frac{\langle\psi_{\rm ev}\rangle}{\Delta\langle\psi_{\rm ev}\rangle}\right| \sim \frac{1}{R^{\rm eff}\tau_\delta}\,. \tag{2.59}$$

From the order-of-magnitude estimate $\psi_\delta = \mathcal{O}[\Delta\psi_\delta]$ we obtain the required estimate for the term $|\psi_\delta|/\langle\psi_{\rm ev}\rangle$ in (2.48b):

$$\frac{|\psi_\delta|}{\langle\psi_{\rm ev}\rangle} = \mathcal{O}\left[\frac{\Delta\psi_\delta}{\Delta\langle\psi_{\rm ev}\rangle}\frac{\Delta\langle\psi_{\rm ev}\rangle}{\langle\psi_{\rm ev}\rangle}\right] \sim \left|\frac{\Delta\psi_\delta}{\Delta\langle\psi_{\rm ev}\rangle}\right| R^{\rm eff}\tau_\delta\,. \tag{2.60}$$

Substituting the estimates given in (2.58) and (2.60), the constraints in (2.48a) and (2.48b) for diffusion and consumption/relaxation processes near to exchange equilibrium can be recast as

$$\frac{\|\mathbf{D}_{\rm is}^{\rm eff} - \mathbf{D}_{\rm ic}^{\rm eff}\|}{\|\mathbf{D}^{\rm eff}\|}\,\frac{\sqrt{v_{\rm is}v_{\rm ic}}\,\ell_{\rm isic}^2}{\ell_{\rm av}\ell_{\rm av1}} \ll 1\,, \tag{2.61a}$$

$$|R_{\rm is} - R_{\rm ic}|\tau_\delta\,\frac{\sqrt{v_{\rm is}v_{\rm ic}}\,\ell_{\rm isic}^2}{\ell_{\rm av}\ell_{\rm av1}} \ll 1\,, \tag{2.61b}$$

where the various characteristic lengths are defined following Eqs (2.52a), (2.52b) and (2.54b). The constraints are below.

When $\|\mathbf{D}_{\rm is}^{\rm eff}\|$ and $\|\mathbf{D}_{\rm ic}^{\rm eff}\|$ are comparable, as is likely the case in biological tissues, the constraint given by (2.61a) is likely satisfied on account of the estimate (2.56h).

To gain some insight into the order of magnitude of the left-hand side of (2.61b) we refer to a simulation study by Strijkers *et al.* [158] which examined dependence

[27] It is easily checked with the use of (2.54b) that the right-hand side of (2.58) remains finite when $v_\nu \to 0$.

of the longitudinal relaxation rate of extravascular water on concentration of an intracellular Gd-based tracer. In this study extracellular, cytoplasmic and vesicular compartments were considered, and the simulations showed [158, Fig. 3g, h] that water exchange, both interstitial–cytoplasmic and cytoplasmic–vesicular, would occur in a fast (respectively, slow) regime for concentrations of paramagnetic tracer below (respectively, above) a small range of concentration values dependent upon cytoplasmic/vesicular compartmentalisation of the tracer.[28]

Fast (respectively, slow) chemical exchange implies that the inversion-recovery time course is accurately described by a monoexponential (respectively, biexponential) curve with apparent relaxation and compartment fraction parameters. Specifically, under fast interstitial–intracellular exchange the relaxation rate is equal to the volume-weighted average of the interstitial and intracellular relaxation rates [89], as given by Eq. (2.45c). Fast interstitial–intracellular exchange occurs when (p. 56)

$$|R_{\mathrm{is}} - R_{\mathrm{ic}}| \ll \frac{1}{\tau_{\mathrm{is}}} + \frac{1}{\tau_{\mathrm{ic}}} \tag{2.62}$$

and it is seen with the use of (2.54a) that $|R_{\mathrm{is}} - R_{\mathrm{ic}}|\tau_{\mathrm{isic}} \ll 1$, but from this it cannot be inferred that $|R_{\mathrm{is}} - R_{\mathrm{ic}}|\tau_{\delta} \ll 1$ since $\tau_{\mathrm{isic}} \ll \tau_{\delta}$, as given by (2.56g). However, if the characteristic time for transient changes in ψ_{δ} is conservatively estimated as $\tau_{\delta} \lesssim 1$ s, the simulation data of Strijkers *et al.* [158] suggests that the constraint (2.61b) might be reasonably well satisfied for typical ASL experiments.

It is appropriate to discuss the above results for extravascular transport and exchange across weakly permeable membrane permeabilities in the light of the Kärger model introduced in Chapter 1 (p. 11). According to this model, the DWI signal can

[28] Model input parameters from Table 1 (Calculation 1) of Ref. [158]: interstitial, cytoplasmic and vesicular volume fractions: 0.5, 0.479 and 0.021, respectively; longitudinal relaxation rate in the absence of exchange: 0.5 s^{-1} in the interstitial and vesicular compartments and 0.4 s^{-1} in the cytoplasmic compartment; diffusive membrane permeability coefficient for water, 10×10^{-3} $\mu\mathrm{m\,ms}^{-1}$. The selected value of interstitial volume fraction is significantly higher than in brain and myocardial tissue; cf. Refs [70, 110]. The selected diffusive permeability to water of generic parenchymal cells is approximately an order of magnitude higher than that for capillary endothelial cells in brain and myocardium; cf. Table 2.1 in this Thesis.

be expressed as a phase-volume weighted sum of decaying exponentials [48, p. 142]. Fieremans *et al.* [49] have shown the Kärger model to be accurate for the case of poorly permeable cell membranes at long measurement times; the effective diffusion coefficient predicted is of the form (2.45b) and is time dependent, cf. Ref. [49, Eq. (13)] and references therein. We note that for weakly permeable membranes a relatively long measurement time is needed for the intrinsic phased-averaged concentrations to reach their equilibrium value.

Specifically, for the case of a random in-plane packing of parallel permeable cylinders investigated by Fieremans *et al.* [49], the long-time effective diffusion coefficient for the Kärger model is given by $v_{\mathrm{is}}D_{\mathrm{is}}(t\to\infty)+v_{\mathrm{iv}}D_{\mathrm{iv}}(t\to\infty)$, where the long-time diffusion coefficients are smaller than those at time zero by a factor dependent upon the respective tortuosity and the orientation angle with respect to cylinder axis, consistent with the intrinsic conductivity parameter in (2.39b). Thus, in the range of validity of the Kärger model the predicted effective diffusion coefficient is of the same form as Eq. (2.45b) above.

Based on the foregoing developments, we hypothesise that for ASL experiments in brain and myocardial tissue, the intrinsic average interstitial and intracellular concentrations likely satisfy nearly-equilibrium conditions on a mesoscopic scale, i.e., $\langle\psi_{\mathrm{ev}}\rangle \approx \langle\psi_{\mathrm{is}}\rangle^{\mathrm{is}} \approx \langle\psi_{\mathrm{ic}}\rangle^{\mathrm{ic}}$ (see p. 63) for moderate parenchymal cell membrane permeabilities. Thus, Eq. (2.45a) is expected to describe diffusion–consumption in the extravascular space of these tissues in terms of the average concentration $\langle\psi_{\mathrm{ev}}\rangle$. This equation is formally identical with the governing equation (2.1b) of the blood–tissue exchange model (Section 2.2.1).

Case 3 *Highly permeable parenchymal cell membranes*

For highly permeable parenchymal cell membranes, one may intuitively expect that the extravascular space can, on a mesoscopic scale, be regarded as a single interstitial–intracellular 'phase', albeit one consisting of distinct regions with microscopic diffusion coefficients D_{is} and D_{ic}, and relaxation/consumption rates R_{is} and

R_{ic}. Let $\psi_{\mathrm{ev}}(\mathbf{r},t)$ and $\mathbf{j}_D(\mathbf{r},t)$ denote the microscopic concentration and flux at a given point and time.

The average extravascular concentration is evaluated from (2.31g) and (2.31e) as

$$\begin{aligned}\left\langle \frac{\partial \psi_{\mathrm{ev}}}{\partial t} \right\rangle &= \frac{\partial \langle \psi_{\mathrm{is}} \rangle}{\partial t} + \frac{\partial \langle \psi_{\mathrm{ic}} \rangle}{\partial t} - \frac{1}{\Delta V} \int_\sigma [\psi_{\mathrm{is}} - \psi_{\mathrm{ic}}]\, \mathbf{u}_\sigma \cdot \mathbf{n}_{\mathrm{is}}\, \mathrm{d}\sigma \\ &= \frac{\partial \langle \psi_{\mathrm{is}} \rangle}{\partial t} + \frac{\partial \langle \psi_{\mathrm{ic}} \rangle}{\partial t} \\ &= \frac{\partial \langle \psi_{\mathrm{ev}} \rangle}{\partial t}\,. \end{aligned} \tag{2.63}$$

The integral vanishes because the difference in microscopic concentration at each face of a highly permeable membrane is very small. The spatial average of $\partial \psi_{\mathrm{ev}}/\partial t$ is equal to minus the spatially averaged divergence of the microscopic diffusive flux, which is evaluated with the use of (2.31i) as

$$\langle \nabla \cdot \mathbf{j}_D \rangle = \nabla \cdot \langle \mathbf{j}_{D\mathrm{is}} \rangle + \nabla \cdot \langle \mathbf{j}_{D\mathrm{ic}} \rangle + \frac{1}{\Delta V} \int_\sigma [\, \mathbf{j}_{D\mathrm{is}} - \mathbf{j}_{D\mathrm{ic}}\,] \cdot \mathbf{n}_{\mathrm{is}}\, \mathrm{d}\sigma \tag{2.64a}$$

and the integral vanishes since the interfacial flux is continuous at the σ-boundary. Further development of the right-hand side of the above equation using the last line of (2.38b) gives

$$\begin{aligned} -\langle \nabla \cdot \mathbf{j}_D \rangle = \nabla \cdot \Bigg\{ & v_{\mathrm{is}} D_{\mathrm{is}} \left[\nabla_{\mathbf{r}} \langle \psi_{\mathrm{is}} \rangle^{\mathrm{is}} + \frac{1}{\Delta V_{\mathrm{is}}} \int_\sigma \widetilde{\psi}_{\mathrm{is}} \mathbf{n}_{\mathrm{is}}\, \mathrm{d}\sigma \right] \\ & + v_{\mathrm{ic}} D_{\mathrm{ic}} \left[\nabla_{\mathbf{r}} \langle \psi_{\mathrm{ic}} \rangle^{\mathrm{ic}} - \frac{1}{\Delta V_{\mathrm{ic}}} \int_\sigma \widetilde{\psi}_{\mathrm{ic}} \mathbf{n}_{\mathrm{is}}\, \mathrm{d}\sigma \right] \Bigg\}. \end{aligned} \tag{2.64b}$$

For the case of highly permeable membranes, a nearly-equilibrium situation implies that spatial deviation concentrations at cell membranes are very nearly equal, $\widetilde{\psi}_{\mathrm{is}}|_\sigma \approx \widetilde{\psi}_{\mathrm{ic}}|_\sigma$. Thus, the above equation simplifies to

$$-\langle \nabla \cdot \mathbf{j}_D \rangle = \nabla \cdot \left\{ (v_{\mathrm{is}} D_{\mathrm{is}} + v_{\mathrm{ic}} D_{\mathrm{ic}})\, \nabla_{\mathbf{r}} \langle \psi_{\mathrm{ev}} \rangle + \frac{D_{\mathrm{is}} - D_{\mathrm{ic}}}{\Delta V} \int_\sigma \widetilde{\psi}_{\mathrm{is}} \mathbf{n}_{\mathrm{is}}\, \mathrm{d}\sigma \right\} \tag{2.64c}$$

and the last term may be assumed small since it is the average of a fluctuation [148, pp. 823 – 824]. Thus,

$$-\langle \nabla \cdot \mathbf{j}_D \rangle \approx (v_{\mathrm{is}} D_{\mathrm{is}} + v_{\mathrm{ic}} D_{\mathrm{ic}})\, \nabla^2 \langle \psi_{\mathrm{ev}} \rangle\,, \tag{2.64d}$$

i.e., the effective diffusion tensor $\mathbf{D}^{\text{eff}}$ reduces to a scalar and is equal to the volume-weighted sum of the microscopic interstitial and intracellular diffusion coefficients. Unlike the case of two phases exchanging through weakly permeable membranes, for highly permeable membranes the effective intrinsic conductivity parameter (73) is unity.

In addition, for highly-permeable membranes with fast interstitial–intracellular exchange, the net consumption/relaxation rate is given by the volume-weighted average of the interstitial and intracellular consumption/relaxation rates [89]. Thus,

$$\frac{\partial\langle\psi_{\text{ev}}\rangle}{\partial t} = (v_{\text{is}}D_{\text{is}} + v_{\text{ic}}D_{\text{ic}})\,\nabla^2\langle\psi_{\text{ev}}\rangle - (v_{\text{is}}R_{\text{is}} + v_{\text{ic}}R_{\text{ic}})\,\langle\psi_{\text{ev}}\rangle\,. \tag{2.65}$$

For highly permeable membranes, the characteristic time τ_δ for a given change in concentration difference ψ_δ and the characteristic time τ_{isic} for well-mixed conditions, given by Eq. (2.54a), are both expected to decrease, whereas the characteristic lengths, ℓ_{av} and ℓ_{av1}, for changes in, respectively, the amplitude and gradient of the spatially averaged concentration $\langle\psi_{\text{ev}}\rangle$, are expected to increase. Thus, the constraints given by (2.61a) and (2.61b) remain valid for the case of highly permeable membranes.

Diffusive permeation flux

Tracer transport across a biological membrane is often characterised in terms of the solute permeability of the membrane, as given by the experimentally determined ratio of transmembrane flux to tracer concentration difference across the membrane; cf., for instance, Refs [60, Eq. (A7)], [148, Eq. (26)] and [154, Section 2.1.2, Eq. (2.19)]. Equation (2.1c) also is of this type; both this equation and the permeation term in (2.1a) are discussed in this Section.

We consider a highly simplified model of the capillary wall that furnishes an estimate of the permeability due to exceedingly narrow pores like fenestrae and interendothelial clefts, which together allow for passive diffusion of gases, water, small hydrophylic molecules and many lipid-soluble solutes (Refs [1, p. 830] and [63]). The pore width is of the order of 10 nm (our own estimate from [1, Fig. 7.30] for intestinal epithelium and [159, Fig. 21] for mouse brain) and defines the microscopic scale.

While in, e.g., brain tissue pore widths are comparable to, but apparently not greater than, the thickness of the interstitial fluid layer (cf. Refs [70, Fig. 1] and [159, Fig. 21]), the total pore volume appears to be much less than the volume of the interstitial space adjacent to the capillary wall. Thus, if the concentration of tracer in the compartments adjacent to the membrane changes slowly, nearly steady-state diffusion inside the pores can be assumed, leading to a uniform microscopic transcapillary flux.

Solving the steady-state one-dimensional diffusion equation shows that the intrapore diffusive flux will be proportional to the concentration difference across the membrane, the appropriate partition coefficient,[29] the diffusion coefficient for tracer molecules in the pores and the reciprocal membrane thickness (see, e.g., Ref. [143, pp. 142 – 145] and the careful discussion given by Friedman in Ref. [154, Sections 2.1.1 and 2.1.2]). The partition coefficient, tracer diffusion coefficient and membrane thickness can be combined into a single pore permeability coefficient, κ_{p}. Thus, the microscopic transcapillary flux is expressed as

$$\mathbf{n}_{\mathrm{p}}\mathbf{j}_{\kappa}|_{\mathrm{microscopic}} = \kappa_{\mathrm{p}}\left[\psi_{\mathrm{iv}}(\mathbf{a}_{\mathrm{p}-}, t) - \psi_{\mathrm{is}}(\mathbf{a}_{\mathrm{p}+}, t)\right] \tag{2.66}$$

inside a pore, and is zero at non-pore locations; $\mathbf{a}_{\mathrm{p}-}$, $\mathbf{a}_{\mathrm{p}+}$ denote pore openings at the luminal and abluminal face, respectively (Fig. 2.9), and the unit vector $\mathbf{n}_{\mathrm{p}}$ is directed from the luminal to the abluminal face.

Since there is a thin plasma layer (respectively, interstitial fluid bath) between the erythrocytes (respectively, parenchymal cells) and the capillary wall (see, e.g., Refs [1, Fig. 38.11] and [108, Fig. 5]), we expect the microscopic concentration of tracer at each face of the capillary wall to vary continuously, as determined by the time course of capillary flow and the distribution of pores on the capillary surface.

In the capillary-wall model described above, the microscopic transcapillary flux is not continuous due to the discrete distribution of pores. On the other hand, the

[29] The partition coefficient is defined as the ratio of the concentration of tracer in oil to that in water. Specifically, it is the ratio of the concentration inside the lipid bilayer of a biological membrane and that in the exterior aqueous environment (Refs [3, p. 19] and [143, pp. 144 – 145]).

mesoscopic flux is expected to vary smoothly over capillary-wall volume elements containing sufficiently many pores (Fig. 2.9) provided that the molecules of tracer do not to stagnate in the endothelial cells. Integrating (2.66) over the abluminal face of this volume element with the use of the mean value theorem for integrals gives the capillary boundary condition on a mesoscopic scale as

$$\begin{aligned}\mathbf{n}\mathbf{j}_\kappa|_{\text{mesoscopic}} &= \frac{1}{\Delta S_\text{m}} \int_{\Delta S_\text{m}} \kappa_\text{p} \left[\psi_\text{iv}(\mathbf{a}_{\text{p}-}, t) - \psi_\text{is}(\mathbf{a}_{\text{p}+}, t)\right] \mathrm{d}S_\text{m} \\ &= \kappa \left[\langle\psi_\text{iv}\rangle^\text{iv}(\mathbf{a}_-, t) - \langle\psi_\text{is}\rangle^\text{is}(\mathbf{a}_+, t)\right], \end{aligned} \tag{2.67a}$$

where $\langle\psi_\text{iv}\rangle^\text{iv}(\mathbf{a}_-, t)$ and $\langle\psi_\text{is}\rangle^\text{is}(\mathbf{a}_+, t)$ denote the intrinsic surface-averaged concentration of tracer over, respectively, the luminal and abluminal face, ΔS_m, of the volume element with centroid position $\mathbf{a}$ (Fig. 2.9), and κ is the mesoscopic capillary wall permeability,

$$\begin{aligned}\kappa &\sim \frac{\Delta S_\text{p}}{\Delta S_\text{m}} \kappa_\text{p} \\ &\sim \text{pore void fraction} \times \text{average pore permeability}, \end{aligned} \tag{2.67b}$$

where ΔS_p is the total pore area in the considered volume element. This order-of-magnitude estimate is obtained by using the decomposition given by (2.31f) that gives

$$\begin{aligned}\mathbf{n}\mathbf{j}_\kappa|_{\text{mesoscopic}} = {} & \frac{\kappa_\text{p}\Delta S_\text{p}}{\Delta S_\text{m}} \left[\langle\psi_\text{iv}\rangle^\text{iv}(\mathbf{a}_-, t) - \langle\psi_\text{is}\rangle^\text{is}(\mathbf{a}_+, t)\right] \\ & + \frac{1}{\Delta S_\text{m}} \int_{\Delta S_\text{m}} \kappa_\text{p} \left[\widetilde{\psi}_\text{iv}(\mathbf{a}_{\text{p}_-}, t) - \widetilde{\psi}_\text{is}(\mathbf{a}_{\text{p}+}, t)\right] \mathrm{d}S_\text{m}. \end{aligned} \tag{2.68}$$

The integral in the above equation gives the difference between the intrinsic surface-averaged spatial deviation for the capillary-wall pore concentration at each face of the capillary wall. If these two averages can be assumed equal to the respective intrinsic volume averages (p. 80), then they are equal to zero from Eq. (2.31f).

Equation (2.67a) is formally analogous to the second line of Eq. (2.1c) in the main body of the text. In order to complete the mesoscopic form of this boundary condition, the average over the capillary surface of the quantity $D_\text{is}\nabla\psi_\text{is}(\mathbf{a}_+, t)$ is required. To that end, we define a generic volume element adjacent to the abluminal capillary

surface and follow an argument analogous to that leading to the mesoscopic form (2.39a) of Fick's law. However, the intrinsic conductivities of such a volume element and another consisting of only interstitial and intracellular phases will, in general, differ. While this may have a bearing for the correct interpretation of estimated permeabilities, it poses no difficulty for the theoretical evaluation of blood–tissue tracer exchange quantities (see Chapter 3) and can be circumvented by absorbing into the mesoscopic capillary wall permeability parameter a scalar term equal to the ratio of intrinsic conductivities for interstitial–intracellular and interstitial–transcapillary volume elements. With this convention, the mesoscopic transcapillary permeation flux in terms of the gradient of the extravascular concentration at the capillary wall is given by the first line of Eq. (2.1c), where the diffusion coefficient is the same as enters in the diffusion–consumption equation (2.1b).

Next, we evaluate the divergence of the microscopic diffusive permeation flux through a capillary-wall pore of volume δV_p and uniform cross-section δS_p. Since the pore width is much smaller than the capillary wall thickness,

$$\begin{aligned} \nabla \cdot \mathbf{j}_\kappa &\approx \frac{\delta S_\mathrm{p}}{\delta V_\mathrm{p}} \, \mathbf{n}_\mathrm{p} \mathbf{j}_\kappa \\ &= \frac{\delta S_\mathrm{p}}{\delta V_\mathrm{p}} \, \kappa_\mathrm{p} \left[\psi_\mathrm{iv}(\mathbf{a}_{\mathrm{p}-}, t) - \psi_\mathrm{is}(\mathbf{a}_{\mathrm{p}+}, t) \right] \end{aligned} \tag{2.69a}$$

and is zero at non-pore locations; the flux into the endothelial cytoplasm is taken to be zero.

In order correctly to evaluate tracer mass balance in intracapillary space, the volume average of the divergence of the blood-to-tissue flux (2.69a) must be taken over a volume element of size ΔV which includes both the capillary lumen and the capillary wall; the capillary wall thickness is taken into account for now and in the considered volume element the capillary wall has a volume ΔV_m. However, the form of (2.69a) indicates that the integral required for evaluation of $\langle \nabla \cdot \mathbf{j}_\kappa \rangle$ is non-zero over only the capillary wall volume. Thus, the volume averaged form of $\nabla \cdot \mathbf{j}_\kappa$ is

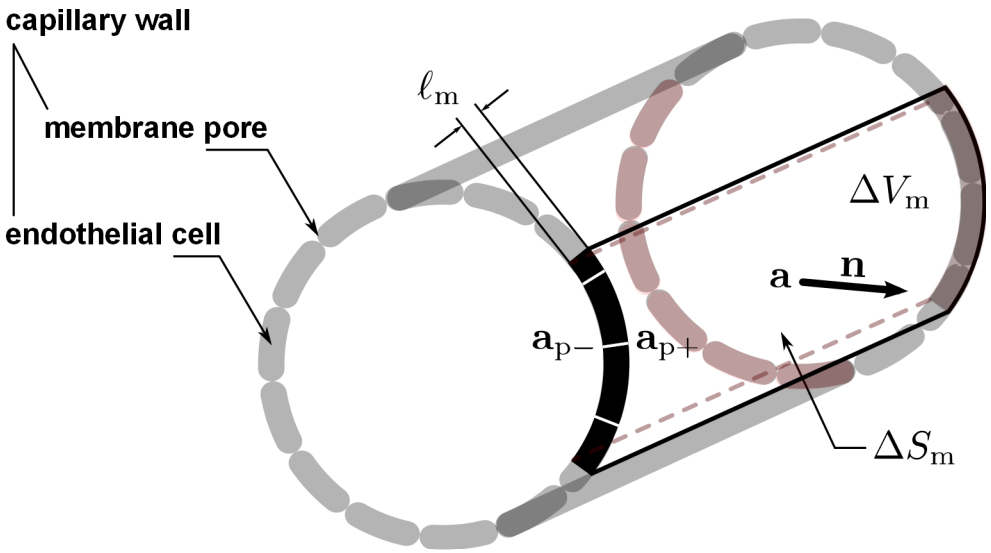

Figure 2.9: **Volume element for evaluation of transcapillary permeation.**

evaluated as

$$\begin{aligned}
\langle \nabla \cdot \mathbf{j}_\kappa \rangle &= \frac{1}{\Delta V} \int_{\Delta V_\mathrm{m}} \nabla \cdot \mathbf{j}_\kappa \, \mathrm{d}V_\mathrm{m} \\
&\approx \frac{1}{\Delta V} \int_{\Delta V_\mathrm{m}} \frac{\delta S_\mathrm{p}}{\delta V_\mathrm{p}} \, \mathbf{n}_\mathrm{p} \mathbf{j}_\kappa \, \mathrm{d}V_\mathrm{m} \\
&\approx \frac{1}{\Delta V} \int_{\Delta S_\mathrm{m}} \frac{\ell_\mathrm{m} \delta S_\mathrm{p}}{\delta V_\mathrm{p}} \, \mathbf{n}_\mathrm{p} \mathbf{j}_\kappa \, \mathrm{d}S_\mathrm{m} \\
&= \frac{\Delta S_\mathrm{m}}{\Delta V} \, \mathbf{n} \mathbf{j}_\kappa |_\mathrm{mesoscopic} \\
&\approx \frac{\kappa \Delta S_\mathrm{m}}{\Delta V} \left[\langle \psi_\mathrm{iv} \rangle^\mathrm{iv}(\mathbf{a}_-, t) - \langle \psi_\mathrm{is} \rangle^\mathrm{is}(\mathbf{a}_+, t) \right] ,
\end{aligned} \tag{2.69b}$$

where Eqs (2.67a) and (2.69a) have been used, and $\delta V_\mathrm{p} = \ell_\mathrm{m} \delta S_\mathrm{p}$ is the volume of a pore. If the capillary wall thickness is much smaller than the capillary radius,[30] $\Delta V_\mathrm{m} \ll \Delta V$ and (2.69b) simplifies to

$$\langle \nabla \cdot \mathbf{j}_\kappa \rangle \approx v_\mathrm{iv} \frac{\langle \psi_\mathrm{iv} \rangle^\mathrm{iv}(\mathbf{a}_-, t) - \langle \psi_\mathrm{is} \rangle^\mathrm{is}(\mathbf{a}_+, t)}{\tau_\mathrm{iv}} \tag{2.70a}$$

where, here, $v_\nu \mapsto v_\mathrm{iv}$ is the tracer-accessible intracapillary volume per volume ele-

[30] Because the thickness of the endothelial layer varies from about 0.5 μm at interendothelial clefts to about 1 μm at the nucleus [63], a negligibly thin capillary wall is only an approximation.

ment[31] and

$$\tau_{\mathrm{iv}} = \frac{v_{\mathrm{iv}}\Delta V}{\kappa \Delta S_{\mathrm{m}}} = \frac{\Delta V_{\mathrm{iv}}}{\kappa \Delta S_{\mathrm{m}}}\,, \tag{2.70b}$$

where the numerator is equal to the fraction of the considered volume element that is accessible to tracer; see Eq. (2.31c), has been used. For cylindrical capillary segments, Eq. (2.70b) becomes Eq. (2.70b) in the main text.

Upon dividing both sides of (2.70a) by v_{iv} we obtain the term due to transcapillary exchange that appears in Eq. (2.1a).

Mesoscopic blood–tissue exchange equations: a summary

In this Thesis we consider the case in which tracer exchange between plasma and erythrocytes is either negligible or else occurs very fast (as for, respectively, Gd-based tracers and magnetically tagged water) relative to exchange between the intracapillary and extravascular spaces. Then the mesoscopic tracer-balance equation taking account of intracapillary convection, diffusive transcapillary permeation and first-order consumption of tracer is obtained from Eqs (2.36) and (2.70a) as

$$\frac{\partial \langle \psi_{\mathrm{iv}} \rangle^{\mathrm{iv}}}{\partial t} = -\langle u_{z,\mathrm{iv}} \rangle^{\mathrm{iv}} \frac{\partial \langle \psi_{\mathrm{iv}} \rangle^{\mathrm{iv}}}{\partial z} - \frac{\langle \psi_{\mathrm{iv}} \rangle^{\mathrm{iv}}(\mathbf{a}_-, t) - \langle \psi_{\mathrm{ev}} \rangle^{\mathrm{ev}}(\mathbf{a}_+, t)}{\tau_{\mathrm{iv}}} - R_{\mathrm{is}} \langle \psi_{\mathrm{iv}} \rangle^{\mathrm{iv}}\,, \tag{2.71}$$

where $\langle \psi_{\mathrm{iv}} \rangle^{\mathrm{iv}}$ and $\langle u_{z,\mathrm{iv}} \rangle^{\mathrm{iv}}$ are the intrinsic phase-averaged concentration and fluid velocity, respectively, over the region of intracapillary space, i.e., plasma or whole blood, which is accessible to tracer; cf. Eq. (2.31b). Under the above-mentioned exchange conditions, the consumption/relaxation term is correctly given by the last term of (2.71).

For extravascular extracellular tracers, the mesoscopic tracer-balance equation taking into account diffusion and consumption/relaxation of tracer in extravascular space is given by Eq. (2.42a) and is repeated here for convenience:

$$\frac{\partial \langle \psi_{\mathrm{is}} \rangle^{\mathrm{is}}}{\partial t} = \nabla \cdot \mathbf{D}_{\mathrm{is}}^{\mathrm{eff}} \nabla \langle \psi_{\mathrm{is}} \rangle^{\mathrm{is}} - R_{\mathrm{is}} \langle \psi_{\mathrm{is}} \rangle^{\mathrm{is}} \tag{2.72a}$$

[31] See footnote 4 on p. 28.

with the boundary condition (2.67a):

$$\mathbf{n}\mathbf{j}_\kappa|_{\text{mesoscopic}} = \kappa\left[\langle\psi_{\text{iv}}\rangle^{\text{iv}}(\mathbf{a}_-,t) - \langle\psi_{\text{is}}\rangle^{\text{is}}(\mathbf{a}_+,t)\right]. \tag{2.72b}$$

Here, $\langle\psi_{\text{is}}\rangle^{\text{is}}$ is the intrinsic phase-averaged concentration over interstitial space and the diffusion tensor $\mathbf{D}_{\text{is}}$ reflects, on a mesoscopic scale, the microscopic tortuosity of interstitial space; see Eq. (2.39b).

On the other hand, for tracers which are able to cross the parenchymal cell membrane, transmembrane exchange, diffusive transport and first-order consumption in interstitial and intracellular space may not in all cases be described by a single tracer-balance equation. However, on a time scale such that nearly-equilibrium conditions exist, i.e., when the intrinsic phase-averaged concentrations $\langle\psi_{\text{is}}\rangle^{\text{is}}$ and $\langle\psi_{\text{ic}}\rangle^{\text{ic}}$ are both very nearly equal to the spatially averaged concentration, $\langle\psi_{\text{ev}}\rangle$ [see Eq. (2.44)], such a unified description is indeed possible. The constraints given by (2.61a) and (2.61b) are indicative of nearly-equilibrium conditions for diffusive transport with first-order consumption/relaxation. The mesoscopic tracer-balance equation is then given by

$$\frac{\partial\langle\psi_{\text{ev}}\rangle}{\partial t} = \nabla\cdot\mathbf{D}^{\text{eff}}\,\nabla\langle\psi_{\text{ev}}\rangle - R^{\text{eff}}\langle\psi_{\text{ev}}\rangle \tag{2.73a}$$

with the boundary condition

$$\mathbf{n}\mathbf{j}_\kappa|_{\text{mesoscopic}} = \kappa\left[\langle\psi_{\text{iv}}\rangle^{\text{iv}}(\mathbf{a}_-,t) - \langle\psi_{\text{ev}}\rangle(\mathbf{a}_+,t)\right]. \tag{2.73b}$$

For this kind of tracer, the effective diffusion tensor, $\mathbf{D}^{\text{eff}}$, is the volume-weighted sum of the effective interstitial and intracellular diffusion tensors; it is given by Eqs (2.45b) and (2.65) for the case of, respectively, weakly permeable and highly permeable membranes. Intracellular transport and exchange between the cytoplasm and various cell organelles could be incorporated, in principle, by following a line of analysis similar to that set forth in this Appendix, however this is outwith the scope of this Thesis.

We conclude this summary with a remark on notation. In the main body of this Thesis, all mesoscopic quantities shall be written without angle brackets, for simplicity. Thus, $\langle u_{z,\text{iv}}\rangle^{\text{iv}} \mapsto u_z$ and $\langle\psi_\nu(\mathbf{r},t)\rangle^\nu \mapsto \psi_\nu(\mathbf{r},t)$. No confusion should arise

with an identical notation for microscopic concentration in the ν-phase [cf., e.g., the integrand of Eq. (2.31a)] which is used in this Appendix only. Also, the mesoscopic extravascular diffusion coefficient shall be denoted simply by D_{ev} instead of $\mathbf{D}_{\mathrm{ev}}^{\mathrm{eff}}$.

2.5.2 Physiologic parameter values

Capillary wall permeabilities to water

In PET experiments Herscovitch and co-workers [160] determined the average global capillary-permeability surface-area product for $H_2^{15}O$ in the human brain as $PS = 1.04\ \mathrm{ml\,min^{-1}\,g^{-1}}$, ranging between $0.78 - 1.52\ \mathrm{ml\,min^{-1}\,g^{-1}}$ for white matter and the central cortex, respectively. Eichling *et al.* [161] obtained $PS = 0.023\ \mathrm{cm^3\,s^{-1}\,g^{-1}}$ $(= 1.4\ \mathrm{ml\,min^{-1}\,g^{-1}})$ in the brain of adult Rhesus monkeys using the same radiotracer. We have estimated the mean intracapillary residence time and the permeability to water of cortical brain capillaries from the relation $2\kappa/a \approx 1/\tau_{\mathrm{iv}} \equiv PS/v_{\mathrm{iv}}$ with the capillary radius parameter a given in Table 2.1 and $PS = 1.5\ \mathrm{min^{-1}}$. The resultant permeability estimate $\kappa = 1.7 \times 10^{-3}\ \mu\mathrm{m\,ms^{-1}}$ (Table 2.1) is in good agreement with the value $\kappa \leq 1.5 \times 10^{-4}\ \mathrm{cm\,s^{-1}}$ for normal rodent and canine brain, obtained by Neuder *et al.* [162].

Wacker *et al.* [134] estimated both the myocardial intracapillary volume ($v_{\mathrm{iv}} = 12.9\%$) and the intracapillary–extravascular water exchange frequency ($f = 0.48\ \mathrm{s^{-1}}$, and equivalent to PS) in subjects with coronary artery disease. The authors fitted a model of Bauer *et al.* [131] to their measurements of longitudinal relaxation rates in blood and myocardium at 1.5 T using an intravascular paramagnetic tracer. Then from these estimates and from the value of capillary diameter given in Table 2.1 we obtain $\kappa = aPS/2v_{\mathrm{iv}} = 5.2 \times 10^{-3}\ \mu\mathrm{m\,ms^{-1}}$ (Table 2.1), which is comparable to the value $6 \times 10^{-3}\ \mu\mathrm{m\,ms^{-1}}$ for tritiated water obtained by Rose *et al.* [163].

Tracer diffusion coefficients

The apparent diffusion coefficient of water in the human brain cortex is taken to be $D_{\mathrm{ev}} = 0.8\ \mu\mathrm{m^2\,ms^{-1}}$ [94]. In rat myocardium, Seland *et al.* determined a pair of values

of the water diffusion coefficient, i.e., 1.2 μm^2 ms^{-1} and 3.0 μm^2 ms^{-1}, each originating from a distinct intracellular compartment; the authors employed a pulse sequence that allowed for combined diffusion and transverse relaxation measurements. Garrido *et al.* [135] obtained 1.8 μm^2 ms^{-1} and 2.5 μm^2 ms^{-1} when the applied diffusion gradients were, respectively, perpendicular, or parallel to, the epicardial surface.

Gordon *et al.* [164] estimated the diffusion coefficient of Gd-DTPA through 10% polyvinyl alcohol-cryogel, a close tissue mimic, to be $D_{\mathrm{Gd}} = 0.26$ μm^2 ms^{-1}. Gillis *et al.* [165] determined by MRI methods the diffusion coefficient of Gd(DTPA)$^{2-}$ (gadopentetate dimeglumine, [166]) in both fresh and glycosaminoglycan-depleted calf cartilage as 0.184 μm^2 ms^{-1} and 0.208 μm^2 ms^{-1}, respectively. For Gd(HPDO3A) (gadoteridol) the appropriate values were 0.155 μm^2 ms^{-1} and 0.183 μm^2 ms^{-1}, respectively [165]. Using the above values, we estimate the characteristic diffusion time in myocardial and brain tissue to be of the order of, respectively, tens and hundreds of milliseconds.

Longitudinal relaxation rates

The longitudinal relaxation rates of arterial and capillary blood differ because of haematocrit dependence of longitudinal (spin–lattice) relaxation. Spees *et al.* [167] reported longitudinal relaxation rates of 0.59 s^{-1} and 0.70 s^{-1} at haematocrits of 0.30 (typical of capillaries) and 0.40 (typical of larger vessels), respectively, in *in vitro* human blood at 1.5 T. Note that the values of R_{iv} listed in Table 2.1 are for whole blood.

In the following paragraphs we estimate the difference $|R_{\mathrm{iv}} - R_{\mathrm{ev}}|$ in the absence of paramagnetic tracers in connection with the condition in (2.7b) for fast intracapillary relaxation. The case in which a paramagnetic tracer is present in the blood is discussed in Section 2.5.4 below.

Let R_{tiss} denote the apparent longitudinal relaxation rate of whole tissue. In the healthy human brain, we estimate $|R_{\mathrm{iv}} - R_{\mathrm{tiss}}|$ to be in the range 3×10^{-5} ms^{-1} (for prefrontal cortex) to 6×10^{-4} ms^{-1} (for corpus callosum and frontal white matter), using $R_{\mathrm{iv}} = 1664^{-1}$ ms^{-1} [132] and T_1 times of various brain regions reported in

Refs [133, 168], all at 3 T. For *in vivo* rat myocardium, we estimate $|R_{\mathrm{iv}} - R_{\mathrm{tiss}}| \sim 3 \times 10^{-4}$ ms^{-1} at 2 T, from measurements reported in Ref. [136].

Since in the above brain studies no paramagnetic tracers were used, and since myocardial T_1 times were baseline (pre-contrast) values, the tissue longitudinal relaxation rates were likely determined under fast chemical exchange conditions, i.e., the net rate of blood–tissue tracer exchange is expected to have been much faster than the difference between the intracapillary and extravascular relaxation rates [129]. In this case, the tissue relaxation rate is accurately expressed as a compartment average [129], i.e., $R_{\mathrm{tiss}} \approx v_{\mathrm{iv}} R_{\mathrm{iv}} + v_{\mathrm{ev}} R_{\mathrm{ev}}$, from which $|R_{\mathrm{iv}} - R_{\mathrm{tiss}}| \approx v_{\mathrm{ev}} |R_{\mathrm{iv}} - R_{\mathrm{ev}}|$. The values of R_{ev} listed in Table 2.1 are apparent tissue relaxation rates in the specified tissues.

Renal proximal tubule

A typical mammalian renal proximal tubule can be modelled as three concentric cylinders representing the luminal, epithelial and interstitial spaces, respectively. The basolateral membrane covers the outer epithelial surface [137]. Verkman and Wong [137] estimated the basolateral diffusive permeability to water in adult rabbit kidneys to be $P_{\mathrm{d}}^{\mathrm{bl}} = 2 \times 10^{-2}$ μm ms^{-1} at 37 °C, corrected for membrane surface convolutions. We then estimate the equivalent basolateral membrane permeability for a right cylindrical surface to be $\kappa = 7 \times 10^{-1}$ μm ms^{-1}, with the use of the relationship $\kappa S_{\mathrm{bl}}/V_{\mathrm{bl}} = P_{\mathrm{d}}^{\mathrm{bl}} (S/V)_{\mathrm{bl}}$, where $(S/V)_{\mathrm{bl}} = 4.1$ μm^{-1} [137] is the basolateral membrane surface-to-volume ratio, S_{bl} is the basolateral surface area and V_{bl} is epithelial volume; we estimated the ratio $S_{\mathrm{bl}}/V_{\mathrm{bl}}$ using the values $r_1 = 11$ μm and $r_2 = 22$ μm for the luminal and basolateral radius, respectively [137]. Quigley and Baum obtained a similar value for the permeability to water of juxtamedullary proximal convoluted tubules of adult rabbits; cf. Fig. 5 of Ref. [140].

2.5.3 An estimate of radial and axial diffusive fluxes

In this Appendix, we assess numerically the validity of the modelling assumption of negligible axial diffusive fluxes (Section 2.1).

At times of the order of one mean capillary-segment transit time ($t \sim \tau_{\mathrm{c}}$), the axial

diffusive flux at a point on the abluminal face of the capillary wall at the arteriolar end of the capillary can be estimated to zero-order as

$$\begin{aligned} |\mathbf{j}_{Dz}| &= -D_z \mathbf{z} \nabla_z \psi_{\mathrm{ev}}(\mathbf{a}_+, t)|_{z=0} \\ &\approx D_z \frac{\psi_{\mathrm{ev}}(\mathbf{a}_+, t)|_{z=0} - \psi_{\mathrm{ev}}(\mathbf{a}_+, t)|_{z=L}}{L} \\ &\leq D_z \frac{\psi_{\mathrm{ev}}(\mathbf{a}_+, t)|_{z=0}}{L}\,, \end{aligned} \tag{2.74a}$$

where it has been assumed that the concentration at the outflow end of the capillary segment is not higher than the concentration at its inflow end.

If t is also much smaller than the characteristic extravascular diffusion time, τ_D, in any direction normal to the capillary axis, the radial diffusive flux can be estimated as

$$|\mathbf{j}_{Dr}| = -D_r \mathbf{n} \nabla_r \psi_{\mathrm{ev}}(\mathbf{a}_+, t)|_{z=0} \geq D_r \frac{\psi_{\mathrm{ev}}(\mathbf{a}_+, t)|_{z=0}}{A}\,. \tag{2.74b}$$

Thus

$$\frac{|\mathbf{j}_{Dz}|}{|\mathbf{j}_{Dr}|} < \frac{D_z A}{D_r L}\,. \tag{2.74c}$$

Opposite inequality signs arise in (2.74a) and (2.74b) since, in the considered time frame ($0 < t \sim \tau_{\mathrm{c}}$), the intracapillary concentration has been assumed to vary almost linearly with distance along the capillary lumen, whereas the extravascular concentration has been assumed to vary non-linearly in all directions perpendicular to the capillary surface. The inequality in (2.74c) might therefore not apply at times $t \ll \tau_{\mathrm{c}}$ because the axial flux of tracer will likely exceed the estimate given by the second line of (2.74a). It might also not apply at times $t > \tau_D$ because the radial flux decreases as the diffusive steady state is approached, in which case the inequality in (2.74b) might be incorrect.

In grey matter, $|\mathbf{j}_{Dz}|/|\mathbf{j}_{Dr}| \approx A/L \sim 0.1\text{–}0.3$, assuming isotropic diffusion, i.e., that $D_z \approx D_r$. In rat ventricular myocardium, we have estimated $|\mathbf{j}_{Dz}|/|\mathbf{j}_{Dr}| \lesssim 0.2$ from the values of capillary segment length (71 – 108 μm) and tissue supply area (395 – 505 $\mu\mathrm{m}^2$) for coronary capillaries given in Ref. [169], and the myocardial diffusion

coefficients determined by Garrido *et al.* [135] (see Section 2.5.2). Thus, in the cases considered here the influence of axial diffusion on transport is expected to be relatively small.

2.5.4 Condition for fast intracapillary relaxation

In this Appendix we provide numerical examples concerning the condition in Eq. (2.7b) for fast intracapillary relaxation for the case in which a paramagnetic tracer is present in capillary blood. An intracapillary paramagnetic tracer present at high concentration in whole blood enhances the nuclear magnetic relaxation of whole blood in a way that is mediated by blood–tissue water exchange [90]. Inducing fast relaxation rates in a given tissue region by loading with paramagnetic tracers can be used for the estimation of water exchange rates [110, 130, 170].

We have estimated $(R_{\mathrm{iv}} - R_{\mathrm{ev}})\tau_{\mathrm{iv}} \sim 10-100$ in human central cortex at 3 T, for Gd-DTPA concentrations in plasma of about 4 – 32 mM. The lower concentration value is appropriate for both the early inflow and late pass phases, while the higher value is an estimate of peak plasma concentration for a single dose of tracer (0.1 mM per kg body weight), as derived by Albert *et al.* [91]. We obtained the required values of longitudinal relaxation times (for blood and tissue) and tracer relaxivity in plasma[32], respectively, from Refs [132, 133, 166].

Similarly, for human myocardium we have estimated $(R_{\mathrm{iv}} - R_{\mathrm{ev}})\tau_{\mathrm{iv}} \sim 0.5-5$ at 1.5 T, at concentrations of 0.5 – 5 mg per kg body weight of the intravascular tracer Feruglose; see Table 1 of Ref. [134].

The condition $\psi_{\mathrm{iv}}(z,t) \ll \psi_{\mathrm{ev}}^{\mathrm{abs}}(\mathbf{r},t)$ might not be satisfied if the tracer-induced shift in the Larmor frequency of whole blood falls in the pass-band of the RF excitation pulse. Typical one-sided excitation bandwidths are of the order of 10^3 Hz [13]. The shift in the Larmor frequency of blood, f_0, in a vessel aligned with the static magnetic field is given in SI units by $\Delta f_0 = \frac{1}{3} f_0 \Delta\chi$ [92], with $\Delta\chi = 0.31 \times$ [Gd-DTPA] the increase, in parts per million (ppm), in the concentration-dependent magnetic sus-

[32] The relaxivity is defined as the slope of the dependence of solvent relaxation rate with concentration of solute paramagnetic tracer [171].

ceptibility of blood, and [Gd-DTPA] the millimolar concentration of tracer in whole blood [91]. For example, at 3 T, a maximum transient Gd-DTPA concentration of 18 mM [91] will shift the proton Larmor frequency of whole blood by about 240 Hz, which may well fall in the pass-band of the excitation pulse. In this case the condition $\psi_{\mathrm{iv}}(z,t) \ll \psi_{\mathrm{ev}}(\mathbf{r},t)$ might be violated at echo times, T_{E}, such that $(R_{\mathrm{iv}} - R_{\mathrm{ev}})T_{\mathrm{E}} \lesssim 1$ [compare to relation (2.7b)].

2.5.5 Eigenfunction representations

In this Appendix, the Green's function method for the evaluation of blood–tissue tracer exchange is briefly reviewed. This method is the basis for a convenient representation of the blood–tissue exchange quantities in terms of the eigenfunctions of the Laplace operator, as developed in this Thesis.

Overview of Green's function methods

The Green's function, $G(\mathbf{r},\mathbf{r}',t)$, for whole extravascular space is the solution to the diffusion equation (2.10a) for the extravascular space, with the initial condition $G(\mathbf{r},\mathbf{r}',0) = \delta(\mathbf{r}-\mathbf{r}')$. In the present case, $G(\mathbf{r},\mathbf{r}',t)$ is identically zero in the intracapillary space and satisfies the boundary conditions (2.10b) and (2.10c). The gradient operator in the right-hand side of Eq. (2.10a) acts on the first argument of $G(\mathbf{r},\mathbf{r}',t)$.

Then the extravascular concentration for absorbing intracapillary boundary conditions is represented in terms of the Green's function as

$$\psi_{\mathrm{ev}}^{\mathrm{abs}}(\mathbf{r},t) = \int_{\mathrm{ev}} G(\mathbf{r},\mathbf{r}',t)\, \psi_{\mathrm{ev}}^{\mathrm{abs}}(\mathbf{r}',0)\, \mathrm{d}^d\mathbf{r}' \,, \tag{2.75}$$

where the integral is taken over the extravascular space. The above expression satisfies Eqs (2.10a) – (2.10d), on account of the above mentioned properties of the Green's function, and is valid for an arbitrary initial condition $\psi_{\mathrm{ev}}^{\mathrm{abs}}(\mathbf{r}',0)$.

Next we review the standard method of *eigenfunction decomposition* for constructing the Green's function for an initial- and boundary-value problem. In the

method of separation of variables, a series solution of the form

$$\sum_n f_n(\mathbf{r}) \exp(-\lambda_n t)$$

is sought. Substitution of the nth term of this series into (2.10a) yields a Sturm–Liouville eigenvalue equation (cf., for example, Refs [97, pp. 251 ff.], [99, p. 249 ff.] and [172, p. 342]) as

$$\nabla \cdot D_{\mathrm{ev}} \nabla f_n(\mathbf{r}) + \lambda_n f_n(\mathbf{r}) = 0 \tag{2.76a}$$

with

$$D_{\mathrm{ev}} \mathbf{n} \nabla f_n(\mathbf{a}_+) = \kappa f_n(\mathbf{a}_+)\,, \tag{2.76b}$$

$$D_{\mathrm{ev}} \mathbf{n} \nabla f_n(|\mathbf{r}| = A) = 0\,. \tag{2.76c}$$

The functions $f_n(\mathbf{r})$ are the eigenfunctions[33] of the Laplace operator $\nabla \cdot D_{\mathrm{ev}} \nabla$, the coefficients λ_n being the corresponding eigenvalues.[34] The eigenvalues form a non-negative increasing sequence, $0 \leq \lambda_1 < \lambda_2 < \cdots < \lambda_n < \cdots$. The first eigenvalue vanishes only in the physically trivial case of an impermeable capillary wall ($\kappa = 0$).

Because, unlike the general transcapillary flux boundary condition (2.1c), the absorbing intracapillary boundary condition (2.76b) is homogenous, the normalised eigenfunctions form a complete orthonormal eigenbasis (Ref. [99], pp. 251, 311). This means that any function of the spatial coordinate $\mathbf{r}$ which satisfies the boundary conditions, and which has piecewise continuous first and second derivatives, can be expanded in an absolutely and uniformly convergent series of the eigenfunctions (Ref. [99], pp. 251, 310 – 312). In particular, the representation of the initial condition $\psi_{\mathrm{ev}}^{\mathrm{abs}}(\mathbf{r}, 0)$ is

$$\psi_{\mathrm{ev}}^{\mathrm{abs}}(\mathbf{r}, 0) = \sum_{n=1}^{\infty} \left[\int_{\mathrm{ev}} \psi_{\mathrm{ev}}^{\mathrm{abs}}(\mathbf{r}', 0) f_n(\mathbf{r}')\, \mathrm{d}^d \mathbf{r}' \right] f_n(\mathbf{r})\,, \tag{2.77}$$

[33] We shall use real-valued eigenfunctions throughout. Where complex-valued eigenfunctions enter into the formulae, any terms of the form $f_n(\mathbf{r}) f_n(\mathbf{r}')$ are to be replaced by the product $f_n(\mathbf{r}) f_n^*(\mathbf{r}')$, where the asterisk denotes complex conjugation.

[34] There exists a one-to-one mapping between eigenvalues and eigenfunctions, except for the case of periodic boundary conditions (Ref. [99], p. 310), which are not imposed here.

where the nth term in brackets represents the projection, $\psi_n(\mathbf{r},0)$, of $\psi_{\rm ev}^{\rm abs}(\mathbf{r},0)$ onto $f_n(\mathbf{r})$. Furthermore, $\psi_{\rm ev}^{\rm abs}(\mathbf{r},t)$ is represented as (Ref. [99], pp. 268, 311)

$$\psi_{\rm ev}^{\rm abs}(\mathbf{r},t) = \sum_{n=1}^{\infty} \left[\int_{\rm ev} \psi_{\rm ev}^{\rm abs}(\mathbf{r}',0) f_n(\mathbf{r}') \, {\rm d}^d\mathbf{r}' \right] f_n(\mathbf{r}) \exp(-\lambda_n t) \, . \tag{2.78a}$$

This can be checked by direct substitution of the above expression in (2.10a) and (2.10b). The validity of this procedure relies on the uniform convergence of the series in (2.78a) with respect to both $\mathbf{r}$ and t, which allows the interchange of summation and termwise differentiation (provided that the resultant series is uniformly convergent) and of summation and integration. This property shall be used in a number of derivations in the sequel and is justified below (see, for example, pp. 193 – 194 of Ref. [173] for the standard results on series referred to in the discussion below):

- Since the series in (2.77) converges, and since $\exp(-\lambda_n t)$ is positive and decreases with n, the series in (2.78a) converges for all $\mathbf{r}$ and t, by Abel's test.

- The uniform convergence of the series in (2.78a) with respect to both $\mathbf{r}$ and t follows from the Weierstrass test, by noting that the $(m-1)$th remainder is upper bounded by a certain constant S_W for all $\mathbf{r}$ and t, i.e.,

$$\left| \sum_{n=m}^{\infty} \psi_n(\mathbf{r},0) f_n(\mathbf{r}) \exp(-\lambda_n t) \right| \leq \sum_{n=m}^{\infty} |\psi_n(\mathbf{r},0) f_n(\mathbf{r})| \leq S_W \, , \tag{2.78b}$$

  on account of the absolute convergence of the series in (2.77).

Making use of the uniform convergence, Eq. (2.77) is rearranged as

$$\psi_{\rm ev}^{\rm abs}(\mathbf{r},t) = \int_{\rm ev} \left[\sum_{n=1}^{\infty} f_n(\mathbf{r}) f_n(\mathbf{r}') \exp(-\lambda_n t) \right] \psi_{\rm ev}^{\rm abs}(\mathbf{r}',0) \, {\rm d}^d\mathbf{r}' \, . \tag{2.78c}$$

On comparison with (2.75), the expression inside the brackets in the above equation is recognised as the representation of the Green's function $G(\mathbf{r},\mathbf{r}',t)$ as a uniformly convergent series of the eigenfunctions [99]:

$$G(\mathbf{r},\mathbf{r}',t) = \sum_{n=1}^{\infty} f_n(\mathbf{r}) f_n(\mathbf{r}') \exp(-\lambda_n t) \, . \tag{2.79}$$

Note that $G(\mathbf{r}, \mathbf{r}', t)$ is symmetric with respect to interchange of its spatial arguments [99, p. 308]. It is verified by direct substitution that (2.79) satisfies equations (2.10a) through (2.10c). On putting $t = 0$ in (2.79) it is seen from (2.78c) that $G(\mathbf{r}, \mathbf{r}', t)$ satisfies the initial condition

$$G(\mathbf{r}, \mathbf{r}', 0) = \sum_{n=1}^{\infty} f_n(\mathbf{r}) f_n(\mathbf{r}') = \delta(\mathbf{r} - \mathbf{r}')\,, \tag{2.80}$$

which is the well-known representation of the Dirac delta function in terms of a discrete eigenbasis. The Green's function thus satisfies the normalisation condition:

$$\int_{\text{ev}} G(\mathbf{r}, \mathbf{r}', 0)\, \mathrm{d}^d\mathbf{r} = 1\,. \tag{2.81}$$

It follows from the preceding discussion that the superposition formula (2.75) does represent the concentration $\psi_{\text{ev}}^{\text{abs}}(\mathbf{r}, t)$. The preceding equations follow from the theory of Green's functions and Sturm–Liouville operators, and are general. The only assumption made is that the tracer diffusion coefficient is invariant with respect to time.

Series representations

In the following paragraphs we use the foregoing results to obtain the eigenfunction representation of the blood–tissue exchange quantities introduced in Chapter 2. It has been deemed convenient first to develop geometry-independent expressions; specific results for one- and two-dimensional geometries are presented in the next Chapter.

Assuming cylindrical symmetry, the Sturm–Liouville equation (2.76a) in d spatial dimensions reads

$$\frac{1}{r^{d-1}} \frac{\mathrm{d}}{\mathrm{d}r} \left(r^{d-1} \frac{\mathrm{d}f_n}{\mathrm{d}r} \right) + q_n^2 f(r) = 0\,, \qquad a < r < A\,, \tag{2.82}$$

where the *spatial eigenfrequency*, q_n, is defined by[35]

$$q_n^2 = \frac{\lambda_n}{D_{\text{ev}}}\,. \tag{2.83}$$

[35]The discrete and continuous eigenfrequencies, respectively denoted by q_n and q, should not be confused with the diffusion-weighting vector, $\mathbf{q}$, of DWI MRI, which also has units of inverse length. See, for example, Ref. [71].

The use of eigenfrequencies rather than eigenvalues is advantageous (as will be seen in Chapter 3) when passing to the continuum limit of the eigenvalue spectrum. Evaluation of (2.82) with the use of the absorbing intracapillary boundary condition and the zero-flux condition at the outer tissue boundary, gives

$$f_n''(\mathbf{a}_+) = -\left(q_n^2 + \frac{d-1}{a^2}\frac{\kappa a}{D_{\mathrm{ev}}}\right) f_n(\mathbf{a}_+)\,, \tag{2.84a}$$

$$f_n''(|\mathbf{r}| = A) = -q_n^2 f_n(|\mathbf{r}| = A)\,. \tag{2.84b}$$

Since $q_n^2 \geq 0$, the amplitude and curvature of f_n at $|\mathbf{r}| = a$ and $|\mathbf{r}| = A$ have opposite signs, hence the eigenfunctions are oscillatory in their respective neighbourhoods. The general behaviour of the eigenfunctions is discussed in detail in Refs [99], pp. 392–397, and [174].

The Rayleigh–Ritz relation expresses the eigenvalues as

$$\lambda_n = \int_S \kappa f_n^2(\mathbf{a}_+)\,\mathrm{d}S + \int_{\mathrm{ev}} \nabla f_n(\mathbf{r}) \cdot D_{\mathrm{ev}} \nabla f_n(\mathbf{r})\,\mathrm{d}^d\mathbf{r}\,. \tag{2.85a}$$

Hence, when D_{ev} is spatially invariant,

$$q_n^2 = \frac{\kappa S}{D_{\mathrm{ev}}} f_n^2(\mathbf{a}_+) + \int_{\mathrm{ev}} |\nabla f_n(\mathbf{r})|^2\,\mathrm{d}^d\mathbf{r}\,, \tag{2.85b}$$

where the $f_n(\mathbf{r})$ are normalised to have unit norm. Identity (2.85a) is obtained on multiplying both sides of the Sturm–Liouville equation (2.76b) by $f_n(\mathbf{r})$ and integrating over the extravascular space with the aid of the vector identity

$$f_n(\nabla \cdot \mathbf{u}) = \nabla \cdot (f_n \mathbf{u}) - \nabla f_n \cdot \mathbf{u}$$

(e.g., Ref. [101, p. 320]) with $\mathbf{u} = D_{\mathrm{ev}} \nabla f_n$, and making use of the Gauss theorem and the usual boundary conditions. Equation (2.85b) shows that the eigenvalues are non-negative; see also Ref. [99, p. 252].

The eigenfunction decomposition of the extravascular concentration with an absorbing intracapillary boundary condition is found by carrying out the integration in the right-hand side of Eq. (2.78c). For $\psi_{\mathrm{ev}}^{\mathrm{abs}}(\mathbf{r}, 0) = 1$ this gives

$$\psi_{\mathrm{ev}}^{\mathrm{abs}}(\mathbf{r}, t) = \sum_{n=1}^{\infty} \left[\int_S \kappa f_n(\mathbf{a}_+)\,\mathrm{d}S\right] f_n(\mathbf{r})\,\frac{\exp(-\lambda_n t)}{\lambda_n} \tag{2.86a}$$

$$= \frac{\kappa S}{D_{\mathrm{ev}}} \sum_{n=1}^{\infty} f_n(\mathbf{a}_+) f_n(\mathbf{r})\,\frac{\exp(-D_{\mathrm{ev}} t q_n^2)}{q_n^2}\,, \tag{2.86b}$$

where in the second line each eigenfunction is assumed uniform on the abluminal face of the capillary wall, $f_n(\mathbf{a}_+) = \text{const}_n$. The above equations follow from the identity

$$\begin{aligned}\lambda_n \int_{\text{ev}} f_n(\mathbf{r})\,\mathrm{d}^d\mathbf{r} &= \int_{\text{ev}} -\nabla\cdot D_{\text{ev}}\nabla f_n(\mathbf{r})\,\mathrm{d}^d\mathbf{r} \\ &= \int_S D_{\text{ev}}\mathbf{n}\nabla f_n(\mathbf{a}_+)\,\mathrm{d}S \\ &= \int_S \kappa f_n(\mathbf{a}_+)\,\mathrm{d}S\,, \end{aligned} \tag{2.87}$$

which results from integration of the Sturm–Liouville equation (2.76a) with the use of the Gauss theorem. Here, $\mathbf{n}$ is a unit normal directed outwards from the abluminal capillary surface.

Substituting (2.85b) into (2.86b), rearranging and evaluating at $\mathbf{r} = \mathbf{a}_+$, we obtain the concentration at the capillary wall, hence also the transcapillary flux (up to a factor of κ), under absorbing intracapillary boundary conditions:

$$\psi_{\text{ev}}^{\text{abs}}(\mathbf{a}_+, t) = \sum_{n=1}^{\infty}\left[1 - \frac{\int_{\text{ev}}|\nabla f_n(\mathbf{r})|^2\,\mathrm{d}^d\mathbf{r}}{q_n^2}\right]\exp(-D_{\text{ev}}tq_n^2) \tag{2.88a}$$

$$= \sum_{n=1}^{\infty}\left[1 + \frac{D_{\text{ev}}}{\kappa S}\frac{\int_{\text{ev}}|\nabla f_n(\mathbf{r})|^2\,\mathrm{d}^d\mathbf{r}}{f_n^2(\mathbf{a}_+)}\right]^{-1}\exp(-D_{\text{ev}}tq_n^2)\,. \tag{2.88b}$$

These equations comprise the effect of capillary permeability and extravascular diffusion, as well as the relative contribution of the eigenfrequencies at different diffusion times. To gain qualitative insight into the role of diffusion, we estimate the interval of eigenfrequencies that contribute most to the transcapillary flux. To estimate the nth term of (2.88b) we use the order-of-magnitude estimates

$$\begin{aligned}\|\nabla f_n\|^2 &\sim q_n^2\|f_n\|^2\,, \\ f_n^2(\mathbf{a}_+) &\sim \frac{\|f_n\|^2}{V_{\text{ev}}}\,,\end{aligned}$$

both of which are plausible for eigenfunctions of the form $\exp(\pm\mathrm{i}q_n|\mathbf{r}| + \delta_n)$ in one linear dimension, or for $|\mathbf{r}|^{-1/2}\exp(\pm\mathrm{i}q_n|\mathbf{r}| + \delta_n)$ in one radial dimension (for large $|\mathbf{r}|$). Thus,

$$\psi_{\text{ev}}^{\text{abs}}(\mathbf{a}_+, t) \sim \sum_{n=1}^{\infty}\frac{1}{1 + D_{\text{ev}}\tau_{\text{ev}}q_n^2}\exp(-D_{\text{ev}}tq_n^2)\,, \tag{2.89}$$

with the mean extravascular residence time $\tau_{\mathrm{ev}} = V_{\mathrm{ev}}/\kappa S$, from Eq. (2.2c). The main contribution to the above sum is due to eigenfrequencies

$$q_n \lesssim \min\left\{\frac{1}{\sqrt{D_{\mathrm{ev}} t}}, \frac{1}{\sqrt{D_{\mathrm{ev}}\tau_{\mathrm{ev}}}}\right\}. \tag{2.90}$$

The interval of contributing eigenfrequencies becomes narrower as the diffusion time increases, as expected. Note that the normalised 'cut-off' eigenfrequency for short diffusion times may be defined by

$$qA \sim \sqrt{\frac{1}{D_{\mathrm{ev}}\tau_{\mathrm{ev}}}} \sim \sqrt{\frac{\kappa a}{D_{\mathrm{ev}}}}\,. \tag{2.91}$$

Integrating (2.86a) and (2.86b) once more yields the spatially averaged extravascular concentration for absorbing intracapillary boundary conditions:

$$\psi_{\mathrm{ev}}^{\mathrm{abs}}(t) = \frac{1}{V_{\mathrm{ev}}}\sum_{n=1}^{\infty}\left[\int_S \kappa f_n(\mathbf{a}_+)\,\mathrm{d}S\right]^2 \frac{\exp(-\lambda_n t)}{\lambda_n^2} \tag{2.92a}$$

$$= \frac{1}{D_{\mathrm{ev}}\tau_{\mathrm{ev}}}\frac{\kappa S}{D_{\mathrm{ev}}}\sum_{n=1}^{\infty}\frac{f_n^2(\mathbf{a}_+)\,\exp(-D_{\mathrm{ev}} t q_n^2)}{q_n^4}\,. \tag{2.92b}$$

The representation of the blood-to-tissue impulse response function, Eq. (2.15), is obtained as follows:

$$\begin{aligned} w(\mathbf{r},t) &= -\frac{\partial \psi_{\mathrm{ev}}^{\mathrm{abs}}(\mathbf{r},t)}{\partial t} \\ &= \int_{\mathrm{ev}} -\frac{\partial G(\mathbf{r},\mathbf{r}',t)}{\partial t}\,\mathrm{d}^d\mathbf{r}' \\ &= \int_{\mathrm{ev}} -\nabla\cdot D_{\mathrm{ev}}\nabla G(\mathbf{r},\mathbf{r}',t)\,\mathrm{d}^d\mathbf{r}' \\ &= \int_{\mathrm{ev}} -\nabla'\cdot D_{\mathrm{ev}}\nabla' G(\mathbf{r},\mathbf{r}',t)\,\mathrm{d}^d\mathbf{r}' \\ &= \int_S D_{\mathrm{ev}}\mathbf{n}\nabla' G(\mathbf{r},\mathbf{a}_+,t)\,\mathrm{d}S \\ &= \int_S \kappa\, G(\mathbf{r},\mathbf{a}_+,t)\,\mathrm{d}S\,. \end{aligned} \tag{2.93}$$

In the second line of (2.93), $\psi_{\mathrm{ev}}^{\mathrm{abs}}(\mathbf{r},t)$ has been represented in terms of the Green's function and the order of differentiation and integration has been interchanged. In the third line, the operator ∇ acts on $\mathbf{r}$, whereas the variable of integration is $\mathbf{r}'$.

However, the symmetry of the Green's function with respect to interchange of its spatial arguments is used to obtain

$$\begin{aligned}\nabla \cdot D_{\mathrm{ev}} \nabla G(\mathbf{r}, \mathbf{r}', t) &= \sum_{n=1}^{\infty} \{\nabla \cdot D_{\mathrm{ev}} \nabla f_n(\mathbf{r})\} f_n(\mathbf{r}') \exp(-\lambda_n t) \\ &= \sum_{n=1}^{\infty} -\lambda_n f_n(\mathbf{r}) f_n(\mathbf{r}') \exp(-\lambda_n t) \\ &= \nabla' \cdot D_{\mathrm{ev}} \nabla' G(\mathbf{r}, \mathbf{r}', t)\,, \end{aligned} \tag{2.94}$$

which follows directly from the Sturm–Liouville equation (2.76a) and the eigenfunction representation of $G(\mathbf{r}, \mathbf{r}', t)$ (2.79); here ∇' acts on the argument $\mathbf{r}'$. In the fourth line of (2.93) the Gauss theorem has been applied with the use of both the transcapillary tracer flux condition (2.10b) and the zero-flux condition at the outer boundary of extravascular space.

The eigenfunction representation of $w(\mathbf{r}, t)$ is obtained by substituting (2.79) in (2.93) as

$$w(\mathbf{r}, t) = \sum_{n=1}^{\infty} \left[\int_S \kappa f_n(\mathbf{a}_+)\, \mathrm{d}S \right] f_n(\mathbf{r}) \exp(-\lambda_n t) \tag{2.95a}$$

$$= \kappa S \sum_{n=1}^{\infty} f_n(\mathbf{a}_+) f_n(\mathbf{r}) \exp(-D_{\mathrm{ev}} t q_n^2)\,. \tag{2.95b}$$

Similarly, the eigenfunction representation of $w_\mu(t)$, Eq. (2.16b), is given by

$$w_\mu(t) = \sum_{n=1}^{\infty} \left[\int_S \kappa f_n(\mathbf{a}_+)\, \mathrm{d}S \right]^2 \frac{\exp(-\lambda_n t)}{\lambda_n} \tag{2.96a}$$

$$= \frac{\kappa^2 S^2}{D_{\mathrm{ev}}} \sum_{n=1}^{\infty} f_n^2(\mathbf{a}_+) \frac{\exp(-D_{\mathrm{ev}} t q_n^2)}{q_n^2}\,. \tag{2.96b}$$

The limiting form of $w(\mathbf{r}, t)$ for small time can be obtained from the asymptotic formula [103]:

$$\sum_{n=1}^{\infty} f_n^2(\mathbf{r}) \exp(-\lambda_n t) \sim \frac{1}{V_{\mathrm{ev}}} \sum_{n=1}^{\infty} \exp(-\lambda_n t)\,, \qquad t \to 0\,. \tag{2.97}$$

The left-hand side of the above expression is equal to $G(\mathbf{r}, \mathbf{r}, t)$, from Eq. (2.79), and is independent of position, as shown by the right-hand side. This is because

the probability for a diffusing molecule to be found within a small volume around its initial position, $\mathbf{r}'$, is, at short observation times, independent of $\mathbf{r}'$. Putting $\mathbf{r} = \mathbf{r}' = \mathbf{a}_+$ in (2.97) and using (2.15) and then (2.2c), the short-time behaviour of the blood-to-tissue impulse response function, evaluated at the capillary wall, is obtained as

$$w(\mathbf{a}_+, t) \sim \frac{1}{\tau_{\mathrm{ev}}} \sum_{n=1}^{\infty} \exp(-\lambda_n t)\,, \qquad t \to 0\,. \tag{2.98}$$

Lastly, the eigenfunction representation of the effective extravascular depolarised volume is written as

$$\Lambda(t) = \sum_{n=1}^{\infty} \left[\int_S \kappa f_n(\mathbf{a}_+)\,\mathrm{d}S\right]^2 \frac{1-\exp(-\lambda_n t)}{\lambda_n^2} \tag{2.99a}$$

$$= \left(\frac{\kappa S}{D_{\mathrm{ev}}}\right)^2 \sum_{n=1}^{\infty} f_n^2(\mathbf{a}_+)\,\frac{1-\exp(-D_{\mathrm{ev}} t q_n^2)}{q_n^4}\,. \tag{2.99b}$$

Equation (2.99a) is obtained from (2.24) with the use of the concentration (2.86a) to obtain the eigenfunction decomposition of unity from the initial condition $\psi_{\mathrm{ev}}^{\mathrm{abs}}(\mathbf{r}, 0) = 1$. Alternatively, one integrates the rate of blood–tissue tracer exchange in the right-hand side of (2.25) and uses the initial value $\Lambda(t = 0) = 0$.

Integral representations

There are two important cases, discussed below, in which equations (2.79), (2.86b), (2.95b) and (2.99b), can be recast as integrals using the well-known fact that the difference between consecutive eigenfrequencies approaches $\Delta q_n \sim 1/A$ for large values of the summation index, n [99]:

1. *When the difference between consecutive eigenfrequencies of the spectrum of the $\nabla\cdot D_{\mathrm{ev}}\nabla$ operator becomes sufficiently small as the outer radius A becomes sufficiently large*: in this case, in addition to an integral sum there usually arises a sum proportional to the ratio $(a/A)^2 \sim v_{\mathrm{iv}}$, which defines the accuracy of the approximation. This limit is approached in the case of sparse capillary networks, in which the extravascular volume is large because intercapillary distances are, typically, much greater than capillary radii.

2. *For relatively short tracer diffusion lengths*, as expressed by Eq. (2.28): as the summation index n increases by one, the non-dimensional argument of the nth eigenfunction, given by $q_n r$, undergoes the small change

$$r\Delta q_n \sim \frac{\sqrt{D_{\mathrm{ev}} t}}{A} \ll 1\,, \tag{2.100}$$

which implies that the amplitude of the eigenfunctions varies by a small amount. This justifies the approximation of all of the above-mentioned sums by integrals.

The procedure is worked out in detail in Chapter 3.

2.5.6 Derivation of arterial-to-intracapillary impulse response function

In this Appendix we show that when the time interval after the first tracer arrival at the capillary is short in terms of the mean extravascular residence time of a well-mixed tracer, such that the condition in Eq. (2.18) holds, the arterial-to-intravascular impulse response function reduces to Eq. (2.19a).

The standard method of taking the time Fourier transform[36] of the intracapillary tracer balance equation (2.17) of the partial differential equation [97] yields, after rearranging, the first-order differential equation

$$\frac{\mathrm{d}\psi_{\mathrm{iv}}(z,\omega)}{\mathrm{d}z} + \frac{B(\omega)}{u_z}\,\psi_{\mathrm{iv}}(z,\omega) = \frac{\psi_{\mathrm{iv}}(z,t=0)}{u_z}\,, \tag{2.101a}$$

where

$$B(\omega) = -\mathrm{i}\omega + R_{\mathrm{iv}} + \frac{1 - w(\mathbf{a}_+,\omega)}{\tau_{\mathrm{iv}}}\,. \tag{2.101b}$$

The solution to Eq. (2.101a) is given by

$$\psi_{\mathrm{iv}}(z,\omega) = h_{\mathrm{a}}^{\mathrm{iv}}(z,\omega)\psi_{\mathrm{iv}}(z=0,\omega) + h_{\mathrm{a}}^{\mathrm{iv}}(z,\omega) *_z \frac{\psi_{\mathrm{iv}}(z,t=0)}{u_z}\,, \tag{2.102a}$$

[36]The definition of the Fourier transform employed here is: $\mathcal{F}\{f(t)\} = \int_{-\infty}^{+\infty} f(t)\exp(\mathrm{i}\omega t)\,\mathrm{d}t$. In present notation, the transformed quantities are distinguished from their time conjugates simply by the second argument, which is ω instead of t.

where $*_z$ denotes convolution with respect to axial distance z, and the Fourier transform of the arterial-to-intravascular impulse response function is given by

$$h_{\mathrm{a}}^{\mathrm{iv}}(z,\omega) = \exp[-B(\omega)t_z]\,, \tag{2.102b}$$

with $t_z = z/u_z$ (2.19b). Back-transformation of Eq. (2.102a) gives

$$\psi_{\mathrm{iv}}(z,t) = h_{\mathrm{a}}^{\mathrm{iv}}(z,t) * \psi_{\mathrm{iv}}(z=0,t) + h_{\mathrm{a}}^{\mathrm{iv}}(z,t) *_z \frac{\psi_{\mathrm{iv}}(z,t=0)}{u_z}\,, \tag{2.103a}$$

where the arterial-to-intravascular impulse response function is expressed as

$$h_{\mathrm{a}}^{\mathrm{iv}}(z,t) = \mathcal{F}^{-1}\left\{\exp\left[\frac{t_z}{\tau_{\mathrm{iv}}}\,w(\mathbf{a}_+,\omega)\right]\right\}\exp(-R_{\mathrm{iv}}^{+}t_z) * \delta(t-t_z)\,, \tag{2.103b}$$

where $\mathcal{F}^{-1}$ denotes the inverse Fourier transformation and $R_{\mathrm{iv}}^{+} = R_{\mathrm{iv}} + \tau_{\mathrm{iv}}^{-1}$ (2.19b).

In the sequel, we assume zero intracapillary concentration initially, hence the second term on the right-hand side of (2.103a) vanishes. The first convolution operand in (2.103b) represents transport and exchange of tracer present at the inflowing end of the capillary. The function $w(\mathbf{a}_+,\omega)$ is evaluated from (2.95a) after multiplication by the extravascular relaxation term, $\exp(-R_{\mathrm{ev}}t)$. This gives

$$w(\mathbf{a}_+,\omega) = \sum_{n=1}^{\infty}\frac{\kappa S f_n^2(\mathbf{a}_+)}{-\mathrm{i}\omega + R_{\mathrm{ev}} + \lambda_n}\,, \tag{2.104}$$

where $f_n(\mathbf{a}_+)$ is assumed constant on the capillary surface. Thus, in (2.103b) we have

$$\exp\left[\frac{t_z}{\tau_{\mathrm{iv}}}\,w(\mathbf{a}_+,\omega)\right] = \prod_{n=1}^{\infty}\exp\left[\frac{b_n}{-\mathrm{i}\omega + R_{\mathrm{ev}} + \lambda_n}\right], \tag{2.105}$$

where

$$b_n \equiv \frac{\kappa S f_n^2(\mathbf{a}_+)}{\tau_{\mathrm{iv}}}\,t_z = \frac{V_{\mathrm{ev}} f_n^2(\mathbf{a}_+)}{\tau_{\mathrm{ev}}}\,\frac{\tau_{\mathrm{c}}}{\tau_{\mathrm{iv}}}\,\frac{z}{L}\,. \tag{2.106}$$

Using the standard Fourier transform pair

$$\exp\left(-\frac{b_n}{\mathrm{i}\omega}\right) \rightleftharpoons \delta(t) + \sqrt{\frac{b_n}{t}}\,I_1(2\sqrt{b_n t})\,, \qquad t \geq 0\,, \tag{2.107}$$

where $I_1(\cdot)$ is the modified Bessel function of the first kind and first order, the arterial-to-intravascular impulse response function (2.103b) is rewritten as

$$h_{\mathrm{a}}^{\mathrm{iv}}(z,t) = \delta(t-t_z)\exp(-R_{\mathrm{iv}}^{+}t_z) * \mathcal{H}_1(t) * \mathcal{H}_2(t) * \cdots * \mathcal{H}_n(t) * \cdots \tag{2.108a}$$

for $t \geq 0$, where

$$\mathcal{H}_n(t) = \delta(t) + \sqrt{\frac{b_n}{t}}\, I_1(2\sqrt{b_n t}) \exp[-(R_{\mathrm{ev}} + \lambda_n)t] \,. \tag{2.108b}$$

The second term in $\mathcal{H}_n(t)$ is non-singular: for small arguments, $z^{-1/2} I_1(z^{1/2}) \sim 1/2$, whereas for large arguments, $z^{-1/2} I_1(z^{1/2}) \sim z^{-3/4} \exp(z^{1/2})$, hence the exponential term due to relaxation and transcapillary exchange dominates; see Ref. [175].

To obtain a useful analytical approximation to (2.108a), we estimate the argument $\sqrt{b_n t}$ as follows. We first note that z/L and $V_{\mathrm{ev}} f_n^2(\mathbf{a}_+)$ appearing in b_n (2.106) are both at most equal to unity [since $f_n(\mathbf{r})$ is normalised]. Thus, the condition $\sqrt{(\tau_{\mathrm{c}}/\tau_{\mathrm{iv}})(t/\tau_{\mathrm{ev}})} \ll 1$ of Eq. (2.18) results in $\sqrt{b_n t} \ll 1$, hence $I_1(2\sqrt{b_n t}\,) \approx \sqrt{b_n t}$ with relative error of order $b_n t$.[37] To this approximation, the nth convolution operand in (2.108b) reduces to

$$\mathcal{H}_n(t) = \delta(t) + b_n \exp[-(\lambda_n + R_{\mathrm{ev}})t] \,, \qquad t \geq 0 \,. \tag{2.108c}$$

By the associativity of convolution, Eq. (2.108a) becomes, after rearranging terms:

$$h_{\mathrm{a}}^{\mathrm{iv}}(z,t) \approx \delta(t - t_z) * \left[\delta(t) + \sum_{n=1}^{\infty} \mathcal{B}_n(t)\right] \exp(-R_{\mathrm{iv}}^{+} t_z) \,, \tag{2.109a}$$

where $\mathcal{B}_n(t)$ is an infinite sum, over all indices $i_1 < i_2 < \cdots < i_n$, of terms each involving $n-1$ convolutions of the form

$$\sum_{i_1 < \cdots < i_n} b_{i_1} \exp[-(\lambda_{i_1} + R_{\mathrm{ev}})t] * \cdots * b_{i_n} \exp[-(\lambda_{i_n} + R_{\mathrm{ev}})t] \,. \tag{2.109b}$$

In particular, from (2.95b) and (2.106) we get

$$\mathcal{B}_1(t) = \sum_{n=1}^{\infty} b_n \exp[-(\lambda_n + R_{\mathrm{ev}})t] = \frac{t_z}{\tau_{\mathrm{iv}}}\, w(\mathbf{a}_+, t) \,. \tag{2.110}$$

[37] This estimate follows from the series expansion [175]:

$$I_\nu(z) = \sum_{k=0}^{\infty} \frac{(z/2)^{2k+\nu}}{k!\,\Gamma(\nu + k + 1)} \,,$$

where $\Gamma(\cdot)$ is the Euler gamma function.

The term $\mathcal{B}_2(t)$ is also easily evaluated as

$$\mathcal{B}_2(t) = \sum_{n=1}^{\infty} c_n b_n \exp[-(\lambda_n + R_{\text{ev}})t] \tag{2.111a}$$

with

$$c_n = \sum_{m=1}^{\infty} \frac{b_m}{\lambda_m - \lambda_n}\,, \qquad\qquad m \neq n\,. \tag{2.111b}$$

Equation (2.109a) can be simplified further by noting that, since $\lambda_{i_1} < \lambda_{i_2} < \cdots < \lambda_{i_n}$, $\mathcal{B}_n(t)$ is upper bounded by

$$\begin{aligned}
\mathcal{B}_n(t) &\leq \sum_{i_1} b_{i_1} \exp[-(\lambda_{i_1} + R_{\text{ev}})t] * \cdots * b_{i_n} \exp[-(\lambda_{i_1} + R_{\text{ev}})t] \\
&= \sum_{i_1} \frac{(b_{i_2} \cdots b_{i_n}) t^{n-1}}{(n-1)!}\, b_{i_1} \exp[-(\lambda_{i_1} + R_{\text{ev}})t] \\
&\ll \frac{C^{2(n-1)}}{(n-1)!}\, \mathcal{B}_1(t)\,,
\end{aligned} \tag{2.112}$$

where $C \ll 1$ is an upper bound of $\sqrt{b_{i_n} t}$ for all i_n. Thus, we can neglect $\mathcal{B}_2(t)$ and subsequent terms in the expression (2.109a) of the arterial-to-intracapillary impulse response function, with relative error of the order of C^2, which is small by assumption. This results in Eq. (2.19a), as was to be shown.

Substitution of $h_{\text{a}}^{\text{iv}}(z,t)$ and $h_{\text{a}}^{\text{ev}}(\mathbf{r},t) = w(\mathbf{r},t) * h_{\text{a}}^{\text{iv}}(z,t)$ into Eq. (2.17) of tracer balance in intracapillary space, gives

$$\begin{aligned}
\frac{\partial h_{\text{a}}^{\text{iv}}(z,t)}{\partial t} = &- u_z \frac{\partial h_{\text{a}}^{\text{iv}}(z,t)}{\partial z} - R_{\text{iv}} h_{\text{a}}^{\text{iv}}(z,t) - \frac{h_{\text{a}}^{\text{iv}}(z,t) - h_{\text{a}}^{\text{iv}}(z,t) * w(\mathbf{a}_+,t)}{\tau_{\text{iv}}} \\
&+ \frac{1}{\tau_{\text{iv}}} \left[\frac{t_z}{\tau_{\text{iv}}}\, w(\mathbf{a}_+,t) * w(\mathbf{a}_+, t - t_z) \right].
\end{aligned} \tag{2.113}$$

The term in brackets in the second line of the above equation represents a correction to $h_{\text{a}}^{\text{ev}}(\mathbf{r},t)$.

Chapter 3

Blood–Tissue Tracer Exchange: Evaluation

In this Chapter we evaluate the quantities, as defined in the previous Chapter, which describe the exchange of a tracer substance between the capillaries and the surrounding tissue, assuming that the single-capillary approximation holds.

As is well known, diffusion consists in the transport of matter from one part of a system to another due to the random molecular motions of the diffusing substance (Ref. [176], p. 1). Random molecular motions also underlie the transfer of heat by conduction (Ref. [176], p. 2). In 1855 the German physiologist A. Fick [153] developed a quantitative description of diffusion which was founded on the mathematical theory of heat conduction of J. Fourier [177], published in 1822; see for example Chapter II, pp. 99 – 103 of this latter work.

In addition to the above-mentioned phenomena, the heat equation unifies the mathematical treatment of numerous important physical problems, including viscous motion, diffusion of liquids in porous media and electrical conduction in good conductors (Ref. [178], pp. 28 – 29; Ref. [179], p. 29).

An extensive collection of solutions of the heat equation for planar, cylindrical, conical and spherical geometries, valid for a variety of initial and boundary conditions, is found in the books by Carslaw and Jaeger [178] and by Crank [176]. Thus,

certain blood–tissue exchange quantities presented in this Chapter have counterparts as heat transfer results which can be consulted in these references.[1] Nonetheless, we have independently worked out all the relevant tracer-exchange quantities for completeness and self-consistency of the material presented in this Thesis. In particular, a quantity analogous to the blood-to-tissue impulse response function, Eq. (2.15), which plays a central role in the theory presented herein, was not found in the above-cited references. We also mention that have consistently made use of the method of eigenfunction decomposition (Appendix 2.5.5), whereas the method most often employed by Carslaw and Jaeger in Ref. [178] involves the Laplace transformation. Further details are given in the discussion of each blood–tissue exchange quantity below.

Because in the model described in this Thesis the effect of axial diffusion on the exchange has been considered negligible (Section 2.2.1), molecular diffusion shall be treated as occurring in plane regions concentric with, and perpendicular to, any given capillary segment at increasing distances from the inflow end of the capillary.

This Chapter devotes considerable attention, first, to diffusion in one spatial dimension. In certain studies (see the Discussion section) both the experimental conditions and measurement method of choice may justify the use of such a simplified model of diffusion in the tissues. Further, at sufficiently short diffusion times the results for this case are valid for the more general case of diffusion in a plane region with cylindrical symmetry, which is also discussed subsequently in detail.

We presented parts of the material found in this Chapter in Ref. [96].

[1] As an example of the existing analogies, it is noted that Eqs (2.10a) – (2.10d) describe the transfer of heat from a body, kept at constant temperature initially, into a medium kept at zero temperature. In heat transfer problems, the boundary condition (2.1c) is sometimes referred to as a radiation boundary condition since it expresses approximately the time course of the temperature at the contact surfaces of two media which exchange heat by radiation (see more details in Ref. [178], pp. 18 – 21, and in Ref. [179], pp. 57 – 58). This boundary condition is also appropriate to the exchange of moisture between, e.g., a solid and a stream of air passing over its surface (Ref. [176], pp. 35 – 36).

3.1 One-dimensional diffusion

The diffusion of tracer molecules may be considered to occur in one spatial dimension (1d) in two distinct, not mutually exclusive cases:

1. *The diffusion of tracer molecules is constrained by physical boundaries* to occur in a region having a principal orientation axis whose dimensions are in a large ratio to those in any perpendicular direction (Fig. 3.1a). An important example of such a medium is provided by the two types of neuronal process, axons and dendrites (see, e.g., Ref. [1] and Table 1.1 of Ref. [180]). A 1d diffusion model may also be appropriate to describe interstitial diffusion in certain normal and neoplastic tissues. (This latter case is considered in some detail in the Discussion section to this Chapter).

2. *At sufficiently short tracer diffusion times*, the difference between the concentration of tracer at any given time and that at initial steady state varies appreciably only in the region near the membranes between adjacent physiological environments. However, at such short times the diffusing molecules are unable to 'sense' the size and curvature of physiological membranes [103]. Since molecular diffusion can then be regarded as occurring in a medium bounded by a large, virtually flat membrane (Fig. 3.1b), and since only the component of the diffusive flux in the direction perpendicular to the membrane is of significance to tracer exchange, one-dimensional diffusion therefore describes this situation with good accuracy. These intuitive arguments will be developed mathematically in Section 3.2.

In heat transfer problems, conduction of heat in a straight rod of small cross section can also be considered spatially linear when no heat is lost through the conductor surface (Ref. [178], p. 50). Further, when the isothermal surfaces are parallel planes, the direction of the heat flow occurs in the direction perpendicular to them and one-dimensional modelling is therefore appropriate [179].

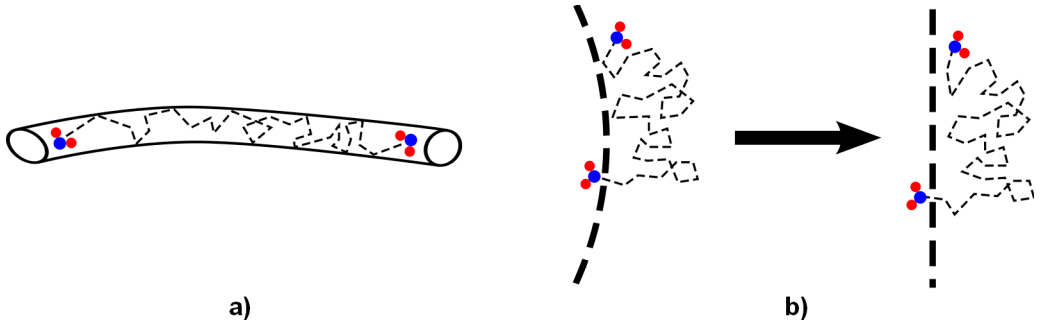

Figure 3.1: **Effective one-dimensional diffusion**: **a)** due to structural constraints of the medium; **b)** diffusion at short diffusion times in the vicinity of a permeable capillary wall (thick broken line); see text for details.

In the case of diffusion in one spatial dimension, the Sturm–Liouville equation (2.82) becomes

$$f_n''(r) + q_n^2 f(r) = 0\,, \qquad a < r < A\,, \tag{3.1}$$

where r denotes a Cartesian coordinate. The (non-normalised) eigenfunctions can be written as the superposition of an incident wave and a reflected wave [96]:

$$f_n(r) = \exp(-\mathrm{i}q_n r) + \exp(\mathrm{i}q_n r - \mathrm{i}2\delta_n) \sim \cos(q_n r - \delta_n) \tag{3.2}$$

for $n = 1, 2, \ldots$, where 'i' denotes the imaginary unit. Imposing the boundary condition at the capillary wall, given by $D_{\mathrm{ev}} f_n'(a) = \kappa f_n(a)$,[2] see Eq. (2.76b) and Fig. 3.2, gives the *scattering phase shift*, δ_n, as

$$\delta_n = q_n a + \operatorname{arc\,cot} \ell q_n\,, \tag{3.3a}$$

where $\ell = D_{\mathrm{ev}}/\kappa$, Eq. (2.4). We define

$$\delta_n' = \operatorname{arc\,cot} \ell q_n\,. \tag{3.3b}$$

[2]The parameter a is used here for notational consistency with the spatially two-dimensional case discussed in Section 3.2, since certain results for the one-dimensional case carry over, with minor modifications, to the two-dimensional case.

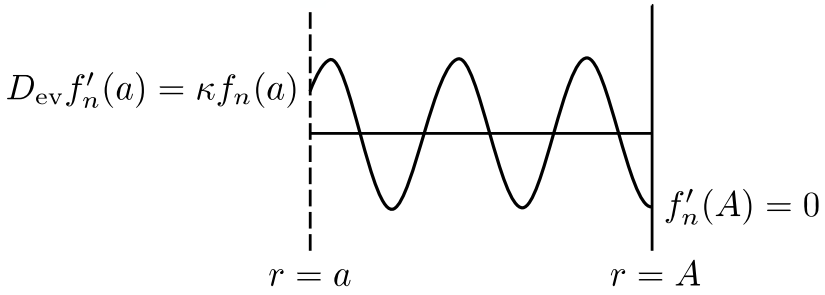

Figure 3.2: **Boundary conditions** for spatially one-dimensional (Section 3.1) and two-dimensional with cylindrical symmetry (Section 3.2) geometries. A hypothetical eigenfunction $f_6(q_6 r) = \cos\left[q_6(r-a) - \pi/3\right]$ for one-dimensional diffusion and exchange is shown by way of example.

The spatial eigenfrequencies are obtained from the zero-flux condition at the outer pericapillary boundary, Eq. (2.76c), as

$$q_n A - \delta_n = (n-1)\pi\,. \tag{3.4a}$$

Substituting δ_n from (3.3a) into the above expression gives

$$q_n = \frac{(n-1)\pi + \delta_n'}{A-a} \qquad \Rightarrow \qquad \tan q_n(A-a) = \frac{1}{\ell q_n}\,. \tag{3.4b}$$

Substituting the foregoing results into Eq. (2.79) yields the Green's function for the 1d case as [96]:

$$G_{1\mathrm{d}}(r, r', t) = \sum_{n=1}^{\infty} \frac{\cos[q_n(r-a) - \delta_n']\cos[q_n(r'-a) - \delta_n']}{\|f_n\|^2} \exp(-D_{\mathrm{ev}} t q_n^2)\,, \tag{3.5}$$

where the eigenfunction norm is given by

$$\|f_n\|^2 = \frac{A-a}{2} + \frac{\sin 2\delta_n'}{4q_n} = \frac{1}{2}\left[A - a + \frac{\ell}{1+\ell^2 q_n^2}\right]. \tag{3.6}$$

Equations (3.5) and (3.6) are a particular case of the result given by Carslaw and Jaeger for heat conduction in a solid bounded by the planes $r = a$ and $r = A$, the outwards heat flux being proportional to the respective surface temperature; see Eqs 14.3.II (3) – (6) of Ref. [178]. Rather than making explicit use of the eigenfunction decomposition – as we have done in this Thesis – these authors expressed the Green's

function for the one-dimensional case as the sum of the Green's function for an infinite one-dimensional medium and an auxiliary function which was required (i) to vanish at time $t = 0$ and (ii) to ensure compliance of the whole $G_{1d}(r, r', t)$ with the boundary conditions [see remark after Eq. (3.54a) of Appendix 3.6.1]. Their calculations involved the Laplace transformation.[3]

The one-dimensional tracer concentration under absorbing intracapillary boundary conditions is obtained by substituting the normalised eigenfunctions in (2.86b) as [96]:

$$\psi_{1d}^{abs}(r,t) = \sum_{n=1}^{\infty} \frac{\sin q_n(r-a) + \ell q_n \cos q_n(r-a)}{\|f_n\|^2 \,(1+\ell^2 q_n^2)\, q_n} \exp(-D_{ev} t q_n^2)\,, \tag{3.7}$$

where the identity $\sin z = (1 + \cot^2 z)^{-1/2}$ has been used. The eigenfrequencies, the Green's function and the concentration of tracer are all functions of distance to the capillary wall, $r - a$, rather than functions of the 'absolute' coordinate r; this is an expected consequence of the 1d geometry. Equation (3.7) may be obtained as a particular case of Eq. 3.11 (21) of Ref. [178].

Analysis of the general term in the right-hand side of (3.7) shows that the main contribution to the series comes from values of n such that

$$q_n \lesssim \min\left\{ \frac{1}{\sqrt{D_{ev} t}}\,, \sqrt{\frac{1}{\ell^2} + \frac{1}{(A-a)\ell}} \right\}, \tag{3.8}$$

which accords with the previous estimate (2.90), noting that $\tau_{ev} = (A-a)/\kappa$ for the 1d case.

Because of the non-linear expression for the eigenfrequencies, the infinite sums in (3.5) and (3.7) cannot, in general, be evaluated analytically. However, as shown next, when $a/A \ll 1$ these sums go over into integrals. Since the difference Δq_n between consecutive eigenfrequencies decreases with A, the eigenfrequency spectrum

[3] In certain simple cases, the use of look-up tables allows straightforward inversion of the Laplace-transformed quantities. In more complicated cases the inversion formula for the Laplace transformation is called for, contour integration resulting in the appropriate eigenfunction decomposition, as in Eq. (3.5).

becomes continuous in the limit as $A \to \infty$. The small increment Δq_n is estimated by expanding the eigenfrequency expression (3.4b) as

$$\Delta q_n = \frac{1}{A-a}\left[\pi - \frac{\ell \Delta q_n}{1+\ell^2 q_n^2} + \mathcal{O}[\ell \Delta q_n]^2\right]. \tag{3.9}$$

Neglecting the small term of order $[\ell \Delta q_n]^2$, rearranging and using (3.6), gives

$$\frac{1}{\|f_n\|^2} \approx \frac{2}{\pi} \Delta q_n \,. \tag{3.10}$$

Therefore, when $a/A \ll 1$ the general terms of (3.5) and (3.7) are both slowly-varying functions of n, hence these infinite sums become integral sums in q.

In particular, the 1d Green's function for sparse capillary networks with absorbing intracapillary boundary conditions evaluates to (see Appendix 3.6.1)

$$\begin{aligned} G_{1\mathrm{d}}(r,r',t) &= \frac{2}{\pi}\int_0^\infty \cos[q(r-a)-\delta']\cos[q(r'-a)-\delta']\exp(-D_{\mathrm{ev}}tq^2)\,\mathrm{d}q \\ &= \frac{1}{\sqrt{4\pi D_{\mathrm{ev}}t}}\left\{\exp\left[-\frac{(r+r'-2a)^2}{4D_{\mathrm{ev}}t}\right] + \exp\left[-\frac{(r-r')^2}{4D_{\mathrm{ev}}t}\right]\right\} \\ &\quad - \frac{1}{\ell}\exp\left(\frac{r+r'-2a}{\ell} + \frac{D_{\mathrm{ev}}t}{\ell^2}\right)\operatorname{erfc}\left(\frac{r+r'-2a}{\sqrt{4D_{\mathrm{ev}}t}} + \frac{\sqrt{D_{\mathrm{ev}}t}}{\ell}\right) \end{aligned} \tag{3.11}$$

with $\delta' = \operatorname{arc\,cot} \ell q$ and $\ell = D_{\mathrm{ev}}/\kappa$.

Equation (3.11) is formally identical with an expression given by Carslaw and Jaeger, see Eq. 14.2.II (6) of Ref. [178], which applies to the transfer of heat from a semi-infinite solid into a medium kept at zero temperature, with the same boundary condition as has been prescribed here. The method employed by the authors was the same as that discussed above (p. 119) in connection with the Green's function for the finite interval $a \le r \le A$.

The various terms of the 1d Green's function (3.11) are illustrated schematically in Fig. 3.3, where the permeable membrane is at $r = a = 0$, for simplicity. The two Gaussian terms (denoted by G_1 and G_2, respectively) in the second line of (3.11) are each recognised as the 1d Green's function for an infinite one-dimensional medium. Their sum gives the Green's function for diffusion in a semi-infinite medium bounded by an impermeable plane surface at $r = a$ when only the component of diffusion in

the direction perpendicular to this surface is considered.[4] Lastly, the term on the third line of (3.11), denoted by G_3, represents the effect of a non-zero flux of diffusing substance and satisfies the (absorbing) boundary condition at $r = a$. This term may be recast as

$$G_3(r, r', t) = -\frac{2/\ell}{\sqrt{4\pi D_{\mathrm{ev}} t}} \int_{-\infty}^{2a-r'} \exp\left(\frac{\xi + r' - 2a}{\ell}\right) \exp\left(-\frac{(r-\xi)^2}{4D_{\mathrm{ev}} t}\right) \mathrm{d}\xi\,, \qquad (3.12)$$

and when put in this form Eq. (3.11) above becomes Eq. (15) of Sommerfeld's book [179, Section 13]. In Fig. 3.3 the terms in the integrand of G_3 are represented with dash-dot lines for clarity. The horizontal axis is doubly scaled for r (i.e., for G_1 and G_2) and ξ [for the integration variable in Eq. (3.12)]. Because G_2 appears in the convolution integral (3.12), the term G_3 is interpreted as the contribution of a line of sinks of position-dependent amplitude $(2/\ell)\exp[(\xi + r' - 2a)/\ell]\mathrm{d}\xi$ extending from $\xi = 2a - r'$ to $-\infty$ [178].

Several important cases are considered below:

- If unit amount of tracer is delivered at position r' at time $t = 0$, then for times $t \ll r'^2/(4D_{\mathrm{ev}})$ the Green's function $G_{1\mathrm{d}}(r, r', t)$ of Eq. (3.11) is approximately equal to the free propagator G_2, since the contributions of the 'mirror' Gaussian term, G_1, and of the line of sinks are both negligibly small.

- For highly permeable membranes (i.e., $\ell/a \ll 1$) the integral in (3.12) evaluates to $-2G_1$, approximately. Thus, the Green's function $G_{1\mathrm{d}}(r, r', t) \approx -G_1 + G_2$, with $G_{1\mathrm{d}}(a_+, r', t) \approx 0$, consistent with the absorbing condition imposed in the region $r < a$.

- For poorly permeable membranes ($\ell/a \gg 1$), the term G_3 is very small at all times. Hence $G_{1\mathrm{d}}(r, r', t) \approx G_1 + G_2$ and $\partial G'_{1\mathrm{d}}(a_+, r', t)/\partial r \approx 0$, i.e., the transmembrane flux is negligibly low.

[4] This part of the required Green's function may be obtained by the *method of images*. See, e.g., Section 10.10 of Ref. [178].

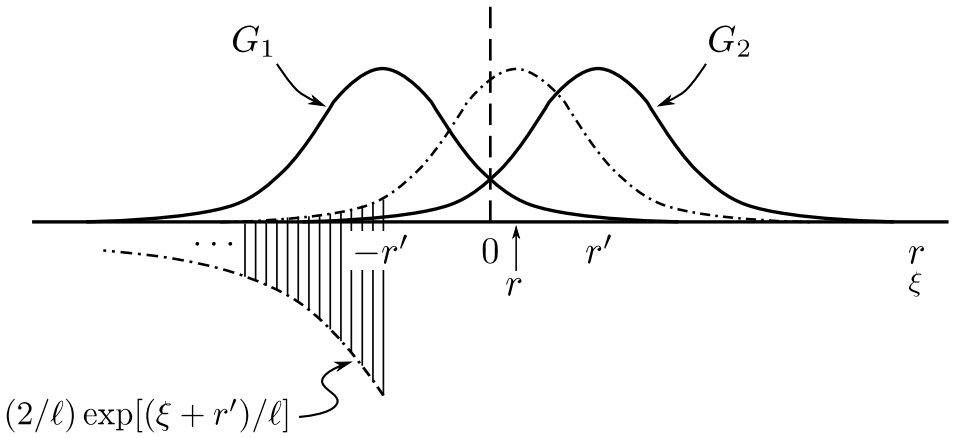

Figure 3.3: **Green's function** (3.11) **for one-dimensional diffusion in the half-space** $r > 0$, adapted from Fig. 14 of Sommerfeld [179]. The boundary condition at the permeable membrane is as in Fig. 3.2.

Passing to the integral in (3.7), or after straightforward integration of the Green's function in the interval $r' \geq a$, the extravascular concentration for absorbing intracapillary conditions becomes

$$\begin{aligned}\psi_{1\mathrm{d}}^{\mathrm{abs}}(r,t) &= \frac{2}{\pi}\int_0^\infty \frac{\sin q(r-a) + \ell q \cos q(r-a)}{(1+\ell^2 q^2)q}\exp(-D_{\mathrm{ev}}tq^2)\,\mathrm{d}q \\ &= 1 - \operatorname{erfc}\left(\frac{r-a}{\sqrt{4D_{\mathrm{ev}}t}}\right) + \exp\left(-\frac{(r-a)^2}{4D_{\mathrm{ev}}t} + \xi^2\right)\operatorname{erfc}(\xi)\,, \end{aligned} \tag{3.13a}$$

where $\operatorname{erfc}(\xi) = 2\pi^{-1/2}\int_\xi^\infty \exp(-z^2)\,\mathrm{d}z$ is the complementary error function [175] and[5]

$$\xi = \frac{r-a}{\sqrt{4D_{\mathrm{ev}}t}} + \frac{\sqrt{D_{\mathrm{ev}}t}}{\ell}\,. \tag{3.13b}$$

[5]The integral in the first line of Eq. (3.13a) is evaluated with the use of formulae (3.954.1) and (3.954.2) of Ref. [181] as well as the following relation, obtained by integrating by parts:

$$\int \exp(\pm r)\operatorname{erfc}(b \pm r/2b)\,\mathrm{d}r = \mp\operatorname{erfc}(b) + \exp(-b^2)\operatorname{erf}(r/2b) \pm \exp(\pm r)\operatorname{erfc}(b \pm r/2b)\,,$$

where $\operatorname{erf}(\cdot) = 1 - \operatorname{erfc}(\cdot) = 2\pi^{-1/2}\int_0^\xi \exp(-z^2)\,\mathrm{d}z$ is the well-known error function and $b = \sqrt{D_{\mathrm{ev}}t}/\ell$.

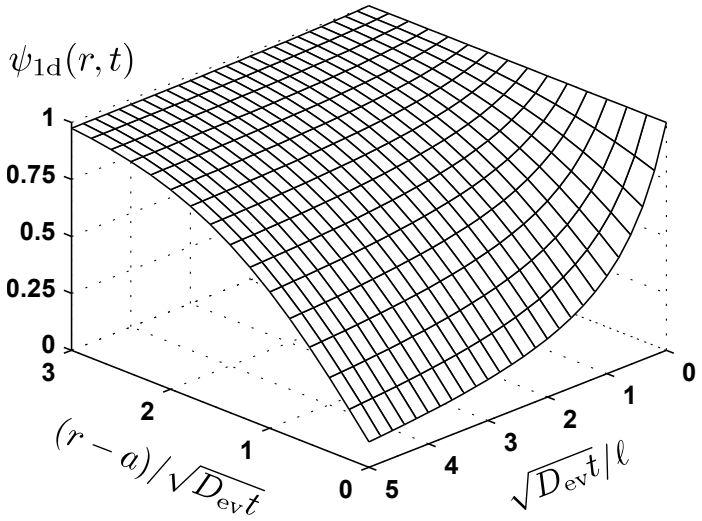

Figure 3.4: **One-dimensional extravascular concentration under absorbing intracapillary conditions for the sparse capillary network approximation** ($a/A \ll 1$).

After minor rearrangements, Eq. (3.13a) may be put in the form of Eq. 2.7 (1) of Ref. [178], which gives the temperature of a semi-infinite solid at uniform temperature initially, heat flowing through its surface into a medium, kept at zero temperature, at a rate proportional to the surface temperature of the solid. With present notation, the method employed by Carslaw and Jaeger involves the change of dependent variable $\psi_{1d}^{abs} \mapsto \psi_{1d}^{abs} - (D_{ev}/\kappa)(\partial\psi_{1d}^{abs}/\partial r)$.

Crank [176] obtained expressions for the related problem in which diffusion occurs also in the left half-space $r < a$, with the same initial conditions as have been considered here. In the absence of consumption, the situation in which the concentration of tracer in $r < a$ is very low at all times may be approximated by setting the diffusion coefficient in that region to a much greater value than that in the region $r > a$. Equation (3.49) of Ref. [176] then reduces to Eq. (3.13a) above.

$\psi_{1d}^{abs}(r,t)$ is graphed in Fig. 3.4. At a distance of approximately three diffusion lengths from the capillary wall, the concentration of tracer is barely influenced by the magnitude of the diffusive flux near the capillary wall. The time course of the tissue-to-blood flux is given by the line $r = a$, up to a factor of κ.

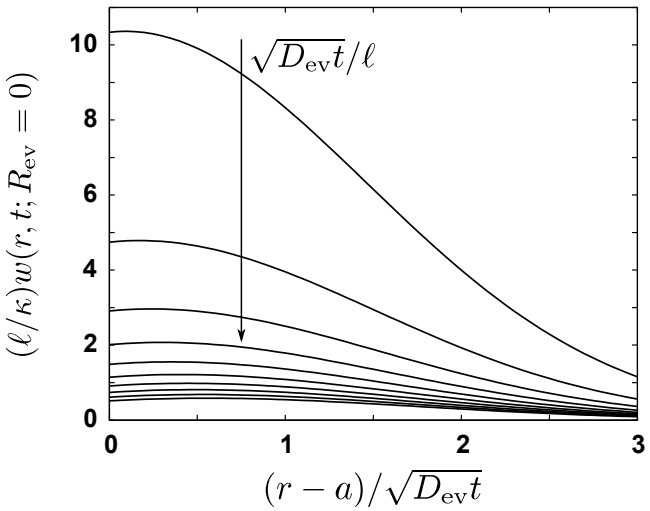

Figure 3.5: **Blood-to-tissue impulse response function in one spatial dimension for the sparse capillary network approximation**. Ten spatial profiles are shown, corresponding to the normalised time instants $\sqrt{D_{\rm ev}t}/\ell = 0.05, 0.1, \ldots, 0.5$.

The blood-to-tissue impulse response function is obtained either by differentiation of (3.13a) or by making use of the general Eq. (2.15). This gives

$$\begin{aligned} w(r,t) &= \kappa\, G_{\rm 1d}(r, a_+, t) \\ &= \frac{\kappa}{\ell}\left[\frac{\ell}{\sqrt{\pi D_{\rm ev}t}} - \exp(\xi^2)\,\mathrm{erfc}(\xi)\right]\exp\left(-\frac{(r-a)^2}{4D_{\rm ev}t} - R_{\rm ev}t\right), \end{aligned} \tag{3.14}$$

where the effect of extravascular relaxation has been included. For small time, use of the asymptotic formula $\sqrt{\pi}\exp(\xi^2)\,\mathrm{erfc}(\xi) \approx \xi^{-1}$ and of the Green's function (3.11) gives

$$w(r,t) \approx \frac{\kappa}{\sqrt{\pi D_{\rm ev}t}}\exp\left(-\frac{(r-a)^2}{4D_{\rm ev}t} - R_{\rm ev}t\right). \tag{3.15}$$

Figure 3.5 plots $(\ell/\kappa)w(r,t)$ as a function of normalised distance from the capillary wall, $(r-a)/\sqrt{D_{\rm ev}t}$, for a range of values of the parameter $\sqrt{D_{\rm ev}t}/\ell$. The amplitude of the blood-to-tissue impulse response function in one spatial dimension is seen to decrease rapidly with diffusion time.

The step response function $W(r,t)$ is evaluated according to Eq. (2.14) with the use of the formula $W(r,t;R_{\rm ev}=0) = 1 - \psi^{\rm abs}_{\rm 1d}(r,t)$, where $\psi^{\rm abs}_{\rm 1d}(r,t)$ is given by

Eq. (3.13a). The result is

$$W(r,t) = \frac{1}{1-\eta_\ell}\left[\sum_{i=1}^{2}\alpha_i \exp(\gamma_i^2)\operatorname{erfc}(\gamma_i) - \exp(\xi^2)\operatorname{erfc}(\xi)\right] \times \exp\left(-\frac{(r-a)^2}{4D_{\mathrm{ev}}t} - R_{\mathrm{ev}}t\right) \tag{3.16a}$$

with

$$\eta_\ell = \frac{\ell^2 R_{\mathrm{ev}}}{D_{\mathrm{ev}}} \tag{3.16b}$$

and

$$\alpha_{1,2} = \frac{1 \pm \sqrt{\eta_\ell}}{2}\,, \qquad \gamma_{1,2} = \frac{r-a}{\sqrt{4D_{\mathrm{ev}}t}} \pm \sqrt{R_{\mathrm{ev}}t}\,. \tag{3.16c}$$

It is easily checked[6] that the right-hand side of (3.16a) remains non-negative and finite for all values of the parameter η_ℓ. We note that $\eta_\ell > 1$ for the tissue parameters listed in Table 2.1. Without consumption or relaxation, Eq. (3.16a) gives

$$W(r,t;R_{\mathrm{ev}}=0) = \operatorname{erfc}\left(\frac{r-a}{\sqrt{4D_{\mathrm{ev}}t}}\right) - \exp\left(-\frac{(r-a)^2}{4D_{\mathrm{ev}}t} + \xi^2\right)\operatorname{erfc}(\xi)\,, \tag{3.17}$$

which is the same as $1-\psi_{\mathrm{ev}}^{\mathrm{abs}}(a_+,t)$ as obtained from (3.13a), as expected. The above expression also gives the temperature of a semi-infinite solid, initially at temperature zero, which is heated through the plane surface $r=a$ by heat flowing from a contiguous body maintained at constant unit temperature; see Eq. 2.7 (5) of Ref. [178]. Equation (3.17) also appears as Eq. (3.35) of Ref. [176].

As expected, when A is large, none of the above quantities depend on pericapillary radius. The time course of tracer exchange is determined by two parameters, namely the ratios of tracer diffusion length to effective thickness of the capillary wall and to distance from the membrane.

Under absorbing intracapillary boundary conditions, the tissue-to-blood flux of tracer is given by

$$\mathbf{nj}_{\kappa,1\mathrm{d}}^{\mathrm{abs}}(a,t) = \kappa\psi_{1\mathrm{d}}^{\mathrm{abs}}(a_+,t) = \kappa\exp\left(\frac{D_{\mathrm{ev}}t}{\ell^2}\right)\operatorname{erfc}\left(\frac{\sqrt{D_{\mathrm{ev}}t}}{\ell}\right). \tag{3.18}$$

[6]For example, for $\eta_\ell > 1$ we have $\alpha_1 > 0$, $\alpha_2 < 0$, $\gamma_2 \le \xi \le \gamma_1$ and the result $W(r,t) \ge 0$ follows from Eq. (3.16a) by noting that $\exp(z^2)\operatorname{erfc}(z)$ is non-negative and decreasing.

The effective 1d extravascular depolarised volume is obtained by integrating the flux to time t. For finite A, the series in Eq. (2.99b) is rewritten as [96]:

$$\Lambda_{1\mathrm{d}}(t) = \sum_{n=1}^{\infty} \frac{1}{\|f_n\|^2} \frac{1 - \exp(-D_{\mathrm{ev}} t q_n^2)}{(1 + \ell^2 q_n^2)\, q_n^2}\,, \tag{3.19}$$

Letting $A \to \infty$ and making use of (3.10) gives, by the same arguments as those leading to Eq. (3.13a),

$$\Lambda_{1\mathrm{d}}(t) = \frac{2}{\pi} \int_0^{\infty} \frac{1 - \exp(-D_{\mathrm{ev}} t q^2)}{1 + \ell^2 q^2} \frac{\mathrm{d}q}{q^2}\,, \tag{3.20}$$

which solves to [96][7]

$$\frac{\Lambda_{1\mathrm{d}}(t)}{\ell} = \frac{2}{\sqrt{\pi}} \frac{\sqrt{D_{\mathrm{ev}} t}}{\ell} + \exp\left(\frac{D_{\mathrm{ev}} t}{\ell^2}\right) \mathrm{erfc}\left(\frac{\sqrt{D_{\mathrm{ev}} t}}{\ell}\right) - 1\,. \tag{3.21}$$

It is therefore convenient to express the effective 1d extravascular depolarised volume in units of effective membrane thickness, and to express diffusion times in units of tracer diffusion length relative to effective membrane thickness.

Equation (3.21) is graphed in Fig. 3.6 jointly with the results of a Monte Carlo simulation (see Appendix 3.6.5 for details). An alternative derivation of Eq. (3.21) is given in Appendix 3.6.2. The above result was obtained by Crank by integrating an expression analogous to Eq. (3.18) from time zero to t; see Eq. (3.37) and Fig. 3.5 of Ref. [176].

The 1d effective depolarised volume is upper bounded by

$$\Lambda_{1\mathrm{d}}(t) \le \kappa t\,, \tag{3.22}$$

as follows by noting that $\exp(z^2)\,\mathrm{erfc}(z) + 2\pi^{-1/2} z - 1 \le z^2$, with $z = \sqrt{D_{\mathrm{ev}} t}/\ell$ in Eq. (3.21).[8] In physical terms, the inequality in (3.22) means that an upper limit

[7] Equation (3.21) also follows directly from integration of Eq. (3.18). A primitive is easily found by integration by parts:

$$\int \exp(z)\,\mathrm{erfc}(z^{1/2})\,\mathrm{d}z = 2\pi^{-1/2} z^{1/2} + \exp(z)\,\mathrm{erfc}(z^{1/2}) + \text{constant}\,.$$

[8] The above inequality is established by noting that both sides vanish at $z = 0$ and that their respective derivatives satisfy $0 \le 2z \exp(z^2)\,\mathrm{erfc}(z) \le 2z$, where the right-hand inequality in this

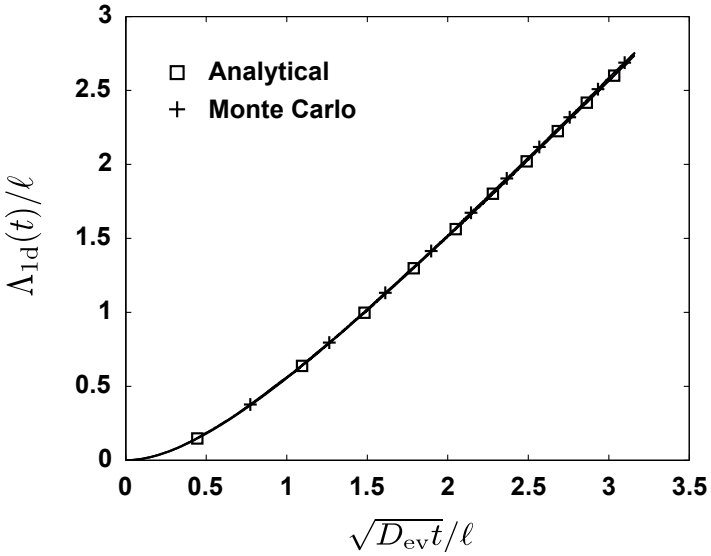

Figure 3.6: **Effective 1d extravascular depolarised volume, Eq. (3.21), with Monte Carlo simulation**. A small subset of computed data points are marked either as squares (analytical formula) or crosses (Monte Carlo simulation) for clarity. The numerical value of the parameters and the deviation of the simulation results from the theoretical expression (3.21) are both found in Appendix 3.6.5.

to the amount of tracer that permeates from extravascular space into the capillaries is attained when the transcapillary exchange is rate-limited by the capillary wall permeability.

3.2 Two-dimensional diffusion

In the case of two-dimensional (2d) diffusion in a plane region with cylindrical symmetry, the Sturm–Liouville equation (2.82) is written as

$$[r f_n'(r)]' + q_n^2 r f(r) = 0\,, \tag{3.23}$$

expression results from

$$\exp(z^2)\operatorname{erfc}(z) = \frac{2}{\sqrt{\pi}}\int_0^\infty \exp(-t^2-2tz)\,\mathrm{d}t \le \frac{2}{\sqrt{\pi}}\int_0^\infty \exp(-t^2)\,\mathrm{d}t = 1\,.$$

for $0 < a < r < A$. The (non-normalised) eigenfunctions can be expressed as [96]:

$$f_n(r) = \cos\delta_n J_0(q_n r) + \sin\delta_n Y_0(q_n r)\,, \tag{3.24}$$

where $J_0(\cdot)$, $Y_0(\cdot)$ are Bessel functions of the first and second kind, respectively, and order zero. The scattering phase shift and the eigenfrequency relation are obtained in the same manner as for the 1d case with the use of the boundary conditions (2.76b) and (2.76c), as shown in Fig. 3.2. This gives [96]:

$$\tan\delta_n = -\frac{J_0(q_n a) + \ell q_n J_1(q_n a)}{Y_0(q_n a) + \ell q_n Y_1(q_n a)} \tag{3.25}$$

and

$$\cos\delta_n J_1(q_n A) + \sin\delta_n Y_1(q_n A) = 0\,. \tag{3.26}$$

Now the following notations are introduced for convenience:

$$P(z) = J_0(z) + (\ell/a) z J_1(z)\,, \qquad Q(z) = Y_0(z) + (\ell/a) z Y_1(z)\,. \tag{3.27}$$

We use the short-hand notation $[P^2+Q^2](z) \equiv P^2(z)+Q^2(z)$, and similarly for other combinations of Bessel functions as in, e.g., $\tan\delta_n = -[P/Q](q_n a)$ and Eqs (3.28) and (3.29) below.

The eigenfunction norm is given by

$$\begin{aligned}
\|f_n\|^2 &= \pi A^2 \left[\cos\delta_n J_0(q_n A) + \sin\delta_n Y_0(q_n A)\right]^2 \\
&\quad - \pi a^2 \left[\cos\delta_n J_0(q_n a) + \sin\delta_n Y_0(q_n a)\right]^2 \\
&\quad - \pi a^2 \left[\cos\delta_n J_1(q_n a) + \sin\delta_n Y_1(q_n a)\right]^2 \\
&= \frac{4\cos^2\delta_n}{\pi q_n^2}\left[\frac{1}{Y_1^2(q_n A)} - \frac{1+\ell^2 q_n^2}{Q^2(q_n a)}\right] \\
&= \frac{4}{\pi q_n^2}\left\{\frac{1}{[J_1^2+Y_1^2](q_n A)} - \frac{1+\ell^2 q_n^2}{[P^2+Q^2](q_n a)}\right\}
\end{aligned} \tag{3.28}$$

with the use of a standard Bessel-function primitive[9] as well as Eqs (3.25) and (3.26),

[9]The required formula is (see, e.g., Ref. [175])

$$\int \left[bJ_0(z) + cY_0(z)\right]^2 z\,\mathrm{d}z = \frac{z^2}{2}\left\{\left[bJ_0(z) + cY_0(z)\right]^2 + \left[bJ_1(z) + cY_1(z)\right]^2\right\}.$$

and the Wronskian of $J_0(\cdot)$ and $Y_0(\cdot)$ [175]:

$$[J_1 Y_0 - J_0 Y_1](z) = \frac{2}{\pi z}\,. \tag{3.29}$$

The expression for the 2d Green's function with cylindrical symmetry on any cross section perpendicular to the capillary axis, and under absorbing intracapillary boundary conditions, is found by inserting $f_n(\cdot)$ and $\|f_n\|^2$, as given, respectively, by Eq. (3.24) and Eq. (3.28), into Eq. (2.79), repeated below for ease of reference:

$$G_{2\mathrm{d}}(r, r', t) = \sum_{n=1}^{\infty} \frac{f_n(r) f_n(r')}{\|f_n\|^2} \exp(-D_{\mathrm{ev}} t q_n^2)\,, \tag{3.30}$$

where the factor $\exp(-R_{\mathrm{ev}} t)$ has been left understood.

The resultant expression is, up to this relaxation term, a particular case of a more general expression given by Carslaw and Jaeger for the loss of heat through the lateral surfaces of an infinite hollow cylinder, the flux of heat being proportional to the respective surface temperature. Imposing an outer zero-flux condition in Eq. 14.8.IV (11) of Ref. [178] yields after some algebra Eq. (3.30) above, with f_n given by (3.24) above. To arrive at their result, Carslaw and Jaeger augmented the response to a unit instantaneous cylindrical surface source with an auxiliary function vanishing at zero time, and such that the Green's function satisfied the boundary conditions at $r = a$ and $r = A$. For this problem, however, the method of the Laplace transformation does not yield a standard transform and the Green's function was obtained in series form by contour integration.

The 2d tracer concentration under absorbing intracapillary boundary conditions is obtained by substituting the normalised eigenfunctions in (2.86b) and making use of (3.25) and (3.29):

$$\psi_{2\mathrm{d}}^{\mathrm{abs}}(r, t) = \sum_{n=1}^{\infty} \frac{4}{\|f_n\|^2} \frac{Y_0(q_n r) P(q_n a) - Q(q_n a) J_0(q_n r)}{[P^2 + Q^2](q_n a)} \frac{\exp(-D_{\mathrm{ev}} t q_n^2)}{q_n^2}\,, \tag{3.31}$$

It may be noted that the abluminal concentration is, in general, non-zero, since the absorbing condition is imposed on the luminal face of the capillary wall (and, moreover, in all of intracapillary space). However, the abluminal concentration does

vanish in the limit that the capillary wall becomes fully permeable ($\ell/a \to 0$) to a given tracer, as is seen from Eq. (3.27).

Neither the Green's function nor the right-hand side of the above expression can, in general, be expressed analytically. However, for sparse capillary networks, Eq. (3.31) can be simplified because the error incurred by the use of Bessel function approximations for large arguments is small; details are found in Appendix 3.6.3. Substituting the asymptotic expansions of $J_1(q_n A)$ and $Y_1(q_n A)$ into (3.26) and using a well-known trigonometric identity, yields an estimate of the eigenfrequencies as

$$q_n A \approx (n+1)\pi + \delta_n \quad \Rightarrow \quad \Delta q_n \approx \frac{\pi + \Delta\delta_n}{A}\,. \tag{3.32}$$

To this accuracy, the eigenfunction norm (3.28) becomes

$$\|f_n\|^2 \approx \frac{4}{\pi q_n^2}\left\{\frac{\pi q_n A}{2} - \frac{1+\ell^2 q_n^2}{[P^2+Q^2](q_n a)}\right\}. \tag{3.33}$$

Lastly, differentiating both sides of (3.25) gives

$$\Delta\delta_n = \frac{2}{\pi}\frac{1+\ell^2 q_n^2}{[P^2+Q^2](q_n a)}\frac{\Delta q_n}{q_n}\,. \tag{3.34}$$

Substituting this expression into (3.32), rearranging and comparing with (3.33) gives

$$\frac{1}{\|f_n\|^2} \approx \frac{q_n \Delta q_n}{2\pi}\,. \tag{3.35}$$

Analogously to the 1d case, when $a/A \ll 1$ the general term of (3.31) is a slowly-varying function of the summation index n, hence the sum becomes an integral in q. The Green's function for sparse capillary networks therefore becomes

$$G_{2\mathrm{d}}(r,r',t) = \frac{1}{2\pi}\int_0^\infty f(r) f(r')\, q \exp(-D_{\mathrm{ev}} t q^2)\,\mathrm{d}q\,, \tag{3.36a}$$

where the non-normalised eigenfunction (3.24) is written as

$$f(r) = \frac{Q(qa)J_0(qr) - P(qa)Y_0(qr)}{\sqrt{[P^2+Q^2](qa)}} \tag{3.36b}$$

with the use of (3.27). The above expressions are formally identical with, respectively, Eq. 14.8 (12) and Eq. 14.8 (13) of Ref. [178].

Similarly, the extravascular concentration for absorbing intracapillary conditions is expressed as [96]:

$$\psi_{\mathrm{2d}}^{\mathrm{abs}}(r,t) = \frac{2}{\pi}\int_0^\infty \frac{P(q')Y_0(q'r') - Q(q')J_0(q'r')}{[P^2+Q^2](q')}\,\frac{\exp(-\varsigma^2 q'^2)}{q'}\,\mathrm{d}q'\,, \tag{3.37}$$

where

$$\varsigma = \frac{\sqrt{D_{\mathrm{ev}}t}}{a} \tag{3.38a}$$

is a normalised diffusion length and

$$r' = r/a\,, \qquad\qquad q' = qa\,. \tag{3.38b}$$

When $q' \to 0$ the integrand of (3.37) has a singularity of order $q'^{-1}(\ln q)^{-2}$, as is seen upon inserting the small-argument forms of the Bessel functions [175]. However, since $\int_0^\epsilon q'^{-1}(\ln q')^{-2}\,\mathrm{d}q' = -(\ln\epsilon)^{-1}$ is finite, the above integral converges, as expected on physical grounds. Equation (3.37) is formally identical with Eq. (15) of Section 13.5.II of Ref. [178], which was obtained by the method of the Laplace transformation.

Differentiating (3.37) with respect to time and accounting for exponential extravascular consumption yields the blood-to-tissue impulse response function for sparse capillary networks. Thus,

$$\begin{aligned} w(\mathbf{r},t) = {} & \frac{2D_{\mathrm{ev}}}{\pi a^2}\int_0^\infty \frac{P(q')Y_0(q'r') - Q(q')J_0(q'r')}{[P^2+Q^2](q')}\,q'\exp(-\varsigma^2 q'^2)\,\mathrm{d}q' \\ & \times \exp(-R_{\mathrm{ev}}t)\,. \end{aligned} \tag{3.39}$$

The fraction in the integrand quantifies the trade-off between capillary permeation and extravascular diffusion through the effective thickness of the capillary wall relative to capillary radius, $\ell/a = D_{\mathrm{ev}}/\kappa a$. In Fig. 3.7a and Fig. 3.7c the blood-to-tissue impulse response function has been plotted for two widely different values of the normalised effective membrane thickness, $\ell/a = D_{\mathrm{ev}}/\kappa a$, and for a range of extravascular diffusion times. The blood-to-tissue impulse response function attains its maximum at a position $r_{\max} > a$, since the gradient at the capillary wall, $\mathbf{n}\nabla w(\mathbf{a}_+,t) = (\kappa/D_{\mathrm{ev}})w(\mathbf{a}_+,t) > 0$.

The approximate arterial-to-intracapillary impulse response function (2.19a) is obtained from (3.39), noting that $[PY_0 - QJ_0](q')$ evaluates to $2\ell/\pi a$ with the use of the Wronskian (3.29). Integrating (3.39) yields the blood-to-tissue step response function as

$$W(\mathbf{r},t) = \frac{2}{\pi}\int_0^\infty \frac{P(q')Y_0(q'r') - Q(q')J_0(q'r')}{[P^2+Q^2](q')}\,\frac{1-\exp[-\varsigma^2(q'^2+\eta_a)]}{q'^2+\eta_a}\,q'\,\mathrm{d}q'\,, \tag{3.40a}$$

where

$$\eta_a = \frac{a^2 R_{\mathrm{ev}}}{D_{\mathrm{ev}}}\,. \tag{3.40b}$$

Several examples of $W(r,t)$ are plotted in Fig. 3.7b and Fig. 3.7d. The amplitude of the step response at the capillary wall is easily evaluated with the use of a standard Bessel-function identity. It can also be obtained from the flux relation (2.25), valid for absorbing intracapillary conditions, which in terms of $W(\mathbf{a}_+,t)$ reads

$$\kappa S[1 - W(\mathbf{a}_+,t;R_{\mathrm{ev}}=0)] = \kappa S\psi_{\mathrm{ev}}^{\mathrm{abs}}(\mathbf{a}_+,t;R_{\mathrm{ev}}=0) = \frac{\mathrm{d}\Lambda(t)}{\mathrm{d}t}\,.$$

Differentiating (3.43) then gives[10]

$$W(\mathbf{a}_+,t;R_{\mathrm{ev}}=0) = 1 - \frac{1}{\kappa S}\frac{\mathrm{d}\Lambda_{2\mathrm{d}}(t)}{\mathrm{d}t} \tag{3.41a}$$

$$= \frac{4\ell}{\pi^2 a}\int_0^\infty \frac{1-\exp(-\varsigma^2 q'^2)}{[P^2+Q^2](q')}\frac{\mathrm{d}q'}{q'}\,. \tag{3.41b}$$

Under absorbing intracapillary conditions, the tissue-to-blood tracer flux is given by

$$\begin{aligned}\mathbf{n}\mathbf{j}_{\kappa,2\mathrm{d}}^{\mathrm{abs}}(\mathbf{a},t) &= \kappa\psi_{2\mathrm{d}}^{\mathrm{abs}}(\mathbf{a}_+,t)\\ &= \frac{4D_{\mathrm{ev}}}{\pi^2 a}\int_0^\infty \frac{\exp(-\varsigma^2 q'^2)}{[P^2+Q^2](q')}\frac{\mathrm{d}q'}{q'}\,,\end{aligned} \tag{3.42}$$

[10]Equation (A12) of Lee and Fronek [44] apparently contains a typographical error which may result in large negative concentrations. If in the integrand of that equation ka/D is written instead of D/ka, and if the exponent is corrected dimensionally by writing a^2 instead of a, then Eq. (A12) of Lee and Fronek coincides with Eq. (3.41b) in this Thesis.

where (3.29) has been used. Integrating the amount of tracer cleared from the peri-capillary region per unit time, given by $2\pi a \mathbf{n}\mathbf{j}^{\mathrm{abs}}_{\kappa,2\mathrm{d}}(\mathbf{a},t)$, yields the effective 2d extra-vascular depolarised volume:

$$\Lambda_{2\mathrm{d}}(t) = \frac{8a^2}{\pi}\int_0^\infty \frac{1-\exp(-\varsigma^2 q'^2)}{[P^2+Q^2](q')}\frac{\mathrm{d}q'}{q'^3}\,, \tag{3.43}$$

which is valid for sparse capillary networks.

When the diffusion length is small in terms of capillary radius, the exchange of tracer molecules is effectively confined to a shallow region adjacent to the capillary wall and can be treated as one-dimensional exchange, as discussed previously. In this situation the effective 2d extravascular depolarised volume is therefore related to its 1d counterpart by [96]:

$$\Lambda_{2\mathrm{d}}(t) \approx 2\pi a \Lambda_{1\mathrm{d}}(t)\,. \tag{3.44}$$

The accuracy of this expression is given by the relative difference between the amplitude of the abluminal concentration under absorbing intracapillary boundary conditions for the 1d and 2d cases. As shown in Fig. 3.8, this difference increases with capillary permeability (i.e., with lower ℓ/a ratios, D_{ev} being held fixed) and diffusion time. There is, however, a wide range of ℓ/a ratios for which (3.44) is reasonably accurate at short diffusion times.

On the other hand, when the diffusion length is much greater than the capillary radius, the exchange becomes essentially two-dimensional and (3.43) evaluates to [96]:

$$\Lambda_{2\mathrm{d}}(t) \approx \frac{2\pi D_{\mathrm{ev}} t}{\ln(\sqrt{D_{\mathrm{ev}}t}/a) + \ell/a - \gamma'}\,, \tag{3.45}$$

with $\gamma' = \gamma - \ln 2 \approx -0.1159$, where $\gamma \approx 0.5772$ is Euler's constant. The above formula is derived in Appendix 3.6.4. Figure 3.9 plots $\Lambda_{2\mathrm{d}}(t)/\pi a^2$ as a function of normalised diffusion length for a range of $D_{\mathrm{ev}}/\kappa a$ ratios. In Fig. 3.10 the results of a Monte Carlo simulation are graphed together with equations (3.43), (3.44) and (3.45). For details on Monte Carlo simulations see Appendix 3.6.5.

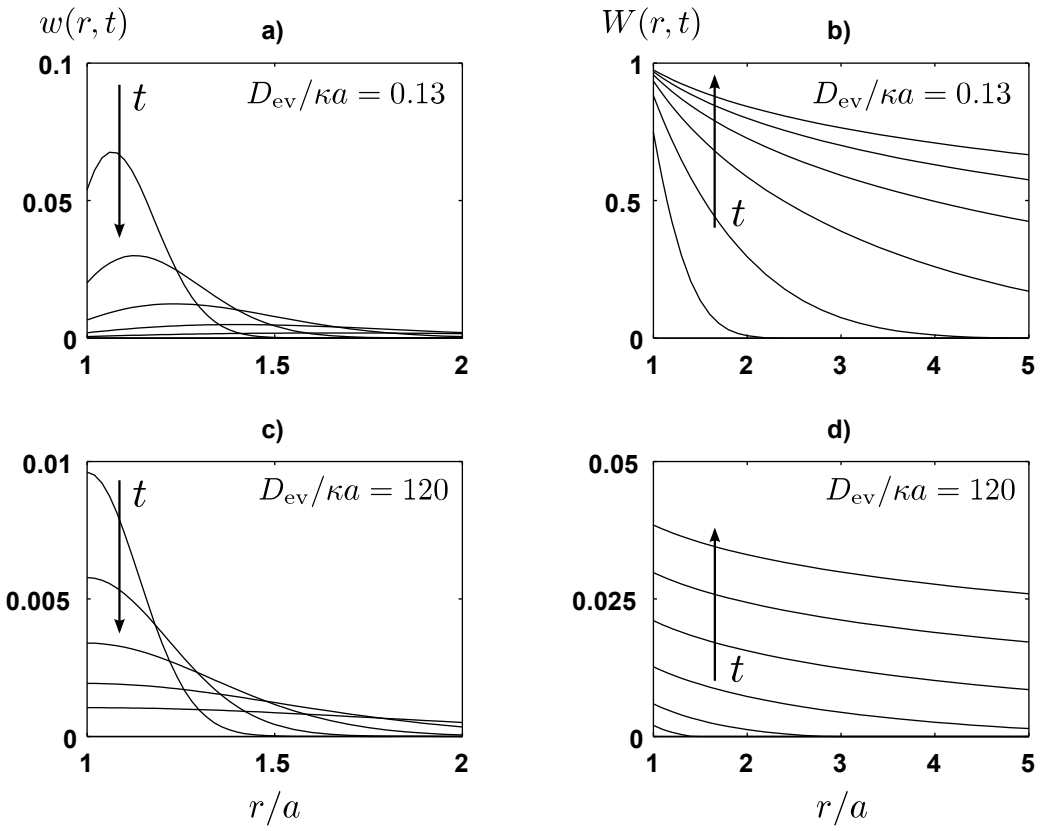

Figure 3.7: **Single-capillary blood-to-tissue impulse response function** $w(r,t)$, Eq. (3.39), **and step response function** $W(r,t)$, Eq. (3.40a), for sparse capillary networks ($a/A \ll 1$) in the absence of tracer consumption, plotted as functions of radial distance (r/a) for a range of diffusion lengths ($\sqrt{D_{\mathrm{ev}}t}/a$) and a pair of values of the normalised effective membrane thickness, $\ell/a = D_{\mathrm{ev}}/\kappa a$. For panels a), c), the time scale is $\sqrt{D_{\mathrm{ev}}t}/a = 10^{-1} - 10^{-0.2}$ with five logarithmically equispaced time instants. For panels b), d), the time scale is $\sqrt{D_{\mathrm{ev}}t}/a = 10^{-0.5} - 10^{2}$ with six logarithmically equispaced time instants. For these examples, maximum numerical integration error is $\sim 0.3\%$, as estimated from the deviation of $1 - W(r > a, t = 0; R_{\mathrm{ev}} = 0)$ from unity.

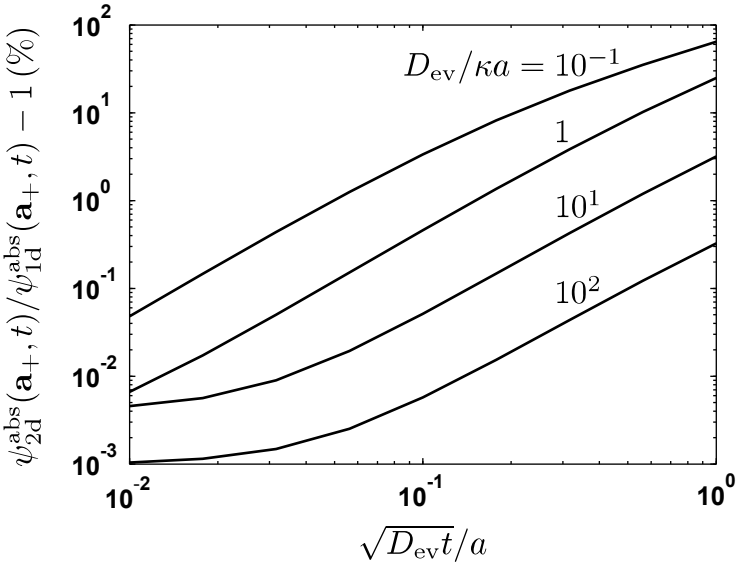

Figure 3.8: **Percentage difference between 1d and 2d abluminal concentrations under absorbing intracapillary boundary conditions for sparse capillary networks at short diffusion times**.

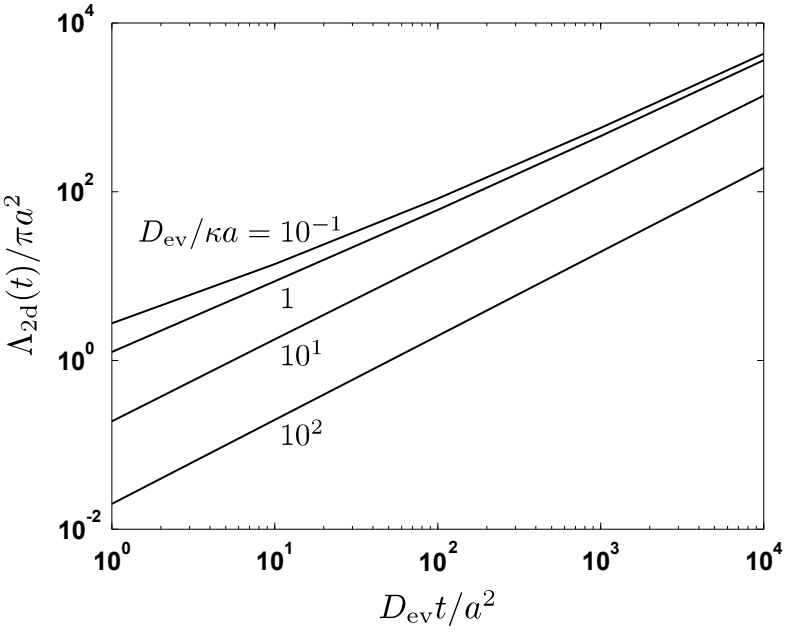

Figure 3.9: **Effective 2d extravascular depolarised volume**. Equation (3.43) was integrated numerically for $D_{\mathrm{ev}}t/a^2 = 10^n$ $(n = 1, 2, 3, 4)$ and the shown values of $D_{\mathrm{ev}}/\kappa a$. The relative error incurred in using the simplified formula (3.45) is plotted in Fig. 3.16 (Appendix 3.6.4).

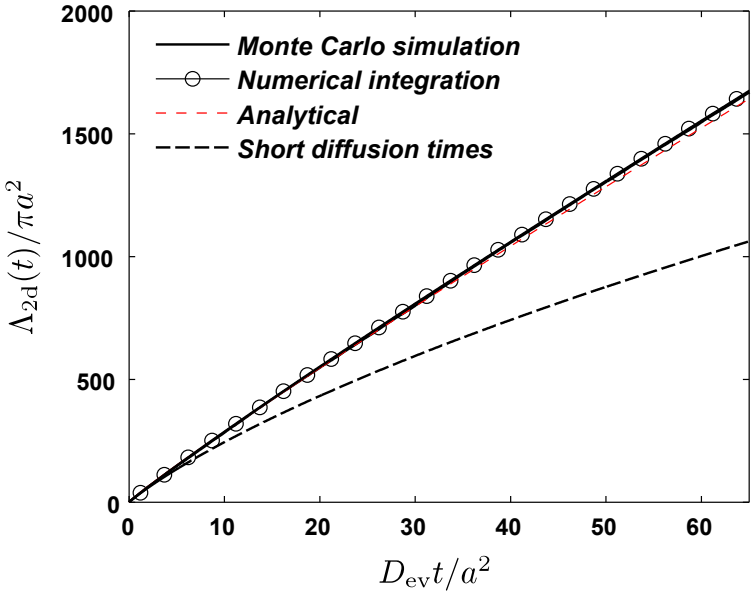

Figure 3.10: **Effective 2d extravascular depolarised volume** vs normalised diffusion length. The curves labelled *Numerical integration* and *Analytical* were obtained, respectively, by numerical integration of (3.43) and from the approximate analytical expression (3.45). Also shown is the asymptotic expression for short diffusion times (3.44). Parameter values: $a = 3.5\ \mu$m, $A/a \approx 49$, $\kappa = 5.0 \times 10^{-2}\ \mu\text{m}\,\text{ms}^{-1}$, $D_{\text{ev}} = 1.0\ \mu\text{m}^2\,\text{ms}^{-1}$.

3.3 Influence of the boundary conditions

Since microvascular networks exhibit highly irregular geometries [55] and, further, are subject to arteriolar vasomotion [72], tracer fluxes can occur across any arbitrarily defined boundaries in the extravascular space [55]. It has been reported [55] that quantitative predictions based on the Krogh model can be quite sensitive to the choice of boundary conditions; for example, imposing a zero-flux condition at the outer cylinder boundary can lead to the extent of hypoxic tissue being artefactually overestimated.

In this Chapter the case is considered in which the tracer diffusion length in extravascular space is small compared to typical intercapillary distances; refer to Sections 2.1.3 and 2.3.5. As shown by the developments leading to Eqs (3.4b) and (3.26), the eigenfrequencies are determined by the boundary conditions at the capillary wall and the outer pericapillary surface. When the pericapillary region is large, or the interval of extravascular diffusion times is small, the effect of the exchange conditions near the capillary wall (resp., near the diffusion watershed) becomes, respectively, more (resp., less) important in relative terms. In order to assess, in a greatly simplified case, the influence of the boundary conditions at the outer boundary of the pericapillary region, we consider the segment $0 \leq r \leq A$ and impose a zero-concentration boundary condition, rather than the zero-flux condition of previous calculations, at the endpoint $r = A$. The nth eigenfrequency for the zero-concentration case, $\hat{q}_n$, and that for the zero-flux condition, Eq. (3.4b), satisfy the relation

$$\hat{q}_n - q_n = \frac{\pi/2 + \hat{\delta}_n - \delta_n}{A} \,. \tag{3.46}$$

Thus, (i) for large pericapillary regions the eigenfrequencies are barely sensitive to the pericapillary boundary conditions, and (ii) the relative difference between corresponding eigenfrequencies for various homogenous boundary conditions decreases as $q_n A \sim n^{-1}$, and is barely sensitive to pericapillary radius.

Next, we estimate the time at which interactions between two neighbouring capillary segments begin to affect the concentration in pericapillary space at some fixed position along the segments. This provides further quantitative insight into the range

of diffusion times for which the single-capillary approximation may be deemed accurate.

First, the case in which capillary interactions are negligibly low is conveniently simulated by applying at time $t = 0$ a step change in concentration at the plane boundary of a semi-infinite medium. Thus, the step response for this case is obtained by letting $\kappa \to \infty$ in (3.17):

$$W(r,t) = \operatorname{erfc}\left(\frac{r}{\sqrt{4D_{\mathrm{ev}}t}}\right), \qquad r \geq 0, \quad t > 0\,. \tag{3.47}$$

At the other extreme, a situation of maximal capillary interaction can be represented by two planar tracer sources a distance $2A$ apart, each producing a constant unit concentration just outside the capillary wall, so that the net flux of tracer is zero at the mid-point position ($r = A$). The step response for this case is thus obtained from Eq. (3.7), with the use of (3.4b) and (3.6), on letting $\kappa \to \infty$. This gives, for $0 \leq r \leq A$ and $t > 0$:

$$W(r,t) = 1 - \frac{4}{\pi}\sum_{n=1}^{\infty}\frac{\sin q_n r}{2n-1}\exp(-D_{\mathrm{ev}}tq_n^2)\,, \qquad q_n = \frac{2n-1}{2A}\,\pi\,. \tag{3.48}$$

Let $t_{\%}$ denote the threshold time at which the deviation between the concentrations given by (3.17) and (3.48) attains a specified percentage. Figure 3.11 shows the variation of $t_{\%}$ with distance to the nearest capillary source. The interval of diffusion times has been chosen so that $D_{\mathrm{ev}}t/A^2 \leq 1$. It is seen that threshold times decrease with increasing distance from the tracer source, i.e., nearer the diffusion watershed, as expected. Variations in threshold time are almost linear for intermediate locations, but markedly non-linear at positions near the capillary, where the concentration of tracer is barely influenced by the chosen boundary conditions. If the acceptable extent of capillary interaction is increased, the threshold times also increase.

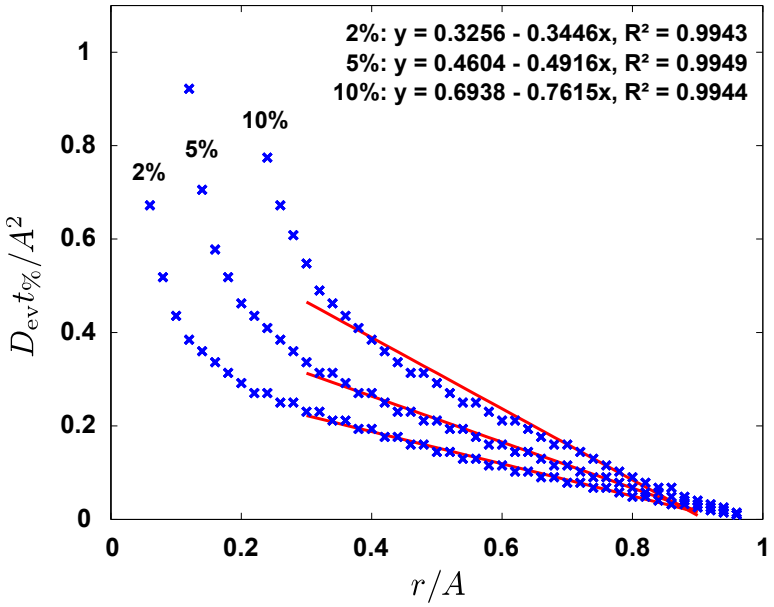

Figure 3.11: **Threshold time, $t_{\%}$, for interactions between two planar tracer sources**. Percentage deviations (2%, 5% and 10%) are with respect to the non-interaction case. Least-squares lines for $0.3 \leq r/A \leq 0.9$ are shown in red.

3.4 Upper bound on spatially averaged step response function and lowest eigenvalue

In the absence of tracer consumption, the difference between the blood-to-tissue step response function and its spatially averaged value is given by

$$\begin{aligned} |W(t) - W(\mathbf{r},t)| &= \left|\psi_{\mathrm{ev}}^{\mathrm{abs}}(t) - \psi_{\mathrm{ev}}^{\mathrm{abs}}(\mathbf{r},t)\right| \\ &= \frac{1}{V_{\mathrm{ev}}} \left| \sum_{n=1}^{\infty} \left[\frac{\kappa S f_n(\mathbf{a}_+)}{\lambda_n}\right]^2 \left[1 - \lambda_n \tau_{\mathrm{ev}} \frac{f_n(\mathbf{r})}{f_n(\mathbf{a}_+)}\right] \exp(-\lambda_n t) \right|, \end{aligned} \tag{3.49a}$$

where Eqs (2.11), (2.2c), (2.86a) and (2.92a) have been used, and the label '$R_{\mathrm{ev}} = 0$' has been omitted for simplicity. Since the extravascular concentration under absorbing intracapillary conditions is a concave function of position, and since the concentration gradient is sharpest at the abluminal face of the capillary wall, the difference (3.49a) between the local and the spatially averaged value of the concentration is

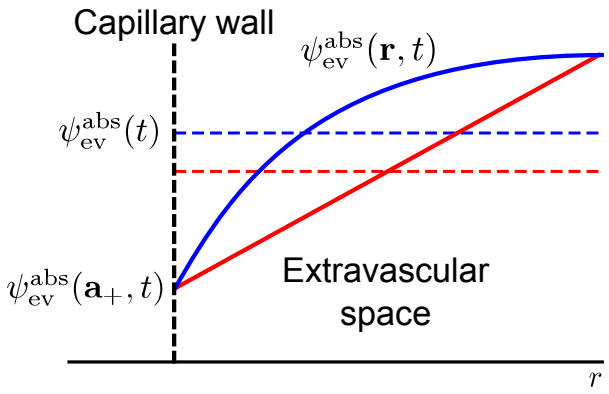

Figure 3.12: **Illustration of inequality** (3.49b). Linear and non-linear concentration profiles are shown; broken lines represent the respective spatially averaged concentrations.

greatest at $\mathbf{r} = \mathbf{a}_+$ (Fig. 3.12), as expected on physical grounds. Thus

$$\begin{aligned} |W(t) - W(\mathbf{r},t)| &\le \psi_{\rm ev}^{\rm abs}(t) - \psi_{\rm ev}^{\rm abs}(\mathbf{a}_+,t) \\ &= \frac{1}{V_{\rm ev}} \sum_{n=1}^{\infty} \left[\frac{\kappa S f_n(\mathbf{a}_+)}{\lambda_n} \right]^2 (1 - \lambda_n \tau_{\rm ev}) \exp(-\lambda_n t) \\ &\le \psi_{\rm ev}^{\rm abs}(t + \tau_{\rm ev}) \end{aligned} \tag{3.49b}$$

with the use of the inequality $1 - z \le \exp(-z)$ and Eq. (2.92a).

Next, we obtain an upper bound on the lowest eigenvalue, λ_1. Since the right-hand side of (3.49b) is non-negative, and since the sequence of eigenvalues is non-decreasing, then at least the first term of the series in (3.49b) must be non-negative. Noting that λ_n maps to $\lambda_n + R_{\rm ev}$ when extravascular absorption occurs, we obtain

$$\lambda_1 \le R_{\rm ev} + \frac{1}{\tau_{\rm ev}} \quad \Rightarrow \quad q_1^2 \lesssim \frac{R_{\rm ev}}{D_{\rm ev}} + \frac{1}{A^2} \frac{\kappa a}{D_{\rm ev}} \,. \tag{3.50}$$

3.5 Discussion

In this Chapter, one-dimensional diffusion has been considered in detail because this case is applicable to (i) two-dimensional diffusion at sufficiently short times and (ii) in cases where the tissue geometry has a dominant direction.

Nugent and Jain [182] quantified transport of various fluorescent test molecules in the rabbit ear chamber using a 1d diffusion model. Test molecules included bovine

serum albumin and several dextrans, all having molecular weights of the order of 1.7 – 6.7×10^4 (i.e., much greater than that of Gd-DTPA). Surgically implanted chambers were approximately 40 μm thick and 5.4 mm in diameter. Because of the zero-flux constraints imposed by the chamber plates above and below the tissue layer, these authors assumed that photometric measurement yielded total integrated concentrations essentially equivalent to those that would arise from a planar source. Interstitial diffusion coefficients were determined by fitting the concentration at positions just outside the capillaries to a series of concentration-time measurements at a set of uniformly spaced positions aligned perpendicularly to capillaries in regions where intercapillary distances were usually 100 μm. These authors made use of the equation in the second line of Eq. (3.51):

$$\begin{aligned}\psi_{\mathrm{ev}}(r,t;R_{\mathrm{ev}}=0;\kappa\to\infty) &= \frac{\mathrm{d}W(r,t;R_{\mathrm{ev}}=0;\kappa\to\infty)}{\mathrm{d}t} * \psi_0(t) \\ &= \frac{2}{\sqrt{\pi}}\int_{r/\sqrt{4D_{\mathrm{ev}}t}}^{\infty} \psi_0\left(t-\frac{r^2}{4D_{\mathrm{ev}}z^2}\right)\exp(-z^2)\,\mathrm{d}z\,, \end{aligned} \tag{3.51}$$

where $\psi_0(t)$ is the concentration measured just outside the capillary wall. Here, the use of Eq. (3.17) is justified because in the limit of high capillary wall permeability the amplitude of the concentration becomes continuous at the capillary wall.

Nugent and Jain estimated the onset of diffusive interactions among neighbouring capillaries by comparing the concentration predicted by the 1d model of non-interaction, and that due to two sources of equal strength separated by one intercapillary distance. The time at which the deviations between these concentrations reached 2% was approximated by the expression $t_{2\%} = 0.57 - 1.30 \times (r/A) + 1.14 \times (r/A)^2$ for $0.1 \leq r/A \leq 0.6$; see Eq. (10) of Ref. [182]. To check this procedure, we fitted a least-squares parabola to the difference between Eqs (3.47) and (3.48) above, and obtained the comparable result, $D_{\mathrm{ev}}t_{\%}/A^2 = 0.5088 - 1.180 \times (r/A) + 0.9008 \times (r/A)^2$, with $R^2 = 0.9724$.

3.6 Appendices

3.6.1 Derivation of the 1d Green's function for sparse capillary networks

In this Appendix we evaluate the 1d Green's function for sparse capillary networks with absorbing intravascular boundary conditions, Eq. (3.11).

Setting $x = r + r' - 2a$ and $x' = r - r'$ for brevity, the Green's function (3.5) for diffusion in one spatial dimension can be rewritten as

$$G(r, r', t) = \sum_{n=1}^{\infty} \left[\frac{\cos q_n x + \cos q_n x'}{2} + \frac{\ell q_n \sin q_n x - \cos q_n x}{1 + \ell^2 q_n^2} \right] \frac{\exp(-D_{\mathrm{ev}} q_n^2 t)}{\|f_n\|^2} , \quad (3.52)$$

where Eq. (3.3b) for δ'_n has been used. The above series becomes an integral in the limit as $A \to \infty$, as discussed previously in Section 3.1. The latter will be decomposed into three simpler integrals, G_1, G_2 and G_3, for ease of evaluation, as follows:

$$\begin{aligned} G_1(r, r', t) &= \frac{1}{2} \sum_{n=1}^{\infty} \frac{\cos(q_n x) \exp(-D_{\mathrm{ev}} q_n^2 t)}{\|f_n\|^2} \\ &= \frac{1}{\pi} \int_0^{\infty} \cos(qx) \exp(-D_{\mathrm{ev}} q^2 t) \, \mathrm{d}q \\ &= \frac{1}{\sqrt{4\pi D_{\mathrm{ev}} t}} \exp\left(-\frac{x^2}{4 D_{\mathrm{ev}} t} \right) , \end{aligned} \quad (3.53a)$$

where the expression (3.10) for the norm has been used. Note that the integral in the second line of (3.53a) reduces to a standard Gaussian integral.[11]

Similarly,

$$G_2(r, r', t) = \frac{1}{\sqrt{4\pi D_{\mathrm{ev}} t}} \exp\left(-\frac{x'^2}{4 D_{\mathrm{ev}} t} \right) . \quad (3.53b)$$

Lastly, the remaining term in the right-hand side of Eq. (3.52) yields the integral

$$G_3(r, r', t) = \frac{2}{\pi} \int_0^{\infty} \frac{\ell q \sin qx - \cos qx}{1 + \ell^2 q^2} \exp(-D_{\mathrm{ev}} t q^2) \, \mathrm{d}q' . \quad (3.53c)$$

[11] The well-known Gaussian integral below (with a, b real numbers and $a > 0$) is evaluated as

$$\int_{-\infty}^{\infty} \exp(-az^2 \pm bz) \, \mathrm{d}z = \sqrt{\frac{\pi}{a}} \exp\left(\frac{b^2}{4a} \right) .$$

The above integral is evaluated below by differentiation with respect to x, with t treated as a parameter. After straightforward manipulations, we get

$$\ell \frac{\mathrm{d}G_3(x,t)}{\mathrm{d}x} = G_3(x,t) + 2G_1(x,t)\,. \tag{3.54a}$$

This expression guarantees that the boundary condition at the capillary wall is satisfied, i.e., that $D_{\mathrm{ev}}\mathbf{n}\nabla G(a_+,r',t) = \kappa G(a_+,r',t)$, upon noting that $G_1(a_+,r',t) = G_2(a_+,r',t)$ and that $G_1'(a_+,r',t) = -G_2'(a_+,r',t)$. The solution of (3.54a) is given by

$$G_3(x,t) = G_3(x=0,t)\exp(x/\ell) + (2/\ell)\exp(x/\ell) * G_1(x,t)\,. \tag{3.54b}$$

The convolution on the right-hand side of the above expression is with respect to x and evaluates to

$$\frac{1}{\ell}\exp\left(\frac{x}{\ell} + \frac{D_{\mathrm{ev}}t}{\ell^2}\right)\left[\mathrm{erfc}\left(\frac{\sqrt{D_{\mathrm{ev}}t}}{\ell}\right) - \mathrm{erfc}\left(\frac{x}{\sqrt{4D_{\mathrm{ev}}t}} + \frac{\sqrt{D_{\mathrm{ev}}t}}{\ell}\right)\right]. \tag{3.54c}$$

On the other hand, the term

$$G_3(x=0,t) = -\frac{2}{\pi}\int_0^\infty \frac{\exp(-D_{\mathrm{ev}}tq^2)}{1+\ell^2q^2}\,\mathrm{d}q' \tag{3.54d}$$

is evaluated by differentiating both sides of the above equation with respect to t. The resultant first-order equation

$$\frac{\mathrm{d}G_3(x=0,t)}{\mathrm{d}t} = \frac{D_{\mathrm{ev}}}{\ell^2}\left[G_3(x=0,t) + \frac{1}{\sqrt{\pi D_{\mathrm{ev}}t}}\right]$$

is solved by standard methods to give

$$G_3(x=0,t) = -\frac{1}{\ell}\exp\left(\frac{D_{\mathrm{ev}}t}{\ell^2}\right)\mathrm{erfc}\left(\frac{\sqrt{D_{\mathrm{ev}}t}}{\ell}\right), \tag{3.54e}$$

which satisfies the initial condition $G_3(x=0,t=0) = -1/\ell$, from Eq. (3.54d). Then substitution of (3.54c) and (3.54e) in (3.54b) gives

$$G_3(r,r',t) = -\frac{1}{\ell}\exp\left(\frac{r+r'-2a}{\ell} + \frac{D_{\mathrm{ev}}t}{\ell^2}\right)\mathrm{erfc}\left(\frac{r+r'-2a}{\sqrt{4D_{\mathrm{ev}}t}} + \frac{\sqrt{D_{\mathrm{ev}}t}}{\ell}\right). \tag{3.54f}$$

Equation (3.11) in the main body of the text then results upon summing the terms $G_1(r,r',t)$, $G_2(r,r',t)$ and $G_3(r,r',t)$ obtained above.

3.6.2 Derivation of $\Lambda_{\mathbf{1d}}(t)$ for sparse capillary networks

In this Appendix we provide an alternative derivation of the expression for the effective 1d extravascular depolarised volume for sparse capillary networks, Eq. (3.20). The method involves perturbing the solution of the eigenvalue problem on the interval $0 \leq r \leq A$ with absorbing and zero-flux boundary conditions at $r = 0$ and $r = A$, respectively. For this latter problem, the eigenfunctions, g_n, and eigenfrequencies, k_n, are given by

$$g_n(r) = \sin k_n r \,, \tag{3.55a}$$

$$k_n = (n - 1/2)(\pi/A) \,, \tag{3.55b}$$

for $n = 1, 2, \ldots$, where $g_n(0) = g_n'(A) = 0$. The norm is

$$\|g_n\|^2 = A/2 \,, \tag{3.55c}$$

Expanding the eigenfrequency (3.4b) and the eigenfunction norm (3.6) in powers of the small ratio a/A gives

$$q_n = k_n \left\{ 1 + \frac{a}{A} - \frac{\delta_n''}{k_n A} + \mathcal{O}[a/A]^2 \right\} \tag{3.56a}$$

and

$$\|f_n\|^2 = \|g_n\|^2 \left[1 - \frac{a}{A} + \frac{\sin 2\delta_n'}{2 q_n A} \right] , \tag{3.56b}$$

where

$$\delta_n'' \equiv \pi/2 - \delta_n' = \arctan \ell q_n \,, \tag{3.56c}$$

see (3.3b). With use of the above equations we obtain

$$\frac{1}{\|f_n\|^2 q_n^2} = \frac{1}{\|g_n\|^2 k_n^2} \left\{ 1 - \frac{a}{A} + \frac{2\delta_n''}{k_n A} - \frac{\sin 2\delta_n''}{2 q_n A} + \mathcal{O}[a/A]^2 \right\} \tag{3.57a}$$

and

$$\exp(-D_{\mathrm{ev}} t q_n^2) = \exp(-D_{\mathrm{ev}} t k_n^2) \left\{ 1 + 2 D_{\mathrm{ev}} t \, \frac{k_n^2 a - k_n \delta_n''}{A} + \mathcal{O}[a/A]^2 \right\} . \tag{3.57b}$$

After substitution of Eq. (3.57a) and Eq. (3.57b) into Eq. (2.24), and rearranging conveniently, the effective 1d extravascular depolarised volume is recast to first order in a/A as

$$\Lambda_{1\mathrm{d}}(t) = A - a - \sum_{n=1}^{\infty} \frac{\sin^2\delta'_n}{\|f_n\|^2} \frac{\exp(-D_{\mathrm{ev}} t q_n^2)}{q_n^2} \tag{3.58a}$$

$$= A - a + \sum_{n=1}^{\infty} \frac{1 - \exp(-D_{\mathrm{ev}} t k_n^2)}{\|g_n\|^2 k_n^2} \tag{3.58b}$$

$$+ \sum_{n=1}^{\infty} \frac{\cos^2\delta'_n}{\|g_n\|^2 k_n^2} \exp(-D_{\mathrm{ev}} t k_n^2) \tag{3.58c}$$

$$- \sum_{n=1}^{\infty} \frac{1}{\|g_n\|^2 k_n^2} \tag{3.58d}$$

$$- \sum_{n=1}^{\infty} \frac{1}{A} \frac{T_n}{\|g_n\|^2 k_n^2} \exp(-D_{\mathrm{ev}} t k_n^2) \tag{3.58e}$$

$$+ \sum_{n=1}^{\infty} \frac{1}{A} \frac{T_n \cos^2\delta'_n}{\|g_n\|^2 k_n^2} \exp(-D_{\mathrm{ev}} t k_n^2)\,, \tag{3.58f}$$

where

$$T_n = -a + \frac{2\delta''_n}{k_n} - \frac{\sin 2\delta'_n}{2q_n}\,. \tag{3.58g}$$

It may be noticed that Eq. (3.58a) has been decomposed into a number of terms which are non-singular in the limit as k_n and q_n approach 0.

First term

Since $\Delta k_n \to \pi/A = (\pi/2)/\|g_n\|^2$ as A grows large, the infinite sum in (3.58b) becomes an integral, which is easily evaluated as

$$\Lambda_1(t) \equiv \sum_{n=1}^{\infty} \frac{1 - \exp(-D_{\mathrm{ev}} t k_n^2)}{\|g_n\|^2 k_n^2} = \frac{2}{\pi} \int_0^{\infty} \frac{1 - \exp(-D_{\mathrm{ev}} t k^2)}{k^2}\, \mathrm{d}k$$
$$= \frac{2}{\sqrt{\pi}} \sqrt{D_{\mathrm{ev}} t}\,. \tag{3.59}$$

Second term

Substituting the identity $\cos^2\delta'_n = (1+\tan^2\delta'_n)^{-1} = \ell^2 q_n^2/(1+\ell^2 q_n^2)$ in (3.58c) and using (3.56a) gives

$$\begin{aligned}\Lambda_2(t) &\equiv \sum_{n=1}^{\infty} \frac{\cos^2\delta'_n}{\|g_n\|^2}\frac{\exp(-D_{\mathrm{ev}}tk_n^2)}{k_n^2} = \sum_{n=1}^{\infty}\frac{1}{\|g_n\|^2}\frac{\ell^2 q_n^2}{1+\ell^2 q_n^2}\frac{\exp(-D_{\mathrm{ev}}tk_n^2)}{k_n^2}\\ &\approx \sum_{n=1}^{\infty}\frac{1}{\|g_n\|^2}\frac{\ell^2}{1+\ell^2 k_n^2}\exp(-D_{\mathrm{ev}}tk_n^2)\end{aligned} \tag{3.60}$$

with approximate termwise relative error

$$\frac{2a/A - 2\delta''_n/k_nA}{1+\ell^2 q_n^2} = \mathcal{O}[a/A]\,.$$

As $A\to\infty$, the infinite sum in the second line of (3.60) becomes an integral:

$$\Lambda_2(t) = \frac{2\ell^2}{\pi}\int_0^{\infty}\frac{\exp(-D_{\mathrm{ev}}tk^2)}{1+\ell^2k^2}\,\mathrm{d}k = \ell\exp\left(\frac{D_{\mathrm{ev}}t}{\ell^2}\right)\mathrm{erfc}\left(\frac{\sqrt{D_{\mathrm{ev}}t}}{\ell}\right), \tag{3.61}$$

which remains bounded for all values of t (see formula 7.1.13 of Ref. [175]). For times such that $\sqrt{D_{\mathrm{ev}}t}/\ell \ll 1$, the main contribution to the integral in Eq. (3.61) comes from the interval $k \lesssim 1/\ell \ll 1/\sqrt{D_{\mathrm{ev}}t}$. Thus, approximating the exponential term in the integrand of (3.61) by unity, we obtain

$$\Lambda_2(t) \approx \frac{2\ell^2}{\pi}\int_0^{\infty}\frac{\mathrm{d}k}{1+\ell^2k^2} = \ell = \frac{D_{\mathrm{ev}}}{\kappa}\,.$$

On the other hand, for large times ($\sqrt{D_{\mathrm{ev}}t}/\ell \gg 1$), practically all the contribution to the integral in Eq. (3.61) is due to values of $k \lesssim 1/\sqrt{D_{\mathrm{ev}}t} \ll 1/\ell$. Hence,

$$\Lambda_2(t) \approx \frac{2\ell^2}{\pi}\int_0^{\infty}\exp(-D_{\mathrm{ev}}tk^2)\,\mathrm{d}k = \frac{\ell^2}{\sqrt{\pi D_{\mathrm{ev}}t}}\,.$$

Third term

Substituting (3.55b) into (3.58d) results in the well-known series

$$\Lambda_3(t) \equiv -\sum_{n=1}^{\infty}\frac{1}{\|g_n\|^2k_n^2} = -\frac{8A}{\pi^2}\sum_{n=1}^{\infty}\frac{1}{(2n-1)^2} = -A\,. \tag{3.62}$$

Fourth term

The fourth term in the decomposition of $\Lambda(t)$, Eq. (3.58e), is repeated here for convenience

$$\Lambda_4(t) \equiv -\sum_{n=1}^{\infty} \frac{\exp(-D_{\rm ev} t k_n^2)}{\|g_n\|^2 k_n^2} \frac{T_n}{A} \,.$$

Since $A\|g_n\|^2 k_n^2 = \mathcal{O}[n^2]$, the leading contribution to the above series comes from terms with a relatively small value of index n; the respective eigenfrequencies are correspondingly small and the exponential term $\exp(-D_{\rm ev} t k_n^2) \sim \exp(-D_{\rm ev} t n^2/A^2)$ is close to unity, since $\sqrt{D_{\rm ev} t} \ll A$ by assumption. Thus, the series in (3.58e) is evaluated with small error by letting $k_n, q_n \to 0$. In this limit, $\delta_n'' = \arctan \ell q_n \to \ell q_n$, hence the approximation $\sin 2\delta_n'' \approx 2\delta_n''$ gives

$$T_n(k_n \to 0) = -a + \frac{2\delta_n''}{k_n} - \frac{\delta_n''}{q_n} + \mathcal{O}[a/A]^2 = -a + \ell + \mathcal{O}[a/A] \,. \tag{3.63}$$

The right-hand side of Eq. (3.58e) is conveniently rewritten as

$$\Lambda_4(t) \equiv -\sum_{n=1}^{\infty} \frac{1}{\|g_n\|^2 k_n^2} \frac{T_n}{A} + \sum_{n=1}^{\infty} \frac{1 - \exp(-D_{\rm ev} t k_n^2)}{\|g_n\|^2 k_n^2} \frac{T_n}{A} \,. \tag{3.64}$$

The first term in (3.64) evaluates, approximately, to

$$-\frac{8}{\pi^2} \sum_{n=1}^{\infty} \frac{T_n(k_n \to 0)}{(2n-1)^2} = a - \ell \,. \tag{3.65}$$

The second term in (3.64) is small, since it can be approximated as

$$T_n(k_n \to 0) \frac{2}{\pi A} \int_0^{\infty} \frac{1 - \exp(-D_{\rm ev} t k^2)}{k^2} \, {\rm d}k = (\ell - a) \frac{\sqrt{D_{\rm ev} t}}{A}$$

with the use of (3.59) and (3.63). Thus, the term (3.58e) evaluates to

$$\Lambda_4(t) \approx a - \ell \,. \tag{3.66}$$

Fifth term

A comparison of the general terms of (3.58f) and (3.58c) shows that $|\Lambda_5(t)| \sim \Lambda_2(t)/A$, since T_n is bounded. Hence the term (3.58f) can be neglected for large A.

Final result

Finally, adding together (3.59), (3.61), (3.62) and (3.66), and inserting the result into (3.58a), yields formula (3.21).

3.6.3 Use of asymptotic expansions of Bessel functions in 2d calculations

In this Appendix we show that it is possible to use the large-argument approximations of the Bessel functions in obtaining the blood–tissue exchange quantities for radial diffusion in two spatial dimensions (Section 3.2). To this end we begin by reviewing the asymptotic behaviour of the eigenfrequencies of the Laplace (more generally, of the Sturm–Liouville) operator.

The eigenfrequencies of the Laplace operator

$$\nabla^2 = \partial^2/\partial x_1^2 + \cdots + \partial^2/\partial x_d^2 \tag{3.67}$$

satisfy the asymptotic relation of H. Weyl,[12]

$$q_n \sim \left(\frac{n}{V_{\text{ev}}}\right)^{1/d} \tag{3.68}$$

for large n, where V_{ev} is the d-dimensional volume of the bounded region (with piecewise smooth boundary) of definition of the operator [99]. Thus, $d = 1$ for a segment. This turns out also to be the case for a plane region in which the argument of the Laplacian exhibits cylindrical symmetry.[13] Indeed, we obtained $q_n \sim n/A$ for both these cases (refer to Sections 3.1 and 3.2). A proof of the asymptotic behaviour of the eigenvalues of Sturm–Liouville operators may be found in, e.g., Ref. [99], pp. 360–361.

[12] Weyl, H. Über die asymptotische Verteilung der Eigenwerte. Nachrichten der Königlichen Gesellschaft der Wissenschaften zu Göttingen. Mathematisch-Naturwissenschaftliche Klasse 1911: 110–117. Cited in Ref. [183].

[13] This may be qualitatively understood by noting that the cylindrical symmetry removes one degree of freedom.

Specifically, the eigenfrequencies of the Sturm–Liouville equation for two-dimensional diffusion in a region with cylindrical symmetry are obtained from the roots of the equation $\cos\delta_n J_1(q_n A) + \sin\delta_n Y_1(q_n A) = 0$, see Eq. (3.26). The large roots of this equation are given by Eq. (8.547) of Ref. [181] as

$$q_n A = (n + 1/4)\pi + \delta_n - \frac{3/8}{(n + 1/4)\pi + \delta_n} + \mathcal{O}[n^{-3}]\,. \tag{3.69}$$

Thus, the estimate $q_n A \approx (n + 1/4)\pi + \delta_n$ of Eq. (3.32) has an error $\mathcal{O}[n^{-1}]$.

Figure 3.13 shows the relative error, $\epsilon(n)$, of the large-argument expansion of the term $[J_1^2 + Y_1^2]^{-1}(q_n A)$ from its true value. An approximate value of the argument, $q_n A \approx (n + 1/4)\pi$, has been used in both the exact and approximate expressions for $[J_1^2 + Y_1^2]^{-1}(\cdot)$ for simplicity. This is reasonable because, as A grows large, q_n becomes small and the scattering phase shift δ_n approaches zero, since $\tan\delta_n \sim -(\ln q_n)^{-1} \to 0$ in this limit.

It is seen in Fig. 3.13 that the relative error $\epsilon(n)$ is small even for $n = 1$ [i.e., $\epsilon(1) \approx 1\%$] and that it decreases approximately as n^{-2}. The corresponding relative error, $\epsilon_{\text{norm}}(n)$, of the squared 2d norm (3.28) is then found, after straightforward manipulations, as

$$\frac{\epsilon_{\text{norm}}(n)}{\epsilon(n)} = \left\{1 - (1 + \ell^2 q_n^2)\,\frac{[J_1^2 + Y_1^2](q_n A)}{[P^2 + Q^2](q_n a)}\right\}^{-1}. \tag{3.70}$$

Figure 3.14 plots the ratio $(\epsilon_{\text{norm}}/\epsilon)(n)$ for a pair of values of the ratio $(a/A)^2 \sim v_{\text{iv}}$ and a range of values of the normalised membrane thickness, ℓ/a; here the estimate $q_n A \approx (n + 1/4)\pi$ has, again, been used. The amplitude of $(\epsilon_{\text{norm}}/\epsilon)(n)$ is seen to be of order unity. In conclusion, the error incurred due to the use of the large-argument approximation in the expression for the squared 2d norm (3.28) is negligibly low.

Various limiting forms and asymptotic expansions of Bessel functions are given below for ease of reference (see, e.g., Refs [99, 175]):

1. For large arguments,

$$J_\nu(z) = \sqrt{2/(\pi z)}\,\cos(z - \pi/4 - \nu\pi/2) + \mathcal{O}[z^{-3/2}]\,, \tag{3.71a}$$

$$Y_\nu(z) = \sqrt{2/(\pi z)}\,\sin(z - \pi/4 - \nu\pi/2) + \mathcal{O}[z^{-3/2}]\,. \tag{3.71b}$$

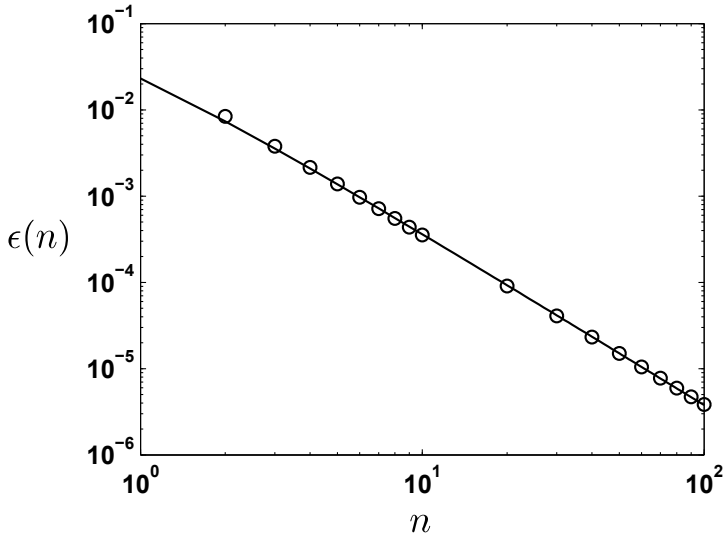

Figure 3.13: **Relative error, $\epsilon(n)$, of the large-argument approximation of** $\left[J_1^2(q_nA) + Y_1^2(q_nA)\right]^{-1}$. The relative error has been fitted (solid line) to the power law expression: $\epsilon(n) = 3.283 \times 10^{-2} n^{-1.966}$ ($r^2 = 0.9992$) for $n = 2, 3, \ldots, 100$. Only a subset (open circles) of fitted data points is shown for clarity.

Hence $[J_1^2 + Y_1^2](z) \approx 2/(\pi z) + \mathcal{O}[z^{-2}]$ for large z. On the other hand, for small arguments, $[J_1^2 + Y_1^2](z) = (2/\pi)^2 z^{-2} + \mathcal{O}[\ln z]$.

2. The function $[P^2 + Q^2]^{-1}(q')$ vanishes at the limits $q' \to 0$ and $q' \to \infty$, and has a maximum of amplitude $\varrho_2(a/\ell)^{\alpha_2}$ at $q'_p = \varrho_1(a/\ell)^{\alpha_1}$, where the constants $\alpha_{1,2}$ and $\varrho_{1,2}$ are both positive and have values near unity, and $\alpha_2/\alpha_1 \gtrsim 1$. An approximation to $[P^2 + Q^2](q')$ for small arguments is given by

$$[P^2 + Q^2](z) = 1 + (4/\pi^2)(\ln z - \ell/a + \gamma')^2 + \mathcal{O}[z^2] + \mathcal{O}[z^2 \ln z]\,, \qquad (3.71c)$$

where $\gamma' = \gamma - \ln 2 \approx -0.1159$ and $\gamma \approx 0.5772$ is Euler's constant.

On the other hand, an approximation for large arguments is given by

$$[P^2 + Q^2](z) = (2/\pi)(\ell/a)^2(z + C^2 z^{-1}) + \mathcal{O}[z^{-3}] \qquad (3.71d)$$

with $C^2 = 3/8 + a/\ell + (a/\ell)^2$.

The relative error incurred by retaining only the leading terms in (3.71c) and (3.71d) is plotted in Fig. 3.15. As expected, this error is largest near $q' = 1$. It

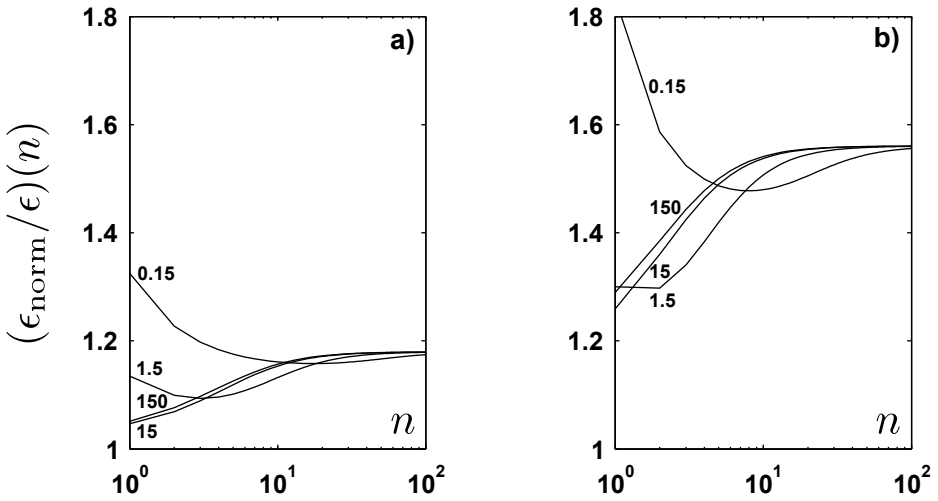

Figure 3.14: **Ratio** $(\epsilon_{\mathbf{norm}}/\epsilon)(n)$, Eq. (3.70), for values of the parameters including those listed in Table 2.1 for grey matter and myocardium: $(a/A)^2 = 0.0232$ and 0.129 (for left and right panel, respectively) and $\ell/a = 0.15, 1.5, 15$ and 150.

should also be noted that if $[P^2+Q^2]^{-1}(q')$ attains its stationary point at some $q'_p < 1$, then the approximation given by the leading term of (3.71c) becomes inaccurate for eigenfrequencies $q'_p < q' < 1$, since this term decreases with z in the range of validity ($z = q' < 1$) of the small-argument approximation. For values of the ℓ/a ratio outwith the shown range, the error curves practically overlap.

3.6.4 Evaluation of $\Lambda_{\mathbf{2d}}(t)$ for intermediate diffusion times

In this Appendix we evaluate the effective 2d extravascular depolarised volume for intermediate diffusion times ($a \ll \sqrt{D_{\rm ev}t} \ll A$, i.e., $1 \ll \varsigma \ll A/a$) by piecewise integration of (3.43). Choice of the appropriate intervals of integration is dependent upon the relative values of ς and the position, q'_p, of the maximum of $[P^2+Q^2]^{-1}(q')$. The eigenfrequency dependence of the integrand in (3.43) is discussed in Appendix 3.6.3.

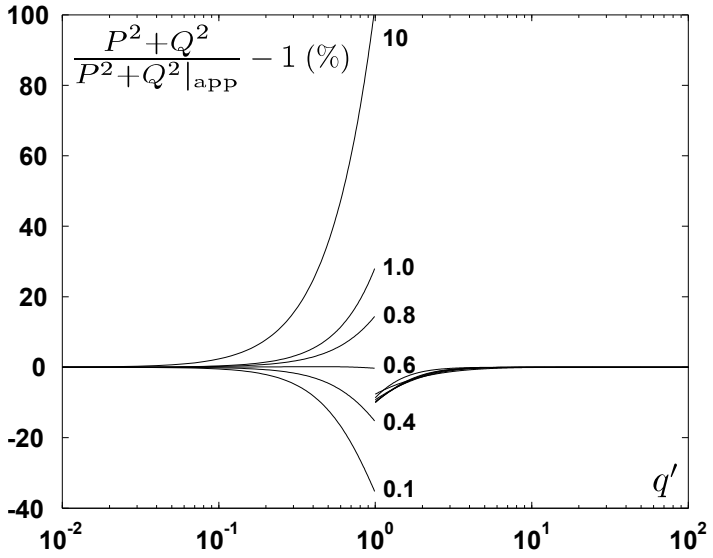

Figure 3.15: **Percentage error of large- and a small-argument approximations of $[P^2+Q^2]^{-1}(q')$ for several values of the ℓ/a ratio**. Only the leading terms in Eq. (3.71c) (applies for $q' < 1$) and Eq. (3.71d) (applies for $q' > 1$) have been used in the calculations.

Case 1: $\varsigma^{-1} < q'_p < 1$

In this case the small-argument approximation (3.71c) is accurate for $q' < \varsigma^{-1}$. The integral in (3.43) is thus evaluated over the eigenfrequency intervals $(0, \varsigma^{-1})$, (ς^{-1}, q'_p), $(q'_p, 1)$ and $(1, \infty)$:

1. In the interval $(0, \varsigma^{-1})$, the exponential term in the integrand of (3.43) becomes $1 - \exp(-\varsigma^2 q'^2) \approx \varsigma^2 q'^2$, whereas the term $[P^2 + Q^2](q')$ is approximated by (3.71c). This gives

$$\begin{aligned}\Lambda_{11}(t) &= \frac{8a^2}{\pi}\int_0^{\varsigma^{-1}} \frac{1-\exp(-\varsigma^2 q'^2)}{[P^2+Q^2](q')}\frac{\mathrm{d}q'}{q'^3} \\ &\approx \frac{8a^2\varsigma^2}{\pi}\int_0^{\varsigma^{-1}} \frac{1}{1+(4/\pi^2)(\ln q' - \ell/a + \gamma')^2}\frac{\mathrm{d}q'}{q'} \\ &= 4\pi a^2\varsigma^2 \,\mathrm{arc\,cot}[(2/\pi)(\ln\varsigma + \ell/a - \gamma')]\,. \end{aligned} \tag{3.72a}$$

If $\ln\varsigma + \ell/a \gg 1$, the Taylor expansion $\mathrm{arc\,cot}\, z = z^{-1} + \mathcal{O}[z^{-3}]$ gives

$$\Lambda_{11}(t) \approx \frac{2\pi a^2\varsigma^2}{\ln\varsigma + \ell/a - \gamma'}\,, \tag{3.72b}$$

which reproduces (3.45).

2. In the interval (ς^{-1}, q'_p), the exponential term may be approximated by unity whereas for $[P^2+Q^2](q')$ the approximation (3.71c) holds. Thus

$$\begin{aligned}\Lambda_{12}(t) &\approx \frac{8a^2}{\pi}\int_{\varsigma^{-1}}^{q'_p}\frac{1}{1+(4/\pi^2)(\ln q'-\ell/a+\gamma')^2}\frac{\mathrm{d}q'}{q'^3}\\ &< 2\pi a^2\varsigma^2\int_{\varsigma^{-1}}^{q'_p}\frac{1}{(\ln q'-\ell/a+\gamma')^2}\frac{\mathrm{d}q'}{q'}\\ &\approx \frac{\ln(q'_p\varsigma)}{-\ln q'_p+\ell/a-\gamma'}\,\Lambda_{11}(t)\,,\end{aligned} \tag{3.72c}$$

where the inequality $q'^{-3}\leq\varsigma^2 q'^{-1}$ and Eq. (3.72b) have been used in the second and third line, respectively, of the above equation. Since, from item 2 above (p. 151), $-\ln q'_p = -\varrho_1+\alpha_1\ln(\ell/a)\lesssim \ell/a$, it follows that $\Lambda_{12}(t)$ is smaller than $\Lambda_{11}(t)$ by a factor of order a/ℓ.

3. In the interval $(q'_p, 1)$, the use of Eq. (3.71c) yields a poor approximation to the term $[P^2+Q^2]^{-1}(q')$. However, since the maximum of this function is of order $(a/\ell)^{\alpha_2}\sim(q'_p)^{\alpha_2/\alpha_1}$, the contribution to the effective 2d extravascular depolarised volume on this interval is upper bounded by

$$\frac{\Lambda_{13}(t)}{a^2}\sim(q'_p)^{\alpha_2/\alpha_1}\int_{q'_p}^{1}\frac{\mathrm{d}q'}{q'^3}\sim(q'_p)^{(\alpha_2/\alpha_1)-2}<\varsigma^{2-(\alpha_2/\alpha_1)}\,, \tag{3.72d}$$

where $1/q'_p<\varsigma$ has been used. Thus, the right-most term is smaller than $\Lambda_{11}(t)$ in (3.72b) by a factor of order $(\ln\varsigma+\ell/a)\varsigma^{-\alpha_2/\alpha_1}$.

4. Lastly, for $q'\geq 1$, the approximation $1-\exp(-\varsigma^2 q'^2)\approx 1$ and Eq. (3.71d) yield an integrand of rational fraction form. The integral is given by right-hand side of

$$\Lambda_{14}(t)\approx\frac{4a^2(a/\ell)^2}{C^2}\left(1-\frac{1}{C}\operatorname{arc\,cot}\frac{1}{C}\right), \tag{3.72e}$$

where C is given below Eq. (3.71d). For $\ell/a>1$, $\Lambda_{14}(t)=\mathcal{O}[(a/\ell)^2]$, whereas $\Lambda_{11}(t)=\mathcal{O}[\varsigma^2(\ln\varsigma)^{-1}]$ or $\mathcal{O}[(a/\ell)\varsigma^2]$, according as $\ln\varsigma>\ell/a$ or vice versa. In the former case, the diffusion lengths may greatly exceed those typical of tracer transport in biological tissues.

The above estimates (3.72a) – (3.72e) have been confirmed by piecewise numerical integration over the intervals $(0, \varsigma^{-1})$, $(\varsigma^{-1}, a/\ell)$, $(a/\ell, 1)$ and $(1, \infty)$, where the parameter a/ℓ instead of q'_p has been used to allow for easier comparison with various values of the ℓ/a ratio across cases. For $\ell/a = 10$ and $\varsigma^2 \equiv D_{\rm ev}t/a^2 = 10^3$ and 10^4, numerical integration gives $[\Lambda_{12}/\Lambda_{11}](t) = 2.9\%$ and 3.1%, respectively. For $\ell/a = 1$ and the same diffusion times, this ratio increases to 12% and 9.1%, respectively. On the other hand, the eigenfrequencies $q' > a/\ell$ contribute to $\Lambda_{2\rm d}(t)$ by less than 1%.

Case 2: $q'_p < \varsigma^{-1} \ll 1$

Here, the small-argument approximation (3.71c) is only accurate for $q' < q'_p$. Thus, the integral in (3.43) is evaluated over the eigenfrequency intervals $(0, q'_p)$, (q'_p, ς^{-1}), $(\varsigma^{-1}, 1)$ and $(1, \infty)$:

1. In the interval $(0, q'_p)$, a similar calculation to that for the previous case yields:

$$\begin{aligned}\Lambda_{21}(t) &\approx \frac{8a^2\varsigma^2}{\pi}\int_0^{q'_p}\frac{1}{1+(4/\pi^2)(\ln q' - \ell/a + \gamma')^2}\frac{{\rm d}q'}{q'} \\ &= 4a^2\varsigma^2\,{\rm arc\,cot}\big[(2/\pi)(-\ln q'_p + \ell/a - \gamma')\big] \\ &\approx \frac{2\pi a^2\varsigma^2}{-\ln q'_p + \ell/a - \gamma'}\,, \end{aligned} \tag{3.73a}$$

   where the last approximation is justified because the argument of ${\rm arc\,cot}(\cdot)$ is large: since $q'_p < \varsigma^{-1} \ll 1$, the ratio $\ell/a \sim (q'_p)^{-\alpha_1} \gg 1$. Moreover, $(\ell/a)^{-\alpha_1} \gg \ln(\ell/a)^{-\alpha_1} \sim -\ln q'_c$ which, in turn, is much greater than $\ln\varsigma$. This implies that $\Lambda_{21}(t)$ can be approximated by $\Lambda_{11}(t)$ with good accuracy.

2. In the interval (q'_p, ς^{-1}), the leading term in (3.71c) cannot be used to obtain an approximation to $[P^2+Q^2]^{-1}(q')$. However, it can be used, instead, to obtain an upper estimate of the contribution to the effective 2d extravascular depolarised volume over this interval. Operating as in the development leading to (3.72c)

gives

$$\Lambda_{22}(t) \leq \frac{8a^2\varsigma^2}{\pi}\int_{q'_p}^{\varsigma^{-1}} \frac{1}{1+(4/\pi^2)(\ln q' - \ell/a + \gamma')^2}\frac{\mathrm{d}q'}{q'}$$
$$< \frac{-\ln(q'_p\varsigma)}{\ln\varsigma + \ell/a - \gamma'}\,\Lambda_{21}(t)\,, \tag{3.73b}$$

where the numerator is non-negative. The relation $1 \ll \varsigma < 1/q'_p \sim (\ell/a)^{\alpha_1}$ implies that $\Lambda_{22}(t)$ is smaller than $\Lambda_{21}(t)$ by approximately a factor of a/ℓ. It is noted that the above result is an upper bound (possibly a conservative one) on the error incurred by the use of the small-argument approximation to $[P^2+Q^2]^{-1}(q')$ in the estimation of the contribution to $\Lambda_{2\mathrm{d}}(t)$ over the interval $0 < q' < \varsigma^{-1}$. The reason is that for $q' \lesssim a/\ell$ the approximation error (Fig. 3.15) is small, whereas for higher frequencies it is bounded by $[P^2+Q^2]^{-1}(q')$.

3. Similarly, in the interval $(\varsigma^{-1}, 1)$ an upper bound is found as

$$\Lambda_{23}(t) \leq \frac{8a^2\varsigma^2}{\pi}\int_{\varsigma^{-1}}^{1} \frac{1}{1+(4/\pi^2)(\ln q' - \ell/a + \gamma')^2}\frac{\mathrm{d}q'}{q'}$$
$$< \frac{\ln\varsigma}{\ell/a - \gamma'}\frac{2\pi a^2\varsigma^2}{\ln\varsigma + \ell/a - \gamma'}$$
$$\approx (a/\ell)\ln\varsigma\,\Lambda_{21}(t) \ll \Lambda_{21}(t)\,, \tag{3.73c}$$

where approximations are based upon the discussion of bullet point 1 above.

4. For $q' \geq 1$ the contribution to $\Lambda_{2\mathrm{d}}(t)$ is the same as that for Case 1 above.

The above discussion shows that the $\Lambda_{21}(t)$ term dominates and differs from $\Lambda_{11}(t)$, given by Eq. (3.45), by a small amount. For $\ell/a = 100$ and $\varsigma^2 = 10^0, \ldots, 10^4$, numerical integration shows that $[\Lambda_{22}/\Lambda_{21}](t)$ is less than 4% and decreases with diffusion time, whereas $[\Lambda_{23}+\Lambda_{24}](t)/\Lambda_{21}(t)$ increases with diffusion time but remains below 0.5%.

Case 3: $\varsigma^{-1} \ll 1 < q'_p$

Here, the integration intervals may be chosen as $(0, \varsigma^{-1})$, $(\varsigma^{-1}, 1)$ and $(1, \infty)$ since for $q' \geq 1$ the large-argument approximation to $[P^2+Q^2]^{-1}(q')$ obtained from (3.71d) is

$\varsigma^2 = D_{\mathrm{ev}}t/a^2$	10^0	10^1	10^2	10^3	10^4
$\Lambda_{32}(t)/\Lambda_{31}(t)\,(\%)$	–	25	21	15	11
$\Lambda_{33}(t)/\Lambda_{31}(t)\,(\%)$	50	10	1.5	0.21	0.026

Table 3.1: **Percentage contributions to effective 2d extravascular depolarised volume at intermediate diffusion times, for $\ell/a = 0.1$ (Case 3 in text)**. Integration intervals were $(0, \varsigma^{-1})$, $(\varsigma^{-1}, 1)$ and $(1, \infty)$. Note that for $\varsigma^2 = 1$ the integration limits in $\Lambda_{32}(t)$ overlap, hence this contribution vanishes.

rather accurate (Fig. 3.15). It follows that $\Lambda_{31}(t) = \Lambda_{11}(t)$ and that $\Lambda_{33}(t) = \Lambda_{14}(t)$. The term

$$\Lambda_{32}(t) \approx \frac{8a^2}{\pi} \int_{\varsigma^{-1}}^{1} \frac{1}{1 + (4/\pi^2)(\ln q' - \ell/a + \gamma')^2} \frac{\mathrm{d}q'}{q'^3} \tag{3.74a}$$

contributes a sizeable amount to the overall integral and has been computed numerically (Table 3.1).

To conclude this Appendix, we show in Fig. 3.16 the relative error of the simplified formula (3.45). For low ℓ/a ratios, and for diffusion times such that $\sqrt{D_{\mathrm{ev}}t}/a$ is of order unity, this formula becomes less accurate.

3.6.5 Monte Carlo simulations

We performed Monte Carlo simulations in order to validate numerically the theoretical expressions for the effective depolarised volume for sparse capillary networks, Eq. (3.21) and Eq. (3.43).

The physical situation addressed in the simulation involves the diffusion of tracer molecules in the extravascular space and their permeation across the capillary wall into the capillary lumen, whereupon they are rapidly cleared from the blood. Axial diffusion and consumption of tracer molecules in the extravascular space is assumed to be negligibly low. The initial condition specifies a constant concentration of tracer molecules in the extravascular space. As may be recalled, for this problem the extravascular concentration was denoted by $\psi_{\mathrm{ev}}^{\mathrm{abs}}(\mathbf{r}, t)$ (Section 2.3.1).

Only a highly simplified case is investigated in the Monte Carlo simulations de-

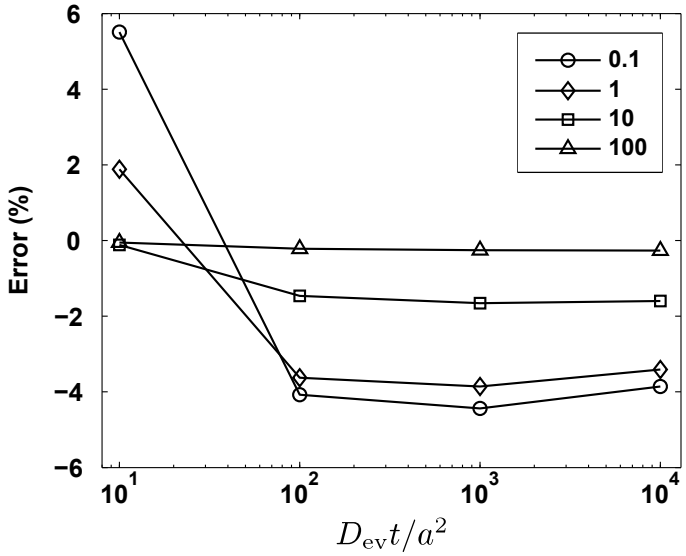

Figure 3.16: **Percentage error of simplified analytical formula** (3.45) **for effective 2d extravascular depolarised volume at intermediate diffusion times, relative to the numerical integration of** (3.43). The legend shows the set of ℓ/a ratios used.

scribed in this Appendix, namely the single-capillary approximation for sparse capillary networks (Section 2.1.3). The numerical results obtained for both the 1d and 2d cases are plotted together with the appropriate analytical expressions in Fig. 3.6 and Fig. 3.10, respectively.

In the sequel we first describe the simulation procedure with an emphasis on the 2d case (for the 1d case, see also Ref. [96]), then both the values of the simulation parameters and plots of the simulation error are given for both the 1d and 2d cases.

Simulation procedure

The two-dimensional diffusion of tracer molecules in the pericapillary region was simulated using an ensemble of random walks, each consisting of (a maximum of) N_t independent, normally distributed steps with root-mean-squared length σ. The capillary lumen was modelled as a circle of radius a and was placed at the centre of a square box of size $2A$ that modelled the extravascular space (Fig. 3.17). An initial population of N_s random walkers (each representing a tracer molecule) was placed

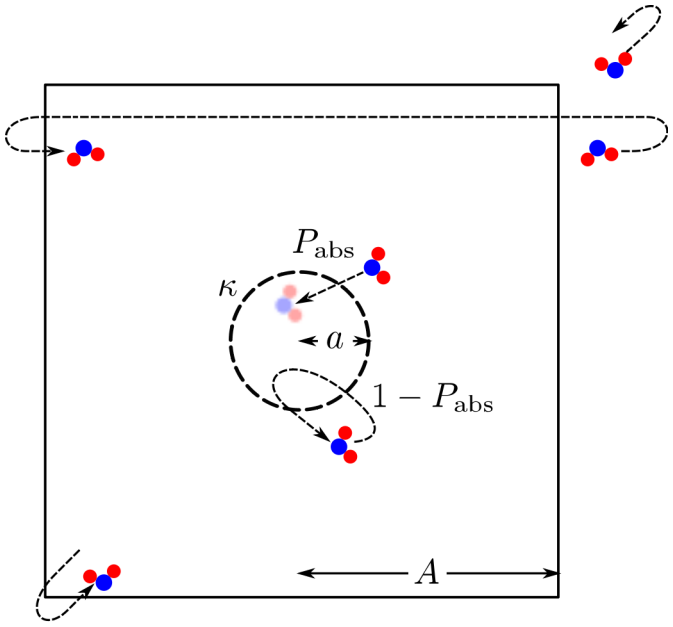

Figure 3.17: **Monte Carlo simulation box** used to model the capillary lumen (circle), the permeable capillary wall (broken line) and the pericapillary region (with square-shaped boundary). The effect of a probability $P_{\text{abs}} < 1$ of traversing the capillary wall and that of periodic boundary conditions at the pericapillary wall are also both shown (dashed lines).

randomly according to a uniform probability distribution in the 'extravascular' region of the box.[14]

The length A of each side of the box must be large enough that near the edges of the box the concentration of walkers remains virtually unaltered throughout the simulation (Fig. 2.5), as has been assumed in the derivation of Eq. (3.21) and Eq. (3.43). A was therefore chosen as a trade-off between the systematic error due to a finite box size, and the size of the initial population of random walkers required to maintain an

[14]It may be noted that a square box does not possess cylindrical symmetry, contrary to what has been assumed in the analytical treatment of the capillary–tissue model. However, the precise shape of the simulation box should be of little consequence provided that $A \gg a$. Moreover, the periodic boundary conditions on the sides of a square are easier to compute than the reflective boundary conditions on a circumference.

adequate concentration initially and throughout the simulation. Thus

$$A = \max\left\{a + 3\sqrt{4D_{\mathrm{ev}}t_{\max}}\,, 10a\right\} \tag{3.75}$$

was chosen based on the total diffusion length for a total simulation time $t_{\max}$, and typical intercapillary distances for brain and myocardium.

Furthermore, in the simulated physical situation, the pericapillary region may be considered a 'large' source of tracer molecules maintaining an almost constant average concentration of tracer (except, possibly, in a region near the capillary wall). The number of 'surviving' random walkers must therefore be sufficiently high at all times throughout the simulation. Thus, the condition

$$\frac{\Lambda_{2\mathrm{d}}(t_{\max})}{A^2} \ll 1 \tag{3.76}$$

should also hold. Equation (3.22) gives the upper bound $\Lambda_{2\mathrm{d}}(t_{\max}) \leq 2\pi a\kappa t_{\max}$. For the 1d case the capillary radius a is not defined and the length of the simulation interval should be chosen such that

$$\frac{\sqrt{D_{\mathrm{ev}}t_{\max}}}{A} \ll 1 \qquad \text{and} \qquad \frac{\kappa t_{\max}}{A} \ll 1\,, \tag{3.77}$$

where (3.22) has been used in the latter inequality.

The probability density of normally distributed, one-dimensional steps from initial position x' to final position x is given by

$$p_x(x, x') = \frac{1}{\sqrt{2\pi\sigma_x^2}} \exp\left[-\frac{(x-x')^2}{2\sigma_x^2}\right], \tag{3.78}$$

and likewise for the y direction. The root-mean-squared length of random steps,

$$\sigma_x = \sigma_y = \sqrt{2D_{\mathrm{ev}}\Delta t}\,, \qquad \sigma = \sqrt{\sigma_x^2 + \sigma_y^2} = \sqrt{4D_{\mathrm{ev}}\Delta t}\,, \tag{3.79}$$

must be chosen to be small relative to the capillary radius.

The time step, Δt, is then determined from Eq. (3.79) with the use of σ and the extravascular diffusion coefficient, D_{ev}. The maximum number of random steps, N_t, performed by any random walker is given by

$$N_t = \frac{t_{\max}}{\Delta t} = \frac{4D_{\mathrm{ev}}t_{\max}}{\sigma^2}\,. \tag{3.80}$$

Note that (3.75) can be rewritten as $A = \max\left\{a + 3\sigma\sqrt{N_t}\,, 10a\right\}$.

Any random walker diffusing beyond the pericapillary boundary re-enters the simulation box according to periodic boundary conditions (Fig. 3.17), thereby simulating tracer mass balance across the whole pericapillary boundary. In the 1d case this type of boundary condition is meaningless, hence a reflective condition was used instead, i.e., if $x(n) > A$, then $x(n) \mapsto 2A - x(n)$, where $x(n)$ denotes the position of any given walker at the nth time step.

The removal of random walkers in the circle of radius a is governed by the 'absorption' probability P_{abs} (evaluated below). Specifically, let $\delta N_{\mathrm{abs}}(n)$ denote the number of random walkers which reach the interior of the circle between the $(n-1)$th and nth time steps. Then, on average, only a fraction P_{abs} of these walkers will actually be removed from the ensemble – thereby simulating fast tracer clearance in the capillaries – whereas a fraction $1 - P_{\mathrm{abs}}$, on average, will be put back in their respective positions outwith the circle at the time step immediately previous. This was realised by extracting at each time step $\delta N_{\mathrm{abs}}(n)$ samples from a uniform variate in the interval $[P_{\mathrm{abs}} - 1, P_{\mathrm{abs}}]$. This process therefore models the permeation of, on average, $\delta N_{\mathrm{abs}}(n) = P_{\mathrm{abs}}\delta N_{\mathrm{abs}}(n)$ tracer molecules into the capillary lumen between the time instants $(n-1)\Delta t$ and $n\Delta t$; see Fig. 3.17.

P_{abs} was calculated by equating two equivalent expressions for the tissue-to-blood tracer flux under absorbing intracapillary conditions: the 'macroscopic' formulation makes use of the definition of membrane permeability, Eq. (2.10b), whereas the 'microscopic' formulation involves the probability density of random displacements, Eq. (3.78). Moreover, since the step size is typically much smaller than the capillary radius, P_{abs} can be calculated with small error from considerations of 1d diffusion near the capillary in the direction normal to the capillary wall surface. Thus

$$-\mathbf{n}\mathbf{j}_{\kappa} = \kappa\psi_{\mathrm{ev}}^{\mathrm{abs}}(a_+, t) = \frac{1}{\Delta t}\left[P_{\mathrm{abs}}\int_0^{\infty}\mathrm{d}x'\int_{-\infty}^{0}\mathrm{d}x\, p_x(x, x')\right]\psi_{\mathrm{ev}}^{\mathrm{abs}}(a_+, t)\,. \tag{3.81}$$

The above iterated integral gives the probability that a walker performs a random step between an arbitrary position in the pericapillary region ($x' > 0$) and another in

the capillary lumen ($x < 0$), and evaluates to $\sigma_x/\sqrt{2\pi}$.[15] Thus, P_{abs} can be expressed in any of the forms:

$$P_{\text{abs}} = \min\left\{\sqrt{2\pi}\,\frac{\kappa\Delta t}{\sigma_x}\,, 1\right\} = \min\left\{\frac{\sqrt{\pi}}{2}\,\frac{\kappa\sigma}{D_{\text{ev}}}\,, 1\right\} = \min\left\{\kappa\sqrt{\frac{\pi\Delta t}{D_{\text{ev}}}}\,, 1\right\}. \tag{3.82}$$

The above expressions suggest that, the permeability coefficient κ being held fixed, the probability of permeating the capillary wall is favoured by efficient diffusion in the extravascular space.

Finally, the simulated effective 2d extravascular depolarised volume is estimated from (2.23b) as

$$\frac{\Lambda_{\text{MC}}(n\Delta t)}{4A^2 - \pi a^2} = \frac{N_{\text{abs}}(n)}{N_{\text{s}}}\,, \tag{3.83}$$

where $N_{\text{abs}}(n)$ is the total number of absorbed random walkers to the nth time step.

Values of the parameters and simulation error: 2d case

The values of the parameters for the simulation depicted in Fig. 3.10 and Fig. 3.18 are discussed next. The simulation box is defined by the parameters $a = 3.5$ μm and $A/a \approx 49$.[16] Seventeen instances of the simulation routine were independently run; care was taken to use different initial states for the random number generators in each run. For each run, one million random walkers were placed at random according to a uniform probability distribution initially; approximately 0.03% of these walkers fell inside the central circle of radius a and were discarded. Thus, there was a total of $N_{\text{s}} \approx 1.7 \times 10^7$ random walkers initially. Of these, a fraction of 0.54%, approximately, was absorbed in the inner circle during the course of the simulation. N_{s} and $N_{\text{abs}}(n)$ in Eq. (3.83) were computed by adding the values of those quantities for all seventeen runs. Because the effect of molecular size was not modelled in the simulation, we have

[15] Since the main contribution to the second integral in (3.81) comes from an interval of length x of the order of $\sigma_x \ll a$, integration over the interval $(-\infty, 0)$ rather than over $(-\infty, -a)$ is justified. The iterated integral is easily evaluated by rotating the coordinate axes by $\pm\pi/4$ radians, thereby exploiting the contour lines $x \pm x' = \text{const}$.

[16] The non-integer value of A/a arises from the value of the parameters used in Eq. (3.75).

neglected the probability that two or more walkers may 'occupy' identical positions at any given time step in the same, or different, runs.

The values of the other simulation parameters were: $\sigma_x/a = \sigma_y/a = 10^{-2}$; $D_{\rm ev} = 1.0\ \mu{\rm m}^2\,{\rm ms}^{-1}$; $\kappa = 5.0 \times 10^{-2}\ \mu{\rm m}\,{\rm ms}^{-1}$; the resultant time step was $\Delta t \approx 1.5 \times 10^{-6}$, in units of $\tau_\kappa = \ell/\kappa = 400$ ms. The simulation time was set to $t_{\rm max} = 2.0$ in the same units; thus each random walker performed a maximum of $N_t = 2 \times 10^4\, D_{\rm ev} t_{\rm max}/a^2 \approx 1.3 \times 10^6$ steps. The resultant absorption probability was $P_{\rm abs} \approx 2.2 \times 10^{-3}$.

The simulation spanned both short and intermediate diffusion times, as is seen from the ratios $\sqrt{D_{\rm ev} t_{\rm max}}/a \approx 8$ and $\sqrt{D_{\rm ev} t_{\rm max}}/A \approx 0.2$. At short diffusion times the tissue-to-blood flux is expected to be rate-limited by the capillary permeability, since the effective membrane thickness is greater than the capillary radius ($\ell/a = 5.7$). On the other hand, at intermediate diffusion times, both permeation and extravascular diffusion are expected to contribute similarly to the tissue-to-blood flux, since the values of the non-dimensional parameters ℓ/a and $\ln(\sqrt{D_{\rm ev} t_{\rm max}}/a) \approx 2.4$ are comparable.

We have found heuristically that, for properly chosen values of the initial number of walkers (N_s) and diffusion time steps (N_t), and for appropriate box dimensions (A/a), the statistical simulation error $\epsilon_{\rm MC}(n)$ decreases as the square root of the amount of absorbed random walkers:

$$\epsilon_{\rm MC}(n) \sim \frac{1}{\sqrt{N_{\rm abs}(n)}}\,. \tag{3.84}$$

In Fig. 3.18 are plotted both the deviation of the simulated effective 2d depolarised volume, $\Lambda_{\rm MC}(n\Delta t)$, from the theoretical value, Eq. (3.43), and the expected simulation error, $\epsilon_{\rm MC}(n)$. The results of this particular Monte Carlo simulation are seen to underestimate (by less than 1%) the value of $\Lambda_{\rm 2d}(n\Delta t)$ in the long run. Since $\Lambda_{\rm 2d}(t_{\rm max})/A^2 = 6.9 \times 10^{-3}$ [see Eq. (3.76)] it may be assumed that the concentration of random walkers near the edge of the square box remains approximately constant at its initial value, and hence that the effect of finite box size introduces only a small statistical error.

The accuracy of the simulation for short diffusion times can be assessed as follows: equating the theoretical and simulated values for the effective 2d depolarised volume,

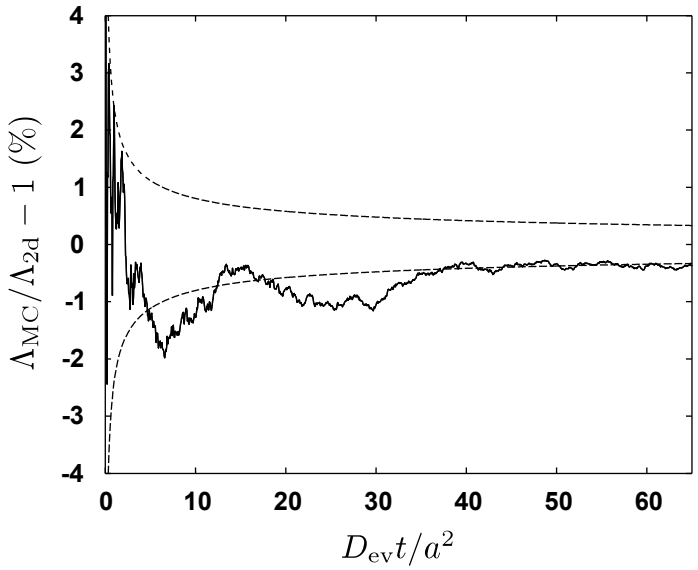

Figure 3.18: **Percentage error of Monte Carlo simulation of effective 2d depolarised volume** relative to numerical integration of Eq. (3.43). Error amplitudes have been plotted in increments of one-thousand time steps starting at $t = \Delta t$. For $t = \Delta t$ and $t = 1001\Delta t$ the error amplitudes are 947% and 10.5%, respectively, and have not been represented for clarity. The broken line represents the expected statistical error, Eq. (3.84).

Eq. (4.7c) and Eq. (3.83), respectively, and solving for the theoretical amount of absorbed random walkers after the nth time step, $N_{\rm abs}^{\rm theo}(n)$, gives

$$N_{\rm abs}^{\rm theo}(n) \approx \frac{\Lambda_{\rm 2d}(n\Delta t)}{V_{\rm ev}} N_{\rm s} \approx \frac{2\pi a\kappa \Delta t N_{\rm s}}{V_{\rm ev}} n = 9.5 \times 10^{-2} n\,. \tag{3.85}$$

According to this expression, for the parameters used in this simulation $N_{\rm abs}^{\rm theo}(n)$ can only take integer values for $n \geq 11$ time steps, thus explaining large initial discretisation errors. For example, after the first nine time steps only one random walker was removed, far exceeding the approximate theoretical value of $N_{\rm abs}^{\rm theo}(1)$ given by (3.85). The ratio $N_{\rm abs}/N_{\rm abs}^{\rm theo} - 1 \approx 948\% = \Lambda_{\rm MC}/\Lambda_{\rm 2d} - 1$ is largest for $n = 1$, i.e., for $t = \Delta t$.

Values of the parameters and simulation error: 1d case

The values of the parameters for the simulation depicted in Fig. 3.6 and Fig. 3.19 are discussed next.

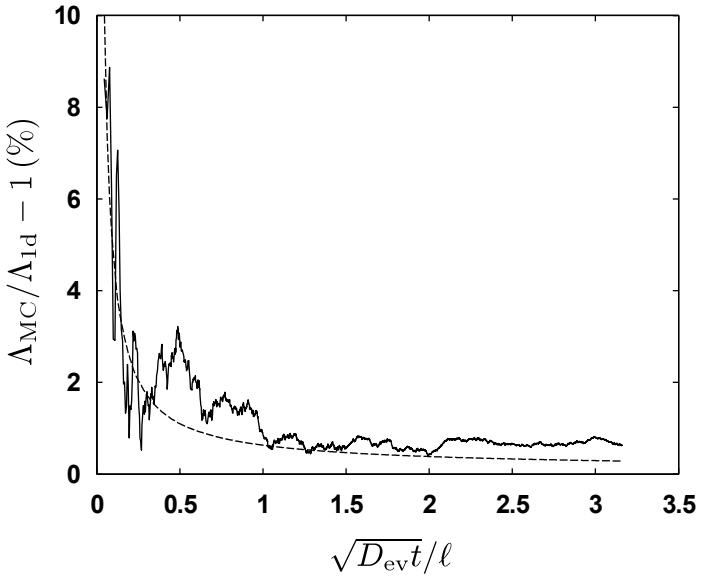

Figure 3.19: **Percentage error of Monte Carlo simulation of effective 1d depolarised volume** relative to formula (3.21). The broken line represents the expected statistical error, Eq. (3.84).

Ten million random walkers were used in the simulation. Of these, a fraction of 1.2%, approximately, was absorbed over a maximum of $N_t = 5000$ diffusion steps. The value of membrane permeability was $\kappa = 1.7 \times 10^{-3}\ \mu\mathrm{m\,ms^{-1}}$ and the diffusion coefficient was $D_{\rm ev} = 1.0\ \mu\mathrm{m^2\,ms^{-1}}$ as for the 2d case. The simulation time was $t_{\rm max} = 10$ in units of $\tau_\kappa \approx 3.5 \times 10^5$ ms (see above), i.e., $t_{\rm max} \approx 1$ hour. The diffusion time step was $\Delta t = 2 \times 10^{-3}\tau_\kappa \approx 690$ ms. The length of the 1d simulation box was $A = 50\sqrt{2D_{\rm ev}t_{\rm max}} \approx 1.3 \times 10^5\ \mu$m; the root-mean-squared diffusion step was $\sigma_x/A \approx 2.8 \times 10^{-4}$. Moreover, with reference to Eq. (3.77), the ratios $\sqrt{D_{\rm ev}t_{\rm max}}/A \approx 1.4 \times 10^{-2}$ and $\kappa t_{\rm max}/A = 4.5 \times 10^{-2}$ are reasonably small. The absorption probability was $P_{\rm abs} = 7.9 \times 10^{-2}$.

All the simulation routines were programmed in MATLAB (The MathWorks, Inc.). The pseudo-random generator number used had a period of $2^{64} \sim 10^{19}$, well exceeding the requirements of the simulation. Part of the simulations were run on the computing cluster at the Medical Physics Section, Department of Radiology, Albert-Ludwigs Universität, Freiburg im Breisgau, Germany.

Chapter 4

Applications and Model Comparisons

This Chapter opens with a description of various regimes in which blood–tissue tracer exchange can occur, as determined by the interplay of extravascular diffusion and transcapillary permeation. This analysis leads to a discussion of potential sources of deviation between the class of lumped tracer-exchange models and the more general class of spatiotemporal models. Subsequently, the predictions of the spatiotemporal model presented in preceding Chapters are compared to those found in previously published work, including gas exchange in the tissues and arterial spin labelling (ASL). Importantly, the ASL signal taking into account diffusion of magnetically tagged water in extravascular space is evaluated using the present spatiotemporal model. This result is then compared to two ASL models from the literature, none of which takes account of water diffusion, by evaluating the signal output of each model for selected boli of inflowing magnetisation (appropriate for both PASL and CASL) using a common set of tissue parameters. A comparison of the spatiotemporal and lumped models at steady state is also provided. The Chapter closes with a brief discussion of earlier chemical exchange results.

4.1 Blood–tissue tracer exchange regimes

4.1.1 Permeability-limited vs diffusion-limited exchange

The exchange of solutes between blood and the surrounding tissue can be rate-limited either by capillary flow, capillary wall permeability to tracer, or tracer diffusion in the extravascular space:

1. In a *flow-limited regime*, the capillary flow is slower than transcapillary permeation: $\tau_c \gg \tau_{iv}$ or, equivalently, $f_{iv} \ll PS$, from Eqs (2.2b) – (2.3b).

   Herscovitch *et al.* [160] estimated capillary flow and permeability surface area in human brain tissue using $H_2^{15}O$ PET. Regional values were in the ranges $f_w = 31.8 - 62.9$ ml $[100\,g]^{-1}$ min^{-1} and $PS_w = 81 - 152$ ml $[100\,g]^{-1}$ min^{-1}, with the lower and higher values corresponding to white matter and central cortex, respectively. The resultant $H_2^{15}O$ extraction was high, i.e., $E_w \approx 0.8$. On the other hand, use of typical capillary-segment values listed in Table 2.1 results in the opposite inequality, $\tau_c < \tau_{iv}$. This discrepancy can be explained by the wide distribution of anatomo-physiological parameters, such as capillary segment length and erythrocyte velocity (see, e.g., Ref. [65]), on the scale of a typical voxel, and warns again straightforward generalisation of conclusions obtained on a single-capillary scale. Furthermore, it suggests that proper quantitative 'up-scaling' from single-capillary to whole-tissue analyses must take into account capillary network statistics.

   The condition $\tau_c \gg \tau_{iv}$ for flow-limited exchange is the converse of Eq. (2.7a) for fast clearance of tracer by the blood flow. Hence, in a flow-limited situation, the assumption that the concentration of tracer in the capillaries is barely influenced by the extravascular concentration (Section 2.2.2) might be violated if any tracer back-flux from extravascular space into the blood is not negligibly low, rendering inaccurate the analysis of Chapter 3. The estimates for τ_c and τ_{iv} for normal brain and myocardial tissue suggest that capillary flow is not expected to be a limiting factor of transcapillary exchange. In this case,

the theoretical analysis becomes independent of the amplitude scale of the intracapillary concentration (as determined by flow and exchange processes) on account of the assumption of linearity (see Section 2.2).

2. In a *permeability-limited regime* the blood–tissue transcapillary flux is rate-limited by a low permeability of the capillary wall to the considered tracer. In this situation, (i) the capillary flow can be assumed high enough to drive the blood-to-tissue flux of tracer and, moreover, wash out any tracer which leaks into the capillaries from the extravascular space; and (ii) efficient diffusion of tracer in the extravascular space results in relatively shallow gradients in tracer concentration (Fig. 3.7d).

   It is intuitively apparent that, under permeability-limited conditions, the average diffusion length travelled by a diffusing molecule during an interval of time equal to the mean extravascular residence time under hypothetical conditions of fast diffusive mixing, τ_{ev}, will be much greater than the characteristic radial dimension, A, of a pericapillary region. Thus, we have the estimate $\sqrt{D_{\mathrm{ev}}\tau_{\mathrm{ev}}} \gg A$. In other words, the root-mean-squared time taken by the molecules of tracer to diffuse in the extravascular space, i.e., their characteristic extravascular diffusion time τ_D, defined by Eq. (4.1) below, will be much smaller than τ_{ev}.

   Under permeability-limited conditions, the concentration of tracer near the capillary wall will reach a quasi-steady state provided that the intracapillary concentration does not vary too rapidly, and that the difference between intra- and extravascular relaxation rates is not too great. As a result, the transcapillary tracer flux will be virtually constant over time. The amount of tracer that permeates across the membrane per unit surface area is therefore expected to increase almost linearly with time.

3. Conversely, in a *diffusion-limited regime*, relatively longer times are required for the tracer to diffuse in the available extravascular space. Therefore, depending on the sense of the transcapillary flux, the tracer will tend to accumulate in, or to be rapidly removed from, the vicinity of the capillary wall. This typically

causes sharp concentration gradients with relatively long diffusion transients (Fig. 3.7b).

If the capillary permeability parameter is allowed to increase but the extravascular diffusion coefficient is held fixed, τ_{ev} decreases but τ_D does not change. On the other hand, if κ is held fixed but D_{ev} is decreased, then τ_{ev} remains unchanged but τ_D increases. The effect of jointly increasing κ and decreasing D_{ev} is to diminish τ_{ev} and to increase τ_D. It is therefore intuitively reasonable that, under diffusion-limited conditions, the mean extravascular residence time (under hypothetical fast diffusive mixing conditions) should be of the same order as the characteristic extravascular diffusion time [80, p. 511]. A related discussion of this diffusion-limited regime in the context of diffusion and reaction phenomena in biofilms is given in Ref. [149, pp. 399 ff.].

We recall that in this Thesis the term 'diffusion' refers to diffusive transport of tracer in extravascular space, and that 'permeation' refers to non-osmotic, diffusive transmembrane transport. The synonymous terms 'permeability-limited exchange' and 'barrier-limited exchange' are both well established in the literature (see, e.g., Refs [28, 69, 184]). We remark, however, that the term 'diffusion-limited exchange' has also been used in the ASL and indicator-dilution literature to refer to exchange which is rate-limited by diffusive transcapillary permeation. In this context, a 'freely diffusible tracer' is an idealised tracer for which transcapillary exchange is rate-limited neither by capillary permeability nor extravascular diffusion. To quote Ziegler and Goresky [184, p. 181], 'The walls of the capillaries in heart muscle present a barrier of varying permeability to a variety of substances. Substances for which this barrier is appreciable may be said to exchange in a barrier-limited or diffusion-limited fashion. Substances which cross the capillary wall freely may be said to exchange in a flow-limited manner (...)'. As a further example, St. Lawrence *et al.* [31, p. 443], citing supporting references, state that 'exchange of water across the blood-brain barrier is diffusion limited' because PS assumes a finite value. The physical situations described in these examples are clear, but the terminology reflects the fact that, in these references, diffusive transport is assumed to occur only across the transcapil-

lary barrier, instantaneous equilibration of tracer occurring in the radial, or lateral, direction (see Ref. [184], p. 182, and Ref. [31], p. 441).

We define below several parameters which are expected to enter into the expressions for blood–tissue exchange based on the foregoing qualitative discussion. The mean residence time for tracer molecules in a well-mixed extravascular compartment has been defined in Eq. (2.2c). We also define the *characteristic radial extravascular diffusion time*[1] for an annulus of inner radius a and outer radius A as

$$\tau_D \equiv \frac{A^2 - a^2}{4D_{\mathrm{ev}}} \sim \frac{A^2}{4D_{\mathrm{ev}}}\,, \tag{4.1}$$

where this latter approximation is valid for sparse capillary networks. Thus, the ratio of tracer residence time to tracer diffusion time in the pericapillary volume, i.e.,

$$\frac{\tau_{\mathrm{ev}}}{\tau_D} = \frac{2D_{\mathrm{ev}}}{a\kappa} = \frac{2\ell}{a} \tag{4.2}$$

is equal (up to a factor of 2) to the normalised membrane thickness and quantifies the 'strength' of tracer extravascular diffusion relative to diffusive transmembrane permeation. The parameter $\kappa a/D_{\mathrm{ev}}$ is known as the Sherwood number [10]. Further note that the normalised diffusion length, $\varsigma = \sqrt{D_{\mathrm{ev}}t}/a$, Eq. (3.38a), defines the diffusion length scale for sparse capillary networks.

Figure 4.1 is central to several sections in this Chapter. It illustrates the various regions in which both diffusion- and permeability-limited exchange may occur in relationship to normalised membrane thickness and normalised diffusion length of the tracer. The notional threshold line at $\sqrt{D_{\mathrm{ev}}t}/a = 10$ is realistic for typical intercapillary distances in human grey matter; for myocardium, this threshold is expected to be somewhat lower, based on parameter values quoted in Table 2.1. Qualitatively, in the cases in which the parameter $D_{\mathrm{ev}}/\kappa a$ is large, the transcapillary exchange will be limited by capillary tracer permeability at all diffusion times. On the other hand, when $D_{\mathrm{ev}}/\kappa a$ is of the order of unity, and if the observation time (i.e., after the arrival of tracer at the capillaries) is long enough, blood–tissue exchange can occur in both permeability- and diffusion-limited regimes.

[1] In the sequel, where no ambiguity arises, the terms 'characteristic' and 'radial' shall both be left understood.

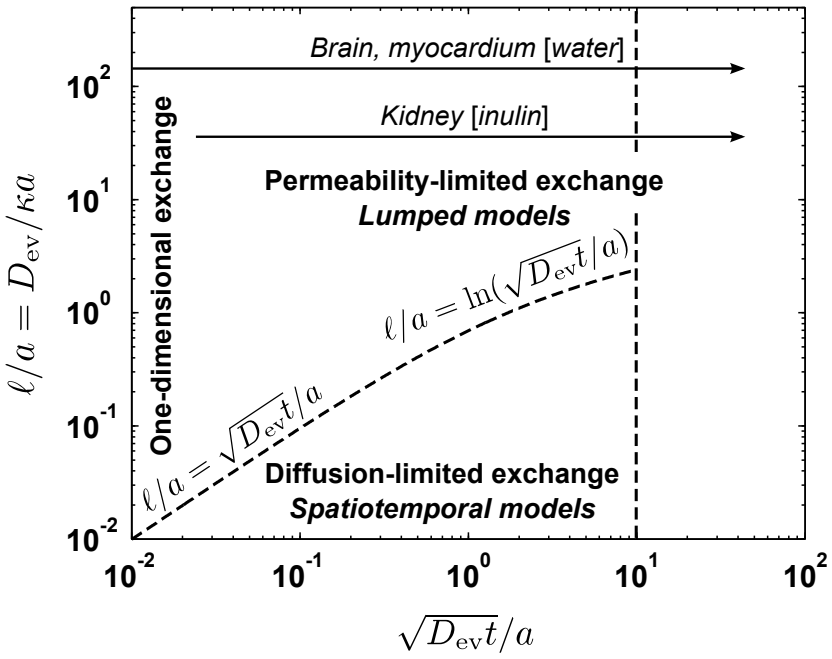

Figure 4.1: **Tracer exchange regimes and validity regions of spatiotemporal and lumped tracer-exchange models for sparse capillary networks**. *Note*: kidney data was reviewed in Ref. [44].

The foregoing qualitative remarks are made precise in the following Section. For this purpose it is sufficient, as well as analytically simpler, to consider the blood-to-tissue flux of tracer and the effective 2d extravascular depolarised volume. The applicability of each class of tracer-exchange model, as shown in Fig. 4.1, is discussed in Section 4.2.

4.1.2 Tracer-exchange time scales

Short diffusion times

At sufficiently short times, the distance which the molecules of a tracer can travel by diffusion is relatively small. Hence, the tracer molecules diffusing in the vicinity of the capillaries have a greater chance to permeate across the capillary wall than

those farther away from the vessels. As a result, the exchange is rate-limited by membrane permeabilities. Thus, the interval of short extravascular diffusion times is such that the tracer diffusion length in extravascular space is much smaller than capillary radius:

$$\frac{\sqrt{D_{\mathrm{ev}}t}}{a} \ll 1\,. \tag{4.3}$$

For example, for brain and myocardium we estimate the upper bound $t \ll 10$ ms, from Table 2.1. During the interval in which (4.3) holds, extravascular diffusion can be regarded as effectively one-dimensional; refer to Section 3.1 and Fig. 4.1.

The step response function at the capillary wall is given by

$$W(\mathbf{a}_+, t; R_{\mathrm{ev}} = 0) = 1 - \exp\left(\frac{D_{\mathrm{ev}}t}{\ell^2}\right) \operatorname{erfc}\left(\frac{\sqrt{D_{\mathrm{ev}}t}}{\ell}\right) \tag{4.4}$$

from (3.13a). The resultant transcapillary flux is given by (3.18). Lastly, the effective extravascular depolarised volume is given by

$$\Lambda_{2\mathrm{d}}(t) \approx 2\pi a\ell \left[\frac{2}{\sqrt{\pi}}\frac{\sqrt{D_{\mathrm{ev}}t}}{\ell} + \exp\left(\frac{D_{\mathrm{ev}}t}{\ell^2}\right) \operatorname{erfc}\left(\frac{\sqrt{D_{\mathrm{ev}}t}}{\ell}\right) - 1\right] \tag{4.5}$$

from (3.44) and (3.21).

The capillary radius is seen to enter in a trivial way into the above expressions as the bulk of exchange involves mostly the periphery of the capillaries. Importantly, it is the ratio of tracer diffusion length to effective membrane thickness that governs the exchange at small times.

1. At short diffusion times, the *permeability-limited regime* is characterised by the condition

$$\frac{\sqrt{D_{\mathrm{ev}}t}}{\ell} \ll 1\,, \tag{4.6}$$

that is, tracer diffusion lengths are much smaller than the effective thickness of the capillary wall (Fig. 4.2a). The small-argument expansion[2]

$$\exp(z^2)\operatorname{erfc}(z) = 1 - \frac{2z}{\sqrt{\pi}} + z^2 - \frac{4z^3}{3\sqrt{\pi}} + \mathcal{O}[z^4]$$

[2] $N(z) = \exp(z^2)\operatorname{erfc}(z)$ is written in integral form as

$$N(z) = \exp(z^2)\frac{2}{\sqrt{\pi}}\int_z^\infty \exp(-t^2)\,\mathrm{d}t = \frac{2}{\sqrt{\pi}}\int_0^\infty \exp(-t^2 - 2zt)\,\mathrm{d}t\,.$$

gives, putting $z = \sqrt{D_{\mathrm{ev}}t}/\ell$ for brevity:

$$W(\mathbf{a}_+, t; R_{\mathrm{ev}} = 0) = \frac{2}{\sqrt{\pi}} \frac{\sqrt{D_{\mathrm{ev}}t}}{\ell} + \mathcal{O}[z^2]\,, \tag{4.7a}$$

$$\mathbf{nj}_\kappa(\mathbf{a}, t) = \kappa \left\{ 1 - \frac{2}{\sqrt{\pi}} \frac{\sqrt{D_{\mathrm{ev}}t}}{\ell} + \mathcal{O}[z^2] \right\}, \tag{4.7b}$$

$$\Lambda_{2\mathrm{d}}(t) = 2\pi a \kappa t + a\ell\, \mathcal{O}[z^3]\,. \tag{4.7c}$$

It is recalled in Eq. (4.7b) that $\mathbf{nj}_\kappa(\mathbf{a}, t)$ represents the blood-to-tissue flux due to a unit step difference between the amplitude of the intracapillary and extravascular concentration at the capillary wall. Thus, this equation is dimensionally correct.

Under permeability-limited conditions the amplitude of the step response function is relatively low but, importantly, it depends upon the extravascular diffusion coefficient as $D_{\mathrm{ev}}^{-1/2}$. Equation (4.7a) coincides with the leading term of Eq. (12) of Lee and Fronek [44], when this latter expression is evaluated at the capillary entrance ($z = 0$, $r = a$); these authors, however, did not specify a time interval in which their result holds.

On the other hand, the transcapillary flux per unit intracapillary concentration of tracer, Eq. (4.7b), is only weakly dependent on diffusion coefficient. Moreover, it is nearly stationary, hence the effective extravascular depolarised volume increases linearly with time, to a first approximation.

The left-hand equality gives $N(0) = 1$, $N'(z) = 2zN(z) - 2\pi^{-1/2}$, $N''(z) = 2N(z) + 2zN'(z)$ and, by induction, $N^{(m)}(z) = 2(m-1)N^{(m-2)}(z) + 2zN^{(m-1)}(z)$. This recurrence relation affords the required Taylor expansion about $z = 0$.

Alternatively, it is noted from the above right-hand equality that for $z \ll 1$ the term $\exp(-2zt)$ in the integrand decreases slowly relative to $\exp(-t^2)$, and that $\exp(-t^2)$ decreases slowly relative to $\exp(-2zt)$ for $z \gg 1$. Taylor expansion of the slowly-varying terms about the origin, followed by termwise integration of the resultant uniformly convergent series [173], yields the same expansion as above.

2. In the *diffusion-limited regime*, the tracer diffusion length is greater than the effective thickness of the capillary wall (Fig. 4.2b), i.e.,

$$\ell \ll \sqrt{D_{\mathrm{ev}} t} \ll a\,. \tag{4.8}$$

This condition implies that membrane permeabilities must be relatively high. The large-argument expansion (Ref. [185], p. 939)

$$\sqrt{\pi}\exp(z^2)\operatorname{erfc}(z) = \frac{1}{z} - \frac{1}{2z^3} + \frac{1\cdot 3}{2^2 z^5} - \cdots$$

gives

$$W(\mathbf{a}_+, t; R_{\mathrm{ev}} = 0) = 1 - \frac{\ell}{\sqrt{\pi D_{\mathrm{ev}} t}} + \mathcal{O}[z^{-3}]\,, \tag{4.9a}$$

$$\mathbf{n}\mathbf{j}_\kappa(\mathbf{a}, t) = \sqrt{\frac{D_{\mathrm{ev}}}{\pi t}} + \kappa\,\mathcal{O}[z^{-3}]\,, \tag{4.9b}$$

$$\Lambda_{2\mathrm{d}}(t) = 2\pi a\ell \left\{ \frac{2}{\sqrt{\pi}} \frac{\sqrt{D_{\mathrm{ev}} t}}{\ell} - 1 + \mathcal{O}[z^{-1}] \right\}, \tag{4.9c}$$

with $z = \sqrt{D_{\mathrm{ev}} t}/\ell$.

Therefore, the concentration just outside the capillary wall rises rapidly (since $\ell/\sqrt{D_{\mathrm{ev}} t}$ is small) and the flux decreases in like proportion. As expected, the effective extravascular depolarised volume is proportional to diffusion length times capillary radius, but includes a correction for the volume, $2\pi a\ell$, ascribed to the effective thickness of the capillary wall.

We note that the condition $\ell/a = D_{\mathrm{ev}}/\kappa a \ll 1$ does not hold either for tracer water or for low molecular weight paramagnetic tracers in brain and myocardial capillaries.

Intermediate diffusion times

At intermediate extravascular diffusion times, tracer diffusion lengths are greater than typical values of capillary radius, but much shorter than typical half-intercapillary distances:

$$a < \sqrt{D_{\mathrm{ev}} t} \ll A\,. \tag{4.10}$$

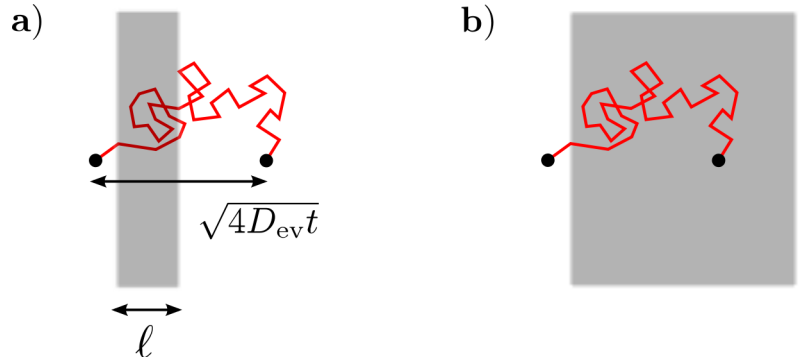

Figure 4.2: **Diffusion-, a), and permeability-limited, b), 1d tracer exchange**. The capillary wall (shaded area) has effective thickness ℓ as well as (when observed from nearby positions) a large apparent radius of curvature.

For example, $t \ll 40-50$ ms in myocardium and $t \ll 200-1000$ ms in brain tissue, from the values of the parameters listed in Table 2.1. In this range of tracer diffusion times, the approximation of one-dimensional extravascular diffusion cannot be made. The effective extravascular depolarised volume is given approximately by Eq. (3.45). Differentiating this quantity with respect to time gives the transcapillary tracer flux, which upon substitution into Eq. (3.41a) gives the step response at the capillary wall. Thus

$$W(\mathbf{a}_+, t; R_{\mathrm{ev}} = 0) \approx 1 - \frac{\ell/a}{\ln(\sqrt{D_{\mathrm{ev}}t}/a) + \ell/a - \gamma'}\,, \tag{4.11a}$$

$$\mathbf{n}\mathbf{j}_\kappa(\mathbf{a}, t) \approx \frac{D_{\mathrm{ev}}/a}{\ln(\sqrt{D_{\mathrm{ev}}t}/a) + \ell/a - \gamma'}\,, \tag{4.11b}$$

plus terms of order $(\ell/a)(\ln(\sqrt{D_{\mathrm{ev}}t}/a) + \ell/a - \gamma')^{-2}$.

When $\ln(\sqrt{D_{\mathrm{ev}}t}/a) \ll \ell/a$, the transcapillary tracer flux is rate-limited by the capillary permeability and the above expressions become

$$W(\mathbf{a}_+, t; R_{\mathrm{ev}} = 0) \approx \frac{a}{\ell} \ln\left(\frac{\sqrt{D_{\mathrm{ev}}t}}{a}\right)\,, \tag{4.12a}$$

$$\mathbf{n}\mathbf{j}_\kappa(\mathbf{a}, t) \approx \kappa\,. \tag{4.12b}$$

The amplitude of the step response function at the capillary wall increases slowly as $\ln t$, rather than as $t^{1/2}$ as is the case for the interval of short times, Eq. (4.7a).[3]

[3]Because of the $\ln t$ dependence of Eq. (4.12a), the choice of logarithmically equispaced time

The expression for the transcapillary tracer flux coincides, to a first approximation, with the right-hand side of Eq. (4.7b) for permeability-limited tracer flux at short diffusion times. Furthermore, the result $\Lambda_{2d}(t) \approx 2\pi a\kappa t$ remains valid at intermediate diffusion times.

On the other hand, when $\ell/a \ll \ln(\sqrt{D_{ev}t}/a)$ the transcapillary tracer flux is limited by extravascular diffusion. In this case,

$$W(\mathbf{a}_+, t; R_{ev} = 0) \approx 1 - \frac{\ell/a}{\ln(\sqrt{D_{ev}t}/a)}\,, \tag{4.13a}$$

$$\mathbf{n}\mathbf{j}_\kappa(\mathbf{a}, t) \approx \frac{D_{ev}/a}{\ln(\sqrt{D_{ev}t}/a)}\,. \tag{4.13b}$$

The effect of an impulse-like amount of tracer reaching a narrow capillary can be studied by evaluating the effective extravascular diffusion volume, $\Lambda_D(t)$, Eq. (2.26). Differentiating both $\mu_{ev}(t) = \Lambda(t)$ and Eq. (4.11a), to account for an impulse-like, rather than step-like, concentration in the capillary, yields the correct value of $\Lambda_D(t)$ for the free diffusion case:

$$\Lambda_D(t) \approx 4\pi D_{ev}t\,[1 + (a/\ell)\ln(\sqrt{4D_{ev}t}/a)] \to 4\pi D_{ev}t$$

as $a \to 0$, with $\kappa > 0$ and finite.

Long diffusion times

At long diffusion times, $\sqrt{D_{ev}t} \gtrsim A$, the single-capillary approximation is no longer accurate. It is nevertheless possible to gain quantitative insight when a steady state is established. This regime is discussed in detail in Section 4.5.

4.1.3 Physiological examples

Tracer exchange across the blood–brain barrier

Water exchange across the normal blood–brain barrier and myocardial capillary wall is strongly permeability limited, as indicated by some typical values of $D_{ev}/\kappa a$ listed in Table 2.1.

instants results in linearly equispaced amplitudes of $W(a_+, t)$ in Fig. 3.7d.

We next discuss the influence of transcapillary water exchange on the dynamic susceptibility contrast (DSC) MRI intensity in both these tissues. It is well known that the first pass of a bolus of intravascular paramagnetic tracer at high concentration through the microvasculature causes a large reduction in DSC MRI tissue intensities: at the time of maximum tracer concentration in the blood plasma, reductions of between 30% to 60% of the baseline (pre-contrast) amplitude can be observed [14, 150]. This strong effect is known to be mediated by long-ranged magnetic field inhomogeneities arising from tracer-induced changes in the magnetic susceptibility of blood; obviously, it cannot be explained by intravascular relaxation alone, given the comparatively small volume fraction of intravascular space [14]. Transcapillary water exchange contributes to tissue intensity reduction by allowing extravascular water molecules to come into contact with the intravascular paramagnetic tracer on a time scale of the order of MRI echo times, e.g., $T_\mathrm{E} = 14-95$ ms [14, 150]. The effective extravascular volume occupied by these molecules in unit length of vessel is estimated from (4.5) as $(2\kappa/a)T_\mathrm{E} \approx T_\mathrm{E}/\tau_\mathrm{iv}$, when expressed as a fraction of microvascular volume, and as $v_\mathrm{iv}T_\mathrm{E}/\tau_\mathrm{iv} = PS \cdot T_\mathrm{E}$ when expressed as a fraction of whole tissue volume [see Eq. (2.2b)]. Using the above echo times and the values of v_iv, τ_iv listed in Table 2.1 or, equivalently, the values of PS given in Appendix 2.5.2, we estimate this latter fraction as $0.04\%-0.2\%$ for grey matter and $0.7\%-5\%$ for myocardium. These estimates corroborate that transcapillary water exchange in normal grey matter and myocardium affects transverse relaxation in whole tissue much less than tracer-induced susceptibility changes. Therefore, transverse magnetic relaxation in the tissues is essentially a mesoscopic phenomenon [150].

Where disruption of the capillary wall allows the extravasation of tracer, both short-ranged relaxivity effects and long-ranged susceptibility effects can arise [14]. The impaired blood–brain barrier appears to be rate-limiting even for small paramagnetic molecules. For example, in a longitudinal study of mice glioma [186], the volume transfer constant [28] of gadopentetate dimeglumine was estimated as $K^\mathrm{trans} \approx PS \sim 0.3$ min^{-1} at one stage in the study; for comparison, PS for $\mathrm{H_2^{15}O}$ exchange in human brain tissue is of the order of 1 min^{-1} [160]. Using a realistic

value of diffusion coefficient of gadopentetate dimeglumine in tissue of 0.26 μm^2 ms^{-1} [164], we estimate $D_{\mathrm{ev}}/\kappa a \sim 2D_{\mathrm{ev}}/A^2PS \sim 10^2 - 10^3$. As another example, in a DCE MRI study of breast tumours, the exchange rate for gadodiamide and gadopentetate dimeglumine was determined to be in the range $k_{\mathrm{ep}} \equiv \tau_{\mathrm{ev}}^{-1} = 0.04 - 3$ min^{-1} [187, Table 1].

Water exchange across the basolateral membrane of renal proximal tubules

The diffusive water permeability of the basolateral membrane of the renal proximal tubule, $\kappa \sim 0.7$ μm ms^{-1}, is about two orders of magnitude higher than that of both the blood–brain barrier and myocardial capillaries. Since the ratio $D_{\mathrm{is}}/r_2\kappa \sim 10^{-1}$, water exchange across the basolateral membrane of renal tubules is likely limited by water diffusion in the interstitial space. (These parameters are listed in Table 2.1 and more details are given in Appendix 2.5.2).

4.2 Spatiotemporal versus lumped tracer-exchange models

As stated in Section 1.1.2, when lumped tracer-exchange models are used in analysing transport and exchange phenomena, compartmental tracer concentrations are considered spatially uniform at all times [9, 32]. However, while diffusion tends to smooth out non-uniform tracer concentrations, this takes time. Moreover, a complete uniformity of tracer concentration might not be achievable in the presence of tracer permeation and consumption. In this Section we consider short to intermediate diffusion times and assume non-steady-state conditions; the steady state is considered in Section 4.5.

To assess the accuracy of a class of lumped tracer-exchange model, we begin by averaging the spatiotemporal tracer-balance equations (2.1a) and (2.1b) over, respectively, the intracapillary and pericapillary spaces associated with any given

capillary segment. For intracapillary space we obtain

$$\frac{\mathrm{d}\psi_{\mathrm{iv}}(t)}{\mathrm{d}t} = \frac{\psi_{\mathrm{iv}}(0,t) - \psi_{\mathrm{iv}}(L,t)}{\tau_{\mathrm{c}}} - \frac{\psi_{\mathrm{iv}}(t)|_{\mathbf{a}_-} - \psi_{\mathrm{ev}}(t)|_{\mathbf{a}_+}}{\tau_{\mathrm{iv}}} - R_{\mathrm{iv}}\psi_{\mathrm{iv}}(t)\,, \tag{4.14}$$

where $\psi_{\mathrm{iv}}(t)$ denotes the spatially averaged concentration of tracer in a capillary segment, in units of quantity of tracer per unit volume of tracer-accessible space, i.e., blood plasma or whole blood, depending on the tracer in question; $\psi_{\mathrm{iv}}(0,t)$, $\psi_{\mathrm{iv}}(L,t)$ denote the average concentration at, respectively, the inflow and outflow ends of that same capillary segment; $\psi_{\mathrm{iv}}(t)|_{\mathbf{a}_-}$, $\psi_{\mathrm{ev}}(t)|_{\mathbf{a}_+}$, denote spatially averaged concentrations over, respectively, the luminal and abluminal face of the capillary wall; the mean capillary-segment transit time is defined by Eq. (2.3a); and the mean intracapillary residence time τ_{iv} is defined on the scale of a capillary segment[4] and is given by Eq. (2.2a).

Next, averaging the diffusion–consumption equation (2.1b) over a pericapillary volume ΔV gives

$$\frac{\mathrm{d}\psi_{\mathrm{ev}}(t)}{\mathrm{d}t} = \frac{1}{\Delta V}\int_{\Delta V} D_{\mathrm{ev}}\nabla^2\psi_{\mathrm{ev}}(\mathbf{r},t)\,\mathrm{d}^d\mathbf{r} - R_{\mathrm{ev}}\psi_{\mathrm{ev}}(t)\,. \tag{4.15a}$$

where $\psi_{\mathrm{ev}}(t)$ is the spatially averaged concentration of tracer in the pericapillary region, expressed in units of quantity of tracer per volume of tracer-accessible pericapillary space. The integral on the right-hand side becomes an integral over the abluminal capillary surface ΔS with the use of the Gauss theorem and the boundary conditions (2.1c) and (2.1d), as given by

$$\frac{1}{\Delta V}\int_{\Delta V} D_{\mathrm{ev}}\nabla^2\psi_{\mathrm{ev}}(\mathbf{r},t)\,\mathrm{d}^d\mathbf{r} = \frac{1}{v_{\mathrm{ev}}\Delta V}\int_{\Delta S} -\mathbf{n}v_{\mathrm{ev}}D_{\mathrm{ev}}\nabla\psi_{\mathrm{ev}}(\mathbf{a}_+,t)\,\mathrm{d}S\,, \tag{4.15b}$$

where $\mathbf{n}$ is a unit normal directed outwards from the abluminal capillary surface and, here, v_{ev} denotes the fraction of tracer-accessible extravascular space in the pericapillary region. The right-hand integrand is recognised as the mesoscopic transcapillary permeation flux [cf. Eqs (2.39a) and (2.39b)] where $\psi_{\mathrm{ev}}(\mathbf{a}_+,t)$ is regarded as a concentration in an effective homogenous medium (p. 21) whose intrinsic conductivity, or reciprocal tortuosity (p. 73), is thus unity. Therefore, the average of this flux over

[4] See footnote 4 on p. 28.

the surface of a capillary segment can be evaluated by a similar procedure to that used in developing the capillary boundary condition on a mesoscopic scale starting from the microscopic (i.e., pore-scale) concentration; cf. Eqs (2.66) and (2.67a) of Appendix 2.5.1. This gives

$$\begin{aligned}\frac{1}{v_{\mathrm{ev}}\Delta V}\int_{\Delta S} -\mathbf{n}v_{\mathrm{ev}}D_{\mathrm{ev}}\nabla\psi_{\mathrm{ev}}(\mathbf{a}_+,t)\,\mathrm{d}S &= \frac{\kappa\Delta S}{v_{\mathrm{ev}}\Delta V}\left[\psi_{\mathrm{iv}}(t)|_{\mathbf{a}_-}-\psi_{\mathrm{ev}}(t)|_{\mathbf{a}_+}\right]\\ &= \frac{\psi_{\mathrm{iv}}(t)|_{\mathbf{a}_-}-\psi_{\mathrm{ev}}(t)|_{\mathbf{a}_+}}{\tau_{\mathrm{ev}}}\,,\end{aligned} \tag{4.15c}$$

where κ is an effective capillary wall permeability on the scale of a typical capillary segment and τ_{ev} is defined on this scale by

$$\tau_{\mathrm{ev}} = \frac{v_{\mathrm{ev}}\Delta V}{\kappa\Delta S} = \frac{\Delta V_{\mathrm{ev}}}{\kappa\Delta S}\,; \tag{4.15d}$$

the numerator is equal to the fraction of the given pericapillary region that is accessible to tracer, with a notation as in Eq. (2.31c). On a whole-tissue scale, Eq. (4.15d) may be expressed as Eq. (2.2c) where in this latter equation v_{ev} stands for the fraction of tracer-accessible extravascular space per unit volume of whole tissue.[5]

The spatially averaged tracer-balance equation for extravascular space is obtained upon substitution of Eq. (4.15c) into Eq. (4.15a) as

$$\frac{\mathrm{d}\psi_{\mathrm{ev}}(t)}{\mathrm{d}t} = \frac{\psi_{\mathrm{iv}}(t)|_{\mathbf{a}_-}-\psi_{\mathrm{ev}}(t)|_{\mathbf{a}_+}}{\tau_{\mathrm{ev}}} - R_{\mathrm{ev}}\psi_{\mathrm{ev}}(t)\,. \tag{4.16}$$

The above spatially averaged equations include the time constants of tracer transport, exchange and consumption/relaxation, which are thus described as first-order, diffusion-independent processes. We note that one can integrate the spatiotemporal Eqs (2.1a) and (2.1b) over the entire intracapillary and pericapillary spaces associated with any given capillary segment because the intrinsic phased-averaged concentrations which enter in these equations are defined for all space in an effective mesoscopic medium; see Appendix 2.5.1, in particular Eqs (2.31a) and (2.31b), and item 1 on p. 65.

Equations (4.14) and (4.16) apply respectively to any given capillary segment and its associated pericapillary region. However, in practice they are often used in the

[5] See footnote 4 on p. 28.

quantification of blood–tissue tracer exchange on the scale of 'macroscopic' measurement volumes (e.g., typical MRI voxels with linear dimensions ~ 1 mm; p. 61) by assuming that all relevant mesoscopic parameters and quantities of interest remain meaningful on a coarser scale. Alternative expressions are obtained by multiplying both sides of (4.14) and (4.16) by the respective fraction of tracer-accessible intracapillary space per unit volume of whole tissue (p. 27), denoted by v_{iv} and v_{ev}, and recalling the definitions of capillary permeability surface area product, PS, and capillary tracer flow per volume of whole tissue, f_{iv}. Thus,

$$\begin{aligned} v_{\mathrm{iv}}\frac{\mathrm{d}\psi_{\mathrm{iv}}(t)}{\mathrm{d}t} &= f_{\mathrm{iv}}\left[\psi_{\mathrm{iv}}(0,t)-\psi_{\mathrm{iv}}(L,t)\right] \\ &\quad - PS\left[\psi_{\mathrm{iv}}(t)|_{\mathbf{a}_-}-\psi_{\mathrm{ev}}(t)|_{\mathbf{a}_+}\right]-v_{\mathrm{iv}}R_{\mathrm{iv}}\psi_{\mathrm{iv}}(t)\,, \qquad (4.17a) \\ v_{\mathrm{ev}}\frac{\mathrm{d}\psi_{\mathrm{ev}}(t)}{\mathrm{d}t} &= PS\left[\psi_{\mathrm{iv}}(t)|_{\mathbf{a}_-}-\psi_{\mathrm{ev}}(t)|_{\mathbf{a}_+}\right]-v_{\mathrm{ev}}R_{\mathrm{ev}}\psi_{\mathrm{ev}}(t)\,. \qquad (4.17b) \end{aligned}$$

Equations of this form including the PS parameter appear frequently in the tracer kinetic literature; e.g., Refs [28, Eq. (16)] and [34, Eqs (11)–(12)], also Ref. [41].

In the limiting case where the blood–tissue tracer flux is rate-limited by capillary wall permeability rather than by capillary flow (i.e., when $\tau_{\mathrm{c}}/\tau_{\mathrm{iv}} \ll 1$), the intracapillary concentration $\psi_{\mathrm{iv}}(t)$ may be regarded as driving the blood–tissue tracer flux and the appropriate two-compartment lumped tracer-exchange model reduces to Eq. (4.16). In lumped modelling approaches, the amplitude of the concentration at the capillary wall is assumed equal to the compartmental average value, hence (4.16) becomes (cf. Eq. (16) of Ref. [28]):

$$\frac{\mathrm{d}\psi_{\mathrm{ev}}(t)}{\mathrm{d}t} = \frac{\psi_{\mathrm{iv}}(t)-\psi_{\mathrm{ev}}(t)}{\tau_{\mathrm{ev}}} - R_{\mathrm{ev}}\psi_{\mathrm{ev}}(t)\,, \qquad (4.18)$$

whose solution for initial-rest extravascular conditions is given by the convolution

$$\psi_{\mathrm{ev}}(t) = w_{\mathrm{lumped}}(t) * \psi_{\mathrm{iv}}(t)\,, \qquad (4.19a)$$

with

$$w_{\mathrm{lumped}}(t) = \frac{1}{\tau_{\mathrm{ev}}}\exp(-R_{\mathrm{ev}}^{+}t)\,, \qquad R_{\mathrm{ev}}^{+} \equiv R_{\mathrm{ev}} + \frac{1}{\tau_{\mathrm{ev}}}\,. \qquad (4.19b)$$

The Green's function, or impulse response function, for the lumped tracer-exchange model given by Eq. (4.18) is obtained by comparing $w_{\text{lumped}}(t)$ with the spatiotemporal blood-to-tissue impulse response function (2.15). Thus

$$G_{\text{lumped}}(\mathbf{r}, \mathbf{a}_+, t) = \frac{1}{\kappa S}\, w_{\text{lumped}}(t) = \frac{1}{V_{\text{ev}}} \exp(-R_{\text{ev}}^{+} t)\,. \tag{4.19c}$$

The physical meaning of this expression is that the concentration of tracer at any position $\mathbf{r}$ due to permeation of a packet of tracer molecules into extravascular space at time zero is independent of position, but depends only on the elapsed time t. This is another statement of the well-mixed assumption of lumped tracer-exchange models.

Importantly, since the spatial concentration average over the abluminal face of the capillary wall, $\psi_{\text{ev}}(t)|_{\mathbf{a}_+}$, differs, in general, from the spatial concentration average over the tracer-accessible extravascular space, $\psi_{\text{ev}}(t)$, and since the ratio $\psi_{\text{ev}}(t)|_{\mathbf{a}_+}/\psi_{\text{ev}}(t)$ is a time-varying quantity, Eq. (4.16) and Eq. (4.18) are not, in general, equivalent descriptions of tracer exchange. To illustrate this point, Fig. 4.3 plots the ratio $W(t)/W(\mathbf{a}_+, t)$ of the average amplitude of the step response function to the amplitude of the step response function at the capillary wall. In this example, two widely different values of capillary permeability have been chosen which are consistent with, respectively, permeability- (solid line) and diffusion-limited (broken line) exchange regimes. The calculations were carried out for radial distances $r/a \leq 10$, consistent with maximal half-intercapillary distances in grey matter of cats [65]; only those step response profiles having negligibly low amplitude at $r = 10a$ were considered in order not to bias the estimate of the average step response. [Note, however, that the ratio $W(t)/W(\mathbf{a}_+, t)$ depends on the choice of pericapillary radius A: in fact, it diminishes when higher values of A are chosen].

As shown in Fig. 4.3, the ratio $W(t)/W(\mathbf{a}_+, t)$ increases as diffusion time progresses, and attains its maximum value at steady state (not shown). For given values of the capillary radius and diffusion coefficient, this ratio becomes higher for lower permeabilities (i.e., lower $D_{\text{ev}}/\kappa a$), as expected. In this example, dependence with capillary permeability is seen to be low, in absolute terms, but varies appreciably over

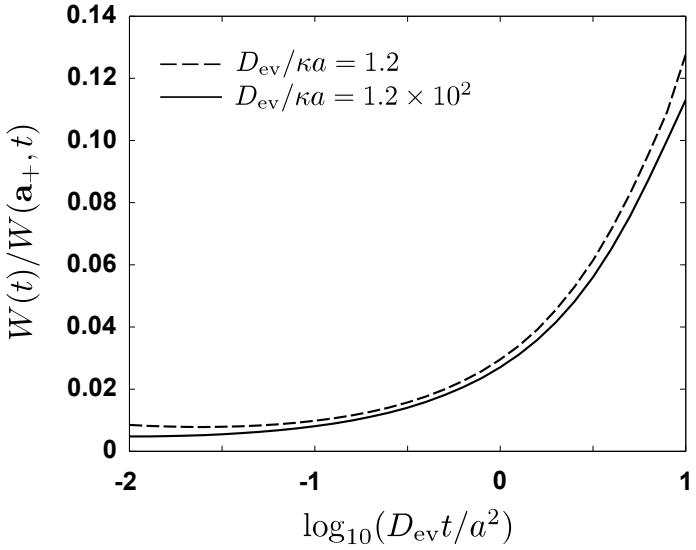

Figure 4.3: **Ratio of spatially averaged to abluminal amplitude of step response function for sparse capillary networks**. Both amplitudes were evaluated from Eq. (3.40a). Values of the parameters: $a = 2.8$ μm; radial distance, $a \leq r \leq 10a$; $D_{\rm ev} = 1.8$ $\mu{\rm m}^2\,{\rm ms}^{-1}$; $\kappa = 5.2\times10^{-3}$ $\mu{\rm m\,ms}^{-1}$ (solid line) and 5.2×10^{-1} $\mu{\rm m\,ms}^{-1}$ (broken line).

the shown range of diffusion times: the shown curves differ by nearly 80% for times such that $\log_{10}(D_{\rm ev}t/a^2) = -2$ diminishing to about 10% for $\log_{10}(D_{\rm ev}t/a^2) \gtrsim 0$.

A comparison of Eqs (4.16) and (4.18) shows that for short to intermediate diffusion times the average extravascular concentration predicted by the lumped tracer-exchange model of Eq. (4.18) agrees with that predicted by the spatiotemporal model when the amplitude of the abluminal concentration is almost equal to the spatially averaged extravascular concentration, or when it is much lower than the intracapillary concentration; these cases are discussed in turn below:

1. For lumped tracer-exchange modelling approaches, the assumption that extravascular diffusion redistributes the tracer efficiently, relative to transcapillary exchange, is valid when $\tau_D \ll \tau_{\rm ev}$, i.e., when $D_{\rm ev}/\kappa a \gg 1$. This condition is characteristic of permeability-limited exchange (Fig. 4.1). As was discussed in Section 4.1, in this situation the transcapillary tracer flux will be only weakly dependent on tracer diffusion. Also, if a diffusive steady state is attained, then

any subsequent variations in the transcapillary flux will, initially, be rate-limited by capillary wall permeability.

2. At sufficiently short diffusion times, given by $t \lesssim \min\{a^2/D_{\mathrm{ev}}, \ell^2/D_{\mathrm{ev}}\}$, the extravascular concentration is low, i.e., $\psi_{\mathrm{ev}}(t)|_{\mathbf{a}_+} \ll \psi_{\mathrm{iv}}(t)|_{\mathbf{a}_-}$ regardless of the value of the $D_{\mathrm{ev}}/\kappa a$ ratio. Thus, the blood-to-tissue flux is given, approximately, by[6]

$$\mathbf{n}\mathbf{j}_\kappa(t) \approx \kappa\psi_{\mathrm{iv}}(t)|_{\mathbf{a}_-} \approx \kappa\psi_{\mathrm{iv}}(t) \tag{4.20}$$

and the amount of tracer in extravascular space therefore increases as

$$\frac{\mathrm{d}\mu_{\mathrm{ev}}(t)}{\mathrm{d}t} = S\mathbf{n}\mathbf{j}_\kappa(t) \approx \frac{\mu_{\mathrm{iv}}(t)}{\tau_{\mathrm{iv}}}\,. \tag{4.21}$$

The rate of tracer permeation into extravascular space at initial time, per unit amount of intracapillary tracer, is equal to the reciprocal of the mean intracapillary residence time, τ_{iv}^{-1}, as expected. Thus, at short diffusion times the average extravascular concentration and the amount of tracer are identical for the spatiotemporal model (4.16) and the lumped model (4.18), to within the approximation made.

The well-mixed assumption prevents the use of lumped tracer-exchange models for the analysis of diffusion-limited exchange (Fig. 4.1). During transient diffusion (i.e., for tracer diffusion lengths not exceeding approximately one-half the typical intercapillary distance), the lumped tracer-exchange model of Eq. (4.18) will overestimate the blood–tissue tracer flux, as it takes no account of the 'jamming effect' due to gradients in tracer concentration at the capillary wall, i.e.,

$$|\psi_{\mathrm{iv}}(t)|_{\mathbf{a}_-} - \psi_{\mathrm{ev}}(t)|_{\mathbf{a}_+}| \leq |\psi_{\mathrm{iv}}(t) - \psi_{\mathrm{ev}}(t)|\,. \tag{4.22}$$

Thus, a lumped tracer-exchange model overestimates the time rate of change of the extravascular concentration. The jamming effect is most apparent in Fig. 3.7b: since

[6]Here, zero initial conditions prior to arrival of tracer at the capillaries have been assumed and the common relaxation term appearing in (4.16) and (4.18) has been omitted.

the tracer concentration at the compartment barrier is distinctly higher than that at positions farther away from the barrier, the tracer flux across the barrier is strongly rate-limited by extravascular diffusion, thus rendering inapplicable the lumped model.

The regions of validity of both spatiotemporal and lumped tracer-exchange models are graphed in Fig. 4.1.

4.3 Diffusion-limited exchange: blood–tissue gas exchange

Cellular respiration requires supply of oxygen to, and removal of carbon dioxide from, the body tissues, involving convection, diffusion and chemical reaction processes [1]. Because both of them are small non-polar molecules, O_2 and CO_2 permeate rapidly across the lipid bilayer of capillary endothelial cells [1, 2]. Kassissia *et al.* [35] estimated $PS = 1.17\ \mathrm{ml\,g^{-1}\,s^{-1}}$ ($= 70.2\ \mathrm{ml\,g^{-1}\,min^{-1}}$) for $^{18}O_2$ in dog brain, i.e., approximately two orders of magnitude higher than regional PS values for $H_2^{15}O$ in human brain, as determined by Herscovitch *et al.* [160].

In this Section, we review several gas exchange models from the literature and compare them to the present blood–tissue exchange model under diffusion-limited conditions. The main conclusions are as follows: (i) oxygen-delivery models are not applicable to first-order extravascular consumption of tracers because tissue oxygen consumption depends non-linearly on local oxygen tension; and (ii) simplified modelling of gas exchange is possible using the results for absorbing intracapillary boundary conditions presented in Chapter 3.

Reneau *et al.* [57] introduced a model for the evaluation of transient oxygen transport in cerebral grey matter that includes oxygen delivery, diffusion (both axial and radial) and consumption in the capillaries and the surrounding tissue. Modified forms of this model were later applied by Lagerlund and Low [58] and by Sharma and Jain [59] to rat peripheral nerve. In all cases, the physical geometry was assumed to be well represented by a Krogh capillary–tissue unit. Equations (4.23a) – (4.24b) be-

low are reproduced from Ref. [59] for convenience.[7] In the capillary, the differential equation for the oxygen partial pressure, or tension, $P(r, z, t)$, reads

$$\frac{\partial P}{\partial t} = D_{\mathrm{iv}} \nabla^2 P - u_z E \frac{\partial P}{\partial z} - K_{\mathrm{f}} P + K_{\mathrm{r}} P \,, \tag{4.23a}$$

and that for the pericapillary region is

$$\frac{\partial P}{\partial t} = D_{\mathrm{ev}} \nabla^2 P - \frac{C(P)}{S_{\mathrm{t}}} \,. \tag{4.23b}$$

Here D_{iv} is an overall diffusion coefficient in whole blood (plasma and erythrocytes) [57]; K_{f}, K_{r} respectively denote forward and reverse chemical reaction rates [59] between plasma and haemoglobin-carrying erythrocytes [73]; E accounts for oxygen bound to haemoglobin and dissolved in blood, and is a highly non-linear function of oxygen tension [57]; and S_{t} is oxygen solubility in the tissue fluid [52]. (The oxygen concentration in interstitial fluid is equal, by Henry's law, to the product of oxygen tension and solubility [52]). The metabolic consumption rate, $C(P)$, is represented by Michaelis–Menten kinetics [58]:

$$C(P) = C_{\max} \frac{P}{P + C_{50}} \,, \tag{4.23c}$$

where $C_{\max}$, C_{50} are constants. Typically, the tissue oxygen tension $P < 40$ mm Hg [1, p. 845] and $C_{50} = 0.5 - 1$ mm Hg [73]. The following boundary conditions stipulated continuity of oxygen tension and oxygen transcapillary flux at the capillary wall:

$$P(\mathbf{a}_-, t) = P(\mathbf{a}_+, t) \,, \tag{4.24a}$$

$$\mathbf{n} D_{\mathrm{iv}} \nabla P(\mathbf{a}_-, t) = \mathbf{n} D_{\mathrm{ev}} \nabla P(\mathbf{a}_+, t) \,. \tag{4.24b}$$

A zero-flux condition was specified at the edge of the oxygen supply region; additional boundary conditions were specified at both the arterial and venous ends of the capillary [58, 59]. The initial condition was set equal to the steady-state solution of the system of equations. Because the modelling was applied to peripheral nerve,

[7] Parameters D_{iv}, D_{ev} and u_z in Eqs (4.23a) and (4.23b) of this Thesis correspond to D_{b}, D_{t} and v in Refs [58, 59].

myoglobin-facilitated diffusion, as occurs in cardiac and skeletal muscle, was not included; consideration of this mechanism leads to a more complex form of the Laplace operator in (4.23b) [73].

Sharma and Jain [59] solved the above equations numerically beginning from a steady-state distribution of oxygen tension, as determined by the geometry of the Krogh capillary–tissue unit and the physiological parameters of the tissue. The aim of these authors was to investigate the adaptation to new steady-state conditions after arterial oxygen tension, blood flow velocity and rate of tissue oxygen consumption were allowed, in turn, to vary in response to a monoexponential time course.

The main differences between the modelling of Eqs (4.23a) – (4.24b) and the one presented in this Thesis are as follows:

1. Radial transport of oxygen within the microvasculature is a complex phenomenon involving gradients in oxygen tension [55]. This contrasts with the assumption of uniform distribution of tracer in intracapillary space made here (Section 2.1.1).

   Moreover, in using the boundary conditions (4.24a) and (4.24b), the capillary wall is assumed to be fully permeable to oxygen (see Ref. [57]. In some cases, the transcapillary oxygen flux is assumed to be proportional to the difference between the radially averaged intracapillary tension and the tissue tension averaged around the circumference of the capillary [55, 73]). On the other hand, it is frequently the case that MRI and PET tracers do not permeate freely across the capillary wall.

2. It is not possible to represent first-order consumption (e.g., local longitudinal magnetic relaxation) by means of the non-linear relationship Eq. (4.23c): the rate of oxygen consumption in the cells reaches a plateau when the oxygen tension is high, but falls off to zero when there is reduced oxygen availability.

Roughton [56] considered the simplified case of a uniform oxygen tension in blood, but allowed for diffusion and both zero- and first-order reactions in the extravascular

tissue. With some notational changes, Eq. (2.1) of Ref. [56] reads[8]

$$\frac{\partial P}{\partial t} = \frac{D}{S_\mathrm{t}}\nabla^2 P - \frac{k}{S_\mathrm{t}}(P - P_0) - \frac{C}{S_\mathrm{t}}\,, \tag{4.25}$$

where $D = S_\mathrm{t} D_\mathrm{ev}$ is the oxygen diffusion coefficient in extravascular tissue, defined in terms of pressure gradient instead of concentration, and k is the rate constant of a first-order reaction. The initial and boundary conditions were specified as[9]

$$P(a < r \leq A, t = 0) = 0\,, \tag{4.26a}$$

$$P(a, t \geq 0) = 1\,, \tag{4.26b}$$

$$\left.\frac{\partial P(r, t \geq 0)}{\partial r}\right|_{r=A} = 0\,. \tag{4.26c}$$

For the case of no zero-order reaction ($C = 0$), the solution representing, on account of Eqs (4.26a) and (4.26b), the step response function, was given as Eq. (3.20) of Ref. [56]. With some notational changes, that expression reads

$$P(r,t) = \pi \sum_{n=1}^{\infty} \frac{J_0(\gamma_n a)Y_0(\gamma_n r) - J_0(\gamma_n r)Y_0(\gamma_n a)}{\left[J_0(\gamma_n a)/J_1(\gamma_n A)\right]^2 - 1} \frac{\exp[-(D_\mathrm{ev}\gamma_n^2 + R_\mathrm{ev})t]}{1 + R_\mathrm{ev} D_\mathrm{ev}^{-1}\gamma_n^{-2}} + P(r, t \to \infty)\,, \tag{4.27a}$$

where γ_n is the nth root of the equation

$$J_0(\gamma_n a)Y_1(\gamma_n A) - Y_0(\gamma_n a)J_1(\gamma_n A) = 0\,. \tag{4.27b}$$

The steady-state term, $P(r, t \to \infty)$, is given by a linear combination of the modified Bessel functions $I_0(\cdot)$ and $K_0(\cdot)$. Eliminating this term with the use of the initial condition in (4.26a), we rewrite Roughton's equation (4.27a) as

$$P(r,t) = \pi \sum_{n=1}^{\infty} \frac{J_0(\gamma_n a)Y_0(\gamma_n r) - J_0(\gamma_n r)Y_0(\gamma_n a)}{\left[J_0(\gamma_n a)/J_1(\gamma_n A)\right]^2 - 1} \frac{1 - \exp[-(D_\mathrm{ev} q_n^2 + R_\mathrm{ev})t]}{1 + R_\mathrm{ev} D_\mathrm{ev}^{-1}\gamma_n^{-2}}\,. \tag{4.28}$$

[8] Roughton's notation has been adapted to that employed in this Thesis as follows: $p \mapsto P$, $b \mapsto a$, $a \mapsto A$, $\alpha \mapsto S_\mathrm{t}$, $k/\alpha \mapsto R_\mathrm{ev}$, $x_n/b \mapsto \gamma_n$.

[9] Roughton actually specified an arbitrary, but constant, oxygen tension p_0 for $a < r \leq A$ at zero time, and a constant tension p_b at the capillary wall at all times. The solution, his Eq. 3.00 of Ref. [56], may be expressed as a function $P(r,t) - p_0$ with parameter $p_b - p_0$.

Because Eq. (4.26b) fixes the abluminal oxygen tension to that in the luminal face of the capillary wall, the modelling of Roughton tacitly assumes a very large capillary permeability to oxygen. In this situation, the rate at which the local oxygen tension approaches a new steady state is assumed to depend solely on extravascular diffusion and reaction rate. We show next that for sparse capillary networks, Eq. (3.20) of Roughton reduces to the step response function obtained in this Thesis, Eq. (3.40a), for the case of vanishing $\ell/a\,(= D_{\mathrm{ev}}/\kappa a)$. In this limit, Eq. (3.27) gives $P(q_n a) \to J_0(q_n a)$ and $Q(q_n a) \to Y_0(q_n a)$. Thus, the scattering phase shift (3.25) satisfies $\tan\delta_n \to -J_0(q_n a)/Y_0(q_n a) = -J_1(q_n A)/Y_1(q_n A)$, which is identical with (4.27b). This shows that the eigenfrequencies $\gamma_n \to q_n$. Next, a term in the integrand of (4.28) is rewritten as[10]

$$\begin{aligned}\left[\frac{J_0^2(q_n a)}{J_1^2(q_n A)} - 1\right]^{-1} &= \frac{J_1^2(q_n A)}{J_0^2(q_n a)}\,\frac{1}{1 - J_1^2(q_n A)/J_0^2(q_n a)} \\ &= \frac{J_1^2(q_n A) + Y_1^2(q_n A)}{J_0^2(q_n a) + Y_0^2(q_n a)}\,\frac{1}{1 - J_1^2(q_n A)/J_0^2(q_n a)} \\ &\approx \frac{2/\pi}{J_0^2(q_n a) + Y_0^2(q_n a)}\,\frac{1}{q_n A} \\ &\approx \frac{2/\pi^2}{J_0^2(q_n a) + Y_0^2(q_n a)}\,\frac{\Delta q_n}{q_n}\,,\end{aligned} \tag{4.29}$$

where the approximations are valid for large $q_n A$. Finally, substituting the last line of (4.29) in (4.28), rearranging with the use of the parameters ς (3.38a) and η_a (3.40b), and passing to the integral, results in the blood-to-tissue step response function (3.40a) for highly permeable capillary walls. This is graphed in Fig. 4.4.

Hudson and Cater [52] in an extensive analysis of factors affecting oxygen delivery considered a model similar to that of Roughton. These authors assumed zero-order, but not first-order, reaction, so that their Eq. (5.1) is obtained by omitting the middle

[10] The substitution made in the second line of (4.29),

$$\frac{J_1^2(q_n A)}{J_0^2(q_n a)} = \frac{J_1^2(q_n A) + Y_1^2(q_n A)}{J_0^2(q_n a) + Y_0^2(q_n a)}$$

follows from the expression of $\tan\delta_n$ for vanishing ℓ/a given in the text. In the third line of Eq. (4.29), the large-argument expansion of the Bessel functions [99, 172] has been used.

term on the right-hand side of (4.25).[11] They considered the effect of a sudden change in oxygen tension at all points on the capillary wall from a steady-state value, P_0, to a new value P_1, and evaluated the local difference in oxygen tension at time t and in the steady state, $\Gamma(r,t) \equiv P(r,t) - P(r, t \to \infty)$, with

$$\Gamma(a < r \leq A, t = 0) = P_0 - P_1 \,, \tag{4.30a}$$

$$\Gamma(a, t \geq 0) = 0 \,, \tag{4.30b}$$

$$\left.\frac{\partial \Gamma(r, t > 0)}{\partial r}\right|_{r=A} = 0 \,. \tag{4.30c}$$

Note that $\Gamma(r,t)$ is not a function of reaction rate C. The solution was given as Eq. (5.10) of Ref. [52], reproduced below:

$$\Gamma(r,t) = (P_1 - P_0) \sum_{n=1}^{\infty} \frac{\pi J_1^2(\gamma_n A)}{J_0^2(\gamma_n a) - J_1^2(\gamma_n A)} \left[J_0(\gamma_n r) Y_0(\gamma_n a) - J_0(\gamma_n a) Y_0(\gamma_n r)\right] \times \exp\left[-(D/S_\mathrm{t})\gamma_n^2 t\right] \,, \tag{4.31a}$$

where γ_n is the nth positive root of Eq. (4.27b) and the substitutions $J_0'(\cdot) = -J_1(\cdot)$, $Y_0'(\cdot) = -Y_1(\cdot)$ have been made in the formula given by Hudson and Cater.

Equations (4.30a) and (4.30b) respectively prescribe a uniform $\Gamma(r,t)$ at the initial time and an absorbing intracapillary boundary condition. $\Gamma(r,t)$ is therefore analogous to the extravascular concentration under absorbing intracapillary conditions, $\psi_\mathrm{ev}^\mathrm{abs}(r,t)$, Eq. (3.31). It should be noted that an instantaneous change in abluminal oxygen tension, as expressed by Eq. (4.30b), can only occur if the capillary permeability is very large. Then, by a similar procedure as was employed in arriving at Eq. (4.28), the extravascular concentration under absorbing intracapillary conditions, Eq. (3.31), is found as

$$\psi_\mathrm{ev}^\mathrm{abs}(r,t;\kappa \to \infty) = \sum_{n=0}^{\infty} \frac{\pi J_1^2(q_n A)}{J_0^2(q_n a) - J_1^2(q_n A)} \left[J_0(q_n a) Y_0(q_n r) - J_0(q_n r) Y_0(q_n a)\right] \times \exp(-D_\mathrm{ev} q_n^2 t) \,, \tag{4.32}$$

[11] Here, the notations p, m, α, r_0 and R of Hudson and Cater [52] have been replaced by P, C, S_t, a and A, respectively.

which is formally identical with Eq. (4.31a) of Hudson and Cater on putting $P_0 = 1$ and $P_1 = 0$, and with Eq. (3.10) of Roughton [56].

For sparse capillary networks, the right-hand side of (4.32) reduces to an integral independent of pericapillary radius A, plus a small term of order a/A (Section 3.2). Letting $\ell \to 0$ in Eq. (3.37) gives

$$\psi_{\mathrm{ev}}^{\mathrm{abs}}(r,t;\kappa\to\infty) = \frac{2}{\pi}\int_0^\infty \frac{J_0(qa)Y_0(qr) - Y_0(qa)J_0(qr)}{[J_0^2+Y_0^2](qa)}\,\frac{\exp(-D_{\mathrm{ev}}tq^2)}{q}\,\mathrm{d}q\,. \qquad (4.33)$$

The above formula was not given in Refs [52, 56] and is plotted in Fig. 4.4 for a range of extravascular diffusion times. (From the values of S_{t} and D quoted in Ref. [52, p. 250], we estimate $D_{\mathrm{ev}} \sim 1\ \mu\mathrm{m}^2\,\mathrm{ms}^{-1}$ in muscle, and using $a = 3\ \mu$m we find a time range $t \sim 10^{-3} - 10^3$ ms). Under extreme diffusion-limited exchange conditions, the expression for the extravascular tracer concentration becomes independent of capillary permeability, as expected. It should be noted that, since κ is very large, the lumped tracer-exchange model of Eq. (4.18) is unsuitable for calculation of the blood–tissue flux in this case. The curves graphed in Fig. 4.4 show that the transcapillary flux becomes infinitely strong at the onset of transcapillary exchange.[12]

Tissue transport of the highly diffusible metabolic gas, carbon dioxide, was studied by Severns and Milton Adams [188] using an approach analogous to that of Ref. [52], with the consumption term replaced by a uniform metabolic generation term. Under these modelling assumptions, Eq. (4.33) can be taken to represent the transient concentration of carbon dioxide cleared from tissues with sparse capillary networks.

To conclude this Section, we mention briefly the work of Secomb *et al.* [55]. These authors developed a Green's function method to analyse steady-state oxygen distribution in realistic three-dimensional microvascular networks. The microvessels and the tissue were respectively represented as a set of discrete oxygen sources and

[12] When viewed as a function of argument qa, with r/a a parameter, the fraction in the integrand of (4.33) involving Bessel functions closely approximates to a sinusoid with period $2\pi(r/a-1)^{-1}$, except the first half cycle has a slightly higher amplitude than the others. Thus, for positions near the capillary wall, the integral (4.33) is small of order $r/a - 1$. On the other hand, for large r/a ratios, differentiation of with respect to r/a yields a Gaussian integral which vanishes as r/a grows large; hence the integral is approximately constant.

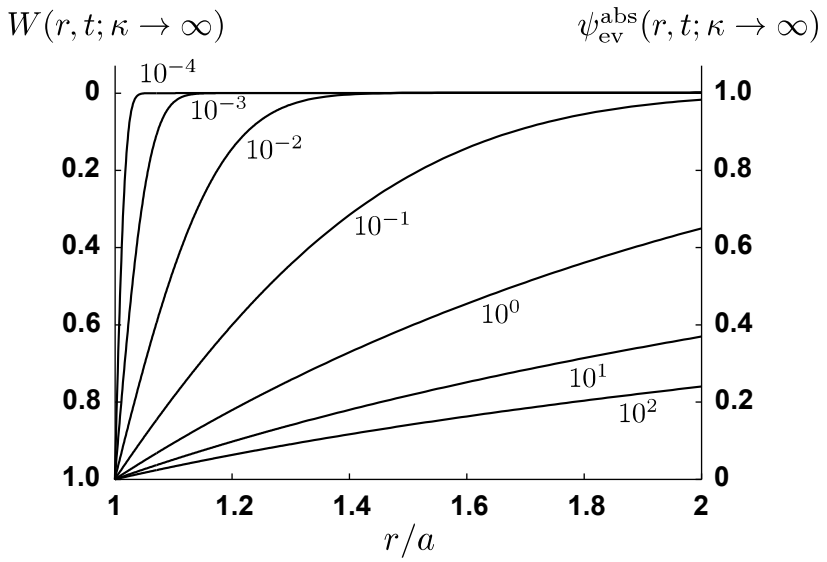

Figure 4.4: **Extravascular tracer concentration under absorbing intracapillary conditions, and blood-to-tissue step response function, for sparse capillary networks with a fully permeable capillary wall, in the absence of extravascular consumption**. Curves are shown for a range of normalised times, $D_{\rm ev}t/a^2 = 10^{-4} - 10^2$. In these curves, numerical integration introduces a maximum error of 0.14%, approximately.

sinks. The Green's function was expressed as a sum of all microvascular point-source terms; the oxygen tension was computed numerically in a tissue region exterior to the microvascular network. These authors obtained realistic microvascular network distributions from samples of several rat tissues, and showed that imposing zero-flux boundary conditions can lead to overestimation of the extent of hypoxia.

4.4 Permeability-limited exchange: arterial spin labelling of brain and myocardium

This Section opens with a discussion of the validity of the modelling assumptions set forth in Chapter 2 for ASL measurements. In Section 4.4.1 two literature models of permeability-limited water exchange are reviewed. In Section 4.4.2 the spatiotemporal tracer-exchange model developed in Chapters 2 and 3 is used to evaluate the ASL

signal. Finally, in Section 4.4.3 the results of the spatiotemporal model and both the examined literature models are compared for typical PASL and CASL experiments in grey matter and myocardium.

The results of Chapter 3 can be applied to blood–tissue water exchange in, e.g., brain and myocardial tissue[13] because the back-flux of tagged tissue water into the capillaries is expected to be low, as discussed in the following paragraph.

The passage of a bolus of tagged blood water through the human microvasculature lasts several seconds (e.g., $3-5$ s in the human brain [189]). Such transit times may be longer than typical ASL measurement times, which are of the order of 1 s and 3 s for pulsed (PASL) and continuous (CASL) arterial spin labelling methods, respectively. This suggests that blood–tissue exchange of magnetically tagged water will occur mostly from blood into the extravascular tissue, provided that extravascular transport by axial diffusion is less efficient than capillary flow, and that the capillary wall permeability is not too high. Furthermore, for typical ASL measurement times the expected ratio of extravascular to intracapillary magnetisation in grey matter and in myocardium is low, perhaps only about $0.03-0.3$, respectively (Fig. 3.7 and Fig. 4.15); the tissue-to-blood flux after the passage of the bolus of tagged blood water, too, is of this order of smallness relative to the blood-to-tissue flux during bolus transit.[14] On the other hand, in ASL animal studies the higher capillary blood flow rates, hence reduced transit times (~ 1 s), may result in greater back-flux of tagged tissue water driven by the clearance of tagged blood water by the microcirculation.

The ASL signal, $S(t)$, is proportional to the total (intra- and extravascular) magnetic moment, i.e., the volume integral of the magnetisation in unit volume of whole

[13]Both these tissues exhibit considerable interregional variations. For example, the longitudinal relaxation time in the brain varies between 850 ms in the prefrontal cortex and 1800 ms in frontal white matter [133]. In the sequel, where the presented results hold regardless of interregional variations, we shall usually refer generically to 'brain' or 'grey matter', and 'myocardium' for simplicity.

[14]For the net transcapillary flux during and after bolus transit are approximately proportional to, respectively, the intracapillary and extravascular concentration at the capillary wall; see Eq. (4.20).

tissue (e.g., a tissue voxel):

$$S(t) \sim \mu_{\mathrm{iv}}(t) + \mu_{\mathrm{ev}}(t) \equiv v_{\mathrm{iv}}\psi_{\mathrm{iv}}(t) + v_{\mathrm{ev}}\psi_{\mathrm{ev}}(t)\,, \tag{4.34}$$

where $\psi_{\mathrm{iv}}(t)$, $\psi_{\mathrm{ev}}(t)$ are spatially averaged magnetisations in units of magnetic moment per unit of water-accessible volume in intracapillary and extravascular space, respectively, and v_{iv}, v_{ev} are water volume fractions per unit volume of whole tissue. Here, the extravascular diffusion time t is equal to the post-tagging delay minus the arterial transit time of tagged blood water; hence $t = 0$ represents the time of arrival of the inflowing magnetisation at the capillary. The intracapillary magnetisation, $\psi_{\mathrm{iv}}(z,t)$, is obtained by convolving the inflowing magnetisation, $\psi_{\mathrm{iv}}(z=0,t)$, with the arterial-to-intracapillary impulse response function, $h_{\mathrm{a}}^{\mathrm{iv}}(z,t)$, Eq. (2.19a). Similarly, the extravascular magnetisation, $\psi_{\mathrm{ev}}(\mathbf{r},t)$, is obtained by convolving the intracapillary magnetisation with the blood-to-tissue impulse response function $w(\mathbf{r},t)$, Eq. (3.39). Further integration over the respective compartment spaces yields the intracapillary and extravascular magnetic moments, $\mu_{\mathrm{iv}}(t)$ and $\mu_{\mathrm{ev}}(t)$. This is done in Section 4.4.2.

4.4.1 Review of selected ASL signal models

The literature water-exchange models to be compared (in Section 4.4.3) against the spatiotemporal model set forth in this Thesis are briefly described below:

1. The one-barrier distributed parameter (1BDP) ASL model of St. Lawrence, Frank and McLaughlin (Ref. [31] an references therein) takes into account position-dependent capillary flow and transcapillary permeation, but not compartmental diffusion. The 1BDP ASL model is specified by Eqs (3a) and (3b) of Ref. [31]. With slight notational changes[15] and rearranging of terms, these

[15]The correspondence between the notation of St. Lawrence *et al.* in Ref. [31] and the one used in this Thesis is as follows: $C_{\mathrm{c}}(x,t) \mapsto \psi_{\mathrm{iv}}(z,t)$, $C_{\mathrm{b}}(x,t) \mapsto \psi_{\mathrm{ev}}(z,t)$, $R_{1\mathrm{c}} \mapsto R_{\mathrm{iv}}$, $R_{1\mathrm{b}} \mapsto R_{\mathrm{ev}}$, $F/A_{\mathrm{c}} \mapsto u_z$ and $PS/A_{\mathrm{c}}L \mapsto 1/\tau_{\mathrm{iv}}$, in appropriate units (see main text).

equations are rewritten as:

$$\frac{\partial \psi_{\mathrm{iv}}(z,t)}{\partial t} = -u_z \frac{\partial \psi_{\mathrm{iv}}(z,t)}{\partial z} - \frac{\psi_{\mathrm{iv}}(z,t) - \lambda^{-1}\psi_{\mathrm{ev}}(z,t)}{\tau_{\mathrm{iv}}} - R_{\mathrm{iv}}\psi_{\mathrm{iv}}(z,t)\,, \quad (4.35a)$$

$$\frac{\partial \psi_{\mathrm{ev}}(z,t)}{\partial t} = \frac{\psi_{\mathrm{iv}}(z,t) - \lambda^{-1}\psi_{\mathrm{ev}}(z,t)}{\tau_{\mathrm{ev}}} - R_{\mathrm{ev}}\psi_{\mathrm{ev}}(z,t)\,, \quad (4.35b)$$

where the magnetisations $\psi_{\mathrm{iv}}(z,t)$, $\psi_{\mathrm{ev}}(z,t)$ are expressed in units of intracapillary and extravascular magnetic moment per volume of whole tissue[16] and λ is the brain–blood partition coefficient [31], given by the ratio of extravascular to intracapillary equilibrium magnetisations [190, p. 22]. (Hence this parameter is perhaps more precisely referred to as the extravascular tissue–blood partition coefficient).

Introducing intracapillary and extravascular water volumes per volume of whole tissue (v_{iv}, v_{ev}), expressing the magnetisation in units of magnetic moment per volume of intracapillary and extravascular water, and noting that the factor λ^{-1} is to be replaced by $\lambda^{-1}(v_{\mathrm{ev}}/v_{\mathrm{iv}}) = 1$, a pair of equations formally identical with (4.35a) and (4.35b) is obtained. This shows that the 1BDP ASL model equations may be obtained from the spatiotemporal model presented in this Thesis by averaging the extravascular mass balance equation (2.1b) with respect to radial position, then approximating the average abluminal concentration $\psi_{\mathrm{ev}}(z,t)|_{a_+}$ by the radially averaged concentration $\psi_{\mathrm{ev}}(z,t)$.

St. Lawrence *et al.* considered, analytically, the case in which tagged water which permeates into the extravascular space relaxes before it can pass again into the capillaries, resulting in negligibly low back-flux of tagged water. The resultant model was termed the *single-pass approximation* (SPA) model [31]. In this case, the term proportional to $\psi_{\mathrm{ev}}(z,t)$ is assumed to be very small and hence the intracapillary and extravascular equations become decoupled [see Eqs (9a) and (9b) of cited reference]. In particular, when $\psi_{\mathrm{ev}}(\mathbf{a}_+) \ll \psi_{\mathrm{ev}}(\mathbf{a}_-)$,

[16] St. Lawrence *et al.* defined the impulse response ('residue') function for a capillary/tissue unit to be the sum of the impulse response functions for intracapillary and extravascular spaces; refer to Eq. (5) of Ref. [31].

intracapillary Eq. (4.35a) of the 1BDP-SPA model reduces to Eq. (2.1a) of the spatiotemporal model developed here.

It is easily seen that the arterial-to-intravascular and arterial-to-extravascular impulse response functions for the 1BDP-SPA model are respectively given by[17]

$$h_{\mathrm{a}}^{\mathrm{iv}}(z,t) = \delta(t-t_z)\exp(-R_{\mathrm{iv}}^{+}t_z)\,, \tag{4.36a}$$

$$h_{\mathrm{a}}^{\mathrm{ev}}(z,t) = \frac{1}{\tau_{\mathrm{ev}}}\exp\bigl[-R_{\mathrm{iv}}^{+}t_z - R_{\mathrm{ev}}(t-t_z)\bigr]\,\theta(t-t_z)\,, \tag{4.36b}$$

where $\theta(\cdot)$ is the unit step function (2.8) and $t_z = z/u_z$. The structure of (4.36b) highlights the effect of intracapillary relaxation and blood–tissue exchange during the interval $0 < t \leq t_z$, then the effect of extravascular relaxation for $t > t_z$. The 1BDP-SPA solutions are given by Eqs (10a) – (17) of Ref. [31].[18]

2. The Parkes–Tofts model [34] is a two-compartment lumped model. Using the present notation, the tracer-balance equations for this model read:

$$\begin{aligned} v_{\mathrm{iv}}\frac{\mathrm{d}\psi_{\mathrm{iv}}(t)}{\mathrm{d}t} &= f_{\mathrm{iv}}\left[\psi_{\mathrm{iv}}(0,t) - \psi_{\mathrm{iv}}(L,t)\right] \\ &\quad - PS\left[\psi_{\mathrm{iv}}(t) - \psi_{\mathrm{ev}}(t)\right] - v_{\mathrm{iv}}R_{\mathrm{iv}}\psi_{\mathrm{iv}}(t)\,, \end{aligned} \tag{4.37a}$$

$$v_{\mathrm{ev}}\frac{\mathrm{d}\psi_{\mathrm{ev}}(t)}{\mathrm{d}t} = PS\left[\psi_{\mathrm{iv}}(t) - \psi_{\mathrm{ev}}(t)\right] - v_{\mathrm{ev}}R_{\mathrm{ev}}\psi_{\mathrm{ev}}(t)\,; \tag{4.37b}$$

see Eqs (11) and (12) of Ref. [34]. In that paper the inflowing and outflowing magnetisations, $\psi_{\mathrm{iv}}(0,t)$ and $\psi_{\mathrm{iv}}(L,t)$, are in units of magnetic moment per volume of blood, hence f_{iv} is capillary blood flow; the average compartmental magnetisations, $\psi_{\mathrm{iv}}(t)$ and $\psi_{\mathrm{ev}}(t)$, are expressed in units of magnetic moment per volume of intracapillary and extravascular water; v_{iv}, v_{ev} respectively denote

[17] Equations (4.36a) and (4.36b) do not appear in the article by St. Lawrence *et al.*, Ref. [31], but only their spatial integrals, Eqs (10a) and (10b) of Ref. [31], which are referred to by these authors as the impulse residue function for blood and extravascular tissue, respectively.

[18] In Ref. [31] the total magnetic moment for CASL is given by Eq. (17), which tends to infinity as the parameter R_{1b} $(= R_{\mathrm{ev}})$ tends to zero. To correct this, the term $\beta E_R[1-\exp(-R_{1b}t)]$ in that equation should be replaced by $-\beta E_R\exp(-R_{1b}t)$.

intracapillary and extravascular water volumes per volume of whole tissue, and PS is also given per volume of whole tissue (cf. Table 1 of Ref. [34]).[19]

Equations (4.37a) and (4.37b) above result from the spatiotemporal model presented here on putting

$$\psi_{\mathrm{iv}}(t)|_{\mathbf{a}_-} - \psi_{\mathrm{ev}}(t)|_{\mathbf{a}_+} \approx \psi_{\mathrm{iv}}(t) - \psi_{\mathrm{ev}}(t)$$

in the spatially averaged equations (4.17a) and (4.17b).

Parkes and Tofts [34] provided closed-form solutions for a rectangular bolus of arterial magnetisation passing through the capillaries without dispersion. For the case of negligible back-flux, the Parkes–Tofts solutions are given by Eqs (20) – (23) of Ref. [34].

Goresky *et al.* [27] and Parkes and Tofts [34] have noted that lumped tracer-exchange models cannot deal with tracer outflow properly because the well-mixed assumption does not allow for position dependent tracer concentrations. To overcome in part this difficulty, Parkes and Tofts assumed the venous magnetisation to be zero for $t < \tau_{\mathrm{c}}$, and equal to the average intracapillary magnetisation for $t > \tau_{\mathrm{c}}$ [34, p. 32]. Thus, after one capillary transit time, the capillary was considered a well-mixed compartment with apparent clearance rate of tagged blood water given by $R_{\mathrm{iv}} + \tau_{\mathrm{iv}}^{-1} + \tau_{\mathrm{c}}^{-1}$, from Eq. (11) of Ref. [34]. In their paper, the authors employed a Gaussian distribution of capillary flow rates in order to obtain more realistic outflow curves.

4.4.2 ASL signal taking into account extravascular diffusion

In the following subsections we evaluate the compartmental magnetisations and magnetic moments predicted by the spatiotemporal model developed in this Thesis.

[19] The correspondence between the notation of Parkes and Tofts in Ref. [34] and the one used in this Thesis is as follows: $v_{\mathrm{bw}} \mapsto v_{\mathrm{iv}}$, $v_{\mathrm{ew}} \mapsto v_{\mathrm{ev}}$; $\Delta m_{\mathrm{b}} \mapsto \psi_{\mathrm{iv}}$, $\Delta m_{\mathrm{e}} \mapsto \psi_{\mathrm{ev}}$; $f\Delta m_{\mathrm{a}}(t) \mapsto f_{\mathrm{iv}}\psi_{\mathrm{iv}}(0,t)$ and $f\Delta m_{\mathrm{v}}(t) \mapsto f_{\mathrm{iv}}\psi_{\mathrm{iv}}(L,t)$.

Intracapillary magnetisation

The magnetisation at the inflowing end of a capillary segment is modelled, following Ref. [34], as a rectangular bolus of duration T that travels without dispersion. Thus,

$$\psi_{\mathrm{iv}}(z=0, 0<t<T) = \exp(-R_{\mathrm{a}}t)\,, \tag{4.38}$$

where the amplitude of the bolus is normalised by the inversion efficiency of the tagging scheme, by the equilibrium magnetisation of arterial blood and by the cumulative longitudinal relaxation experienced by the tagged blood water in the arterial tree. Due to the differing tagging schemes employed, the decay rate R_{a} is zero for CASL and is equal to the longitudinal relaxation rate of arterial blood [23] for PASL.

Convolving the inflowing magnetisation (4.38) with the arterial-to-intracapillary impulse response function (2.19a) gives:

- Before the bolus appears at position z, the intracapillary magnetisation is zero: $\psi_{\mathrm{iv}}(z,t) = 0$ for $t < t_z = z/u_z$.

- In the interval $t_z < t < t_z + T$ the bolus traverses the capillary cross-section at position z; the intracapillary concentration is given by

$$\psi_{\mathrm{iv}}(z,t) \approx \left[\theta(t-t_z) + \frac{t_z}{\tau_{\mathrm{iv}}}\,U_1(z,t)\right] \exp\!\left[-R_{\mathrm{a}}(t-t_z) - R_{\mathrm{iv}}^{+}t_z\right], \tag{4.39a}$$

  where $R_{\mathrm{iv}}^{+} = R_{\mathrm{iv}} + \tau_{\mathrm{iv}}^{-1}$, Eq. (2.19b), and

$$U_1(z,t) = \int_0^{t-t_z} w(a_+, z, t')\exp(R_{\mathrm{a}}t')\,\mathrm{d}t'\,.$$

- Lastly, in the interval $t > t_z + T$ the intracapillary magnetisation is due solely to the back-flux of magnetisation into the capillary and is given by

$$\psi_{\mathrm{iv}}(z,t) \approx \frac{t_z}{\tau_{\mathrm{iv}}}\,U_2(z,t)\exp\!\left[-R_{\mathrm{a}}(t-t_z) - R_{\mathrm{iv}}^{+}t_z\right], \tag{4.39b}$$

  where

$$U_2(z,t) = \int_{t-t_z-T}^{t-t_z} w(a_+, z, t')\exp(R_{\mathrm{a}}t')\,\mathrm{d}t'\,.$$

Extravascular magnetisation

The extravascular magnetisation is obtained by convolving $\psi_{\rm iv}(z,t)$ with the blood-to-tissue impulse response function, $w(\mathbf{r},t)$. In the remainder of this Section we present results which are valid for sparse capillary networks with negligible back-flux of magnetisation from extravascular into intracapillary space.[20] This entails neglecting the 'feedback' term in the simplified arterial-to-intravascular impulse response function (2.19a), hence also in (4.39a). That is, the intracapillary magnetisation due to the inflowing magnetisation of Eq. (4.38) is given, approximately, by

$$\psi_{\rm iv}(z,t) \approx \exp\bigl[-R_{\rm a}(t-t_z) - R_{\rm iv}^{+}t_z\bigr]\,, \qquad\qquad t \geq t_z\,. \tag{4.40}$$

- In the interval $t_z < t < t_z+T$, the convolution of (4.40) with the blood-to-tissue impulse response function (3.39) yields the extravascular magnetisation as

$$\psi_{\rm ev}(\mathbf{r},t) \approx \frac{2}{\pi}\int_0^{\infty} \frac{P(q')Y_0(q'r') - Q(q')J_0(q'r')}{[P^2+Q^2](q')}\,\frac{1-\exp[-(q'^2+\eta)\varsigma_z^2]}{q'^2+\eta}\,q'\,{\rm d}q' \\ \times \exp\bigl[-R_{\rm a}(t-t_z) - R_{\rm iv}^{+}t_z\bigr] \tag{4.41a}$$

  where

$$\varsigma_z^2 = \frac{D_{\rm ev}}{a^2}(t-t_z)\,, \qquad\qquad \eta = \frac{a^2}{D_{\rm ev}}(R_{\rm ev}-R_{\rm a})\,. \tag{4.41b}$$

  The parameter ς_z represents a normalised diffusion length for the interval $t-t_z$, following transit of the leading edge of the bolus past position z along a capillary segment. The parameter η quantifies the trade-off between tracer relaxation and extravascular diffusion at short diffusion times and is pulse-sequence dependent through the parameter $R_{\rm a}$. Putting $z=0$, $r'=1$ and $R_{\rm a}=R_{\rm iv}=R_{\rm ev}=0$ in (4.41a) gives $\psi_{\rm ev}(a_+,0,t) = 1-\psi_{\rm 2d}^{\rm abs}(a_+,0,t)$, as expected; see Eq. (3.37).

[20] For permeability-limited exchange, the right hand-side of (4.39b) is small compared to (4.39a):

$$U_2(z,t) \leq U_1(z,t) \leq \int_0^T w(a_+,z,t')\exp(R_{\rm a}t')\,{\rm d}t' \sim W(a_+,z,T;R_{\rm ev}=0)\exp(|R_{\rm a}-R_{\rm ev}|T)\,,$$

where $\exp(|R_{\rm a}-R_{\rm ev}|T) \sim 1$ and, under permeability-limited conditions, the amplitude of the blood-to-tissue step response function is small (see Fig. 3.7d).

Intracapillary and extravascular magnetic moment

Integration of (4.39a) and (4.41a) over, respectively, intracapillary and pericapillary space yields the respective magnetic moments in unit volume of whole tissue.[21] For the time interval $0 < t \leq \tau_c + T$ we find:

$$\mu_{iv}(t) \approx f_{iv} \frac{\exp[-\beta_1(t - t_{lead})] - \exp[-\beta_1(t - t_{trail})]}{\beta_1} \exp(-R_{iv}^{+} t) \tag{4.42}$$

and

$$\begin{aligned} \mu_{ev}(t) \approx f_{iv} \exp(-R_{iv}^{+} t) \int_0^\infty & \frac{8D_{ev}/\pi^2 a^2}{[P^2 + Q^2](q')} \frac{1}{\beta_2 - \beta_1} \\ & \times \left\{ \frac{\exp[-\beta_1(t - t_{lead})] - \exp[-\beta_1(t - t_{trail})]}{\beta_1} \right. \\ & \left. - \frac{\exp[-\beta_2(t - t_{lead})] - \exp[-\beta_2(t - t_{trail})]}{\beta_2} \right\} \frac{\mathrm{d}q'}{q'} , \end{aligned} \tag{4.43a}$$

where[22]

$$\beta_1 = R_a - R_{iv}^{+} , \qquad \beta_2 = \beta_1 + \frac{D_{ev}}{a^2}(q'^2 + \eta) . \tag{4.43b}$$

The time instants $0 \leq t_{trail}, t_{lead} \leq \tau_c$ mark the advance of the leading and trailing edge, respectively, of the dispersionless bolus as it travels along the capillary (Fig. 4.5):

1. For times $0 < t < \min\{\tau_c, T\}$, the leading edge of the bolus is in transit along the capillary segment but the trailing edge is still in the feeding vessel; in this phase, $t_{trail} = 0$ and $t_{lead} = t$.

2. In the interval $\min\{\tau_c, T\} < t < \max\{\tau_c, T\}$ a short (i.e., $T < \tau_c$) bolus is fully in transit along the capillary, hence $t_{trail} = t - T$ and $t_{lead} = t$. On the other hand, for a long (i.e., $T > \tau_c$) bolus $t_{trail} = 0$ and $t_{lead} = \tau_c$.

[21] Averaging with respect to axial coordinate z leads to integrals of the form:

$$\frac{1}{L} \int_{z_{trail}}^{z_{lead}} \exp(\alpha t_z)\, \mathrm{d}z = \frac{\exp(\alpha t_{lead}) - \exp(\alpha t_{trail})}{\alpha \tau_c} ,$$

while averaging with respect to radial coordinate r involves the evaluation of standard integrals of Bessel functions. Use of (3.25) and (3.26) gives: $\int_a^A [P(q')Y_0(q'r') - Q(q')J_0(q'r')]\, 2\pi r' \mathrm{d}r' = 4/q'^2$.

[22] While $\beta_2 = R_{ev} - R_{iv}^{+} + D_{ev} q'^2/a^2$ may vanish for some $q' > 0$, no singularity will appear in the integrand of (4.43a) since $[\exp(\beta_2 t_{trail}) - \exp(\beta_2 t_{lead})]/\beta_2 \to t_{trail} - t_{lead}$ as $\beta_2 \to 0$.

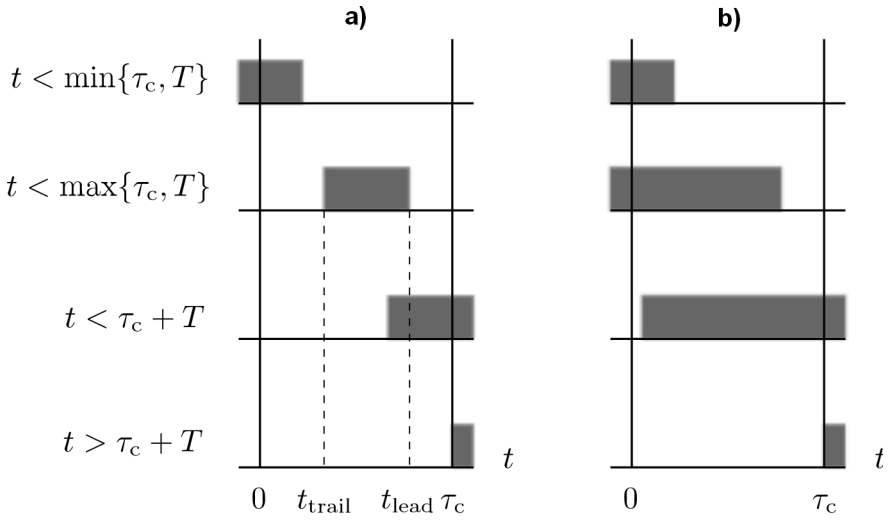

Figure 4.5: **Passage of a dispersionless bolus through a capillary segment**. The respective temporal widths are T and τ_c. **a)** Short bolus: $T < \tau_c$. **b)** Long bolus: $T > \tau_c$. The capillary is depicted as a segment of temporal length τ_c.

3. In the time interval $\max\{\tau_c, T\} < t < \tau_c + T$, the leading edge of the bolus is past the capillary segment, while the trailing edge is still in transit. Thus, in this phase $t_{trail} = t - T$ and $t_{lead} = \tau_c$.

4. Finally, for times $t > \tau_c + T$, the bolus has flowed past the capillary segment and $t_{trail} = t_{lead}$ gives $\mu_{iv}(t) = 0$ in the absence of back-flux.

From (4.42) it follows that, at times much shorter than the mean intracapillary residence time for tracer molecules, τ_{iv}, the rate of increase of magnetic moment in the capillary due to a rectangular bolus equals the capillary flow rate, f_{iv}. On the other hand, at sufficiently long times ($\tau_c, \tau_{iv} \ll t < \tau_c + T$) the intracapillary magnetic moment equals approximately $f_{iv}\tau_{iv}[1 + (R_{iv} - R_a)\tau_{iv}]^{-1} \exp(-R_a t)$ for a long bolus.[23] For PASL, this expression becomes $f_{iv}\tau_{iv} \exp(-R_{iv} t)$ and the average magnetisation in the capillary segment therefore equals τ_{iv}/τ_c, up to a relaxation term.

The magnetic moment expressions (4.42) and (4.43a) can be rewritten in terms

[23] This is seen on rewriting (4.42) as $\mu_{iv}(t) = (f_{iv}/\beta_1)[\exp(\beta_1 t_{lead}) - \exp(\beta_1 t_{trail})] \exp(-R_a t)$, with $t_{trail} = 0$ and $\tau_c = t_{lead} \leq t \leq \tau_c + T$.

of the non-dimensional parameters $D_{\mathrm{ev}}t/a^2$, $D_{\mathrm{ev}}/\kappa a$, $\overline{f}_{\mathrm{iv}} \equiv a^2 f_{\mathrm{iv}}/D_{\mathrm{ev}}$, $\overline{\tau}_{\mathrm{c}} \equiv D_{\mathrm{ev}}\tau_{\mathrm{c}}/a^2$, $\overline{R}_{\mathrm{iv}} \equiv a^2 R_{\mathrm{iv}}/D_{\mathrm{ev}}$ and $\overline{R}_{\mathrm{ev}} \equiv a^2 R_{\mathrm{ev}}/D_{\mathrm{ev}}$. We have evaluated numerically the magnetic moment dependence with respect to these parameters[24] for the case of a long bolus of steady inflowing magnetisation, given by $\psi_{\mathrm{iv}}(z = 0, t > 0) = 1$; the results are shown in Fig. 4.6 and Fig. 4.7 and are discussed in the sequel.

Figure 4.6 plots the percentage fraction of intravascular magnetic moment. Assuming $a^2/D_{\mathrm{ev}} = 10$ ms for magnetically tagged water in brain and myocardium, the range of observation times is $\lesssim 1$ s and covers characteristic extravascular diffusion times in brain tissue; transit times of ~ 300 ms ($\overline{\tau}_{\mathrm{c}} \sim 30$) are realistic for medium-sized capillary segments ($L \sim 100-500$ μm); the extravascular relaxation rates used in Fig. 4.6a are comparable to literature values in thalamus and *globus pallidus* at 3 T, while those in Fig. 4.6b are appropriate for cerebral white matter at 3 T [133, 168]. The value $\overline{R}_{\mathrm{iv}} = 6.25 \times 10^{-3}$ corresponding to $R_{\mathrm{iv}} = 1/1600$ ms^{-1} was used. For comparison, setting $R_{\mathrm{iv}} = 1/1400$ ms^{-1} (cf. Fig. 5.3 of Ref. [5]) results in diminution of intravascular magnetic moment fraction by less than 0.12%.

The fraction of intracapillary magnetic moment is seen to decrease steadily with time while the amount of extravascular magnetic moment rises. In the leakier capillaries (i.e., for lower $D_{\mathrm{ev}}/\kappa a$ ratios) higher blood-to-tissue fluxes cause the fraction of intracapillary magnetic moment to fall off sharply. The long-time value (not attained in the time scale depicted in the Figure) is zero because the model equations from which the fraction of intracapillary magnetic moment was calculated are valid for a very large extravascular region. This implies that the fraction of intracapillary magnetic moment will actually be somewhat higher than that shown in Fig. 4.6.

The fraction of intracapillary magnetic moment is greater for the case shown in Fig. 4.6b (faster relaxation) than for that shown in Fig. 4.6a (slower relaxation). This behaviour is consistent with the simplifying assumption (see Section 4.4.2) that the intracapillary magnetisation (4.40), hence also the intracapillary magnetic moment

[24]Parameter values employed in the computation: $D_{\mathrm{ev}}t/a^2 = 0.1-100$, $D_{\mathrm{ev}}/\kappa a = 0.1-100$, $\overline{\tau}_{\mathrm{c}} = 10-100$, $\overline{R}_{\mathrm{iv}} \leq 12.5 \times 10^{-3}$ and $\overline{R}_{\mathrm{ev}} = 5 \times 10^{-3} - 12.5 \times 10^{-3}$. Note that other combinations are possible, for example $D_{\mathrm{ev}}t/a^2$, $D_{\mathrm{ev}}/\kappa a$, $v_{\mathrm{iv}} = f_{\mathrm{iv}}\tau_{\mathrm{c}}$, $D_{\mathrm{ev}}\tau_{\mathrm{c}}/a^2$, $R_{\mathrm{iv}}\tau_{\mathrm{c}}$ and $R_{\mathrm{ev}}\tau_{\mathrm{c}}$.

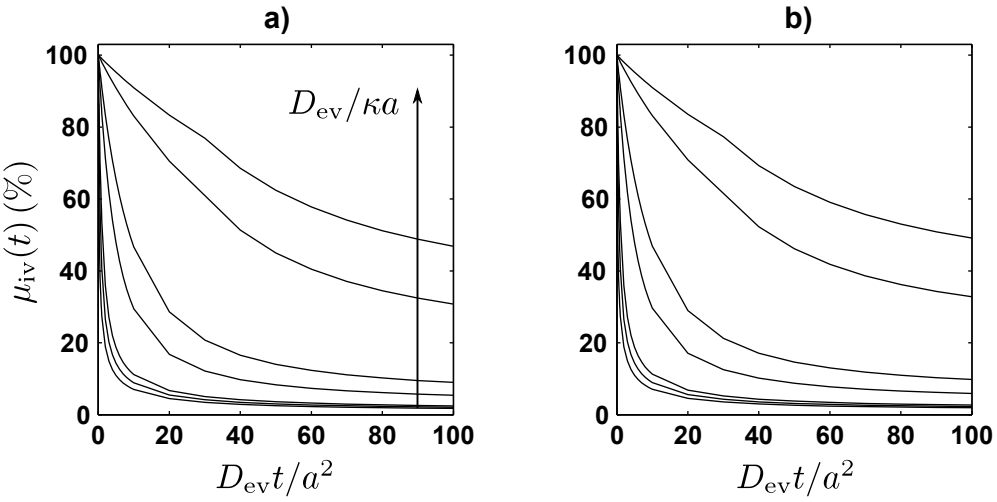

Figure 4.6: **Time-dependent fraction of intravascular magnetic moment for a range of effective membrane thickness values**, $D_{\mathrm{ev}}/\kappa a = 0.1,\ 0.5,\ 1,\ 5,\ 10,\ 50,\ 100$; normalised capillary-segment length, $\overline{\tau}_{\mathrm{c}} = 30$; $\overline{R}_{\mathrm{iv}} = 6.25 \times 10^{-3}$; $\overline{R}_{\mathrm{ev}} = 10 \times 10^{-3}$ (left panel) and 12.5×10^{-3} (right panel). All barred quantities are defined on p. 202.

(4.42), is largely independent of extravascular conditions. In practice, with fast extravascular consumption the transcapillary flux will tend to increase to a certain extent. This may, in turn, result in a reduced fraction of intracapillary magnetic moment if the rate of tissue-to-blood permeation exceeds the difference between intracapillary and extravascular consumption rates, i.e., if $\tau_{\mathrm{iv}}^{-1} \gg R_{\mathrm{ev}} - R_{\mathrm{iv}}$; this latter condition which holds when the abluminal concentration is low enough not to cause significant jamming effects.

Figure 4.6 also shows that the time rate of the fraction of intracapillary magnetic moment becomes somewhat sharper (i.e., more negative) at times $t \approx \tau_{\mathrm{c}}$, since the amount of tracer in the capillary segment can no longer increase and attains a steady-state value which is dependent upon inflow of fresh magnetisation, transcapillary exchange, and outflow of partially relaxed magnetisation. The change in slope is more pronounced for lowly permeable capillaries ($D_{\mathrm{ev}}/\kappa a \gtrsim 100$ in the Figure), as expected.

Figure 4.7 shows the ratio, expressed as percentage deviation, of the total amount of tracer for the case of very slow consumption, $\mu(t; R_{\mathrm{iv}} \to 0; R_{\mathrm{ev}} \to 0)$, to the

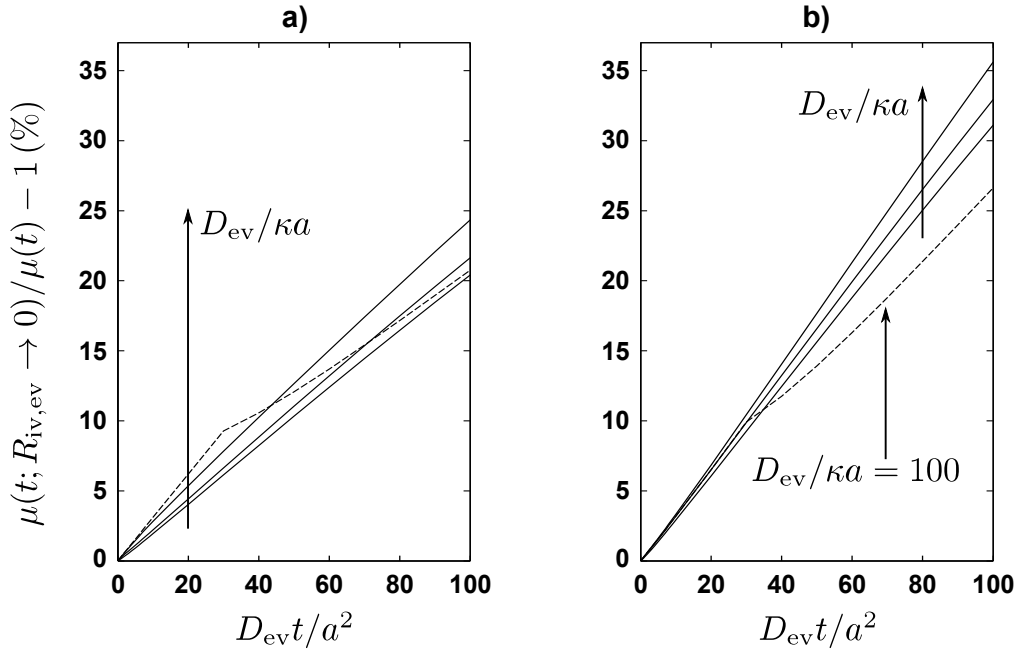

Figure 4.7: **Percentage deviation of total magnetic moment for the case of slow relaxation from that for typical water relaxation rates in blood and tissue**. Parameter values: $R_{\mathrm{a}} = 0$; $D_{\mathrm{ev}}/\kappa a = 0.1, 1, 10$ (solid lines) and 100 (broken lines); $\overline{\tau}_{\mathrm{c}} = 30$; $\overline{R}_{\mathrm{iv}} = 6.25 \times 10^{-3}$; $\overline{R}_{\mathrm{ev}} = 10 \times 10^{-3}$ (left panel) and $\overline{R}_{\mathrm{ev}} = 12.5 \times 10^{-3}$ (right panel). All barred quantities are defined on page 202.

total amount of tracer, $\mu(t; R_{\mathrm{iv}}, R_{\mathrm{ev}})$, corresponding to consumption rates in capillary blood and tissue as in Fig. 4.6. We simulated the case of very slow relaxation by setting $\overline{R}_{\mathrm{iv}} = 0$ and $\overline{R}_{\mathrm{ev}} = 5.0 \times 10^{-3} \ll 1/\overline{\tau}_{\mathrm{c}}$. Also note that the chosen range of extravascular diffusion lengths, i.e., $\sqrt{D_{\mathrm{ev}}t}/a \leq 10$, is appropriate for both brain and myocardial tissue.

This Figure demonstrates that the spatiotemporal model for indicator-dilution studies developed by Lee and Fronek [44] is not applicable to ASL experiments. The cumulative deviation incurred by unrealistic modelling of consumption/relaxation effects in blood and extravascular tissue is seen to increase rapidly with diffusion time. Further, the deviation becomes higher as the blood–tissue exchange becomes increasingly permeability-limited, for in the presence of lowly permeable capillaries the amount of extravascular magnetic moment lost to relaxation is not replenished

by the fresh arterial magnetisation as efficiently as it would in the case of highly permeable capillaries. However, at sufficiently high values of the $D_{\mathrm{ev}}/\kappa a$ ratio (≈ 100 in the example; broken lines in Fig. 4.7), for times $t > \tau_{\mathrm{c}}$ the computed deviation between magnetic moments for the two cases compared is seen to increase at a slower rate than that for $t < \tau_{\mathrm{c}}$. This may be understood by noting that, since the intracapillary magnetic moment represents a large proportion of the total magnetic moment ($\sim 50-80\%$ for normalised times $D_{\mathrm{ev}}t/a^2 \gtrsim \overline{\tau}_{\mathrm{c}} = 30$ for $D_{\mathrm{ev}}/\kappa a = 100$; Fig. 4.6), for $t > \tau_{\mathrm{c}}$ the inflow of fresh magnetisation can compensate in part the outflow of partially relaxed magnetisation, the net effect being a reduced apparent relaxation rate.

Furthermore, for times $t \lesssim \tau_{\mathrm{c}}$ an increased extravascular relaxation rate (Fig. 4.7b, bottom left) causes the deviation of the 'true' magnetic moment from that for the case of very slow relaxation to become less sensitive to capillary wall permeability. This occurs because, in the case under consideration, $\mu_{\mathrm{iv}}(t)$ is only weakly dependent on intracapillary relaxation rate.[25] Thus, when the fraction of intracapillary magnetic moment is low, so is $\mu_{\mathrm{ev}}(t)$, irrespective of extravascular consumption rate; on the other hand, when the intracapillary magnetic moment is large, it dominates the expression for the deviation.

Expressions for permeability-limited exchange in sparse capillary networks

The expression (4.43a) for the extravascular magnetic moment cannot, in general, be integrated analytically. However, under permeability-limited exchange conditions, the eigenfrequency dependence of β_2 is shown below to be relatively unimportant, leading to a simplified expression for $\mu_{\mathrm{ev}}(t)$. Specifically, if

1. observation times are shorter than typical extravascular residence times (i.e.,

[25] For $R_{\mathrm{a}} = 0$, Eq. (4.42) becomes $\mu_{\mathrm{iv}}(t) = f_{\mathrm{iv}}[1 - \exp(-R^{+}_{\mathrm{iv}}t)]/R^{+}_{\mathrm{iv}}$. A review of T_1 values in Fig. 5.3 of Ref. [5] and of capillary $H_2{}^{15}O$ permeability values in Ref. [160] shows that at magnetic field strengths of ≤ 3 T, $R_{\mathrm{iv}}\tau_{\mathrm{iv}} \lesssim 1$ (blood relaxation data at higher fields was not available in the cited reference). Thus, blood–tissue water exchange, not intracapillary water relaxation, is the dominant cause of reduced intracapillary magnetic moment in brain and myocardium.

$t < \tau_{\rm ev}$), so that according to (2.90) the main contribution to the integral in (4.43a) comes from the interval $q'_{\rm c} \lesssim a/\sqrt{D_{\rm ev}\tau_{\rm ev}}$;

2. the product $|R_{\rm iv} - R_{\rm ev}|\tau_{\rm iv}$ is much smaller than one, i.e., any differences in the compartmental relaxation rates barely influence the transcapillary exchange; and

3. the capillary volume fraction is low ($v_{\rm iv} \ll v_{\rm ev}$), so that the mean residence time in extravascular space is much greater than that in capillary blood ($\tau_{\rm ev} \gg \tau_{\rm iv}$);

then in the second Eq. (4.43b) we have

$$\frac{D_{\rm ev}}{a^2}\, q'^2 \lesssim \frac{1}{\tau_{\rm ev}} \ll \frac{1}{\tau_{\rm iv}} \approx |R_{\rm ev} - R^+_{\rm iv}|$$

and hence $\beta_2 = R_{\rm ev} - R^+_{\rm iv} + (D_{\rm ev}/a^2)q'^2 \approx R_{\rm ev} - R^+_{\rm iv}$ is approximately independent of eigenfrequency q'. In this case the integral in (4.43a) can be replaced, to a good approximation, with

$$\int_0^\infty \frac{8D_{\rm ev}/\pi^2 a^2}{[P^2 + Q^2](q')} \frac{{\rm d}q'}{q'} = \frac{2\kappa}{a} = \frac{1}{\tau_{\rm iv}}\,,$$

which follows on comparison with $\psi^{\rm abs}_{\rm 2d}(\mathbf{a}_+, 0)$, given by Eq. (3.37), with the use of the Wronskian (3.29). Inserting this result into (4.43a) gives an approximate expression for the amount of tracer in extravascular space due to a rectangular arterial bolus, under permeability-limited exchange conditions, as

$$\begin{aligned}\mu_{\rm ev}(t) \approx \frac{f_{\rm iv}}{\tau_{\rm iv}} \frac{1}{\beta'_2 - \beta_1} \Bigg\{ & \frac{\exp[-\beta_1(t - t_{\rm lead})] - \exp[-\beta_1(t - t_{\rm trail})]}{\beta_1} \\ & - \frac{\exp[-\beta'_2(t - t_{\rm lead})] - \exp[-\beta'_2(t - t_{\rm trail})]}{\beta'_2} \Bigg\} \exp(-R^+_{\rm iv} t)\,, \end{aligned} \tag{4.44}$$

with $\beta_1 = R_{\rm a} - R^+_{\rm iv}$ as previously defined and $\beta'_2 = R_{\rm ev} - R^+_{\rm iv}$.

Conditions 1–3 above hold for brain and myocardial ASL (values of the relevant parameters are given in Table 2.1). First, since the time delay between earliest arrival of tagged arterial blood at the capillaries and image acquisition is shorter than typical extravascular residence times, an upper bound on the interval of eigenfrequencies which make the greatest contribution to the integral in (4.43a), is correctly estimated

as $q_c' \lesssim a/\sqrt{D_{ev}\tau_{ev}}$. Second, the order-of-magnitude estimates $|R_{iv} - R_{ev}| \sim 10^{-5}$–$10^{-4}$ ms^{-1} and $1/\tau_{iv} \sim 10^{-3}$ ms^{-1} give $|R_{iv} - R_{ev}|\tau_{iv} \sim 10^{-2}$–$10^{-1}$. Lastly, capillary volume fractions in brain and myocardial tissues are a small percentage.

Equation (4.44) can be shown to be identical with the expression for the extravascular magnetic moment for the 1BDP-SPA model of St. Lawrence *et al.*, Ref. [31]. This follows by convolving the arterial bolus (4.38) with the arterial-to-extravascular impulse response function (4.36b) and integrating in the extravascular space. Equation (4.44) is also identical with the expressions predicted by the Parkes–Tofts model on the interval $0 < t \leq \tau_c$, see Eqs (20) and (22) of Ref. [34] for PASL and CASL, respectively. This result suggests that conditions 1–3 above specify quantitatively the conditions under which low extravascular concentrations may be expected, as is assumed in the 1BDP-SPA model; see Ref. [31].

In the interval $0 < t \leq \min\{\tau_c, T\}$ the leading edge of the bolus is inside the capillary ($t_{lead} = t$) and the trailing edge is in the feeding vessel ($t_{trail} = 0$). At short times such that $|\beta_1 t| \ll 1$ and $|\beta_2 t| \ll 1$, i.e., $t/\tau_{iv} \ll 1$ with the approximations made above, expanding the terms inside the brackets in the right-hand side of (4.44) gives

$$\mu_{ev}(t) \approx \frac{f_{iv}t^2}{2\tau_{iv}} \exp(-R_{iv}^{+}t) = PSt\,\frac{t}{2\tau_c} \exp(-R_{iv}^{+}t)\,. \tag{4.45}$$

The term PSt represents the amount of tracer in the extravascular space per unit concentration difference (intracapillary minus extravascular) at the capillary wall, and per unit volume of whole tissue; the term $t/2\tau_c$ comprises the effect of capillary flow; and the term $\exp(-R_{iv}^{+}t)$ represents a diminution in extravascular magnetic moment due to both intracapillary relaxation and capillary wall barriers. Thus, the term $(t/2\tau_c)\exp(-R_{iv}^{+}t)$ can be interpreted as the fraction of intracapillary tracer that is actually available for exchange at short times, relative to the intracapillary residence time, after the arrival of tracer at the capillary.

The variation of $\mu_{ev}(t)$ in (4.45) with the second power of time can be deduced by noting that, during the initial course of transcapillary exchange, both the amount of tracer present in the capillary and the exchanging capillary surface area, increase linearly with time: $\mu_{iv}(t) \sim f_{iv}t$ and $S \sim 2\pi a u_z t$, respectively. In the considered

time interval, i.e., $t < \{\tau_c, T, \beta_1^{-1}, \beta_2^{-1}\}$, the ratio of extravascular to intracapillary magnetisation is obtained from (4.42) and (4.45) as

$$\frac{\mu_{ev}(t)}{\mu_{iv}(t)} \sim \frac{t}{2\tau_{iv}} \ll 1\,. \tag{4.46a}$$

An upper bound on the ratio $\mu_{ev}(t)/\mu_{iv}(t)$ valid for longer times is estimated by considering the idealised case of a uniform intracapillary magnetisation and neglecting any differences between the intra- and extravascular relaxation rates:

$$\frac{\mu_{ev}(t)}{\mu_{iv}(t)} \sim \frac{\Lambda(t)}{V_{iv}} \approx \frac{\kappa S t}{V_{iv}} = \frac{t}{\tau_{iv}}\,, \tag{4.46b}$$

which is not necessarily a small quantity. The effective extravascular depolarised volume enters into the above expression through Eq. (2.25).

4.4.3 Comparison of ASL signal models

Figure 4.8 shows an example of the percentage deviation of the total (intra- and extravascular) magnetic moment predicted by the 1BDP-SPA model from that predicted by the spatiotemporal model set forth in this Thesis, for a long rectangular bolus of constant inflowing magnetisation (CASL). The values of the parameters used are appropriate for, e.g., myocardium, thalamus, *globus pallidus* and cerebral white matter. Because it does not account for jamming effects (discussed in Section 4.2) at the capillary wall, the 1BDP-SPA model overestimates the total (intracapillary and pericapillary) magnetic moment, compared to the spatiotemporal model. The deviation increases with observation time, but tends to stabilise at sufficiently long times as the extravascular magnetisation approaches a steady state. The graph shows that a ten-fold increase in capillary wall permeability causes 1BDP-SPA deviations to increase by, approximately, two orders of magnitude at short times ($D_{ev}t/a^2 \sim 0.1$–1) and by one order of magnitude at longer diffusion times ($D_{ev}t/a^2 \sim 10$–100). It is noted that overestimation of the total magnetic moment will, in turn, lead to overestimation of capillary blood flow.

Figure 4.8 also shows that when the blood–tissue exchange is rate-limited by extravascular diffusion (i.e., for low $D_{ev}/\kappa a$ ratios), the deviation of the 1BDP-SPA

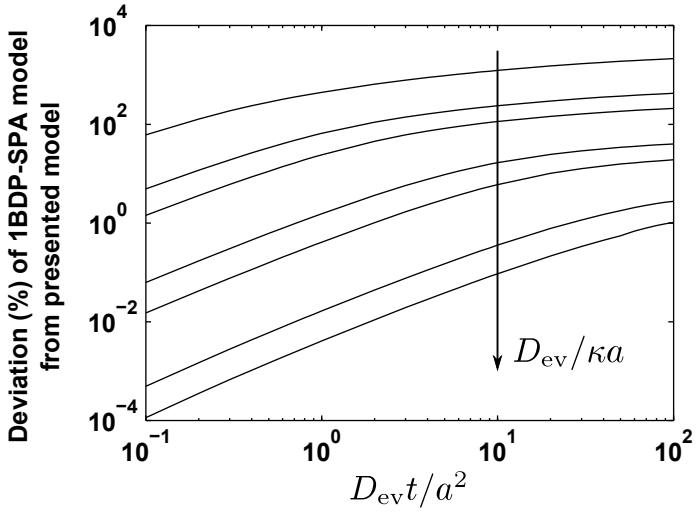

Figure 4.8: **Total magnetic moment due to a long rectangular bolus of inflowing magnetisation (CASL): percentage deviation of 1BDP-SPA model from spatiotemporal model presented in this Thesis**. Parameter values: $D_{\rm ev}/\kappa a = 0.1$, 0.5, 1, 5, 10, 50, 100; $\overline{\tau}_{\rm c} = 30$; $\overline{R}_{\rm iv} = 6.25 \times 10^{-3}$ and $\overline{R}_{\rm ev} = 10 \times 10^{-3}$.

model from the presented spatiotemporal model is large for all observation times. On the other hand, under permeability-limited conditions the 1BDP-SPA expression for total extravascular magnetic moment, given by the sum of Eqs (4.42) and (4.44), is quite accurate for $D_{\rm ev}/\kappa a \gtrsim 50$ (deviation $< 3\%$ in the time interval shown in the Figure). Thus, in the presence of an intact blood-brain barrier ($D_{\rm ev}/\kappa a \gtrsim 100$) the total amount of tracer predicted by the 1BDP-SPA model is in close agreement to the spatiotemporal model set forth in this Thesis. Similar results (data not shown) are obtained for myocardium using values of the parameters similar to those listed in Table 2.1.

The deviation of the 1BDP-SPA model from the spatiotemporal model developed in this Thesis depends moderately upon relaxation rate and capillary-segment length. For each capillary-segment length used in the simulation, the deviation for each pair of intracapillary and extravascular relaxation rates was divided by the corresponding deviation for the case of slowest relaxation considered in the computation ($\overline{R}_{\rm iv} = 0$, $\overline{R}_{\rm ev} = 5 \times 10^{-3}$); the resultant ratio ranged between $84\% - 107\%$.

In the remainder of this Section we consider the case of negligibly low back-flux of magnetically tagged water from extravascular space into the capillaries and compare the time course the ASL signal predicted by the spatiotemporal model presented here, equations (4.42) and (4.43a), to those for the 1BDP-SPA model, given by (4.42) and (4.44), and the Parkes–Tofts model, described by equations (20) and (22) of Ref. [34].

Figure 4.9 and Fig. 4.10 illustrate the time course of magnetic moment per unit capillary flow for PASL and CASL, respectively, as predicted by these three models. In these examples, the inflowing magnetisation is described as a long rectangular bolus of duration T, see Eq. (4.38); the value of T differs for PASL and CASL but in both cases T is greater than the capillary-transit time τ_c. Capillary segment length, L, and mean speed of tracer flow, u_z, are the same throughout. The values of tissue parameters used in the computations are appropriate for human grey matter (e.g., R_{iv} is for prefrontal cortex) and rat myocardium, and normal values of capillary water permeability are used.

Although the longitudinal relaxation rate of arterial blood, R_a, is higher than that of capillary blood, R_{iv}, due to a higher arterial haematocrit [167], for PASL calculations we set $R_a = R_{iv}$ both for simplicity and for consistency with the literature ASL models utilised in this comparison. For the longitudinal relaxation rate of capillary blood we used the literature value $R_{iv} = 1/1664$ ms$^{-1} \approx 0.60$ s^{-1} from *in vitro* measurements at 3 T of bovine blood with a haematocrit (Hct) of 0.42 [132]; this estimate is comparable to 0.59 s^{-1}, as obtained in another *in vitro* study [167] at 1.5 T with Hct = 0.30, which is a realistic value of capillary haematocrit.

In addition, we have assumed the value of the extravascular relaxation rate, R_{ev}, to be almost equal to that of the relaxation rate in whole tissue, R_{tiss}, on the basis that the volume fraction of water-accessible extravascular space is large, and that transcapillary exchange is sufficiently fast relative to the difference between the intracapillary and extravascular relaxation rates. As discussed in Appendix 2.5.2, under these conditions it is reasonable to assume $|R_{iv} - R_{tiss}| \approx v_{ev}|R_{iv} - R_{ev}|$, where $v_{ev} \gtrsim 0.9$ (see Table 2.1).

The results shown in Fig. 4.9 and Fig. 4.10 are discussed below:

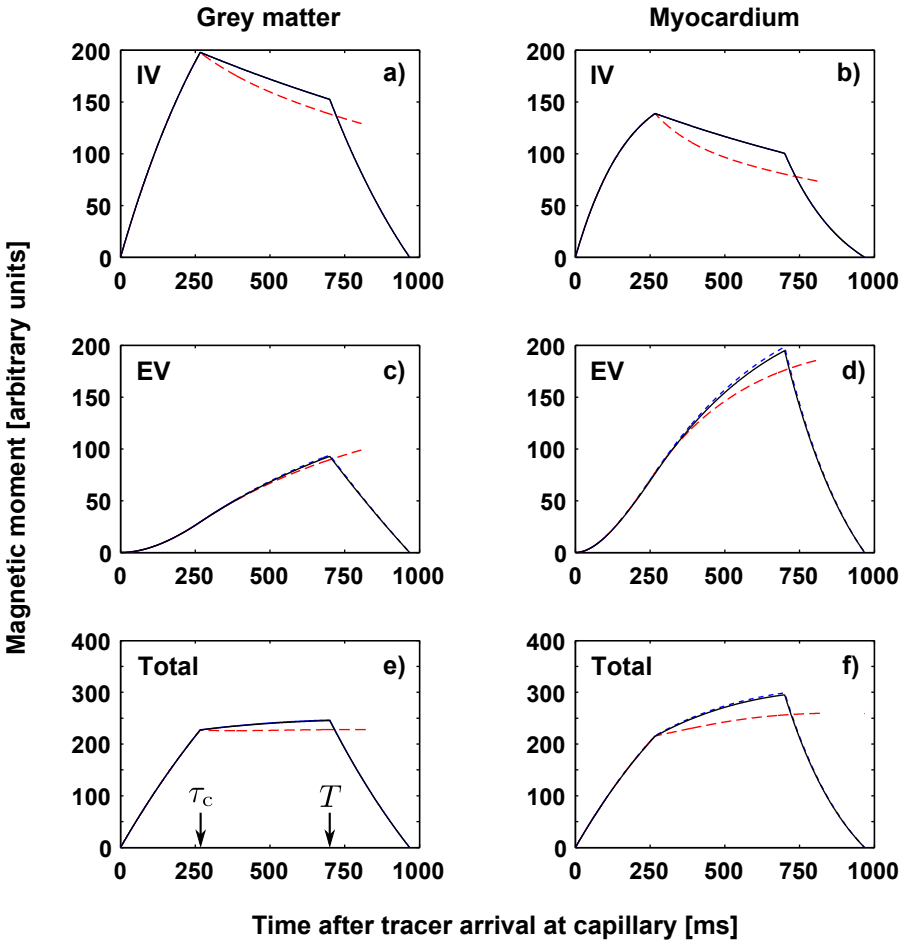

Figure 4.9: **Magnetic moment per unit capillary flow for PASL** of grey matter [prefrontal cortex, panels a), c), e)] and myocardium [panels b), d), f)]. Black solid line: spatiotemporal model presented here, Eqs (4.42) and (4.43a); blue dashed line - - - -: 1BDP-SPA model [31]; red broken line – – –: two-compartment lumped model of Parkes and Tofts [34] for times less than bolus duration T (see p. 214 in text). Parameter values: capillary wall permeability, diffusion coefficient and relaxation rates of water are as in Table 2.1; capillary-segment transit time, $\tau_c = 267$ ms (from $L = 400$ μm, $u_z = 1.5$ μm ms^{-1}); bolus duration, $T = 700$ ms.

- Because of their different capillary water permeabilities, for prefrontal cortex and myocardium the relative proportions of intracapillary and extravascular magnetic moment – hence the relative contribution of each physiological compartment to the ASL signal – are noticeably different; see panels a) through d)

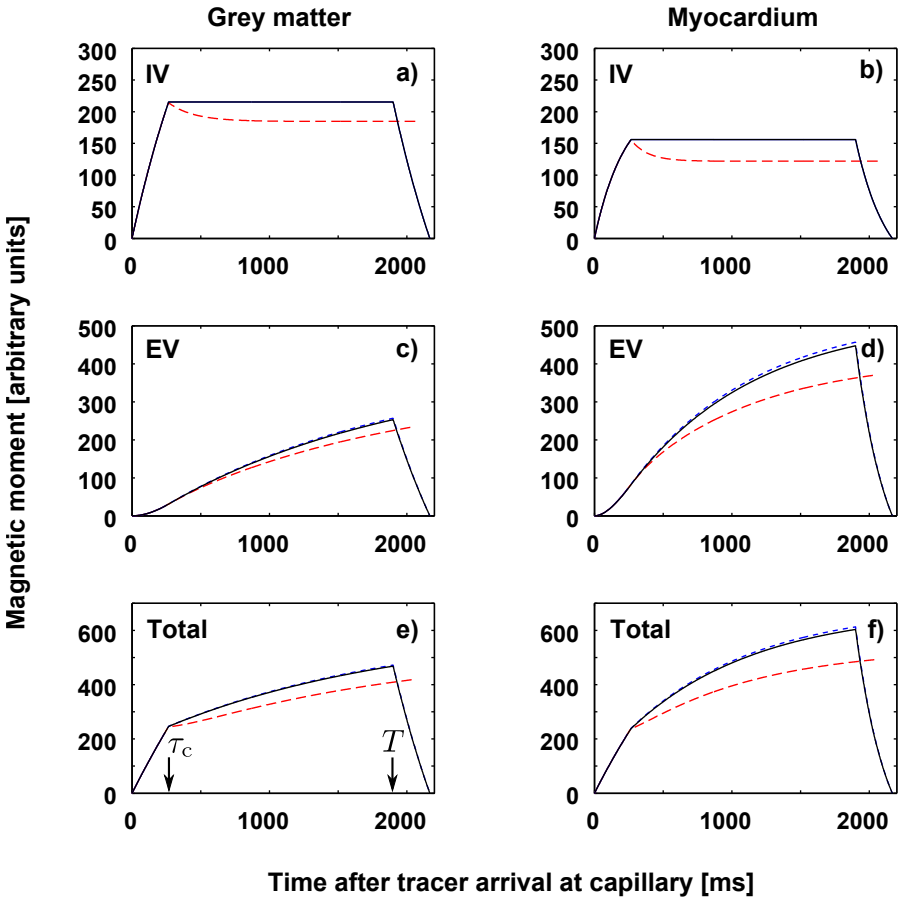

Figure 4.10: **Magnetic moment per unit capillary flow for CASL** of grey matter [prefrontal cortex, panels a), c), e)] and myocardium [panels b), d) f)]. Black solid line: spatiotemporal model presented herein; blue dashed line - - - -: 1BDP-SPA model; red broken line – – –: Parkes–Tofts model for times not exceeding the bolus duration T (see text). The values of the parameters are as in Fig. 4.9 except bolus duration, $T = 1900$ ms.

in these Figures.

- During the transit time (for $t < \tau_c$) of the leading edge of the bolus through the capillary segment, the predicted total magnetic moment per unit capillary flow is slightly higher in prefrontal cortex than in myocardium, due to faster intra- and extravascular relaxation in this latter tissue.

  On the other hand, in the interval $\tau_c < t < T$, the capillary lumen is filled with magnetically tagged blood and the spatiotemporal model predicts the total

magnetic moment per unit capillary flow in myocardium to be higher than in prefrontal cortex because the myocardial capillary wall is more permeable to water than the blood–brain barrier; see panels e), f). For PASL, intracapillary relaxation over an interval of duration $T - \tau_c$ results in almost linear reduction (since $R_{iv}|T - \tau_c| \ll 1$) in intracapillary magnetic moment predicted by both the spatiotemporal and 1BDP-SPA models, whereas for CASL the predicted intracapillary magnetic moment remains constant due to the steady inflow of fresh magnetisation; see panels a), b).

Lastly, in the interval $\tau_c < t < \tau_c + T$ the amount of tagged blood in both intracapillary space and the pericapillary region decreases steadily to zero. In this time interval, the effect of a higher capillary permeability, which allows for higher total magnetic moment, is eventually counterbalanced by that of faster relaxation. As a result, in myocardium the total magnetic moment per unit capillary flow is predicted to decrease faster than in prefrontal cortex; see panels e), f).

- Compared to the spatiotemporal model presented here, the 1BDP-SPA model overestimates both the extravascular and total magnetic moments due to the jamming effect. The deviation increases steadily for all time after arrival of the bolus at the capillary, but is rather small for normal myocardial and blood–brain barrier permeabilities. Specifically, for the values of the parameters used in Fig. 4.9 and Fig. 4.10, the peak deviations in extravascular magnetic moment are as follows: for PASL, 1.3% in prefrontal cortex and 1.9% in myocardium; for CASL, 1.5% and 2.1%, respectively. The respective deviations in total magnetic moment are smaller, as expected: for PASL, 0.56% (prefrontal cortex) and 1.3% (myocardium); for CASL, 0.84% and 1.6%, respectively.

- The time course of the ASL signal predicted by the Parkes–Tofts model is valid for times not exceeding the bolus duration T, but in Fig. 4.9 and Fig. 4.10 the corresponding curves (red broken line) have been extrapolated for times $t > T$ so as to avoid confusion with the curves for the other two models. In these

examples, the deviations of the Parkes–Tofts model from the spatiotemporal model developed here are, in general, more pronounced than those of the 1BDP-SPA model. However, for sufficiently high capillary permeabilities, this latter model may deviate from the spatiotemporal model more strongly than the Parkes–Tofts model, as discussed later in this Section.

In the interval $0 < t < \tau_c$, the Parkes–Tofts expression for intracapillary magnetic moment for negligibly low back-flux is identical with that given by the spatiotemporal model presented in this Thesis. However, for times greater than the capillary-segment transit time, the value of $\mu_{iv}(t)$ predicted by the Parkes–Tofts model is lower than that predicted by the spatiotemporal model. This is due to the fact that, in this interval, the Parkes–Tofts model regards the intracapillary space as a well-mixed compartment for tagged blood water (refer to Section 4.4.1, p. 198).

As regards extravascular magnetic moment, in the interval $0 < t < \tau_c$ the Parkes–Tofts and 1BDP-SPA models each predict the same value, which overestimates the value obtained using the spatiotemporal model; the deviation is greatest at $t \approx \tau_c$. Then in the interval $\tau_c < t < \tau_c + T$, the deviation of the value of extravascular magnetic moment predicted by the Parkes–Tofts starts to decrease and eventually changes sign, consistent with the underestimation of intracapillary magnetic moment illustrated in panels a), b). Specifically, for the considered values of the parameters, greatest deviations with respect to the spatiotemporal model occur at $t \approx T$ and are as follows: for PASL, -3.6% in prefrontal cortex and -9.7% in myocardium, whereas for CASL the deviations are -11% and -19%, respectively. For the total magnetic moment, the respective deviations rise to -7.1%, -13%, -13% and -20%.

Figure 4.11 illustrates the predicted effect of a ten-fold increase in capillary water permeability on PASL signal, all other parameters being as in Fig. 4.9. (Note that in spite of this substantial increase, blood–tissue water exchange in brain and myocardial tissue remains rate limited by capillary permeability; see Fig. 4.1). An elevated wall permeability causes the intracapillary (respectively, extravascular) magnetic moment

per unit capillary flow to decrease (respectively, increase) and, furthermore, may modify the shape of the time course of total magnetic moment from trapezoid-like for lower (normal) permeabilities to wave-like for higher permeabilities; compare panels e), f) in Fig. 4.9 and Fig. 4.11.

Unlike was the case for normal capillary permeabilities, for the high-permeability cases considered in Fig. 4.11 the total magnetic moment predicted by the Parkes–Tofts model deviates from the spatiotemporal model by a smaller percentage than does the 1BDP-SPA model. This is due to partial compensation between underestimation of intracapillary magnetic moment (for reasons explained above) and overestimation of extravascular magnetic moment (because concentration gradients at the capillary are not taken into account) in the Parkes–Tofts model; panel f) suggests that for values of the parameters appropriate for myocardial tissue, the Parkes–Tofts model may predict a higher total magnetic moment than the spatiotemporal model.

On the other hand, in a situation of elevated capillary permeability, one expects increased deviations of the 1BDP-SPA model from the spatiotemporal model presented in this Thesis, as compared to the case of normal permeability; this is illustrated in Fig. 4.8 for CASL. Also, the deviation of the total magnetic moment predicted by the 1BDP-SPA and Parkes–Tofts models from the value given by the spatiotemporal model, varies in time much in the same manner as described for the above-discussed examples using lower capillary permeability parameter values. For the 1BDP-SPA model, peak deviations of 12% for prefrontal cortex and 19% for myocardium are predicted at a time equal to the bolus duration; for the Parkes–Tofts model, peak deviations occur a time equal to the mean capillary-segment transit time and are 6.1% for prefrontal cortex and 14% for myocardium.

Deviations of the 1BDP-SPA model from the spatiotemporal model described here are more pronounced for the set of parameters representative of myocardium than for those representative of prefrontal cortex (see examples in the foregoing paragraphs; full data not shown). For the case of permeability-limited exchange this result is consistent with the set of conditions (p. 206) leading to Eq. (4.44) for the extravascular magnetic moment, since both intracapillary volume fraction, v_{iv}, and the product

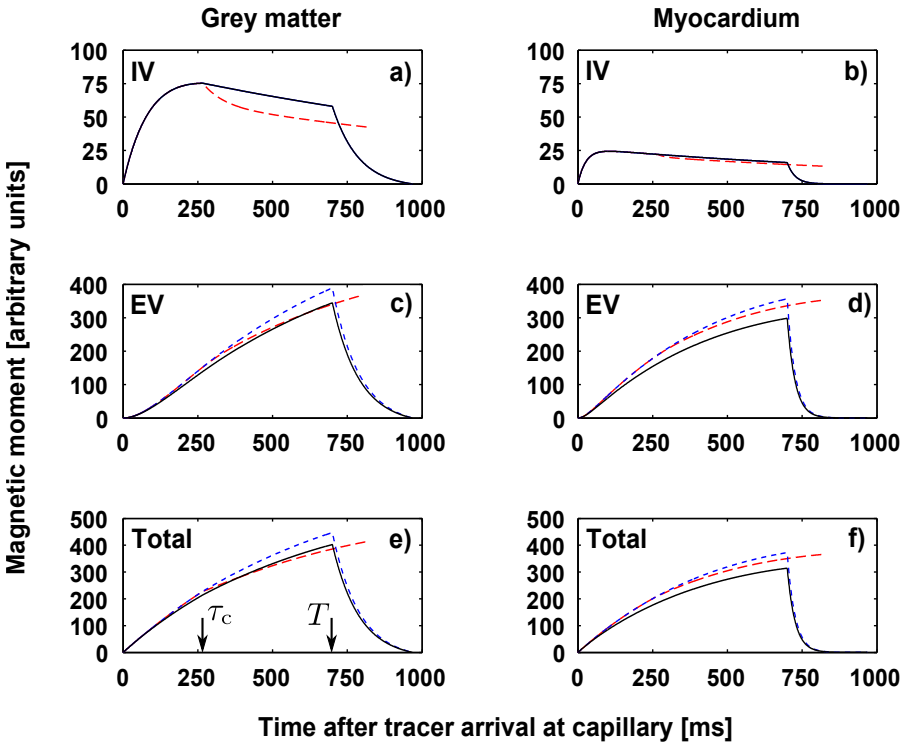

Figure 4.11: **Effect of elevated capillary water permeability on PASL signal**. A hypothetical value of capillary water permeability for grey matter and myocardium each ten times greater than its value in Table 2.1 was used; the remaining parameters are as in Fig. 4.9. Black solid line: spatiotemporal model presented here; blue dashed line - - - -: 1BDP-SPA model of St. Lawrence *et al.*; red broken line – – –: Parkes–Tofts model.

$|R_{iv} - R_{ev}|\tau_{iv}$ are greater in myocardium than in prefrontal cortex (Table 2.1).

Figure 4.12 illustrates the total magnetic moment per unit capillary flow for PASL and CASL predicted by each of the three models compared in this Section, for various combinations of capillary water permeability and extravascular relaxation rate parameters appropriate for brain tissue (literature values of relaxation rate in prefrontal cortex and putamen at 3 T were used). As expected, the total magnetic moment is largest for the pair of parameters consisting of the higher capillary water permeability (κ^+) and the lower extravascular relaxation rate (R_{ev}^-).

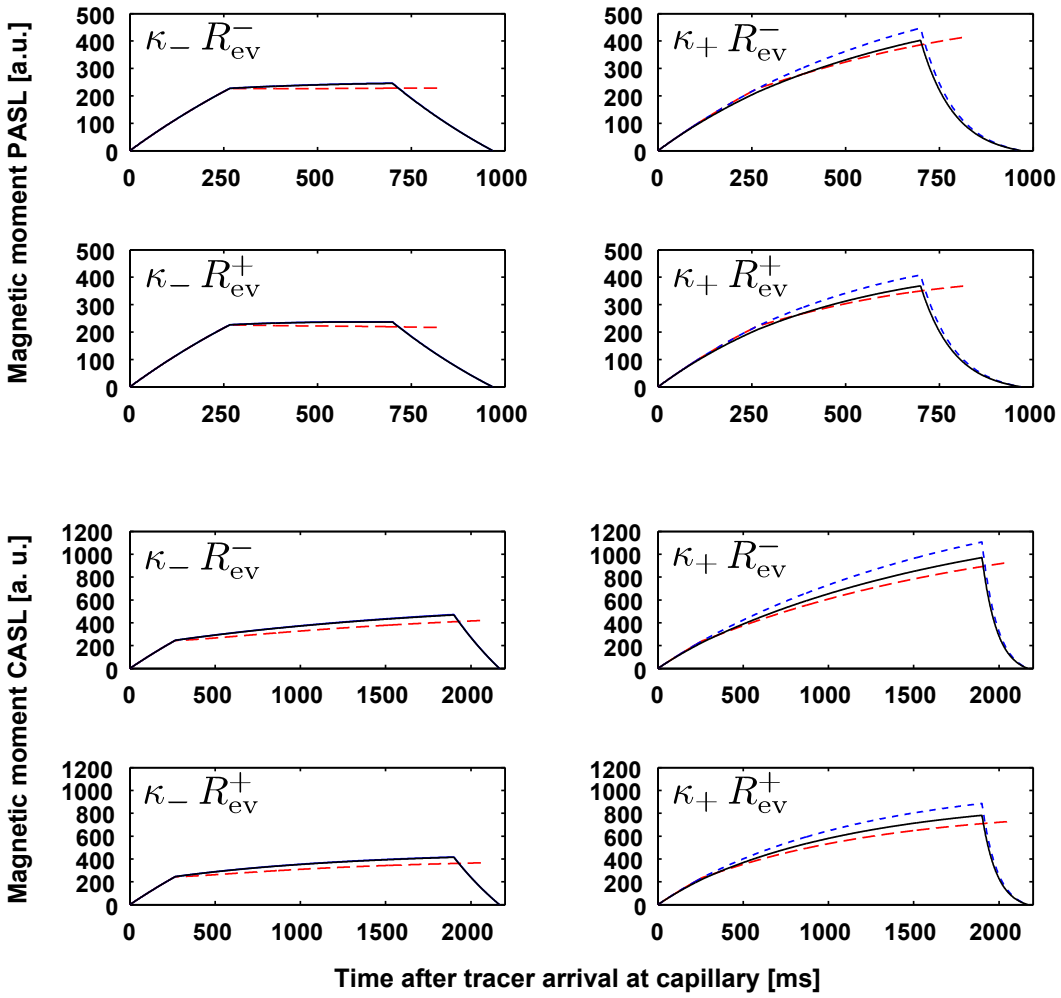

Figure 4.12: **Joint effect of capillary permeability and extravascular relaxation on total magnetic moment for PASL and CASL**. Black solid line: spatiotemporal model presented here; blue dashed line - - - -: 1BDP-SPA model; red broken line – – –: Parkes–Tofts model. Values of the parameters: $\kappa^- = 1.7{\times}10^{-3}\ \mu\text{m}\,\text{ms}^{-1}$, $\kappa^+ = 1.7{\times}10^{-2}\ \mu\text{m}\,\text{ms}^{-1}$; $R_{ev}^- = 1763^{-1}\ \text{ms}^{-1}$ [133], $R_{ev}^+ = 1100^{-1}\ \text{ms}^{-1}$ [168]; the remaining parameters are as in Fig. 4.9 (for PASL) and Fig. 4.10 (for CASL).

4.4.4 Extravascular diffusion times in ASL measurements

We conclude this Section with a discussion of the range of extravascular diffusion times that may be expected in typical ASL measurements. The time course of the inflowing bolus is in most cases unknown. However, the post-exchange time, t_{ev}, de-

fined here as the time that tagged water molecules spend, on average, in extravascular space before NMR signal acquisition, can be reasonably estimated. Assuming that the bolus travels without dispersion, and further negligible back-diffusion of tagged water into the capillaries,

$$t_{\mathrm{ev}} \sim \tau_{\mathrm{tag}} + \tau_{\mathrm{w}} - \delta\tau_{\mathrm{tag}} - \tau_{\mathrm{a}} - \tau_{\mathrm{iv}}\,, \tag{4.47}$$

see Fig. 4.13. Here, τ_{tag} is the duration of the tag and is in general different from the duration, T, of the tagged bolus reaching the imaging region; τ_{w} is the post-tagging delay (also known as the inversion time or tagging–imaging delay) between the end of tagging and the time of image acquisition;[26] τ_{a} is the arterial transit time (also known as the arterial, or bolus, arrival time) from the tagging region to the imaging location; and $\delta\tau_{\mathrm{tag}}$ is a transit delay which is dependent on both position (either proximal or distal end of tagging region) and time of tagging (either at the start of tagging or at time T) for a packet of tagged blood water molecules. Letting Denoting τ_L denote the transit time through any given tagging region of width L, $\delta\tau_{\mathrm{tag}} = 0$ for the leading edge of the bolus and $\delta\tau_{\mathrm{tag}} = \tau_{\mathrm{tag}} + \tau_L$ for the trailing edge. Clearly, the time of image acquisition, $\tau_{\mathrm{tag}} + \tau_{\mathrm{w}}$, must be chosen in the range $\tau_{\mathrm{a}} < \tau_{\mathrm{tag}} + \tau_{\mathrm{w}} < \tau_{\mathrm{tag}} + \tau_L + \tau_{\mathrm{a}} + \tau_{\mathrm{c}}$.

In Appendix 4.8.2 we estimate the range of post-exchange times for typical ASL experiments in myocardium and brain tissue. According to these estimates, t_{ev} can be as high as 1 – 2 s, depending on both biophysical and pulse-sequence parameters. Because water exchange in brain and myocardium is strongly permeability limited (Fig. 3.7d), the spatiotemporal model can reasonably be extrapolated to long extravascular diffusion times. Comparison with characteristic diffusion times in extravascular space suggests that a significant fraction of tagged tissue water is likely to have reached a diffusive steady state by the time of NMR signal acquisition. It should be noted, however, that tagged water might not have attained an equilibrium with

[26] The parameters τ_{tag}, τ_{w} are often denoted in the literature by τ, w (for CASL) and by TI_1, $\Delta\mathrm{TI} = \mathrm{TI}_2 - \mathrm{TI}_1$ (for PASL) [23]. In PASL the QUIPSS II (Quantitative Imaging of Perfusion using a Single Subtraction – 2nd version) scheme can be used to attempt to control the duration of the tag, τ_{tag}, by applying a saturation pulse to the tagging region.

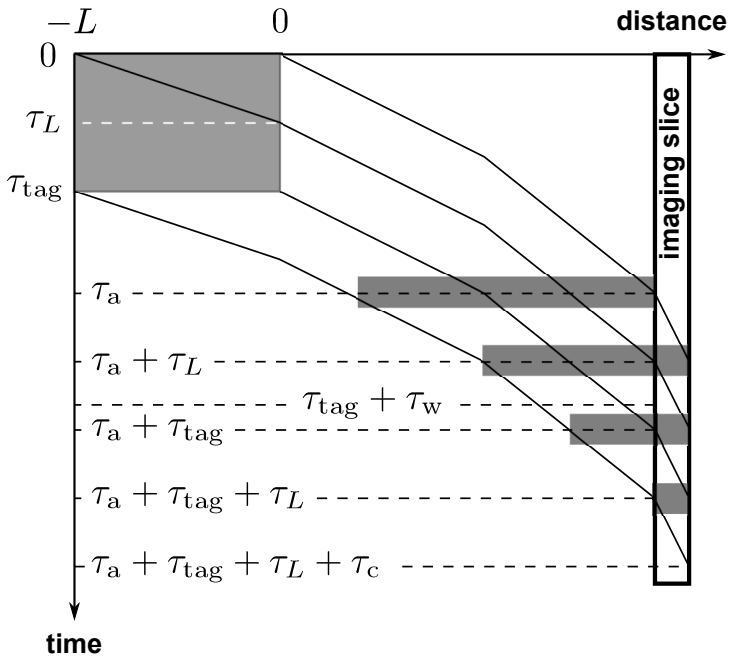

Figure 4.13: **Transit of arterial bolus from tagging region to imaging slice.** The parameters are defined in the text. The mean flow velocity decreases with vascular depth and causes the width of the bolus to change as it travels down the arterial tree and into the imaged region.

intracellular water, due to limited water permeability of parenchymal cell membrane [119].

4.5 Steady-state tracer exchange

A compartmental steady state is achieved when the net tracer flux of tracer through the given compartment remains constant in time [190]. Steady-state tracer concentrations will, in general, be spatially non-uniform, but will remain constant in time for the duration of steady state.

In this Section we compare the spatiotemporal and the lumped tracer-exchange models when both the intracapillary and extravascular compartments have attained a steady state: in intracapillary space, tracer inflow is equal to tracer outflow plus total transcapillary flux; in extravascular space tracer consumption (or relaxation) is exactly balanced by the change in tracer diffusive flux.

Setting the time derivative in Eq. (2.1a) equal to zero, the steady-state intracapillary tracer balance equation becomes

$$u_z \frac{\mathrm{d}\psi_{\mathrm{iv}}^{\mathrm{ss}}(z)}{\mathrm{d}z} + R_{\mathrm{iv}}\psi_{\mathrm{iv}}^{\mathrm{ss}}(z) + \frac{\psi_{\mathrm{iv}}^{\mathrm{ss}}(z) - \psi_{\mathrm{ev}}^{\mathrm{ss}}(\mathbf{a}_+)}{\tau_{\mathrm{iv}}} = 0\,, \tag{4.48a}$$

with $\mathbf{a}_+ \equiv (z, a_+)$. The steady-state abluminal concentration is expressed as

$$\psi_{\mathrm{ev}}^{\mathrm{ss}}(\mathbf{a}_+) \approx \psi_{\mathrm{iv}}^{\mathrm{ss}}(z) \int_0^{t_{\mathrm{ss}}} w(\mathbf{a}_+, t')\,\mathrm{d}t'\,, \tag{4.48b}$$

where the time t_{ss} to attain extravascular steady state is much greater than all the time constants of tracer exchange. Introducing this expression into (4.48a) and solving the resultant differential equation yields the intracapillary tracer concentration:

$$\psi_{\mathrm{iv}}^{\mathrm{ss}}(z) = \exp\left[-R_{\mathrm{iv}}t_z - \frac{1 - \int_0^{t_{\mathrm{ss}}} w(\mathbf{a}_+, t')\,\mathrm{d}t'}{\tau_{\mathrm{iv}}}\, t_z\right] \tag{4.48c}$$

with $t_z = z/u_z$, Eq. (2.19b), and the inflowing concentration is normalised to unit amplitude. As shown in Appendix 4.8.1, the axial diffusive flux due to the gradient of the approximate steady-state intracapillary concentration is in fact negligibly low, as required by the modelling of Section 2.2.1.

The time to extravascular steady state is estimated by evaluating the integral in the exponent of (4.48c) with the use of the eigenfunction decomposition (2.95a): this shows that the intracapillary concentration is approximately constant for $t \sim t_{\mathrm{ss}} \gg \lambda_1^{-1}$, and the eigenvalue relation $\lambda_1 \leq R_{\mathrm{ev}} + \tau_{\mathrm{ev}}^{-1}$, Eq. (3.50) gives $t_{\mathrm{ss}} \gg \tau_{\mathrm{ev}}/(1 + R_{\mathrm{ev}}\tau_{\mathrm{ev}})$.

When the rate of tracer consumption is high, the trivial steady-state, $\psi_{\mathrm{ev}}^{\mathrm{ss}}(\mathbf{r}) \approx 0$, is established very rapidly. At the other extreme, when no tracer is consumed, the steady state is attained at $t_{\mathrm{ss}} \gg \tau_{\mathrm{ev}}$. Clearly, for the whole system to attain the steady state, the tracer bolus must have a duration $T \sim t_{\mathrm{ss}}$. For magnetically tagged water, $R_{\mathrm{ev}} \sim 1\ \mathrm{s}^{-1}$, whereas τ_{ev} for myocardium and brain cortex is of the order of 1 s and tens of seconds, respectively (Table 2.1); thus in ASL experiments in these tissues, establishment of a steady state requires that the bolus duration be greater than about 1 s. As another example, the radiotracer ^{15}O has a half-life of 2 min [191], hence the bolus duration for $\mathrm{H_2}^{15}\mathrm{O}$ PET should be greater than τ_{ev} in this case.

Since the above estimate of the onset of the steady state is not a function of diffusion, it is but a rough estimate for diffusion-limited situations, such as gas exchange in tissue. Hudson and Cater [52] estimated $t_{\mathrm{ss}} \approx 5/D_{\mathrm{ev}}\gamma_1^2$, where $\gamma_1 r_0\,(= q_1 a$, in our notation) is the first root of Eq. (4.27b) for a Krogh annulus. For tissue oxygen uptake, the resultant time to steady state is several seconds.

The steady-state extravascular diffusion–consumption equation is

$$D_{\mathrm{ev}}\nabla^2\psi_{\mathrm{ev}}^{\mathrm{ss}}(\mathbf{r}) - R_{\mathrm{ev}}\psi_{\mathrm{ev}}^{\mathrm{ss}}(\mathbf{r}) = 0\,, \tag{4.49a}$$

with the usual boundary conditions (2.1c), (2.1d). Its solution is

$$\psi_{\mathrm{ev}}^{\mathrm{ss}}(\mathbf{r}) = C_1(z)[g_1(q_{\mathrm{ss}}\mathbf{r}) + C_2 g_2(q_{\mathrm{ss}}\mathbf{r})]\,, \tag{4.49b}$$

where $q_{\mathrm{ss}} = \sqrt{R_{\mathrm{ev}}/D_{\mathrm{ev}}}$ and $g_1(\cdot)$, $g_2(\cdot)$ are functions of position which are determined solely by the geometry of the pericapillary region. For a cylindrical annulus with cylindrical symmetry, $g_1(\cdot) = I_0(q_{\mathrm{ss}}r)$, $g_2(\cdot) = K_0(q_{\mathrm{ss}}r)$ are the modified Bessel functions of zero order. The coefficient $C_2 = -(g_1'/g_2')|_{r=A}$ is determined from the zero-flux boundary condition at the outer surface of the pericapillary region[27] and is independent of κ. The coefficient $C_1(z)$ is determined from the boundary condition at the capillary wall as

$$C_1(z) = \frac{\kappa}{\kappa G_1 + G_2}\,\psi_{\mathrm{iv}}^{\mathrm{ss}}(a_-, z)\,, \tag{4.50}$$

[27]Here, the primes denote the gradient operator with respect to the non-dimensional argument $q_{\mathrm{ss}}r$.

where $G_1 = (g_1 + C_2 g_2)(\mathbf{a}_+)$, $G_2 = -q_{\rm ss} D_{\rm ev}(g_1' + C_2 g_2')(\mathbf{a}_+)$ are dependent on peri-capillary geometry, tracer diffusion coefficient and tracer consumption, but not (as may expected on physical grounds) on capillary permeability. Then

$$\psi_{\rm ev}^{\rm ss}(\mathbf{a}_+) = \frac{\kappa G_1}{\kappa G_1 + G_2}\, \psi_{\rm iv}^{\rm ss}(\mathbf{a}_-)\,, \tag{4.51a}$$

which is an increasing function of capillary wall permeability, with limiting values $\psi_{\rm ev}^{\rm ss}(\mathbf{a}_+) \to 0$ for an impermeable capillary wall, and $\psi_{\rm ev}^{\rm ss}(\mathbf{a}_+) \to \psi_{\rm iv}^{\rm ss}(\mathbf{a}_-)$ for a highly permeable capillary wall. Similarly, the transcapillary flux is expressed as

$$\begin{aligned} \mathbf{n}\mathbf{j}_\kappa^{\rm ss} &= -D_{\rm ev}\mathbf{n}\nabla\psi_{\rm ev}^{\rm ss}(\mathbf{a}_+) = \kappa\left[\psi_{\rm iv}^{\rm ss}(\mathbf{a}_-) - \psi_{\rm ev}^{\rm ss}(\mathbf{a}_+)\right] \\ &= \frac{\kappa G_2}{\kappa G_1 + G_2}\, \psi_{\rm iv}^{\rm ss}(\mathbf{a}_-)\,. \end{aligned} \tag{4.51b}$$

Combining the above two equations shows that the steady-state ratio of transcapillary tracer flux to abluminal tracer concentration is independent of membrane permeability (provided that the membrane is not impermeable):

$$\frac{\mathbf{n}\mathbf{j}_\kappa^{\rm ss}}{\psi_{\rm ev}^{\rm ss}(\mathbf{a}_+)} = \frac{G_2}{G_1} = \frac{\mathbf{n}\mathbf{j}_\kappa^{\rm ss}|_{\kappa\to\infty}}{\psi_{\rm iv}^{\rm ss}(\mathbf{a}_-)|_{\kappa\to\infty}} = \frac{\mathbf{n}\mathbf{j}_\kappa^{\rm ss}|_{\kappa\to\infty}}{\psi_{\rm ev}^{\rm ss}(\mathbf{a}_+)|_{\kappa\to\infty}}\,. \tag{4.51c}$$

In Fig. 4.14, the non-dimensional ratio $aD_{\rm ev}^{-1}\mathbf{n}\mathbf{j}_\kappa^{\rm ss}/\psi_{\rm ev}^{\rm ss}(\mathbf{a}_+)$ is plotted as a function of $q_{\rm ss}a = a\sqrt{R_{\rm ev}/D_{\rm ev}}$ for a range of compartment radii. When $R_{\rm ev}$ is small, the steady-state concentrations will be nearly the same on both sides of the membrane, hence the transmembrane flux will be correspondingly low. On the other hand, when $R_{\rm ev}$ is relatively large, the extravascular concentration will be low and $\mathbf{n}\mathbf{j}_\kappa^{\rm ss}/\psi_{\rm ev}^{\rm ss}(\mathbf{a}_+)$ will increase approximately as $\sqrt{D_{\rm ev}R_{\rm ev}}$. For tissue NMR relaxation, $a\sqrt{R_{\rm ev}/D_{\rm ev}} \sim 10^{-1}$.

To assess the accuracy of a lumped tracer-exchange model, we evaluate the spatially averaged extravascular concentration, $\psi_{\rm ev}^{\rm ss}$, and the transcapillary flux, $\mathbf{n}\hat{\mathbf{j}}_\kappa^{\rm ss}$, predicted by lumped tracer-exchange modelling. The latter quantity is estimated as

$$\mathbf{n}\hat{\mathbf{j}}_\kappa^{\rm ss} = \kappa\left[\psi_{\rm iv}^{\rm ss} - \psi_{\rm ev}^{\rm ss}\right], \tag{4.52a}$$

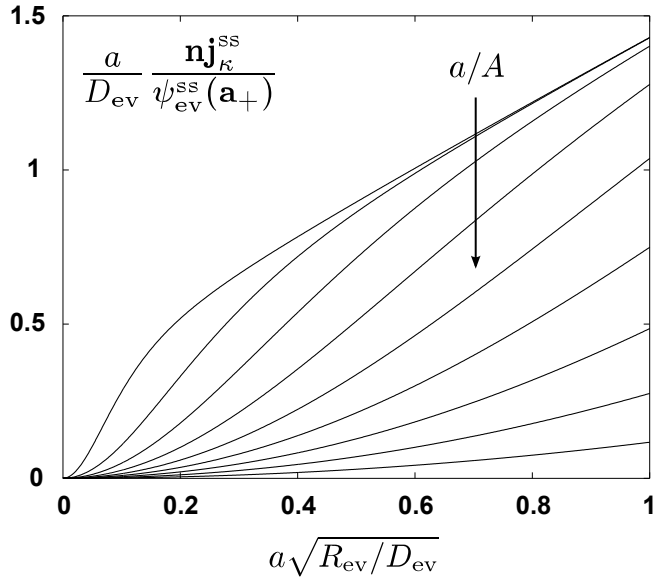

Figure 4.14: **Steady-state ratio of transmembrane tracer flux to tracer concentration at the outer face of the membrane for a cylindrical annulus**. The ratio $a/A = 0.1, 0.2, \ldots, 0.9$ in the direction indicated by the arrow line.

where

$$\begin{aligned}\psi_{\rm ev}^{\rm ss} &= \frac{1}{R_{\rm ev}V_{\rm ev}} \int_{\rm ev} D_{\rm ev}\nabla^2\psi_{\rm ev}^{\rm ss}(\mathbf{r})\,\mathrm{d}^d\mathbf{r} \\ &= \frac{1}{R_{\rm ev}V_{\rm ev}} \int_S -D_{\rm ev}\mathbf{n}\nabla\psi_{\rm ev}^{\rm ss}(\mathbf{a}_+)\,\mathrm{d}S \\ &= \frac{1}{\kappa R_{\rm ev}\tau_{\rm ev}}\,\mathbf{n}\mathbf{j}_\kappa^{\rm ss}\,, \end{aligned} \tag{4.52b}$$

with the use of the Gauss theorem and the zero-flux condition at the pericapillary boundary.[28] If there is a net flux of tracer from blood into tissue, $\psi_{\rm ev}^{\rm ss} \le \psi_{\rm ev}^{\rm ss}(\mathbf{a}_+)$; combining this with (4.52b) then (4.51b) gives the following lower bound on the amplitude of the steady state extravascular concentration:

$$\frac{\psi_{\rm ev}^{\rm ss}(\mathbf{a}_+)}{\psi_{\rm iv}^{\rm ss}(\mathbf{a}_-)} \ge \frac{1}{1 + R_{\rm ev}\tau_{\rm ev}}\,. \tag{4.53}$$

[28]The second line of Eq. (4.52b) is proportional to steady-state transcapillary flux averaged over the capillary wall. The last line of this equation gives the result for a thin axial slice with uniform tracer concentration gradient at the capillary surface, without loss of essential physical meaning.

In the sequel we show that there may be sizeable differences between steady-state tracer concentrations and/or tracer fluxes as predicted by, respectively, the spatiotemporal and the lumped tracer-exchange models. Two simple 'measures' of deviations between these models may be defined as follows:

$$\varepsilon_{\psi} \equiv \frac{\psi_{\mathrm{ev}}^{\mathrm{ss}} - \psi_{\mathrm{ev}}^{\mathrm{ss}}(\mathbf{a}_+)}{\psi_{\mathrm{ev}}^{\mathrm{ss}}(\mathbf{a}_+)} = \frac{1}{\kappa R_{\mathrm{ev}} \tau_{\mathrm{ev}}} \frac{G_2}{G_1} - 1 \tag{4.54a}$$

and

$$\varepsilon_{\mathbf{j}_\kappa} \equiv \frac{\mathbf{n}\hat{\mathbf{j}}_\kappa^{\mathrm{ss}} - \mathbf{n}\mathbf{j}_\kappa^{\mathrm{ss}}}{\mathbf{n}\mathbf{j}_\kappa^{\mathrm{ss}}} = -\frac{\kappa G_1}{G_2}\, \varepsilon_{\psi}\,, \tag{4.54b}$$

where equations (4.51c), (4.52a) and (4.52b) have been used. From these equations the following may be noted:

- The concentration deviation ε_{ψ} does not vary with capillary wall permeability, whereas $|\varepsilon_{\mathbf{j}_\kappa}|$ increases linearly as a function of capillary permeability.

- For small values of $A\sqrt{R_{\mathrm{ev}}/D_{\mathrm{ev}}} \sim \sqrt{R_{\mathrm{ev}}\tau_D}$, as is the case for magnetically tagged water in myocardium and, to a lesser extent, grey matter, Eq. (4.54a) becomes

$$\varepsilon_{\psi} \approx -\frac{A^2 R_{\mathrm{ev}}}{8D_{\mathrm{ev}}} \frac{4v_{\mathrm{iv}} - v_{\mathrm{iv}}^2 - \ln v_{\mathrm{iv}}^2 - 3}{1 - v_{\mathrm{iv}}} < 0\,. \tag{4.55}$$

  This expression implies that $|\varepsilon_{\psi}|$ increases with extravascular relaxation rate and decreasing capillary volume fraction (since both result in lower extravascular concentrations per unit intracapillary concentration) and with decreasing tracer diffusion coefficients (since this slows down redistribution of tracer).

- Using (4.52a) and (4.54a) in (4.54b) we obtain the relation

$$\varepsilon_{\mathbf{j}_\kappa} = -\frac{\kappa \psi_{\mathrm{ev}}^{\mathrm{ss}}(\mathbf{a}_+)}{\mathbf{n}\mathbf{j}_\kappa^{\mathrm{ss}}}\, \varepsilon_{\psi} = -\frac{\psi_{\mathrm{ev}}^{\mathrm{ss}}(\mathbf{a}_+)}{\psi_{\mathrm{iv}}^{\mathrm{ss}} - \psi_{\mathrm{ev}}^{\mathrm{ss}}(\mathbf{a}_+)}\, \varepsilon_{\psi}\,. \tag{4.56}$$

  When $\psi_{\mathrm{ev}}^{\mathrm{ss}}(\mathbf{a}_+)/\psi_{\mathrm{iv}}^{\mathrm{ss}} < 1/2$, the relative difference in tracer concentrations for the spatiotemporal model and for the lumped tracer-exchange model is greater than the relative difference in transcapillary fluxes, $|\varepsilon_{\psi}| > |\varepsilon_{\mathbf{j}_\kappa}|$; conversely, if $\psi_{\mathrm{ev}}^{\mathrm{ss}}(\mathbf{a}_+)/\psi_{\mathrm{iv}}^{\mathrm{ss}} > 1/2$, then $|\varepsilon_{\mathbf{j}_\kappa}| > |\varepsilon_{\psi}|$, and so the smaller of the two

quantities, $\psi_{\mathrm{ev}}^{\mathrm{ss}}(\mathbf{a}_+)$ and $\mathbf{n}\mathbf{j}_{\kappa}^{\mathrm{ss}}$, is estimated with poorer accuracy, as expected. Therefore, an important conclusion is that, for permeability-limited exchange, steady-state fluxes can, in principle, be more accurately estimated by means of a lumped tracer-exchange model than can steady-state concentrations; for diffusion-limited exchange the opposite conclusion holds.

In order further to investigate the third bulleted item above, we estimated ε_{ψ} and $\varepsilon_{\mathbf{j}_{\kappa}}$ for a Krogh cylindrical annulus model for values of the parameters appropriate for water exchange in three different tissues, as explained below. The numerical results are presented in Fig. 4.15 and in Table 4.1; in all three cases the steady-state intracapillary concentration was set to unit amplitude, i.e., $\psi_{\mathrm{iv}}^{\mathrm{ss}} = 1$.

For values of the parameters (particularly the tissue relaxation rate) appropriate for human prefrontal cortex (Fig. 4.15a) the steady-state extravascular concentration is seen to be a small percentage ($\lesssim 3\%$) of the intracapillary concentration, due both to a low blood–brain barrier permeability to water, and to relatively long intercapillary distances.[29] The amplitude of the spatially averaged concentration is significantly lower ($\sim 31\%$) than the amplitude of the abluminal concentration. However, since the resultant blood–tissue flux is driven mainly by the intracapillary concentration, the difference between the estimated blood–tissue fluxes for the two models is small ($\sim 1\%$).

The second row of Table 4.1 illustrates the effect of a hypothetical ten-fold increase in blood–brain barrier permeability to water. This causes the transcapillary tracer flux and the amplitude of the abluminal concentration to increase nearly ten-fold. The relative difference between the abluminal concentration and the spatially averaged concentration remains unchanged, whereas the relative difference in transcapillary tracer flux increases exactly ten-fold, as predicted by Eq. (4.54a) and Eq. (4.56),

[29] This amplitude is of the same order as that predicted by the blood-to-tissue step response for sparse capillary networks and $D_{\mathrm{ev}}/\kappa a \sim 10^2$, since at $t_{\mathrm{ss}} \approx 4$ s after the appearance of a bolus of tracer water at the capillary, the abluminal amplitude of the step response is ~ 0.03 in the absence of tracer relaxation; see second curve from top in Fig. 3.7d. Since $|R_{\mathrm{ev}} - R_{\mathrm{iv}}|t_{\mathrm{ss}} \ll 1$, this estimate is reasonably accurate.

respectively.

For parameter values appropriate for myocardium, the steady-state concentration (Fig. 4.15b) is likely an order of magnitude higher than the estimate obtained above for human prefrontal cortex parameters. This may be understood by noting that, on average, myocardial intercapillary distances and capillary wall permeabilities to water are smaller and higher, respectively, than those in the brain cortex, and these factors seem to compensate for a comparatively faster myocardial relaxation rate. Thus, both the transcapillary flux and abluminal concentration are predicted with good accuracy. Note that the ratio $\tau_{\mathrm{ev}}/\tau_D \sim D_{\mathrm{ev}}/\kappa a$ is similar for both these tissues.

For values of the parameters consistent with a simplified renal proximal tubule geometry (Fig. 4.15c and Fig. 4.15d), a diffusive steady state in interstitial (peritubular) space is likely established within a few milliseconds, water concentrations at each side of the basolateral membrane being very nearly equal (fourth row of Table 4.1). In this highly simplified model, the lumped tracer-exchange model predicts the concentration at the outer face of the basolateral membrane very accurately. However, because the basolateral permeability to water is large, the lumped tracer-exchange model overestimates the transmembrane water flux by a large percentage ($\sim 30\%$). With lower values of tubule volume fraction (last row of Table 4.1), as can be obtained in preparations of partially distended tubules [137], the lumped tracer-exchange model increasingly deviates from the presented spatiotemporal model; in particular, the transmembrane flux of water appears to be grossly overestimated ($\sim 270\%$).

It is worth noting that since a Krogh annulus model was used to obtain the results shown in Table 4.1, they should be viewed merely as reasonable estimates. The values of pericapillary radius for human brain cortex and myocardium used in the above examples are upper-range values, according to Table 2.1. Therefore, we expect the calculated deviations ϵ_ψ and $\epsilon_{\mathbf{j}\kappa}$ to be worst-case values. For example, setting $A = 21$ μm and 7.8 μm for grey matter and myocardium, respectively,[30] the

[30]These values are obtained from the formula $A = a/\sqrt{v_{\mathrm{iv}}}$, for values of intracapillary volume fraction v_{iv} as given in Table 2.1.

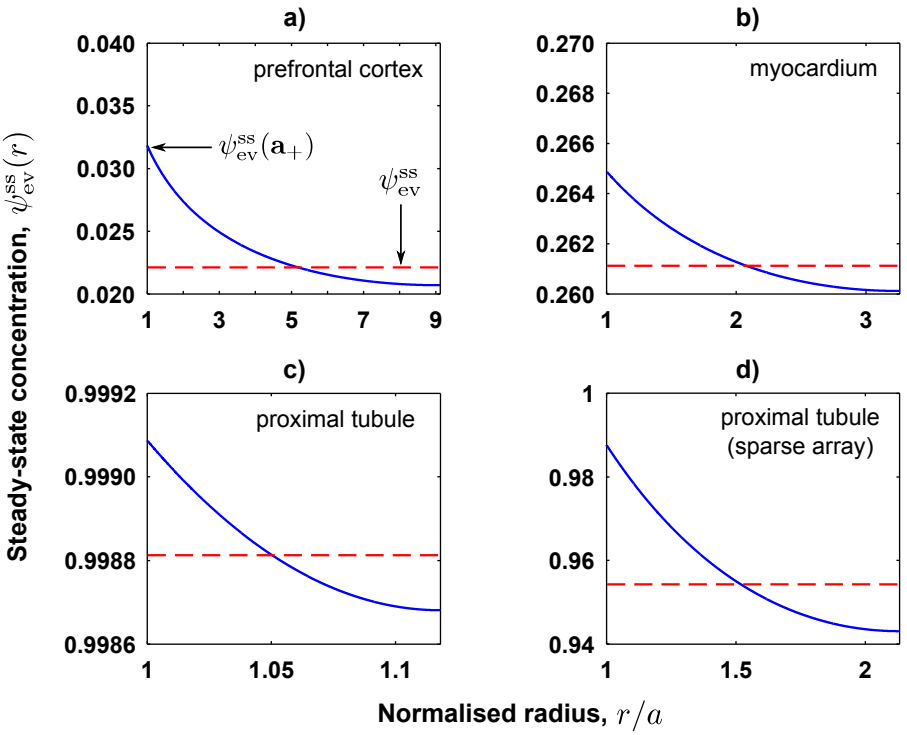

Figure 4.15: **Steady-state water concentration for various Krogh-type models of interstitial space**. Red broken lines denote spatially averaged compartment concentrations. **a)** Human brain cortex (with $R_{\rm ev}$ appropriate for prefrontal cortex). **b)** Human myocardium. **c)** *In vivo* renal proximal convoluted tubules; tubular volume fraction is 80%. **d)** Suspension of distended renal proximal tubules; tubular volume fraction is 22%. The values of a, $D_{\rm ev}$, κ and $R_{\rm ev}$ are as in Table 2.1, and the outer radius $A = 29.1$ μm, 9.125 μm, 24.6 μm and 46.9 μm, respectively, consistent with the literature values shown in Table 2.1.

respective deviations of the amplitude of the spatially averaged concentration from that of the abluminal concentration diminish to 15% and 0.8%, approximately. It is noted that the Krogh annulus geometry used in the foregoing discussion may prove inaccurate for the evaluation of water exchange in, for example, the renal cortex, due to the dense packing and highly convoluted arrangement of renal proximal tubules.

	R_{ev}	τ_{ev}	$D_{\mathrm{ev}}/\kappa a$	$\mathbf{nj}_{\kappa}^{\mathrm{ss}}$	$\psi_{\mathrm{ev}}^{\mathrm{ss}}(\mathbf{a}_+)/\psi_{\mathrm{iv}}^{\mathrm{ss}}$	$\psi_{\mathrm{ev}}^{\mathrm{ss}}/\psi_{\mathrm{ev}}^{\mathrm{ss}}(\mathbf{a}_+)$	ε_{ψ}	$\varepsilon_{\mathbf{j}_{\kappa}}$
	$[\mathrm{ms}^{-1}]$	[ms]	–	$[\mu\mathrm{m}^{-2}\,\mathrm{ms}^{-1}]$	[%]	[%]	[%]	[%]
Prefrontal cortex	1763^{-1}	7.7×10^4	150	1.6×10^{-3}	3.2	69	−31	1.0
——[a]	1763^{-1}	7.7×10^3	15	1.3×10^{-2}	25	69	−31	10
Myocardium	920^{-1}	2.6×10^3	120	3.8×10^{-3}	26	99	−1.4	0.52
Renal tubule[b]	4300^{-1}	3.9	0.13	6.4×10^{-4}	100	100	−0.028	30
——[c]	4300^{-1}	56	0.13	8.7×10^{-3}	99	97	−3.4	2.7×10^2

Table 4.1: **Comparison of steady-state transmembrane tracer flux and tracer concentration at outer face of membrane**. The values of a, D_{ev}, κ and R_{ev} are as in Table 2.1, and the outer radius $A = 29.1$ μm, 29.1 μm, 9.125 μm, 24.6 μm and 46.9 μm, respectively, consistent with data in Table 2.1. [a]For a hypothetical capillary water permeability of 1.7×10^{-2} $\mu\mathrm{m}\,\mathrm{ms}^{-1}$, i.e., an order of magnitude higher than typical values of the blood–brain barrier permeability to water. [b,c]Simplified model of *in vivo* renal proximal convoluted tubules and suspension of half-distended tubules, with tubular volume fractions of 80% and 22%, respectively; refer to Table 2.1.

4.6 Comparison with chemical exchange theory

The theory of chemical exchange is well established; see, e.g., Refs [128, 129] and earlier references therein. In essence, the Bloch equations are modified to incorporate exchange terms, thus enabling interpretation of relaxation measurements for species exchanging between magnetically distinct compartments [128]. Compartmental diffusion is considered fast enough not to hinder the exchange. In this Section we show that some results of the theory, namely (i) the apparent relaxation rate under slow chemical exchange conditions, and (ii) the apparent tissue blood volume, also follow from the results for permeability-limited exchange set forth in this Thesis; we presented these results previously in Ref. [96].

Apparent relaxation rate

It is well-known that compartmental exchange can alter the observed relaxation rates [192]. In particular, when the net exchange rate (or rate of equilibration [129]) between the intracapillary and extravascular spaces is much slower than the difference between the respective relaxation rates, i.e.,

$$|R_{\mathrm{iv}} - R_{\mathrm{ev}}| \gg \frac{1}{\tau_{\mathrm{iv}}} + \frac{1}{\tau_{\mathrm{ev}}}\,, \tag{4.57}$$

relaxation dominates over permeation and the system is said to undergo slow chemical exchange [129]. In this situation, the intracapillary and extravascular spaces will relax independently with respective rates $R_{\mathrm{iv}} + \tau_{\mathrm{iv}}^{-1}$ and $R_{\mathrm{ev}} + \tau_{\mathrm{ev}}^{-1}$, where R_{iv}, R_{ev} are the relaxation rates in the absence of exchange [129].

This result can also be obtained by noting that, for times $t \sim \min\{\tau_{\mathrm{iv}}, \tau_{\mathrm{ev}}\}$, the intracapillary and extravascular concentrations will differ exponentially from each other, and so the results for absorbing boundary conditions developed here are therefore applicable. Letting $R_{\mathrm{iv}} > R_{\mathrm{ev}}$ for definiteness, and substituting the effective extravascular depolarised volume for permeability-limited exchange, given by $\Lambda(t) \approx \kappa S t = V_{\mathrm{ev}} t/\tau_{\mathrm{ev}}$, Eq. (4.7c), in the expression for the average extravascular

concentration, Eq. (2.27), gives

$$\frac{\psi_{\mathrm{ev}}(t)}{\psi_{\mathrm{ev}}(0)} \approx \left(1 - \frac{t}{\tau_{\mathrm{ev}}}\right) \exp(-R_{\mathrm{ev}} t) \approx \exp(-R_{\mathrm{ev}}^{+} t)\,, \tag{4.58}$$

where the last approximation is valid for $t < \tau_{\mathrm{ev}}$.

Apparent tissue blood volume

Donahue *et al.* investigated the effect of transcapillary water exchange on the quantification of tissue blood volume [170]. These investigators performed T_1 and T_1-weighted MR measurements in a rat model and demonstrated that tissue blood volume estimates are highly sensitive both to exchange modelling assumptions and to experimental parameters, including imaging time and dose of paramagnetic tracer. Under slow exchange conditions and further assuming a fully relaxed intravascular space, the apparent tissue blood volume fraction, $v_{\mathrm{iv}}^{\mathrm{app}}$, was found to approach the value given by Eq. (10) of Ref. [170]:

$$v_{\mathrm{iv}}^{\mathrm{app}} = v_{\mathrm{iv}} \left[1 + \left(\frac{1}{\tau_{\mathrm{iv}}} + \frac{1}{\tau_{\mathrm{ev}}}\right) \mathrm{TI}\right], \tag{4.59}$$

where TI is the pulse-sequence inversion time. For sparse capillary networks, as in rat myocardium, the net transcapillary exchange rate is given by τ_{iv}^{-1}, to zero-order in the intracapillary volume fraction. Thus, Eq. (4.59) predicts the difference between the apparent and true tissue blood volumes to be $v_{\mathrm{iv}}\mathrm{TI}/\tau_{\mathrm{iv}} = \kappa S \mathrm{TI}$. This correction term is equal, to the stated accuracy, to the effective extravascular depolarised volume under permeability-limited conditions, Eq. (4.7c), evaluated at time $t = \mathrm{TI}$.

4.7 Discussion

We begin by reviewing the relative merits of spatiotemporal vs lumped tracer-exchange models, by way of introduction to a discussion of the ASL results developed in this Chapter and the feasibility of parameter estimation using the presented spatiotemporal model.

The higher complexity of spatiotemporal models results from the necessity to specify the geometry of tissue, from the greater number of time- and position-dependent

quantities to be considered, and from the fact that certain mechanisms, like diffusion, can only be adequately described by spatiotemporal, but not lumped, models. Despite their higher complexity, spatiotemporal models have inherent advantages beyond their ability to describe physiological processes more realistically than lumped models.

Importantly, upon averaging the time- and position-dependent solutions (e.g., the extravascular magnetisation) of the spatiotemporal model, the resultant time-dependent variables (e.g., the extravascular magnetic moment) reveal the role of certain physical parameters (e.g., the diffusion coefficient) which are not available with simpler lumped tracer-exchange approaches. Alternatively, by taking spatial averages in the governing model equations, consistent with the employed measurement technique, more accurate lumped formulations can be obtained. Spatial averaging yields the amplitude of the concentration at the boundary between adjacent compartments; these quantities cannot be completely taken into account by the class of lumped tracer-exchange models.

It may also be noted that, for spatiotemporal models, the necessity to specify both a tractable geometry and reasonable boundary conditions may bias to some degree the estimation of physiological parameters. On the other hand, lumped models suffer from the rather abstract definition of the well-mixed kinetic compartment.

In Section 4.2, the permeability-limited and diffusion-limited tracer exchange regimes were both discussed in physical terms at length. Subsequently, the spatiotemporal model developed in this Thesis was compared against four literature models, namely the model of Hudson and Cater [52] for diffusion-limited gas exchange in tissue (Section 4.3); the spatiotemporal model of Lee and Fronek [44] for microvascular transport and extravascular diffusion of non-absorbed indicators (Section 4.4); and the models of St. Lawrence *et al.* [31] and Parkes and Tofts [34] for permeability-limited water exchange in brain and myocardium (Section 4.4). The analysis shows that it is important properly to account for different relaxation rates in intracapillary and extravascular space in order to avoid large errors in the estimated total magnetic moment. As expected, lumped tracer-exchange models were

found to be adequate for the analysis of permeability-limited, but not diffusion-limited, exchange. Importantly, however, it was shown that tracer concentrations and permeation fluxes for spatiotemporal and lumped tracer-exchange models may differ substantially even at steady state. To maximise accuracy, the governing system of equations for the spatially-averaged tracer concentrations should be obtained from a suitable spatiotemporal model by volume integration.

In the remainder of this Discussion we assess, briefly, how well the main modelling assumptions made in this Chapter and in Chapter 2 apply to conventional ASL approaches.

The issue of whether extravascular tissue may be considered a homogenous environment for water diffusion was discussed in Section 2.4.3. Further, the assumption that in brain and myocardial ASL the back-flux of tagged water into the capillaries is negligible, is seen to be correct for the examples of Fig. 4.9 and Fig. 4.10. This assumption may, however, prove incorrect when the exchange is rate-limited by compartmental diffusion rather than barrier permeability, since the concentrations at compartment barriers may be much higher than the respective spatially averaged concentrations.

Equation (2.21) is the basis for the estimation of haemodynamic and tracer-exchange parameters using the spatiotemporal model presented in this Thesis. A two-step estimation process involves time deconvolution of the time course of the ASL signal with the inflowing tracer concentration, $\psi_{\mathrm{iv}}(z=0,t)$, followed by curve fitting of the output of deconvolution to the term in brackets in (2.21), which comprises the two impulse response functions obtained in this work, $h_{\mathrm{a}}^{\mathrm{iv}}(z,t)$ and $w(\mathbf{r},t)$. The spatiotemporal model involves six independent parameters, namely f_{iv}, τ_{c}, τ_{iv}, R_{iv}, R_{ev} and D_{ev}/a^2, or combinations thereof. As an approximate rule, we suggest that the number of samples of inflowing magnetisation to be collected be an order of magnitude greater than the number of independent model parameters. Practical limitations (e.g., time resolution and signal-to-noise ratio) may prevent accurate estimation of all of the above parameters even when the ASL signal is time sampled using currently available fast sequences. By way of example, Günther *et al.* [193]

were able to estimate capillary flow and arterial transit time in the human brain with a fast ASL pulse sequence capable of acquiring 23 images of a single tissue slice during a repetition time of 2.5 s, with a temporal resolution of 100 ms (due to hardware restrictions); including bolus duration in the non-linear fitting algorithm made it unstable at low signal-to-noise ratios.

Under permeability-limited conditions, Eq. (4.42) and Eq. (4.44) can, in principle, be used for the estimation of a reduced set of parameters, namely f_{iv}, τ_{c}, τ_{iv}, R_{iv} and R_{ev}. In practice, the longitudinal relaxation rates in blood and whole tissue may be estimated independently using any of a number of available techniques. (This approach may be justified for sparse capillary networks, in which the relaxation rate in extravascular tissue is reasonably well approximated by that in whole tissue including its contained intracapillary space; see Section *Longitudinal relaxation rates* of Appendix 2.5.2, pp. 98 ff.).

Another difficulty consists in the accurate estimation of the inflowing tracer concentration for tracer-exchange models that perform deconvolution. Numerical deconvolution is, in general, sensitive to signal noise, hence it is sometimes avoided in practice by assuming a suitable analytic expression for the inflowing concentration. This results in a 'simple' analytical signal expression which can be fitted to the experimental data. For example, a number of ASL models [24, 31, 34] describe the arterial magnetisation as a dispersionless bolus with exponentially decaying amplitude, Eq. (4.38). However, a problem with this approach is that it may bias the fitting procedure if the assumed bolus shape differs markedly from the true one [18, p. 716]. In this situation, faster sampling of the time course of the ASL signal will not improve the fit.

Several ASL acquisition methods and/or signal models have been proposed that aim to overcome in part these issues. Petersen, Lim and Golay [194] introduced a method for the quantification of arterial blood volume and perfusion rate which required no modelling of the underlying exchange. Their approach followed the model of Buxton *et al.* [24] and deconvolution was aided by first estimating the local arterial magnetisation using an appropriate magnetic field gradient scheme and image sub-

traction. The model of Kelly, Blau and Kerskens [37] also does not quantify the underlying blood–tissue water exchange explicitly, thus resembling a single-compartment approach. Rather, pseudo-diffusion of tagged water molecules within whole tissue was considered to contribute stochastically to the total (blood and tissue) volume occupied by tagged water as the bolus flows from the tagging region into the tissue. This model allowed estimation of arterial and microvascular transit times.

One expects increased water-exchange model accuracy if the amount of tagged water present in, respectively, intracapillary, venous and extravascular space can be determined. The longitudinal relaxation rate of blood practically does not vary with blood oxygenation level [167] and any differences between intracapillary and extravascular transverse relaxation rates at low main fields can reasonably be neglected. However, at higher fields ($\sim$ 4 T and above) the influence of increasing differences in the transverse relaxation time of blood and tissue (both of which become closer to typical echo-time values) caused by stronger susceptibility effects of partially deoxygenated blood, should be taken into account [195] in order to avoid bias in the estimated parameters.

Several studies have incorporated transverse relaxation effects by assuming monoexponential reduction in compartmental magnetic moments [34, 195], possibly with an oxygen-level dependent intracapillary relaxation rate [195]. Other studies [119] also have modelled the effect of microvessel orientation on signal decay and have suggested the presence of multiple extravascular compartments with distinct transverse relaxation rates detectable on the ASL time scale. In this Thesis, the transverse relaxation of magnetically tagged water is not considered because long-ranged magnetic susceptibility effects between erythrocytes, blood vessels and extravascular tissue likely invalid the assumption of independent exchange in neighbouring pericapillary regions.

4.8 Appendices

4.8.1 Axial intracapillary diffusion in the steady state

Tracer diffusion in the direction parallel to the capillary axis has been neglected in our treatment, for reasons discussed in Section 2.2. In this Appendix we obtain a condition for negligible axial diffusion effects in the steady-state.

The steady-state intracapillary concentration (4.48c) is given by

$$\psi_{\mathrm{iv}}^{\mathrm{ss}}(z) = \exp(-kz)\,, \tag{4.60a}$$

where

$$k^{-1} = u_z \left[R_{\mathrm{iv}} + \frac{1 - \int_0^{t_{\mathrm{ss}}} w(\mathbf{a}_+, t')\,\mathrm{d}t'}{\tau_{\mathrm{iv}}} \right]^{-1} \tag{4.60b}$$

is a characteristic concentration fall-off length. The resultant non-zero axial gradient in tracer concentration creates a position-dependent axial diffusive flux. If the steady-state intracapillary equation is augmented with an axial diffusion term, and if the solution to this latter equation is compared to the right-hand side of (4.48c), the axial diffusion term is seen to be much smaller than both the convection and transcapillary permeation terms when the time for tracer molecules to diffuse over the fall-off length is much greater than the characteristic time for tracer relaxation/consumption and transcapillary permeation, i.e., when

$$\frac{1}{D_z k^2} \gg \left[R_{\mathrm{iv}} + \frac{1 - \int_0^{t_{\mathrm{ss}}} w(\mathbf{a}_+, t')\,\mathrm{d}t'}{\tau_{\mathrm{iv}}} \right]^{-1}. \tag{4.61}$$

For example, by the time a packet of magnetically tagged blood water molecules has diffused axially a distance of order k^{-1}, its NMR signal should be negligibly low.

Condition 4.61 is well satisfied for the parameter values listed in Table 2.1: from these we estimate $k^{-1} \sim 10^2 - 10^3$ μm, which is comparable to typical capillary lengths.

4.8.2 Typical diffusion times in ASL measurements

In this Appendix we estimate the average extravascular diffusion time, or post-exchange time $t_{\rm ev}$, as defined by equation (4.47) of Section 4.4.4 and reproduced below for convenience:

$$t_{\rm ev} \sim \tau_{\rm tag} + \tau_{\rm w} - \delta\tau_{\rm tag} - \tau_{\rm a} - \tau_{\rm iv}\,.$$

Next we review a number of ASL studies of myocardium and brain tissue available in the literature.

Wang *et al.* [196] adapted flow-sensitive alternating inversion recovery (FAIR) PASL for free-breathing myocardial imaging at 1.5 T. A single slice along the short axis of the left ventricle was imaged with post-tagging delays of 200 – 1700 ms. The arterial transit time was estimated as $\sim$ 400 ms, using a single-compartment pharmacokinetic model. We assume $\tau_{\rm tag} = 700$ ms [23], $\tau_L = 300$ ms [31] and $\tau_{\rm iv} = 300$ ms (from Table 2.1). For a post-tagging delay of 200 ms, early-arriving water molecules will have tissue post-exchange times of up to 200 ms; for a post-tagging delay of 1700 ms, post-exchange times for late- and early-arriving water molecules are 700 ms and 1700 ms, respectively.

MacIntosh *et al.* [197] estimated arterial transit times in brain tissue of normal subjects by fitting the kinetic model of Buxton *et al.* [24] to three-dimensional gradient- and spin-echo PASL data at 3 T. Mean arterial transit times were, approximately, 600 ms in the temporal lobe and 1000 ms in the occipital lobe.[32] The median

[31] Wong *et al.* [23] measured transit times through a 10-cm wide tag (placed presumably in the head) of 700 – 800 ms. In the study of Wang *et al.* [196] the tagging region was 3 – 4 cm thick.

[32] Arterial transit time estimates appear to be consistent across a range of measurement conditions. Alsop and Detre [198] estimated a minimum arrival time of 600 ms using gradient-echo echoplanar CASL at 1.5 T in the thalamic region; the inversion plane was located 40 mm proximal to the imaging slice, as was located the tagging region below the imaging volume in the above-mentioned study of MacIntosh *et al.* Gallichan and Jezzard estimated arterial transit times of 300 – 1200 ms (see Fig. 8, left panel, of Ref. [199]) on eight anatomical regions of interest situated at the level of the thalamus by fitting a single-compartment model, with assumed Gaussian bolus dispersion, to gradient-echo echoplanar PASL data at 3 T. In this study the offset between tagging region and imaging slice was 15 mm.

tagging time was 1000 ms and post-tagging delays between 400 – 2400 ms were applied; we assume $\tau_L = 300$ ms and $\tau_{\text{iv}} = 900$ ms. Equation (4.47) gives estimated post-exchange times of 200 – 1500 ms and 600 – 1900 ms in the occipital and temporal lobes, respectively, for a post-tagging delay of 2400 ms. (Note that this value of τ_{w} is probably an upper limit for 1.5 – 3 T measurements, to avoid excessive bolus relaxation).

In another study, Fernández-Seara *et al.* [200] used CASL with three-dimensional gradient- and spin-echo readout at 3 T; the parameters $\tau_{\text{tag}} = 2000$ ms, $\tau_{\text{w}} = 1200$ ms were used. For the arterial transit times given by MacIntosh *et al.* [197], we estimate $t_{\text{ev}} \sim 1700$ ms in the temporal lobe and $t_{\text{ev}} \sim 1300$ ms in the occipital lobe for water molecules tagged at the start of the ASL pulse.

Chapter 5

Conclusions

The purpose of the research work described in this Thesis was to investigate the joint effect of diffusion and first-order consumption in physiological exchange processes between blood and extravascular tissue. A natural application of this work is to arterial spin labelling (ASL) methods in magnetic resonance imaging (MRI).

The joint effect of diffusion and first-order consumption (e.g., magnetic relaxation) can be assessed with the aid of tracer substances under both steady and non-steady state conditions. This latter case has not been sufficiently addressed in the literature, despite the fact that in recent years much research has been devoted to advancing MRI-based quantification of physiological processes [5]. Theoretical spatiotemporal models of blood–tissue tracer exchange taking into account extravascular diffusion were presented by Lee and Fronek [44] and by Kuo, Gustafson and Friedman [45] in the early 1970s. However, since they focussed on the kinetics of non-metabolised indicators, these studies did not consider tracer consumption in blood or extravascular tissue.

Another research area in which spatiotemporal models have found widespread use is in the quantification of oxygen supply to extravascular tissues by the microcirculation. However, because tissue oxygen consumption varies non-linearly with local oxygen tension, oxygen delivery models are, in principle, not directly applicable to MRI experiments with magnetically tagged water or paramagnetic tracers.

5.1 Main contributions of this Thesis

The main contributions of this Thesis are discussed in the following subsections. The stated research aims may be reviewed in Section 1.2.

Modelling blood–tissue tracer exchange

We began by discussing the main anatomical and physiological assumptions based on which a model of capillary networks and extravascular tissue was adopted in this work. Then we introduced the governing spatiotemporal equations of blood–tissue tracer exchange. In the capillaries, we considered the effect of convective flow and first-order consumption. In the extravascular space, we considered the effect of first-order consumption and extravascular diffusion of a tracer substance. A distinguishing feature of the present tracer-exchange model is its taking into account extravascular diffusion and first-order consumption in intracapillary and extravascular space under non-steady-state conditions. The exchange of tracer between blood and extravascular tissue was assumed to occur by diffusive permeation only; other forms of transmembrane transport, such as facilitated diffusion, were not considered in the analysis. The extravascular space was modelled as a medium with homogenous diffusion and consumption properties throughout.

We obtained rather general expressions for the arterial-to-intracapillary impulse response function and for the intracapillary-to-extravascular (i.e., blood-to-tissue) impulse, and step, response functions for whole tissue, under idealised conditions of linearity and time invariance of the microcirculation. In addition, we introduced a quantity termed the effective extravascular depolarised volume, which measures the clearance of extravascular tracer due to tissue-to-blood exchange under absorbing intracapillary conditions. The main theoretical tool employed in these developments was the Green's function of the diffusion–consumption equation for whole extravascular tissue.

The above framework is rather general, hence difficult to evaluate mathematically for realistic capillary networks as found in macroscopic tissue volumes. We therefore described a physical situation in which blood–tissue exchange could be evaluated

on the basis of individual capillary segments, provided that any interactions among neighbouring capillary segments had a negligible effect on the extravascular distribution of tracer; this was called the single-capillary approximation. We reasoned this situation to be expected for diffusion times such that the diffusion lengths covered by the tracer during the experiment is smaller, on average, than typical intercapillary distances in the tissue in question. The single-capillary approximation was deemed reasonable for sparse capillary networks as found in, e.g., brain and myocardium, for extravascular diffusion times in the range of typical ASL measurements.

Based on this theoretical framework, we evaluated all the blood–tissue exchange quantities analytically, where possible, and otherwise expressed them in terms of integrals which were easily computed numerically. Steady-state exchange was also considered under somewhat simplified capillary–tissue assumptions (see the next Subsection).

The spatiotemporal tracer-exchange model developed in this work made possible a quantitative discussion of the main rate-limiting mechanisms encountered in blood–tissue exchange, namely capillary wall permeability and extravascular diffusion.

The foregoing results were presented in Chapters 2 – 4.

Validity of tracer-exchange models

A number of literature studies [62] have addressed the scope and physiological interpretation of certain lumped tracer-exchange models, while other researchers [38, 61] have compared various such models for relative performance. However, analyses of the validity of lumped tracer-exchange models when compared to the more realistic class of spatiotemporal models appear, to the best of this author's knowledge, to be lacking in the literature. In this Thesis we have therefore presented such a discussion.

We showed that the class of lumped tracer-exchange models cannot deal properly with the effect of the boundary conditions between adjacent tracer-accessible compartments. Because the value of the concentration at each face of the membrane dividing any two physiological compartments differs, in general, from the respective spatially averaged concentration (this is referred to as the jamming effect), the es-

timation of transmembrane fluxes using lumped tracer-exchange models is prone to inaccuracies. We showed the class of lumped tracer-exchange models to be adequate, in general, for the quantification of transmembrane fluxes under permeability-limited, but not diffusion-limited, conditions. Under diffusion-limited exchange contitions, both the time course and spatial profile of the extravascular concentration of tracer predicted by the spatiotemporal model presented in this Thesis were shown to deviate strongly from those predicted by lumped tracer-exchange models.

In addition, we evaluated the steady state as a limiting case for the assessment of the assumption of uniform concentrations which underlies any lumped tracer-exchange approach. We found that this assumption might be inaccurate even in certain permeability-limited cases. By evaluating theoretically the response of both the spatiotemporal model presented herein and an appropriate two-compartment lumped model for radially finite Krogh cylinders representative of grey matter and myocardium, we found that the lumped model did predict correctly the amount of tracer (labelled water, in this case) in extravascular space, but that it might fail accurately to predict the spatially varying concentration in grey matter when compared against the spatiotemporal model. Specifically, the abluminal concentration would be underestimated, whereas at points far from the capillary wall the concentration would be overestimated. Here the interplay of capillary wall permeability, relaxation rates and tracer-accessible extravascular volume for each tissue seemed to be of significance. On the other hand, under diffusion-limited conditions the lumped model predicted the extravascular concentration – but not the amount of extravascular tracer – in close agreement with the spatiotemporal model.

These results were presented in Chapter 4.

ASL model comparisons

We compared the presented spatiotemporal model to two literature models of water exchange in brain tissue, namely the two-compartment lumped model of Parkes and Tofts [34] and the one-barrier distributed-parameter, single-pass approximation (1BDP-SPA) model of St. Lawrence, Frank and McLaughlin [31]. This latter model

does not take into account tracer diffusion but does take account of axial distribution of tracer in intracapillary space due to capillary flow and transcapillary exchange. Model comparisons were made by generating the output of all three models using a common set of test tissue parameters and boli of inflowing magnetisation. Independent estimation of blood–tissue exchange parameters was not performed at this stage.

Our results indicated that in the cases considered (i.e., pulsed and continuous ASL modelling of water exchange in myocardial and cortical brain tissue), the time course of total (intra- and extravascular) magnetic moment (or amount of ASL tracer) in unit volume of tissue predicted by the 1BDP-SPA model agrees well with those of predicted by the model presented in this Thesis, provided that transcapillary water permeation is the rate-limiting mechanism. On the other hand, the 1BDP-SPA model was found to deviate strongly from the spatiotemporal model presented here in the case that inefficient redistribution of tracer by extravascular diffusion limited the rate of transcapillary exchange. Predicted deviations of the 1BDP-SPA model from the spatiotemporal model were evaluated numerically as a function of observation time for a wide range of values of the non-dimensional parameter in Eq. (4.2), which quantifies the trade-off between transcapillary exchange and extravascular diffusion.

On the other hand, for normal brain and capillary water permeabilities the total magnetic moment in unit volume of tissue predicted by the lumped water-exchange model of Parkes and Tofts is lower than that predicted by the spatiotemporal model presented in this Thesis. This was attributed to the fact that a 'black-box' modelling of intracapillary convection in this model makes it difficult to estimate the outflow of tracer accurately, without further assumptions. For elevated capillary permeabilities, however, the amount of tracer predicted by the Parkes–Tofts model can be more nearly equal to that predicted by the presented spatiotemporal model than is the case for the 1BDP-SPA model.

Finally, comparison of the spatiotemporal model developed herein and the model of Lee and Fronek [44] – which accounts for capillary flow, transcapillary permeation and extravascular diffusion, but not for tracer consumption – shows that unrealistic

modelling of consumption/relaxation effects in blood and extravascular tissue leads to rapidly increasing deviations as the time after arrival of tracer (e.g., arterial magnetisation) at the capillary increases, thus rendering this model unsuitable for ASL studies.

The foregoing results were developed in Chapter 4.

5.2 Further work

In this Section we outline a number of potential extensions to the research work described in this Thesis.

1. The treatment of tracer diffusion presented spatiotemporal tracer-exchange model can be enhanced by (i) taking into account the non-trivial time dependence of the mesoscopic tracer diffusion coefficient; and by (ii) considering diffusion in more than one exchanging compartment.

2. The method of solution of the spatiotemporal model presented in this Thesis must be extended to account for the case in which the concentration of tracer in the capillaries is significantly altered by the back-flux of tracer from extravascular space into the blood. This situation might occur under diffusion-limited conditions, in particular if tracer is rapidly removed from the capillary blood, or in tissues with low fractions of tracer-accessible extravascular space. A full analytical treatment of tracer back-flux is rather involved, suggesting that numerical solutions should be sought.

   In fact, analysis of blood–tissue exchange in realistic capillary networks as obtained from, e.g., electron micrographs of tissue specimens [55], usually demands computational approaches. For the case of thin, highly permeable capillaries, the extravascular impulse-response distribution of tracer can be obtained approximately by convolving the spatial profile of the capillary network with the Green's function for a discrete source in free space; at points far from the edge of the sample, any boundary conditions effects can be neglected to a first

approximation. (This method is also applicable to the mapping of magnetic susceptibility effects, provided that the extravascular magnetic field induced by the intracapillary magnetisation is much smaller than the main static field, thus avoiding higher-order interactions; here the dipole field takes on the role of basic free-space field). However, when it is a finite capillary permeability that limits the blood-to-tissue flux of tracer, the Green's function for a discrete source must be replaced by the blood-to-tissue impulse response function (2.15), which is valid for the case of negligibly low back-flux of tracer into the capillaries. The blood-to-tissue impulse function involves spatial integration of the Green's function for the given tissue sample, and in practice the latter can only be obtained by numerical methods.

3. As MRI field strengths continue to increase ($\geq$ 4 T), any differences in transverse relaxation rate between blood and extravascular tissue due to magnetic susceptibility effects of partially deoxygenated blood become more important and can no longer be neglected; see Ref. [195, p. 425] and references therein. Because spatial heterogeneities in magnetic susceptibility of tissue – as induced by, e.g., the compartmentalisation of a paramagnetic tracer – can profoundly affect the NMR signal [14, p. 252], both the modelling of whole tissue and the accompanying governing equations of diffusion, consumption and exchange should be refined to account for long-ranged magnetic susceptibility effects between erythrocytes, blood vessels and the various physiological compartments that can be identified in extravascular space.

4. The interval of extravascular diffusion times during which the single-capillary method of solution presented in this Thesis applies is approximately 100 ms in myocardium and is somewhat longer in brain tissue. Therefore, as discussed in Section 4.7, analysis of transient water diffusion in these tissues requires temporal resolutions well below $\sim$ 100 ms in order to estimate transport and exchange model parameters. At present, this may pose a practical limitation to implementation of the presented model. Strategies for robust parameter

estimation from measured tracer-exchange data have not been considered in this Thesis.

The research work described in this Thesis was for the most part theoretical; selected results were tested, as appropriate, using Monte Carlo simulations involving random walks of tracer particles. The presented model was not tested on subjects at the present stage of development. Further advances will require designing and performing dedicated experiments to answer specific theory-motivated questions (for example, the characterisation of the transport properties of larger vessels is an important issue that remains an open research topic) and to demonstrate the capability of the presented model to produce robust estimates of blood–tissue exchange parameters in subjects.

5.3 Concluding remark

In conclusion, in this Thesis we have presented a spatiotemporal model of blood–tissue tracer exchange whose main distinguishing feature is its taking account of the joint effect of extravascular diffusion and first-order consumption in intracapillary and extravascular spaces. Notwithstanding its above-discussed limitations, this model should prove useful in those cases in which extravascular diffusion is the dominant rate-limiting mechanism of blood–tissue exchange, a physical situation which is not covered by the class of lumped tracer-exchange models. The model presented in this Thesis is anticipated to be applicable to, e.g., the quantitative assessment of water exchange between physiological compartments under non-steady-state conditions, as in arterial spin labelling MRI with fast image acquisition.

List of Publications

Journal articles

1. Solera Ureña JR, Olmos S, Kiselev VG. Tissue–blood exchange of extravascular longitudinal magnetisation with account of intracompartmental diffusion. Magn Reson Med 2011;66(5):1445–1455.

2. Solera Ureña JR, Olmos S, Kiselev VG. The role of consumption and extravascular diffusion in blood–tissue tracer exchange. Submitted to *Physics in Medicine and Biology* on 6 June 2013.

Proceedings

1. Solera Ureña JR, Olmos S, Kiselev VG. On the role of tissue–blood exchange on the relaxation effect of paramagnetic blood tracers. Proc. Intl. Soc. Mag. Reson. Med. 18 (2010):627

2. Solera Ureña JR, Olmos S. Quantification of systematic error in standard formula for computing transverse relaxation rates in DSC–MRI. Implications for blood volume and flow calculations. Proc. Intl. Soc. Mag. Reson. Med. 18 (2010):4118

Bibliography

1. Campbell NA. Biology. Menlo Park, California: The Benjamin/Cummings Publishing Company, Inc., 4th edition, 1996.

2. Alberts B, Bray D, Lewis J, Raff M, Roberts K, Watson JD. Molecular Biology of the Cell. New York: Garland Publishing, Inc., 3rd edition, 1994.

3. Barber Cárcamo AM, Ponz Piedrafita F. Fisiología animal. Funciones vegetativas. Madrid: Editorial Síntesis, 1991.

4. Jacobs MH. Diffusion processes in living systems. J Appl Phys 1938;9(2):81–87.

5. Tofts PS, ed. Quantitative MRI of the Brain. Measuring Changes Caused by Disease. Chichester, England: John Wiley & Sons, 2004.

6. Gerber BL, Raman SV, Nayak K, Epstein FH, Ferreira P, Axel L, Kraitchman DL. Myocardial first-pass perfusion cardiovascular magnetic resonance: history, theory, and current state of the art. J Cardiovasc Magn Reson 2008;10:10–18.

7. Notohamiprodjo M, Reiser MF, Sourbron SP. Diffusion and perfusion of the kidney. Eur J Radiol 2010;76(3):337–347.

8. Josephs D, Spicer J, O'Doherty M. Molecular imaging in clinical trials. Target Oncol 2009;4(3):151–168.

9. Sourbron SP, Buckley DL. Tracer kinetic modelling in MRI: estimating perfusion and capillary permeability. Phys Med Biol 2012;57(2):R1–33.

10. Leonard EF, Jørgensen SB. The analysis of convection and diffusion in capillary beds. Annu Rev Biophys Bioeng 1974;3(0):293–339.

11. Liang ZP, Lauterbur PC. Principles of Magnetic Resonance Imaging: A Signal Processing Perspective. New York: Wiley–IEEE Press, 1999.

12. Haacke E, Brown, RW, Thompson M, Venkatesan R. Magnetic Resonance Imaging Physical Principles and Sequence Design. New York: Wiley-Liss, 1999.

13. Bernstein MA, King K, Zhou XJ. Handbook of MRI Pulse Sequences. Elsevier Academic Press, Burlington, MA, 2004.

14. Rosen B, Belliveau J, Vevea J, Brady T. Perfusion imaging with NMR contrast agents. Magn Reson Med 1990;14:249–265.

15. Kiselev VG, Posse S. Analytical model of susceptibility-induced MR signal dephasing: effect of diffusion in a microvascular network. Magn Reson Med 1999;41(3):499–509.

16. Pauling L. General Chemistry. Mineola, NY: Dover Publications, Inc., 1988.

17. Bellin MF, Van Der Molen AJ. Extracellular gadolinium-based contrast media: an overview. Eur J Radiol 2008;66(2):160–167.

18. Østergaard L, Weisskoff R, Chesler D, Gyldensted C, Rosen B. High resolution measurement of cerebral blood flow using intravascular tracer bolus passages. Part I: Mathematical approach and statistical analysis. Magn Reson Med 1996; 36(5):715–25.

19. Kiselev VG. On the theoretical basis of perfusion measurements by dynamic susceptibility contrast MRI. Magn Reson Med 2001;46(6):1113–1122.

20. Stejskal EO, Tanner JE. Spin diffusion measurements: Spin echoes in the presence of a time-dependent field gradient. J Chem Phys 1965;42:288–292.

21. Kiselev VG. Calculation of diffusion effect for arbitrary pulse sequences. J Magn Reson 2003;164(2):205–211.

22. Detre JA, Wang J. Technical aspects and utility of fMRI using BOLD and ASL. Clinical Neurophysiology 2002;113(5):621–634.

23. Wong EC, Buxton RB, Frank LR. A theoretical and experimental comparison of continuous and pulsed arterial spin labeling techniques for quantitative perfusion imaging. Magn Reson Med 1998;40(3):348–355.

24. Buxton RB, Frank LR, Wong EC, Siewert B, Warach S, Edelman RR. A general kinetic model for quantitative perfusion imaging with arterial spin labeling. Magn Reson Med 1998;40(3):383–396.

25. Petersen ET, Zimine I, Ho YCL, Golay X. Non-invasive measurement of perfusion: a critical review of arterial spin labelling techniques. Br J Radiol 2006; 79(944):688–701.

26. Golay X, Hendrikse J, Tchoyoson C. Perfusion imaging using Arterial Spin Labeling. Top Magn Reson Imaging 2004;15(1):10–27.

27. Goresky CA, Ziegler WH, Bach GG. Capillary exchange modeling. Barrier-limited and flow-limited distribution. Circ Res 1970;27(5):739–764.

28. Tofts PS, Brix G, Buckley DL, Evelhoch JL, Henderson E, Knopp MV, Larsson HB, Lee TY, Mayr NA, Parker GJ, Port RE, Taylor J, Weisskoff RM. Estimating kinetic parameters from dynamic contrast-enhanced T_1-weighted MRI of a diffusable tracer: standardized quantities and symbols. J Magn Reson Imaging 1999;10(3):223–232.

29. Larson KB, Markham J, Raichle ME. Tracer-kinetic models for measuring cerebral blood flow using externally detected radiotracers. J Cereb Blood Flow Metab 1987;7(4):443–463.

30. Li X, Rooney WD, Springer Jr CS. A unified magnetic resonance imaging pharmacokinetic theory: Intravascular and extracellular reagents. Magn Reson Med 2005;54(6):1351–1359. Erratum in: Magn Reson Med. 2006 May;55(5):1217.

31. St Lawrence KS, Frank JA, McLaughlin AC. Effect of restricted water exchange on cerebral blood flow values calculated with arterial spin tagging: a theoretical investigation. Magn Reson Med 2000;44(3):440–449.

32. Tofts PS. Modeling tracer kinetics in dynamic Gd-DTPA MR imaging. J Mag Reson Imag 1997;7(1):91–101.

33. Kety SS. The theory and applications of the exchange of inert gas at the lungs and tissues. Pharmacol Rev 1951;3(1):1–41.

34. Parkes LM, Tofts PS. Improved accuracy of human cerebral blood perfusion measurements using arterial spin labeling: accounting for capillary water permeability. Magn Reson Med 2002;48(1):27–41.

35. Kassissia IG, Goresky CA, Rose CP, Schwab AJ, Simard A, Huet PM, Bach GG. Tracer oxygen distribution is barrier-limited in the cerebral microcirculation. Circ Res 1995;77(6):1201–1211.

36. Detre J, Leigh J, Williams D, Koretsky A. Perfusion imaging. Magn Reson Med 1992;23(1):37–45.

37. Kelly ME, Blau CW, Kerskens CM. Bolus-tracking arterial spin labelling: theoretical and experimental results. Phys Med Biol 2009;54(5):1235–1251.

38. Larsson H, Tofts P. Measurement of blood-brain barrier permeability using dynamic Gd-DTPA scanning: a comparison of methods. Magn Reson Med 1992;24(1):174–176.

39. Sangren WC, Sheppard CW. A mathematical derivation of the exchange of a labeled substance between a liquid flowing in a vessel and an external compartment. Bull Math Biophys 1953;15(4):387–394.

40. Johnson JA, Wilson TA. A model for capillary exchange. Am J Physiol 1966; 210(6):1299–1303.

41. St Lawrence KS, Lee TY. An adiabatic approximation to the Tissue Homogeneity Model for water exchange in the brain: I. Theoretical derivation. J Cereb Blood Flow Metab 1998;18(18):1365–1377.

42. Perl W, Chinard FP. A convection-diffusion model of indicator transport through an organ. Circ Res 1968;22(2):273–298.

43. Bassingthwaighte JB, Wang CY, Chan IS. Blood-tissue exchange via transport and transformation by capillary endothelial cells. Circ Res 1989;65(4):997–1020.

44. Lee JS, Fronek A. An analysis on the exchange of indicators in single capillaries. Microvasc Res 1970;2(3):302–318.

45. Kuo YM, Gustafson WA, Friedman JJ. Radial diffusion effects in a finite extravascular space surrounding a single capillary. Microvasc Res 1973;5(2):148–154.

46. Beard DA, Bassingthwaighte JB. Advection and diffusion of substances in biological tissues with complex vascular networks. Ann Biomed Eng 2000; 28(3):253–268.

47. Krogh A. The number and distribution of capillaries in muscles with calculation of the oxygen pressure head necessary for supplying the tissue. J Physiol 1919; 52(6):409–415.

48. Kärger J. NMR self-diffusion studies in heterogeneous systems. Adv Colloid and Interface Sci 1985;23:129–148.

49. Fieremans E, Novikov DS, Jensen JH, Helpern JA. Monte Carlo study of a two-compartment exchange model of diffusion. NMR Biomed 2010;23(7):711–724.

50. Hoofd L. Calculation of oxygen pressures in tissue with anisotropic capillary orientation. I. Two-dimensional analytical solution for arbitrary capillary characteristics. Math Biosci 1995;129(1):1–23.

51. Hoofd L. Calculation of oxygen pressures in tissue with anisotropic capillary orientation. II. Coupling of two-dimensional planes. Math Biosci 1995;129(1):25–39.

52. Hudson JA, Cater DB. An analysis of factors affecting tissue oxygen tension. Proc R Soc Lond B Biol Sci 1964;161:247–274.

53. Brockmeyer E, Halstrøm H, Jensen A. (The Copenhagen Telephone Company) The Life and Works of A.K. Erlang. København, Danmark: Transactions of the Danish Academy of Technical Sciences, No. 2., 1948.

54. Wang CY, Bassingthwaighte JB. Capillary supply regions. Math Biosci 2001; 173(2):103–114.

55. Secomb TW, Hsu R, Park EYH, Dewhirst MW. Green's function methods for analysis of oxygen delivery to tissue by microvascular networks. Ann Biomed Eng 2004;32(11):1519–1529.

56. Roughton FJW. Diffusion and chemical reaction velocity in cylindrical and spherical systems of physiological interest. Proc R Soc Lond B Biol Sci 1952; 140(899):203–229.

57. Reneau DDJ, Bruley DF, Knisely MH. A digital simulation of transient oxygen transport in capillary-tissue systems (cerebral grey matter). Development of a numerical method for solution of transport equations describing coupled convection-diffusion systems. A I Ch E 1969;15(6):916–925.

58. Lagerlund TD, Low PA. Mathematical modeling of time-dependent oxygen transport in rat peripheral nerve. Comput Biol Med 1993;23(1):29–47.

59. Sharma GC, Jain M. A computational solution of mathematical model for oxygen transport in peripheral nerve. Comput Biol Med 2004;34(7):633–645.

60. Nicholson C, Phillips JM. Ion diffusion modified by tortuosity and volume fraction in the extracellular microenvironment of the rat cerebellum. J Physiol 1981;321:225–257.

61. Zwick S, Brix G, Tofts P, Strecker R, Kopp-Schneider A, Laue H, Kiessling F. Simulation-based comparison of two approaches frequently used for dynamic contrast-enhanced MRI. Eur Radiol 2010;20:432–442.

62. Sourbron SP, Buckley DL. On the scope and interpretation of the Tofts models for DCE-MRI. Magn Reson Med 2011;66(3):735–745.

63. Bassingthwaighte JB. Capillary Permeability. In Wiley Enciclopedia of Biomedical Engineering. Akay, M (ed.). John Wiley and Sons, Inc., 2006; digital object identifier (doi): 10.1002/9780471740360.ebs0211.

64. Meier-Ruge W, Hunziker O, Schulz U, Tobler HJ, Schweizer A. Stereological changes in the capillary network and nerve cells of the aging human brain. Mech Ageing Devel 1980;14:233–243.

65. Pawlik G, Rackl A, Bing RJ. Quantitative capillary topography and blood flow in the cerebral cortex of cats: an *in vivo* microscopic study. Brain Res 1981; 208:35–58.

66. Bassingthwaighte JB, Yipintsoi T, Harvey RB. Microvasculature of the dog left ventricular myocardium. Microvasc Res 1974;7(2):229–249.

67. Honig CR, Feldstein ML, Frierson JL. Capillary lengths, anastomoses, and estimated capillary transit times in skeletal muscle. Am J Physiol 1977; 233(1):H122–H129.

68. Moffat DB, Fourman J. The vascular pattern of the rat kidney. J Anat 1963; 97(4):543–553.

69. Goresky CA. The nature of transcapillary exchange in the liver. Can Med Assoc J 1965;92:517–522.

70. Nicholson C, Syková E. Extracellular space structure revealed by diffusion analysis. Trends in Neurosciences 1998;21(5):207–215.

71. Novikov DS, Kiselev VG. Effective medium theory of a diffusion-weighted signal. NMR Biomed 2010;23(7):682–697.

72. Zweifach BW. Permeability aspects of blood tissue exchange. Invest Ophthalmol 1965;4(6):1065–1074.

73. Goldman D. Theoretical models of microvascular oxygen transport to tissue. Microcirculation 2008;15(8):795–811.

74. Kiselev VG, Posse S. Analytical theory of susceptibility induced NMR signal dephasing in a cerebrovascular network. Phys Rev Lett 1998;81:5696–5699.

75. Kiselev VG, Novikov DS. Transverse NMR relaxation as a probe of mesoscopic structure. Phys Rev Lett 2002;89:278101.

76. Landis CS, Li X, Telang FW, Molina PE, Palyka I, Vetek G, Springer CS. Equilibrium transcytolemmal water-exchange kinetics in skeletal muscle in vivo. Magn Reson Med 1999;42(3):467–478.

77. Paganelli CV, Solomon AK. The rate of exchange of tritiated water across the human red cell membrane. J Gen Physiol 1957;41(2):259–277.

78. Fenstermacher J, Gross P, Sposito N, Acuff V, Pettersen S, Gruber K. Structural and functional variations in capillary systems within the brain. Ann N Y Acad Sci 1988;529:21–30.

79. Abramson HA. The mechanism of the inflammatory process: III. Electrophoretic migration of inert particles and blood cells in gelatin sols and gels with reference to leucocyte emigration through the capillary wall. J Gen Physiol 1928;11(6):743–756.

80. Novikov DS, Fieremans E, Jensen JH, Helpern JA. Random walks with barriers. Nat Phys 2011;7(6):508–514.

81. Crone C. The permeability of capillaries in various organs as determined by use of the 'indicator diffusion' method. Acta Physiol Scand 1963;58:292–305.

82. Fung YC. Blood flow in the capillary bed. J Biomech 1969;2(4):353–372.

83. Mitra PP, Sen PN, Schwartz LM, Le Doussal P. Diffusion propagator as a probe of the structure of porous media. Phys Rev Lett 1992;68(24):3555–3558.

84. Latour LL, Kleinberg RL, Mitra PP, Sotak CH. Pore-size distributions and tortuosity in heterogeneous media. J Magn Reson Series A 1995;112:83–91.

85. Kiselev VG. In Diffusion MRI: Theory, Methods and Applications. New York: Oxford University Press, Inc., 2011; 152–168.

86. Fieremans E, Jensen JH, Helpern JA. White matter characterization with diffusional kurtosis imaging. Neuroimage 2011;58(1):177–188.

87. Nicholson C. Diffusion and related transport mechanisms in brain tissue. Rep Prog Phys 2001;64:815–884.

88. Leigh JS. Relaxation times in systems with chemical exchange: Some exact solutions. J Magn Reson 1971;4:308–311.

89. Donahue KM, Weisskoff RM, Burstein D. Water diffusion and exchange as they influence contrast enhancement. J Mag Reson Imag 1997;7(1):102–110.

90. Bauer WR, Schulten K. Theory of contrast agents in magnetic resonance imaging: coupling of spin relaxation and transport. Magn Reson Med 1992;26(1):16–39.

91. Albert MS, Huang W, Lee JH, Patlak CS, Springer Jr CS. Susceptibility changes following bolus injections. Magn Reson Med 1993;29(5):700–708.

92. van Osch MJP, Vonken EJPA, Wu O, Viergever MA, van der Grond J, Bakker CJG. Model of the human vasculature for studying the influence of contrast injection speed on cerebral perfusion MRI. Magn Reson Med 2003;50(3):614–622.

93. Seylaz J, Charbonné R, Nanri K, Euw DV, Borredon J, Kacem K, Méric P, Pinard E. Dynamic in vivo measurement of erythrocyte velocity and flow in capillaries and of microvessel diameter in the rat brain by confocal laser microscopy. J Cereb Blood Flow Metab 1999;19(8):863–870.

94. Le Bihan D, Turner R, Patronas N. Diffusion MR imaging in normal brain and in brain tumor. In D Le Bihan, ed., Diffusion and perfusion. Magnetic resonance imaging: Applications to functional MRI. New York: Raven Press, 1995; 134–140.

95. Berg HC. Random Walks in Biology. Princeton, NJ: Princeton Univesity Press, new, expanded edition, 1993.

96. Solera Ureña JR, Olmos S, Kiselev VG. Tissue–blood exchange of extravascular longitudinal magnetisation with account of intracompartmental diffusion. Magn Reson Med 2011;66(5):1445–1455.

97. Rey Pastor J, Pi Calleja P, Trejo CA. Análisis Matemático, Vol. 3, 3.ª edición. Buenos Aires: Editorial Kapelusz, 1965.

98. Danckwerts PV. Absorption by simultaneous diffusion and chemical reaction into particles of various shapes and into falling drops. Trans Faraday Soc 1951; 47:1014–1023.

99. Courant R, Hilbert D. Methoden der Mathematischen Physik, 4. Auflage. Berlin: Springer Verlag, 1993.

100. Grattan-Guinness I. Why did George Green Write His Essay of 1828 on Electricity and Magnetism? The American Mathematical Monthly 1995;102(5):387–396.

101. Kaplan W. Advanced Calculus. Boston, USA: Addison–Wesley Publishing Company, 5th edition, 2003.

102. Yablonskiy DA, Haacke EM. Theory of NMR signal behavior in magnetically inhomogeneous tissues: the static dephasing regime. Magn Reson Med 1994; 32(6):749–763.

103. Kac M. Can one hear the shape of a drum? The American Mathematical Monthy 1966;73(4, Part 2):1–23.

104. Kiselev VG, Shnir YM, Tregubovich AY. Introduction to Quantum Field Theory. Amsterdam: Gordon and Breach Science Publishers, 2000.

105. Meier P, Zierler KL. On the theory of the indicator-dilution method for measurement of blood flow and volume. J Appl Physiol 1954;6(12):731–744.

106. Bassingthwaighte JB, Chinard FP, Crone C, Goresky CA, Lassen NA, Reneman RS, Zierler KL. Terminology for mass transport and exchange. Am J Physiol 1986;250(4 Pt 2):H539–H545.

107. Vann PG, Fitz-Gerald JM. Flow mechanics of red cell trains in very narrow capillaries. I. Trains of uniform cells. Microvasc Res 1982;24(3):296–313.

108. Hochmuth RM, Marple RN, Sutera SP. Capillary blood flow. I. Erythrocyte deformation in glass capillaries. Microvasc Res 1970;2(4):409–419.

109. Prasassarakich P, Walawender WP. On application of the concentric annular flow model to the flow of blood in small-diameter tubes. Microvasc Res 1980; 20(2):165–181.

110. Judd RM, Reeder SB, May-Newman K. Effects of water exchange on the measurement of myocardial perfusion using paramagnetic contrast agents. Magn Reson Med 1999;41(2):334–342.

111. Bauer WR, Nadler W, Bock M, Schad LR, Wacker C, Hartlep A, Ertl G. Theory of the BOLD effect in the capillary region: an analytical approach for the determination of T_2^* in the capillary myocardium. Magn Reson Med 1999;41(1):51–62.

112. Meier-Ruge W, Ulrich J, Brühlmann M, Meier E. Age-related white matter atrophy in the human brain. Ann N Y Acad Sci 1992;673:260–269.

113. Vestergaard-Poulsen P, Hansen B, Østergaard L, Jakobsen R. Microstructural changes in ischemic cortical gray matter predicted by a model of diffusion-weighted MRI. J Magn Reson Imaging 2007;26(3):529–540.

114. Quirk JD, Bretthorst GL, Duong TQ, Snyder AZ, Springer Jr CS, Ackermann JJH, Neil JJ. Equilibrium water exchange between the intra- and extracellular spaces of mammalian brain. Magn Reson Med 2003;50(3):493–499.

115. Pedley TJ. The interaction between stirring and osmosis. Part 2. Journal of Fluid Mechanics 1981;107:281–296.

116. Pohl P, Saparov SM, Antonenko YN. The size of the unstirred layer as a function of the solute diffusion coefficient. Biophys J 1998;75(3):1403–1409.

117. Patlak CS, Paulson OB. The role of unstirred layers for water exchange across the blood-brain barrier. Microvasc Res 1981;21(1):117–127.

118. Pedley TJ. The interaction between stirring and osmosis. Part 1. Journal of Fluid Mechanics 1980;101:843–861.

119. He X, Raichle ME, Yablonskiy DA. Transmembrane dynamics of water exchange in human brain. Magn Reson Med 2012;67(2):562–571.

120. Donahue KM, Burstein D, Manning WJ, Gray ML. Studies of Gd-DTPA relaxivity and proton exchange rates in tissue. Magn Reson Med 1994;32(1):66–76.

121. Su MY, Jao JC, Nalcioglu O. Measurement of vascular volume fraction and blood-tissue permeability constants with a pharmacokinetic model: studies in rat muscle tumors with dynamic Gd–DTPA enhanced MRI. Magn Reson Med 1994;32(6):714–724.

122. Mitra PP, Sen PN, Schwartz LM. Short-time behavior of the diffusion coefficient as a geometrical probe of porous media. Phys Rev B Condens Matter 1993; 47(14):8565–8574.

123. Jones DK, ed. Diffusion MRI: Theory, Methods and Applications. New York, USA: Oxford University Press, Inc., 1st edition, 2010.

124. Hrabe J, Hrabětová S, Segeth K. A model of effective diffusion and tortuosity in the extracellular space of the brain. Biophys J 2004;87(3):1606–1617.

125. Fieremans E, De Deene Y, Delputte S, Ozdemir MS, D'Asseler Y, Vlassenbroeck J, Deblaere K, Achten E, Lemahieu I. Simulation and experimental verification of the diffusion in an anisotropic fiber phantom. J Magn Reson 2008;190(2):189–199.

126. Mills R. Self-diffusion in normal and heavy waterin the range $1 - 45°$. J Phys Chem 1975;77(5):685–688.

127. Barazany D, Basser PJ, Assaf Y. In vivo measurement of axon diameter distribution in the corpus callosum of rat brain. Brain 2009;132(Pt 5):1210–1220.

128. McConnell HM. Reaction rates by nuclear magnetic resonance. J Chem Phys 1958;28:430–431.

129. McLaughlin AC, Leigh JS. Relaxation times in systems with chemical exchange: approximate solutions for the nondilute case. J Magn Reson Med 1973;9:296–304.

130. Sobol WT, Jackels SC, Cothran RL, Hinson WH. NMR spin-lattice relaxation in tissues with high concentration of paramagnetic contrast media: evaluation of water exchange rates in intact muscle. Med Phys 1991;18(2):243–250.

131. Bauer WR, Hiller KH, Roder F, Rommel E, Ertl G, Haase A. Magnetization exchange in capillaries by microcirculation affects diffusion-controlled spin-relaxation: a model which describes the effect of perfusion on relaxation en-

hancement by intravascular contrast agents. Magn Reson Med 1996;35(1):43–55.

132. Lu H, Clingman C, Golay X, van Zijl PCM. Determining the longitudinal relaxation time (T_1) of blood at 3.0 Tesla. Magn Reson Med 2004;52(3):679–682.

133. Gelman N, Ewing JR, Gorell JM, Spickler EM, Solomon EG. Interregional variation of longitudinal relaxation rates in human brain at 3.0 T: relation to estimated iron and water contents. Magn Reson Med 2001;45(1):71–79.

134. Wacker CM, Wiesman F, Bock M, Jakob P, Sanstede JJW, Lehning A, Ertl G, Schad LR, Haase A, Bauer WR. Determination of regional blood volume and intra-extracapillary water exchange in human myocardium using Feruglose: First clinical results in patiens with coronary artery disease. Magn Reson Med 2002;47(5):1013–1016.

135. Garrido L, Wedeen VJ, Kwong KK, Spencer UM, Kantor HL. Anisotropy of water diffusion in the myocardium of the rat. Circ Res 1994;74(5):789–793.

136. Saeed M, Higgins CB, Geschwind JF, Wendland MF. T_1-relaxation kinetics of extracellular, intracellular and intravascular MR contrast agents in normal and acutely reperfused infarcted myocardium using echo-planar MR imaging. Eur Radiol 2000;10(2):310–318.

137. Verkman AS, Wong KR. Proton nuclear magnetic resonance measurement of diffusional water permeability in suspended renal proximal tubules. Biophys J 1987;51(5):717–723.

138. Moskowitz DW, Schneider AN, Lane PH, Schmitz PG, Gillespie KN. Effect of epidermal growth factor in the rat 5/6 renal ablation model. J Am Soc Nephrol 1992;3(5):1113–1118.

139. Thoeny HC, Keyzer FD. Diffusion-weighted MR imaging of native and transplanted kidneys. Radiology 2011;259(1):25–38.

140. Quigley R, Baum M. Water transport in neonatal and adult rabbit proximal tubules. Am J Physiol Renal Physiol 2002;283(2):F280–F285.

141. Rooney WD, Johnson G, Li X, Cohen ER, Kim SG, Ugurbil K, Springer CJS. Magnetic field and tissue dependencies of human brain longitudinal ^1H_2O relaxation in vivo. Magn Reson Med 2007;57(2):308–318.

142. Landau LD, Lifshitz EM. Fluid Mechanics. Course of Theoretical Physics, volume 6. Oxford, UK: Pergamon Press, 1959.

143. Nelson P. Física biológica. Energía, información, vida. Barcelona: Ed. Reverté, 2005.

144. Feynman RP, Leighton RB, Sands M. The Feynman Lectures on Physics. The Definitive Edition (3 volumes). San Francisco, USA: Pearson Addison Wesley, 2006.

145. Whitaker S. Advances in theory of fluid motion in porous media. Industrial & Engineering Chemistry 1969;61(12):14–28.

146. Wood BD, Whitaker S. Diffusion and reaction in biofilms. Chem Eng Sci 1998; 53(3):397–425.

147. Gray WG, Lee PCY. On the theorems for local volume averaging of multiphase systems. Int J Multiphase Flow 1977;3(4):333–340.

148. Lehner FK. On the validity of Fick's law for transient diffusion through a porous medium. Chemical Engineering Science 1979;34(6):821–825.

149. Brian D Wood SW. Multi-species diffusion and reaction in biofilms and cellular media. Chem Eng Sci 2000;55(17):3397–3418.

150. Kiselev VG. Transverse relaxation effect of MRI contrast agents: a crucial issue for quantitative measurements of cerebral perfusion. J Magn Reson Imaging 2005;22(6):693–696.

151. Whitaker S. The Method of Volume Averaging. Theory and Applications of Transport in Porous Media. Dordrecht, The Netherlands: Kluwer Academic Publishers, 1999.

152. Gray WG. A derivation of the equations for multi-phase transport. Chem Eng Sci 1975;30(2):229–233.

153. Fick A. Ueber Diffusion. Annalen der Physik 1855;170(1):59–86.

154. Friedman MH. Principles and Models of Biological Transport. New York, NY: Springer Business+Science Media, LLC, 2nd edition, 2008.

155. Spiegel MR. Vector Analysis and an Introduction to Tensor Analysis. Schaum's Outline of Theory and Problems. New York: The Schaum Publishing Co., 1959.

156. Isaacson E, Keller HB. Analysis of Numerical Methods. New York: John Wiley & Sons, Inc, 1966.

157. Martínez Salas J. Elementos de Matemáticas, 11.ª edición. Valladolid: Editorial Lex Nova, 1995.

158. Strijkers GJ, Hak S, Kok MB, Springer Jr CS, Nicolay K. Three-compartment T_1 relaxation model for intracellular paramagnetic contrast agents. Magn Reson Med 2009;61(5):1049–1058.

159. Brightman MW, Reese TS. Junctions between intimately apposed cell membranes in the vertebrate brain. J Cell Biol 1969;40(3):648–677.

160. Herscovitch P, Raichle M, Kilbourn M, Welch M. Positron emission tomographic measurement of cerebral blood flow and permeability–surface area product of water using [^{15}O]water and [^{11}C]butanol. J Cereb Blood Flow Metab 1987; 7(5):527–542.

161. Eichling J, Raichle M, Grubb R, MM TP. Evidence of the limitations of water as a freely diffusible tracer in brain of the rhesus monkey. Circ Res 1974;35:358–364.

162. Neuder MS, Jenkins BG, Chesler DA, Moore JB, Lauffer RB, Rosen BR. Estimation of the permeability of the blood brain barrier to water *in vivo* under normal and perturbed conditions. In Proc ISMRM, Issue S2. San Francisco, California, USA, 1991; 707.

163. Rose CP, Goresky CA, Bach GG. The capillary and sarcolemmal barriers in the heart. An exploration of labeled water permeability. Circ Res 1977;41(4):515–533.

164. Gordon MJ, Chu KC, Margaritis A, Ethier C, Rutt BK. Measurement of Gd-DTPA diffusion through PVA hydrogel using a novel magnetic resonance imaging method. Biotechnol Bioeng 2000;65(4):459–467.

165. Gillis A, Gray M, Burstein D. Relaxivity and diffusion of gadolinium agents in cartilage. Magn Reson Med 2002;48(6):1068–1071.

166. Rohrer M, Bauer H, Mintorovitch J, Requardt M, Weinmann HJ. Comparison of magnetic properties of MRI contrast media solutions at different magnetic field strengths. Invest Radiol 2005;40(11):715–724.

167. Spees WM, Yablonskiy DA, Oswood MC, Ackerman JJ. Water proton MR properties of human blood at 1.5 Tesla: magnetic susceptibility, T_1, T_2, T_2^*, and non-Lorentzian signal behavior. Magn Reson Med 2001;45(4):533–542.

168. Clare S, Jezzard P. Rapid T_1 mapping using multislice echo planar imaging. Magn Reson Med 2001;45(4):630–634.

169. Batra S, Rakusan K. Geometry of capillary networks in volume overloaded rat heart. Microvasc Res 1991;42(1):39–50.

170. Donahue KM, Weisskoff RM, Chesler DA, Kwong K, Bogdanov AA, Mandeville JB, Rosen BR. Improving MR quantification of regional blood volume with intravascular T_1 contrast agents: accuracy, precision, and water exchange. Magn Reson Med 1996;36(6):858–867.

171. Lauffer RB. Paramagnetic metal complexes as water proton relaxation agents for NMR imaging: theory and design. Chemical Reviews 1987;87(5):901–927.

172. Balanzat M. Matemática avanzada para la Física. Buenos Aires: Editorial Universitaria de Buenos Aires (Eudeba S.E.M.), 1973.

173. Rey Pastor J. Curso de Cálculo Infinitesimal, 8.ª edición. Madrid: Biblioteca Matemática, S. L., 1973.

174. Grebenkov DS, Nguyen BT. Geometric structure of Laplacian eigenfunctions. SIAM Reviews 2013;arXiv:1206.1278v2.

175. Abramowitz M, Stegun I, eds. Handbook of Mathematical Functions. Washington D.C.: National Bureau of Standards, 10th printing, 1972.

176. Crank J. The Mathematics of Diffusion. Oxford: Oxford University Press, 2nd edition, 1975.

177. Fourier J. Théorie Analytique de la Chaleur. Paris: Chez Firmin Didot, Père et Fils, 1822. Facisimile, Éditions Jacques Gabay, Sceaux, 1988.

178. Carslaw HS, Jaeger JC. Conduction of Heat in Solids. Oxford: Oxford University Press, 2nd edition, 1959.

179. Sommerfeld A. Vorlesungen über Teoretische Physik. Band VI. Partielle Differentialgleichungen der Physik, 6. Auflage. Thun, Deutschland: Verlag Harri Deutsch, 1992.

180. Fiala JC, Spacek J, Harris KM. Dendrites. New York: Oxford University Press, Inc., 2nd edition, 2008; John C. Fiala and Josef Spacek and Kristen M. Harris, eds, pp. 3–41.

181. Gradshteyn IS, Ryzhik IM. Table of Integrals, Series, and Products. San Diego, CA: Academic Press, 6th edition, 2000.

182. Nugent LJ, Jain RK. Plasma pharmacokinetics and interstitial diffusion of macromolecules in a capillary bed. Am J Physiol 1984;246(1 Pt 2):H129–H137.

183. McKean HP, Singer IM. Curvature and the eigenvalues of the Laplacian. J Differential Geometry 1967;1(1):43–69.

184. Ziegler WH, Goresky CA. Transcapillary exchange in the working left ventricle of the dog. Circ Res 1971;29(2):181–207.

185. Kreyszig E. Matemáticas avanzadas para ingeniería, Vol. II. 1.ª edición, 6.ª reimpresión. México D.F.: Editorial Limusa, 1976.

186. Pike MM, Stoops CN, Langford CP, Akella NS, Nabors LB, Gillespie GY. High-resolution longitudinal assessment of flow and permeability in mouse glioma vasculature: Sequential small molecule and SPIO dynamic contrast agent MRI. Magn Reson Med 2009;61(3):615–625.

187. Huang W, Li X, Morris EA, Tudorica LA, Seshan VE, Rooney WD, Tagge I, Wang Y, Xu J, Springer Jr CS. The magnetic resonance shutter speed discriminates vascular properties of malignant and benign breast tumors *in vivo*. Proc Natl Acad Sci USA 2008;105(46):17943–8.

188. Severns ML, Adams JM. The relation between Krogh and compartmental transport models. J Theor Biol 1982;97(2):239–249.

189. Ibaraki M, Ito H, Shimosegawa E, Toyoshima H, Ishigame K, Takahashi K, Kanno I, Miura S. Cerebral vascular mean transit time in healthy humans: a comparative study with PET and dynamic susceptibility contrast-enhanced MRI. J Cereb Blood Flow Metab 2007;27(2):404–413.

190. Leenders KL. In PET pharmacokinetics course manual. Maguire, RP and Leenders, KL (eds); Chapter 3. Kobe, Japan: International Society of Cerebral Blood Flow and Metabolism, 2007; 21–28.

191. Strauss LG. Positron Emission Tomography: Current Role for Diagnosis and Therapy Monitoring in Oncology. Oncologist 1997;2(6):381–388.

192. Hazlewood CF, Chang DC, Nichols BL, Woessner DE. Nuclear magnetic resonance transverse relaxation times of water protons in skeletal muscle. Biophys J 1974;14(8):583–606.

193. Günther M, Bock M, Schad LR. Arterial spin labeling in combination with a look-locker sampling strategy: inflow turbo-sampling EPI-FAIR (ITS-FAIR). Magn Reson Med 2001;46(5):974–984.

194. Petersen ET, Lim T, Golay X. Model-free arterial spin labeling quantification approach for perfusion MRI. Magn Reson Med 2006;55(2):219–232.

195. St Lawrence KS, Wang J. Effects of the apparent transverse relaxation time on cerebral blood flow measurements obtained by arterial spin labeling. Magn Reson Med 2005;53(2):425–433.

196. Wang DJJ, Bi X, Avants BB, Meng T, Zuehlsdorff S, Detre JA. Estimation of perfusion and arterial transit time in myocardium using free-breathing myocardial arterial spin labeling with navigator-echo. Magn Reson Med 2010; 64(5):1289–1295.

197. MacIntosh BJ, Filippini N, Chappell MA, Woolrich MW, Mackay CE, Jezzard P. Assessment of arterial arrival times derived from multiple inversion time pulsed arterial spin labeling MRI. Magn Reson Med 2010;63(3):641–647.

198. Alsop DC, Detre JA. Reduced transit-time sensitivity in noninvasive magnetic resonance imaging of human cerebral blood flow. J Cereb Blood Flow Metab 1996;16(6):1236–1249.

199. Gallichan D, Jezzard P. Variation in the shape of pulsed arterial spin labeling kinetic curves across the healthy human brain and its implications for CBF quantification. Magn Reson Med 2009;61(3):686–695.

200. Fernández-Seara MA, Wang Z, Wang J, Rao HY, Guenther M, Feinberg DA, Detre JA. Continuous arterial spin labeling perfusion measurements using single shot 3D GRASE at 3 T. Magn Reson Med 2005;54(5):1241–1247.

Index